

Bore-Driven Swash on a Mobile Beach

David M. Kelly

Thesis submitted to The University of Nottingham
for the degree of Doctor of Philosophy

January 2009

GEORGE GREEN LIBRARY OF
SCIENCE AND ENGINEERING¹

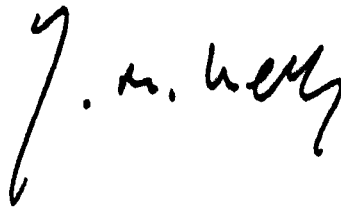
Acknowledgements

I am extremely grateful to my supervisor Professor Nicholas Dodd for putting his trust in me and providing me with the opportunity to undertake this research. I wish to thank him for all that I have learnt under his guidance, his help, his suggestions and, above all, his dedicated support over the last three-years. I would also like to thank Dr. Stephen Hibberd for his helpful advice, encouragement and for the three-year loan of his own PhD thesis. Additionally, I would like to acknowledge the help and support of my colleagues at the Environmental Fluid Mechanics research group both past and present; in particular Mr. Anurak Sriariyawat, Dr. Riccardo Briganti and Dr. Haider Hasan. I wish to thank my parents for translating a number of papers from the original German or French. Lastly, I wish to thank my beautiful wife Louise who put her own life on hold to help make this PhD thesis a reality.

Throughout the course of this research I was in receipt of a generous grant from the UK Engineering and Physical Sciences Research Council to whom I am indebted.

Memorandum

The work for this thesis, "Bore-Driven Swash on a Mobile Beach", was carried out in the School of Civil Engineering at the University of Nottingham during the period January 2006 to December 2008 and has not been submitted for any other degree or diploma of any examining body. All the work discussed is the original work of the author, except for that acknowledged in the text.

A handwritten signature in black ink, appearing to read 'D. M. Kelly', with a stylized, cursive script.

D. M. KELLY

December 2008

Synopsis

The problem of cross-shore beach face evolution in the swash zone is examined within the framework of the shallow water theory. A system comprising the shallow water and Exner equations is solved numerically using both uncoupled and fully coupled approaches. The uncoupled model assumes that changes in bed height have a negligible effect on the flow over a swash event, whereas the fully coupled model updates the hydrodynamic variables and beach profile simultaneously. In order to obtain accurate results over a single swash event several new numerical solvers based on the method of characteristics (MOC) and the MacCormack (1969) explicit finite-difference scheme are detailed. Particular attention is given to the treatment of discontinuities. A procedure for the explicit treatment of discontinuities, derived from techniques employed in gas dynamical problems, is developed and applied. Certain rather novel shock capturing approaches are also investigated. The shoreline boundary is discussed and a new robust algorithm for the treatment of this boundary on both fixed and mobile beds is presented. The resulting numerical models are used to simulate a variety of different swash events on an initially plane sloping mobile beach. Predictions of beach face evolution are made using the fully coupled approach and are compared with predictions made using an uncoupled analytical beach evolution model based on that of Pritchard and Hogg (2005). The fully coupled model leads to some interesting observations, in

particular the possibility of local onshore sediment transport and the occurrence of a seaward facing sediment bore in the backwash. A characteristics based analysis is performed and reveals important differences in the flow structure of coupled and uncoupled swash events. The maximum wave run-up is also considered and it is shown that for the fully coupled system the run-up is significantly less than that predicted by the Shen and Meyer (1963) theory and motion of the leading edge can no longer be determined using simple ballistics concepts. Additionally, for verification purposes, new quasi-analytical solutions are constructed for the mobile bed dam-break problem using two distinct sediment transport formulae.

Contents

1	Introduction	7
2	Literature Review	14
2.1	Analysis of swash zone hydrodynamics	14
2.2	Numerical modelling of bore-driven swash	19
2.3	Modelling beach face evolution in the swash zone	23
2.4	Fixed bed dam-break problem	26
2.5	Mobile bed dam-break problem	29
3	1 D Mathematical Model	33
3.1	Introduction	33
3.2	Governing Equations	34
3.2.1	Nonlinear Shallow Water Equations (NLSWE)	34
3.2.2	Bed Evolution (Exner) Equation	36
3.3	Sediment Transport Processes and Formulae	38
3.3.1	Relating A to physical parameters	39

3.3.2	Closing the Exner equation	40
3.3.3	Values for sediment mobility parameters from field data	41
3.4	Characteristic Decomposition	42
3.4.1	Shallow water system: fixed bed case	42
3.4.2	Shallow water–Exner system: mobile bed case	44
3.4.3	Variation of eigenvalues with Froude number	48
3.5	Eigenvalues of the shallow water–Exner system at the wave tip	51
3.6	Eigenvectors of the shallow water–Exner system	52
3.6.1	Closure given by $q = Au^3$	52
3.6.2	Closure given by $q = \bar{A}u^3h$	54
3.6.3	A note on the sediment flux formulation used for closure	54
4	Numerical Methods	56
4.1	Hydrodynamic (fixed bed) solver	56
4.1.1	The method of characteristics	57
4.1.2	MOC GC technique	57
4.1.3	A note on the formal accuracy of MOC GC schemes	64
4.2	Morphodynamic (mobile bed) solvers	65
4.2.1	Specified time interval (STI) method of characteristics	65
4.2.2	Initial time step for dam–break IC	68
4.2.3	Finite difference method – MacCormack’s scheme	69
4.2.4	Conservation form	71

- 4.2.5 Treatment of source terms for the conservation form 72
- 4.3 Boundary conditions for non-GC schemes 73
 - 4.3.1 Upstream (seaward) transmissive boundary 73
 - 4.3.2 Downstream (shoreline) boundary 74
 - 4.3.3 Stencil for the penultimate mesh point when using MacCormack
based schemes 80
 - 4.3.4 Treatment of the penultimate mesh point in shock capturing schemes 80
- 4.4 Model verification 81
- 5 Discontinuous Flow 87
 - 5.1 Shock Capturing Schemes 87
 - 5.1.1 The philosophy behind shock capturing 87
 - 5.1.2 On the instability of shock capturing schemes 88
 - 5.1.3 Entropy violating shocks 91
 - 5.1.4 Classic filtering 92
 - 5.1.5 Hybrid scheme 94
 - 5.1.6 Breuss Filter 98
 - 5.2 Shock fitting 102
 - 5.2.1 The philosophy behind shock fitting 102
 - 5.2.2 Types of fitting procedure 103
 - 5.3 Rankine Hugoniot (jump) conditions 104
 - 5.3.1 Rankine Hugoniot conditions for the shallow water-Exner system 104

5.3.2 Bore relations for a uniform bore advancing into still water over
a mobile bed ($q = Au^3$) 109

5.3.3 Analysis of the wave tip discontinuity when $q = Au^3$ 110

5.4 Implementation of shock fitting procedure for swash flow 113

5.4.1 Shock detection 113

5.4.2 Shock inception on a characteristics grid 114

5.4.3 Shock inception on a fixed grid 115

5.4.4 Shock evolution on a characteristics grid 116

5.4.5 Shock evolution on a fixed grid 119

5.5 Comparison of fitted and captured shocks on a mobile bed 124

5.6 Comparison of hybrid and WAF results 129

6 Mobile bed dam-break: quasi-analytical solutions 131

6.0.1 Background 131

6.0.2 Wave structure 132

6.0.3 Generalised Riemann invariants 135

6.0.4 Constructing the solution 136

6.0.5 Sediment conservation 139

6.1 Self-similarity 139

6.2 Validation 140

6.3 Non-dimensionalisation 141

6.3.1 Sediment flux given by $q = Au^3$ 143

6.3.2	Sediment flux given by $q = \bar{A}u^3h$	144
6.3.3	Values for the bed evolution parameters σ and $\bar{\sigma}$	145
6.4	Shock relation at the wave tip	145
6.5	Example results for $q = Au^3$ and $q = \bar{A}u^3h$	146
6.5.1	Bed profile and tip velocity when $q = \bar{A}u^3h$	147
6.6	Comparison with experimental results	154
7	Uncoupled swash simulations	158
7.1	SM63 swash	159
7.1.1	Analytical solution for both flux formulations	159
7.1.2	Uncoupled beachface evolution for SM63 swash	161
7.2	HP79 swash	163
7.2.1	Flow variables and instantaneous sediment fluxes	168
7.2.2	Uncoupled beachface evolution for HP79 swash	168
8	Fully coupled swash simulatons	175
8.1	SM63 swash with $q = Au^3$	176
8.1.1	Model set-up	176
8.1.2	Flow structure	176
8.1.3	Beachface evolution	178
8.1.4	Relationship between final beach profile and bed evolution parameter (σ)	182
8.1.5	Analysis of shoreline motion in the run-up when $q = Au^3$	187

8.2 HP79 swash 190

8.2.1 Model set-up 190

8.2.2 Results for $q = Au^3$ 191

8.2.3 Results for $q = \tilde{A}u^3h$ 195

9 Conclusions and recommendations 204

9.1 Review and conclusions 204

9.2 Recommendations 208

A Obtaining initial conditions for SM63 swash on a mobile beach 212

A.0.1 Discontinuous initial conditions 212

A.0.2 Convergence 214

B Riemann equations at the wave tip for $q = Au^3$ 216

C Rankine Hugoniot conditions for the shallow water system 219

D Validation of numerical schemes 224

References 233

List of Figures

1.1	Schematic of the nearshore	9
1.2	Breaker types. From top to bottom: Spilling, Plunging, Collapsing and Surging. Reproduced from Galvin (1972)	11
2.1	Schematic of a bore climbing a planar beach showing the notation used in the derivation of Whitham's characteristic rule.	15
3.1	Definition sketch for mobile bed flow in the swash zone	37
3.2	Variation of dimensionless wave speeds with Froude number (Fr) for $q = Au^3$ transport ($A = 0.001 \text{ s}^2\text{m}^{-1}$, $p=0.4$).	49
3.3	Variation of dimensionless wave speeds with Froude number (Fr) for $q = \bar{A}u^3h$ transport ($\bar{A} = 0.01 \text{ s}^2\text{m}^{-2}$, $p=0.4$)	50
4.1	The region of integration for a single swash event showing the limiting characteristics, i.e. the seaward boundary characteristic (bold solid line) the shoreline boundary C^- characteristic (solid line) and the last C^+ characteristic (dashed line).	58

4.2 Close-up of the initial, seaward boundary, characteristic (bold solid line) and the adjacent C^- characteristic illustrating the notation employed to describe the MOC GC scheme. 59

4.3 Computational mesh for MOC GC fixed bed scheme showing close-up of a typical (subcritical) cell. 61

4.4 Characteristics attending to an ordinary mesh point for the mobile bed MOC STI scheme (sub-critical flow). 66

4.5 Computational stencil for the MacCormack predictor-corrector scheme. 71

4.6 Characteristics based treatment of the upstream (seaward) boundary for mobile bed flow 73

4.7 Downstream (shoreline) boundary treatment using a time dependent space step for mobile bed flow 75

4.8 Snapshots of water height at $t=5s$ for a fixed bed wet-dry dam-break showing the effect of thin film depth (h_{tf}) on wave profile and tip velocity. 76

4.9 Comparison of analytical (lines) and Mac-mLxF numerical (circles) predictions of the water height h at times shown for SM63 swash with $A = 1 \times 10^{-10}s^2m^{-1}$ 84

4.10 Comparison of analytical (lines) and STI MOC numerical (circles) predictions of the water height h at times shown for SM63 swash with $A = 1 \times 10^{-10}s^2m^{-1}$ 85

4.11 Comparison of analytical and numerical predictions of the instantaneous shoreline position for SM63 swash with $A = 1 \times 10^{-10}s^2m^{-1}$ here $\Delta x = 5 \times 10^{-3}m$ 86

5.1	Formation of parasitic oscillations near a shock. Initial configuration (solid line) and profile after two time steps (dashed line) following the argument of Moretti (1969).	88
5.2	Snapshots of Stoker (1948) analytical solution (red line) and solution by MacCormack–mLxF hybrid solver (squares) without (left) and with (right) Breuss filtering at $t=1,2,3$ and $4s$	99
5.3	Schematic diagram illustrating removal of artificial diffusion by Breuss filtering.	100
5.4	Schematic of a uniform bore advancing into still water over a mobile bed	110
5.5	Schematic diagram of the sediment bore observed at the wave tip ($x = x_1$) when a transport formula of the form $q = Au^3$ is used	112
5.6	Schematic of the characteristics grid illustrating shock development . . .	117
5.7	Configuration of characteristics in the $x-t$ plane attending to a.) type 1, b.) type 2 and c.) type 3 shocks. The shock path is shown by the thick line whereas C^+ , C^- and C_b characteristics are represented by thinner solid, dotted and dashed lines respectively.	122
5.8	Uniform bore moving over a mobile bed ($A=0.004s^2m^{-1}$, $p=0$). Snapshots of water and bed elevations after 100 time steps using MacCormack shock capturing scheme with (solid) and without (dashed) the Engquist nonlinear filter.	126
5.9	As in Figure 5.8 but using STI MOC shock fitting scheme (circles) and analytical solution (solid line).	126

5.10 Snapshots of water depth for a bore climbing a mobile beach with $A=0.004s^2m^{-1}$ and $p=0$. Blue solid line shows hybrid shock capturing solution and red dashed line is MOC solution with shock fitting. 127

5.11 Values of dependent variables immediately behind an initially uniform subcritical incident bore as the bore approaches the original shoreline (at $\zeta=10m$), also shown is the bore velocity (W). 128

5.12 Comparison of numerical results at 3000 time-steps with Stoker (1948) analytical solution using WAF-HLL and MacCormack-mLxF hybrid schemes both without (top) and with (bottom) Breuss filter. 130

6.1 Wave structure for the shallow water-Exner mobile bed dam-break for both sediment flux formulations (refer to the accompanying text for details). 132

6.2 Mobile bed dam-break in the flume at the University of Nottingham (Picture courtesy of Dr. R. Munro) 133

6.3 Comparison of "fixed bed" numerical solution with the Ritter analytical solution. For plot details see the accompanying text. 142

6.4 Snapshots of dimensionless dependent variables from the quasi-analytical solution for mobile bed dam-break with $q = Au^3$ where $A = 1 \times 10^{-3}s^2m^{-1}$ and porosity is zero (hence $\sigma = 0.00981$). 149

6.5 Snapshots of dimensionless dependent variables from the quasi-analytical solution for mobile bed dam-break with $q = Au^3$ where $A = 4 \times 10^{-3}s^2m^{-1}$ and porosity is zero (hence $\sigma = 0.039$). 150

6.6 Snapshots of dimensionless dependent variables from the quasi-analytical solution for mobile bed dam-break with $q = Au^3$ where $A = 0.02 \times 10^{-3} \text{s}^2 \text{m}^{-1}$ and porosity is zero (hence $\sigma = 0.2$). 151

6.7 Snapshots of dimensionless dependent variables from the quasi-analytical solution for mobile bed dam-break with $q = \bar{A}u^3h$ where $\bar{A} = 1.5 \times 10^{-2} \text{s}^2 \text{m}^{-2}$ and porosity is zero (hence $\bar{\sigma} = 0.00981$). 152

6.8 Snapshots of dimensionless dependent variables from the quasi-analytical solution for mobile bed dam-break with $q = \bar{A}u^3h$ where $\bar{A} = 4 \times 10^{-3} \text{s}^2 \text{m}^{-2}$ and porosity is zero (hence $\bar{\sigma} = 0.039$). 153

6.9 Snapshots of dimensionless instantaneous sediment fluxes (with $q = \bar{A}u^3h$) for the dam-break of Figure 6.7. 154

6.10 Profile at $t=1\text{s}$ for the dam-break of Figure 6.7 (with $q = \bar{A}u^3h$); inset: close-up of the tip region. 155

6.11 Comparison of the theoretical solution with $\sigma = 0.0164$ (green lines) and measured (black lines) profiles for the Louvaine experiment reported in Fraccarollo and Capart (2002) at $t = 0.75\text{s}$ 157

6.12 Comparison of the theoretical solution with $\sigma = 0.2$ (green lines) and measured (black lines) profiles for the Louvaine experiment reported in Fraccarollo and Capart (2002) at $t = 0.75\text{s}$ 157

7.1 Initial conditions for SM63 swash 159

7.2 Contours of dimensionless instantaneous sediment flux (q^*) where top: $q^* = u^{*3}$. Bottom: $q^* = u^{*3}h^*$; the shoreline is bold and contours are individually labelled. 160

7.3 Top: Dimensionless net sediment flux (Q^*) after one SM63 swash cycle for uncoupled transport model using $Q^* = \int_{t_i(x^*)}^{t_d(x^*)} u^{*3} dt^*$. Bottom: dimensionless net sediment flux (Q^*) after one SM63 swash cycle for uncoupled transport model using $Q^* = \int_{t_i(x^*)}^{t_d(x^*)} u^{*3} h dt^*$ 164

7.4 Top: Dimensionless change in bed level relative to the initially plane beach after one swash cycle with $q^* = u^{*3}$ using $\Delta B^* = -\sigma \frac{\partial Q^*}{\partial x^*}$ with $\sigma = 0.0654$. Bottom: Final beach profile for the same event. The initial (plane) beach profile is shown by a dot-dashed line. 165

7.5 Top: Dimensionless change in bed level relative to the initially plane beach after one swash cycle with $q^* = u^{*3} h^*$ using $\Delta B^* = -\bar{\sigma} \frac{\partial Q^*}{\partial x^*}$ with $\bar{\sigma} = 0.15$. Bottom: Final beach profile for the same event. The initial (plane) beach profile is shown by a dot-dashed line. 166

7.6 Notation and initial bathymetry for a uniform bore approaching a plane sloping beach. 167

7.7 Top: contours of dimensionless water height $h^* = 0.1$ to 2.4 at intervals of 0.1 . Bottom: contours of dimensionless water velocity $u^* = -1.8$ to 1.8 . 169

7.8 Contours of dimensionless instantaneous sediment flux (q^*) for HP79 swash where top: $q^* = u^{*3}$. Bottom: $q^* = u^{*3} h^*$; the shoreline is bold and contours are individually labelled. 170

7.9 Dimensionless instantaneous sediment fluxes, $q^* = u^{*3}$, for SM63 (dashed line) and HP79 (solid line) swash at, clockwise from top, 30%, 40%, 60% and 80% of the respective maximum run-up distances. 173

7.10 Dimensionless net sediment flux (Q^*) after one HP79 swash cycle for the uncoupled transport model using $q^* = u^{*3}$ 174

7.11 Dimensionless net sediment flux (Q^*) after one HP79 swash cycle for the uncoupled transport model using $q^* = u^{*3}h^*$ 174

8.1 Space-time plot showing showing contours of dimensionless water depth (h^*) for SM63 type swash with $\sigma = 0.01$ top, $\sigma = 0.0654$ middle and $\sigma = 0.2$ bottom. 179

8.2 Space-time plot showing showing contours of dimensionless water velocity (u^*) for SM63 type swash with $\sigma = 0.01$ top, $\sigma = 0.0654$ middle and $\sigma = 0.2$ bottom. 180

8.3 Space-time plot showing showing contours of dimensionless change in beach level (ΔB^*) for SM63 type swash with $\sigma = 0.01$ top, $\sigma = 0.0654$ middle and $\sigma = 0.2$ bottom. 181

8.4 Sequence of run-up and backwash for SM63 initial conditions over a mobile beach where sediment flux is of the form $q = Au^3$ and $\sigma=0.0654$. 183

8.5 Grid of characteristics for mobile bed SM63 swash. Advancing (C^+) characteristics dashed lines, receding (C^-) characteristics grey solid lines and bed (C_b) characteristics black solid lines. 184

8.6 Comparison of the instantaneous shoreline position for SM63 swash on a fixed (dashed line) and mobile (solid line) beach. 184

8.7 Left: change in bed level relative to the initially plane beach for uncoupled (dashed) and fully coupled (solid) transport models after one SM63 swash cycle. Right: final beach profile for uncoupled (dashed) and fully coupled (solid) transport models. Top: $\sigma = 0.01$, middle: $\sigma = 0.0654$, bottom: $\sigma = 0.2$. Dot-dashed lines show the initial bed profile. 186

8.8 Left: variation of the (dimensionless) amount of net onshore transport with the bed evolution parameter σ . Right: variation of the (dimensionless) amount of sediment mobilised at t_I with the bed evolution parameter σ 187

8.9 Top: Change in bed level relative to the initially plane beach for fully coupled transport model after one swash cycle for $\sigma = 0.01$, $\sigma = 0.0654$ and $\sigma = 0.2$. Bottom: close up of the regions of accretion for these swash events. 188

8.10 Variation of $\frac{\partial h}{\partial x}$ (solid line) and $\frac{\partial u}{\partial x}$ (dashed line) with t at the meshpoint immediately before the wave tip for the mobile bed dam-break when $\sigma = 0.0654$ 189

8.11 Variation of $\frac{\partial h}{\partial x}$ (left) and $\frac{\partial u}{\partial x}$ (right) with time at the meshpoint immediately before the shoreline during the run-up according to the Riemann wave solution with $\sigma = 0.0654$ 190

8.12 Space-time plot showing contours of (top) dimensionless water depth (h^*) and (bottom) dimensionless water velocity (u^*) for HP79 type swash with $q = Au^3$ ($\sigma = 0.0654$). 193

8.13 Space-time plot showing contours of (top) dimensionless change in beach height (ΔB^*) and (bottom) grid of characteristics for HP79 type swash with $q = Au^3$ ($\sigma = 0.0654$). Black dashed lines are C^+ characteristics, red solid lines C^- characteristics and black solid lines C_b characteristics. 194

8.14 Run-up of the HP79 uniform bore over a mobile beach where sediment flux is of the form the $q = Au^3$ and $\sigma = 0.004$ 196

- 8.15 Backwash of the HP79 uniform bore over a mobile beach where sediment flux is of the form the $q = Au^3$ and $\sigma=0.004$ 197
- 8.16 Space-time plot showing contours of (top) dimensionless water depth (h^*) and (bottom) dimensionless water velocity (u^*) for HP79 type swash with $q = \bar{A}u^3h$ ($\bar{\sigma} = 0.15$). 200
- 8.17 Space-time plot showing contours of (top) dimensionless change in beach height (ΔB^*) and (bottom) grid of characteristics for HP79 type swash with $q = \bar{A}u^3h$ ($\bar{\sigma} = 0.15$). Black dashed lines are C^+ characteristics, red solid lines C^- characteristics and black solid lines C_b characteristics. . . . 201
- 8.18 Top: Snapshots of ΔB^* in the run-up at $t^* = 5$ to 40 at intervals of 5 and bottom: Change in bed level relative to the initially plane beach for one HP79 swash cycle (inset close-up of erosion) with $q = \bar{A}u^3h$ ($\bar{\sigma} = 0.245$). 202
- 8.19 Top: Snapshots of ΔB^* in the run-up at $t^* = 5$ to 35 at intervals of 5 and bottom: Change in bed level relative to the initially plane beach for one HP79 swash cycle (inset close-up of erosion) with $q = \bar{A}u^3h$ ($\bar{\sigma} = 0.15$). . 203
- A.1 Top: convergence of solution as as $t_I \rightarrow 0$ for figure details refer to the accompanying text and bottom: convergence of the shoreline trajectory as as $t_I \rightarrow 0$ with Δx fixed at 0.001m. 215
- D.1 Snapshots of water velocity (top) and depth (bottom) at 1s intervals computed using second-order GC MOC scheme (red dashed) and SM63 analytical solution (cyan solid) for run-up (left) and backwash (right). . . . 225

D.2 Non-dimensional water surface elevation for a single swash event showing run-up (top) and backwash (bottom) computed using second-order GC MOC scheme. The backwash bore was detected and fitted using the techniques detailed in §§5.4.2 and 5.4.4. Circles indicate the shoreline position. 227

D.3 Snapshots of the wet-dry mobile bed dam-break problem with $q = Au^3$ solved using the MacCormack-mLxF scheme (blue dashed lines) compared with the quasi-analytical solution (red solid lines). Here $\Delta x = 0.01\text{m}$ 228

D.4 Snapshots of all dependent variables at $t=1\text{s}$ for mobile bed dam-break with $\sigma=0.03924$. First-order STI MOC results with $\Delta x=0.01\text{m}$ plotted every 5 data points (circles) and quasi-analytical solution (lines). 230

D.5 Snapshots of all dependent variables at $t=1\text{s}$ for mobile bed dam-break with $\sigma=0.03924$. Second-order STI MOC results with $\Delta x=0.01\text{m}$ plotted every 5 data points (circles) and quasi-analytical solution (lines). 231

D.6 Testing convergence of the STI MOC scheme as Δx is meshed down using (top) final bed level change (ΔB) as an indicator and (bottom) using the instantaneous shoreline position ($x_*[\text{m}]$) as an indicator ($\sigma=0.0654$ and t_f is fixed at 0.2s). 232

List of Tables

2.1	Results of several different shoreline boundary treatments for a Riemann-type scheme. The table shows the maximum computed run-up $x_{s,max}$ and swash period T_{swash} . Model PW01 gives the analytical results of Shen and Meyer (1963) ($\Delta x = 0.09\text{m}$). From Briganti and Dodd (2008) with permission of the authors.	22
4.1	Computational parameters used for the verification of both STI MOC and MacCormack based numerical schemes.	82
6.1	Comparison of bed heights predicted using (5.3.38) and computed by the Riemann wave technique.	146

Nomenclature

[*] Denotes units of the parameter or variable

g [ms^{-2}]	Acceleration due to gravity
ρ [kgm^{-3}]	Water density
ρ_s [kgm^{-3}]	Sediment density
ρ_{rel} [-]	Ratio of densities of sediment and water
A [s^2m^{-1}]	Sediment mobility parameter ($q = u^3$)
\bar{A} [s^2m^{-2}]	Sediment mobility parameter ($q = u^3 h$)
σ [-]	Dimensionless bed evolution parameter
$\bar{\sigma}$ [-]	Dimensionless bed evolution parameter
p [-]	Bed porosity
D_{50} [m]	Median grain size of sediment
ζ [-]	Bed porosity parameter $\frac{1}{1-p}$
$\tan \beta$ [-]	Initial beach slope (plane sloping beach)
f_R [-]	Friction coefficient
ϑ [-]	Dimensionless quantity in the Meyer-Peter and Müller formula
x [m]	Cross-shore distance
x^* [-]	Dimensionless cross-shore distance

x_* [m]	Shoreline or wave tip abscissa
z [m]	Vertical abscissa
t [s]	Time
t^* [-]	Dimensionless time
t_I [s]	Output time for Riemann wave solution
t_i [s]	Inundation time
t_d [s]	Denudation time
h [m]	Water depth
h^* [-]	Dimensionless water depth
h_{tf} [m]	Thin film depth
h_{co} [m]	Cut-off depth used for constructing Riemann wave solutions
h_{cs} [m]	Water depth in the constant state region of a mobile bed dam-break
h_b [m]	Bore height
h_B [m]	Uniform bore amplitude
h_o [m]	Initial water depth used for dam-break problems
h_i [m]	Still water depth in front of uniform bore
u [ms ⁻¹]	Water velocity in x direction (depth averaged)
u^* [-]	Dimensionless water velocity in x direction (depth averaged)
c [ms ⁻¹]	Gravity wave celerity ($g^{\frac{1}{2}}h^{\frac{1}{2}}$)
c_o [ms ⁻¹]	Initial gravity wave celerity for dam-break problems ($g^{\frac{1}{2}}h_o^{\frac{1}{2}}$)
U_b [ms ⁻¹]	Bore velocity at the shoreline
u_* [ms ⁻¹]	Shoreline or wave tip velocity
W [ms ⁻¹]	Bore (shock) velocity

$W_{in} [\text{ms}^{-1}]$	Bore (shock) velocity at inception
$\zeta [\text{m}]$	Bore (shock) position (used in derivation)
$\varrho [-]$	Quantity used in hydrodynamical shock computations
$Y [-]$	Empirical coefficient used in the shock detection procedure
$B [\text{m}]$	Bed height
$B^* [-]$	Dimensionless bed height
$B_* [\text{m}]$	Bed height at the shoreline or wave tip
$\bar{z} [\text{m}]$	$\bar{z} = B(x)$ used to derive shock conditions at bed step
$q [\text{m}^2\text{s}^{-1}]$	Instantaneous sediment flux
$q^* [-]$	Dimensionless instantaneous sediment flux
q_t	Total suspended sediment flux
$[\text{Kgm}^{-1}\text{s}^{-1}]$	
$Q [\text{m}^2]$	Net sediment flux over one swash cycle
$Q [\text{m}^2]$	Final volume of onshore sediment after one swash cycle
$V_s [\text{m}^2]$	Sediment volume
$Fr [-]$	Froude number
$Fr_{rel} [-]$	Relative Froude number
$\mathbf{f} [-]$	Vector of conserved variables
$\mathbf{F} [-]$	Vector of flux conservative variables
$\mathbf{S} [-]$	Vector of source terms
$\Delta x [\text{m}]$	Space step
$\Delta t [\text{s}]$	Time step
$\epsilon [-]$	Parameter used in the MacCormack scheme

θ [-]	Switch function to compute weighted average of first- and second-order fluxes
μ [s ⁻¹]	Constant used to perform characteristic decomposition
ω [s ⁻¹]	Constant used to perform characteristic decomposition
Γ [m ² s ⁻²]	Quantity in the solution of characteristic polynomial
R [m ² s ⁻²]	Quantity in the solution of characteristic polynomial
C^+ [-]	Incoming (forward) characteristic
C^- [-]	Outgoing (backward) characteristic
C_b [-]	Bed characteristic
λ_1 [ms ⁻¹]	Wave speed associated with C^- characteristic
λ_2 [ms ⁻¹]	Wave speed associated with C^+ characteristic
λ_3 [ms ⁻¹]	Wave speed associated with C_b characteristic
λ_{1h} [ms ⁻¹]	Purely hydrodynamic wave speed (C^- characteristic)
λ_{2h} [ms ⁻¹]	Purely hydrodynamic wave speed (C^+ characteristic)
R^- [ms ⁻¹]	Hydrodynamic Riemann invariant associated with C^- characteristic
R^+ [ms ⁻¹]	Hydrodynamic Riemann invariant associated with C^+ characteristic
\mathfrak{R}_1 [ms ⁻²]	Morphodynamic Riemann invariant associated with C^- characteristic
\mathfrak{R}_2 [ms ⁻²]	Morphodynamic Riemann invariant associated with C^+ characteristic
\mathfrak{R}_3 [ms ⁻²]	Morphodynamic Riemann invariant associated with C_b characteristic

LIST OF TABLES

d' [m]	Function used to resolve step discontinuity in bed profile
d [m^2]	Integral of d' with respect to z
MB_+ [m^2]	Volume of sediment deposited per unit width
MB_- [m^2]	Volume of sediment scoured out per unit width
tol [m^2]	Tolerance level used to determine if sediment is conserved (mobile bed dam-break)

Subscripts:

s	Number of meshpoint in x -direction
H	High side of discontinuity
L	Low side of discontinuity
tf	Thin film
cs	Constant state (mobile bed dam-break)
co	Cut-off (mobile bed dam-break)
$*$	Denotes value of a variable at the shoreline/wave tip boundary
SB	Denotes value of a variable at the seaward (upstream) boundary

Superscripts:

n	Time level
$*$	Denotes dimensionless variable
$'$	Denotes scaled variables

Abbreviations:

LHS	Left hand side
RHS	Right hand side
PDE	Partial differential equation
ODE	Ordinary differential equation

LIST OF TABLES

MOC	Method of characteristics
GC	Grid of characteristics
STI	Specified time interval
mLxF	Modified Lax–Friedrichs
MPM	Meyer–Peter and Müller sediment transport formula

CHAPTER 1

Introduction

Perhaps the most vivid image conjured up when one thinks of the coast is that of waves breaking and the resulting turbulent bores. These bores move landward as steep foaming white fronts driving water up and down the beach. The near-shore region where the waves break and bores move shoreward is known as the surf zone. The cross-shore extent of the surf zone varies between beaches, depending primarily on beach slope. Gently sloping sand beaches tend to have several lines of breakers, in different stages of breaking, in a wide surf zone, steeper beaches tends to have fewer lines of breaking waves and a relatively narrow surf zone. Landwards of the surf zone is the swash zone. The swash zone is the flow region successively covered and uncovered by the run-up and backwash of a body of water known as the swash lens. Boundaries of the swash zone are dynamic and at the landward boundary, known as the shoreline, water depths are vanishingly small. It is for this reason that the shoreline is difficult to define practically, particularly during the backwash when a thin film of water may remain on the beach (Packwood, 1980). Fluid motion within the swash zone is understood to be governed not only by incident bores but also infra-gravity waves. These two forcing mechanisms do not act in isolation; instead one predominates according

to incident wave shape and beach slope (Erikson et al., 2004). Infra-gravity waves are low frequency (0.003–0.03Hz) non-breaking waves that tend to occur on very shallow beaches in calm conditions; under more stormy conditions bores begin to dominate the swash even on beaches with a very mild slope (Brocchini and Baldock, 2008). Swash on steeper beaches is typically bore-driven, unless the beach is so steep the wave does not break at all; instead, in this instance, the waves surge up and down the beach. It is now widely understood that, excluding surging "breakers", there are three principal breaker types classified as spilling, collapsing or plunging breakers with a continuous transition in between types (Figure 1.2). How a wave breaks as it approaches the near-shore depends on its period, height and the beach topography (Galvin, 1968). The variables that determine how a given wave will break can be combined to give a mathematical expression, this is the so-called surf similarity parameter (Mei, 1989). Assuming that waves break and an incident bore is formed, motion in the swash zone can be generalised in the following manner: upon reaching the initial shoreline position the bore collapses and climbs the beach as a progressively thinning tongue of water or rarefaction wave. The wave running up the beach is termed the up-rush and reaches a maximum height before it returns seaward under gravity as the backwash. The collapse of an incident bore followed by the up-rush and subsequent backwash comprises a single swash event. Despite the fact that in reality bore collapse occurs over finite time and length scales several investigators (e.g. Freeman and LeMéhauté (1964); Barker and Whitham (1980); Chanson (2005); Guard and Baldock (2007)) have noted that the problem of bore collapse can effectively be reduced to that of the more severe case of a dam-break on a slope. Moreover, Peregrine and Williams (2001) have shown that a specific dam-break initial value problem actually produces an identical flow field to that described by the only available analytical description of bore-driven

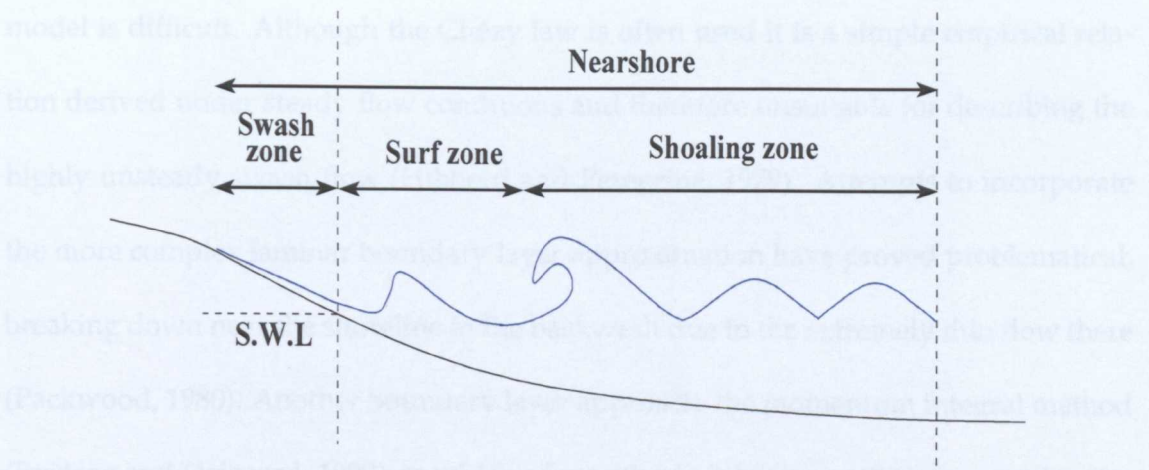


Figure 1.1: Schematic of the nearshore

swash, i.e. that of Shen and Meyer (1963) – see §2.1. Thus, the dam-break problem is of particular relevance to any theoretical study of bore-driven swash. Clearly, unless the surf has a very long period there will be interaction between swash events, with the backwash of the previous event modifying the up-rush of the next event. Often this interaction takes the form of a stationary turbulent hydraulic jump known as the "backwash vortex" (Matsunaga and Honji, 1980).

The swash zone is perhaps the most dynamic region of the entire nearshore; here, flow velocities are high ($> 2 \text{ ms}^{-1}$) and water depths are very small close to the leading edge or wave tip. Due to these high flow velocities the swash zone is characterised by rapid morphological change (Masselink and Puleo, 2006). Swash events typically involve both sub- and supercritical flow, meaning that trans-critical flow is common in the swash zone. Turbulence is another feature of the swash, being initially advected into the swash zone by incident bores then being smoothed out during the up-rush phase before forming again due to bed friction as water gathers speed in the backwash (Petti and Longo, 2001). Bed friction is clearly important in the swash zone, however, the correct parameterisation of representative terms within a mathematical

model is difficult. Although the Chézy law is often used it is a simple empirical relation derived under steady flow conditions and therefore unsuitable for describing the highly unsteady swash flow (Hibberd and Peregrine, 1979). Attempts to incorporate the more complex laminar boundary layer approximation have proved problematical, breaking down near the shoreline in the backwash due to the extremely thin flow there (Packwood, 1980). Another boundary layer approach, the momentum integral method (Fredsoe and Deigaard, 1992), in which a logarithmic velocity profile is assumed in the boundary layer, is perhaps the most promising line of attack. The momentum integral method, adapted for flow over a porous bed, was successfully applied in a swash context by Clarke et al. (2004).

Collecting meaningful field data from the swash zone is a particularly challenging task due to the small water depths and intermittent nature of the flow. These inherent difficulties have historically led to problems when obtaining field data especially for sediment fluxes and short term beach profile change. However, primarily due to technological advances, field studies of the swash are becoming increasingly popular. Studies of swash zone hydrodynamics have primarily investigated the variation of water depth and velocity with time at a fixed cross-shore location using wire and photographic techniques (see Butt and Russell (2000) for a comprehensive review up to that date). Measurements of instantaneous and net sediment transport in the swash zone have benefited in recent years from the development of accurate non-obtrusive instrumentation. Use of optical backscatter sensors and acoustic Doppler velocimeters has enabled measurement of sediment concentrations and flow velocities within the swash zone. Importantly, field studies have shown that water in the run-up phase transports much more sediment than water of the same velocity in the backwash (Masselink et al., 2005). Moreover, the net sediment transport over a single swash event is often found to

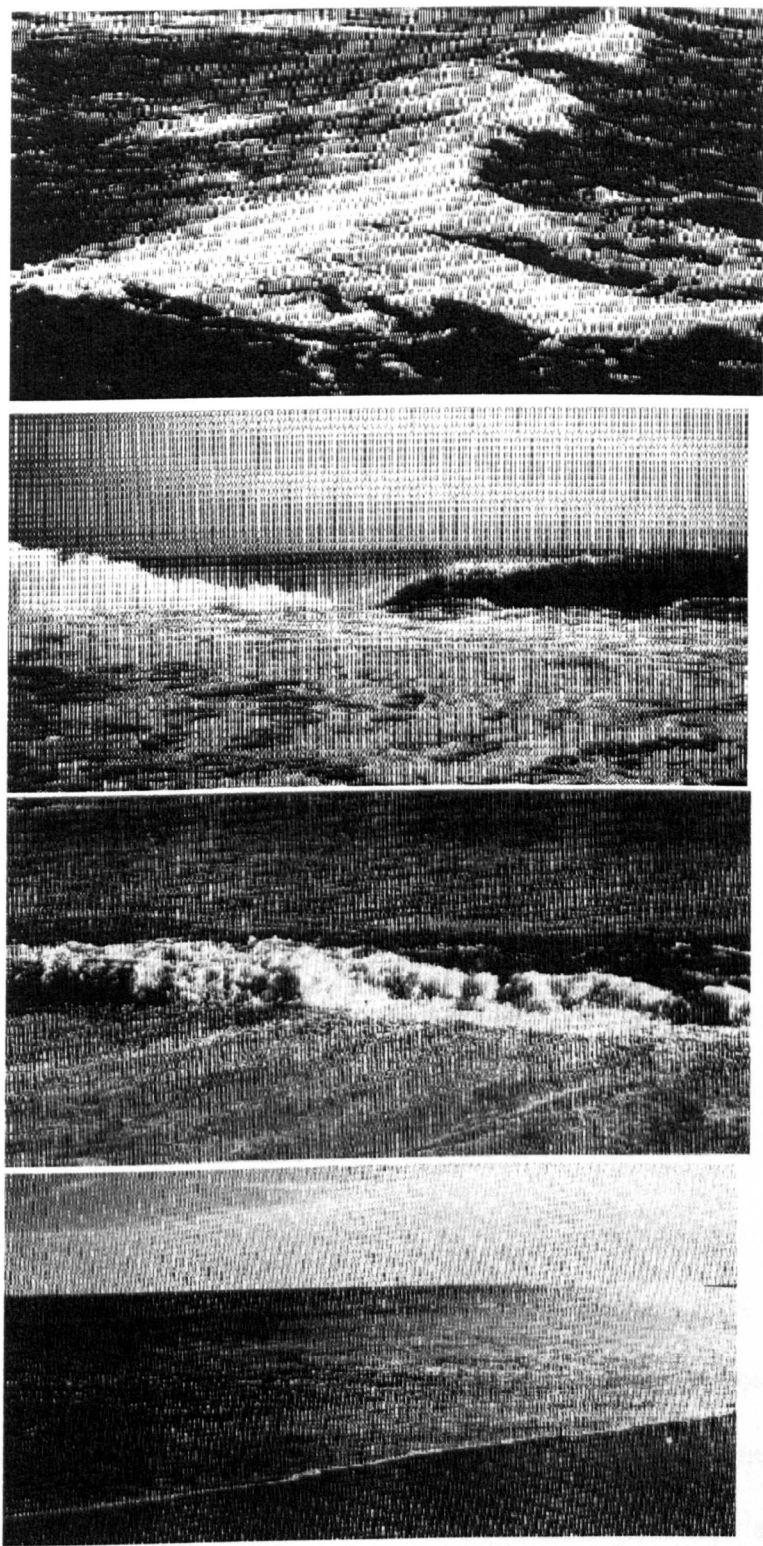


Figure 1.2: Breaker types. From top to bottom: Spilling, Plunging, Collapsing and Surging. Reproduced from Galvin (1972)

be a small difference between two large quantities (Osborne and Rooker, 1999). These two findings have important implications for the modelling of beach evolution in the swash zone.

The aim of this work is to develop a highly accurate wave-resolving numerical solver for use over a single swash event. The model should have the ability to model bore-driven swash in such a way that the hydro- and morphodynamics are fully coupled, i.e. there will be no morphodynamical time stepping. In so doing it is envisaged that information will be obtained relating to the underlying (morpho) dynamics of the swash zone. The effect of coupling on beachface evolution will also be investigated to see if this makes modelling more realistic, i.e. whether a coupled model allows the growth of a beach under conditions that an uncoupled model does not. The following Chapter details some relevant work on swash zone and dam-break hydro- and morphodynamics. Chapter 3 discusses the equations used to govern both the hydro- and morphodynamical evolution as well as their decomposition into so-called characteristic form. The numerical methods used for solution are detailed in Chapter 4, including methods for the treatment of initial and boundary conditions. The derivation of suitable Rankine-Hugoniot (jump) conditions as well as a comparison between shock-capturing and shock-fitting approaches is given in Chapter 5. In Chapter 6 quasi-analytical solutions to the mobile bed dam-break problem based on the Riemann wave technique are presented for two distinct sediment transport formulae. These dam-break solutions provide a means for checking the accuracy of the MOC and MacCormack codes, as well as providing starting conditions for Shen and Meyer (1963) type swash events. Chapter 7 presents analytical results and the results of a number of numerical experiments describing uncoupled modelling of beachface evolution. Numerical results for beachface evolution according to fully coupled models are presented in Chapter 8. Fi-

nally, Chapter 9 provides conclusions of the work as well as outlining future research topics that will further improve modelling of swash zone morphodynamics.

CHAPTER 2

Literature Review

2.1 Analysis of swash zone hydrodynamics

Whether or not a wave breaks is important as it determines how the water will behave in the swash zone. For non-breaking waves Carrier and Greenspan (1958) found a set of analytical solutions using the hodograph transformation, a technique in which the shallow water equations are cast in characteristic form (refer to §3.4) and then transformed in such a way that space and time become the dependent variables. Using this technique allows the two first-order nonlinear shallow water equations to be reduced to a single linear second-order equation the solutions of which are well documented (Johnson, 1997). The Carrier and Greenspan (1958) solutions provide a valuable tool for checking numerical schemes; however, their relevance to progressive waves arriving at a beach is somewhat questionable as they require either a full reflection of the incident wave, and the subsequent development of a standing wave, or an initial water velocity of zero throughout the flow field. Moreover, in order for waves not to break combinations of wave height, wave period and beach slope are required that are relatively rare on real beaches. In the majority of cases waves arriving in the near-shore will break

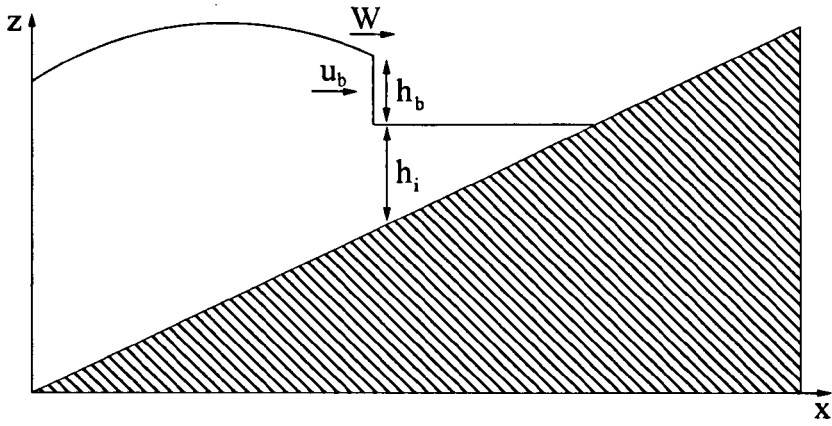


Figure 2.1: Schematic of a bore climbing a planar beach showing the notation used in the derivation of Whitham's characteristic rule.

and form bores. Consequently this thesis is concerned only with bore-driven swash. Major advances in the theoretical analysis of bore-driven swash were made by Whitham, Meyer and co-workers (Whitham, 1958; Keller et al., 1960; Barker and Whitham, 1980; Ho and Meyer, 1962; Shen and Meyer, 1963). The first of these came when research into gas dynamical shock waves propagating into non-uniform regions led Whitham (1958) to propose his, now famous, characteristic rule. The rule is in effect an approximation allowing the differential relations valid along the characteristic arriving from the high pressure side of the shock to be valid behind the shock front. Doing this provides an ordinary differential equation for shock velocity in terms of the pressure immediately in front of the shock. In the same paper Whitham (1958) speculatively applied this rule within the framework of the shallow water theory to a bore moving into still water of non-uniform depth. A summary of the characteristics rule, applied within the shallow water framework, is given here. The Riemann invariants (R^+) valid along advancing characteristics in (dimensional) differential form are:

$$dR^+ = du + 2dc + g \tan \beta dt = 0, \quad (2.1.1)$$

where the trajectory of the advancing characteristics is given by:

$$\frac{dx}{dt} = u + c, \quad (2.1.2)$$

where g is the acceleration due to gravity, u is the (depth-averaged) water velocity, h is water depth, $c = (gh)^{\frac{1}{2}}$ is gravity wave celerity x is the horizontal distance, t is time and $\tan \beta$ is the beach slope; see §3.4.1 for a derivation of (2.1.1) and (2.1.2). In order to proceed it is necessary to denote values of variables immediately behind the bore with the subscript b and also to note that $\tan \beta = \frac{h_i}{x}$ where $h_i = h_i(x)$ is the still water depth in front of the bore, see Figure 2.1. Whitham's characteristic rule combines (2.1.1) and (2.1.2) giving the following differential relation:

$$du_b + 2dc_b + \frac{g dh_i}{u_b + c_b} = 0. \quad (2.1.3)$$

This differential relation can be augmented by the shallow water Rankine Hugoniot conditions (see §5.3.1) to give an ordinary differential equation for bore velocity in terms of the water depth in front of the bore. Crucially, if the still water depth in front of the bore tends to zero at some point (as it does on a beach) the characteristics rule requires that the bore height must also tend to zero as the bore approaches this point while the bore velocity tends to some limiting value. While checking the validity of Whitham's characteristic rule numerically for the case of a bore climbing a beach Keller et al. (1960) noted that the behaviour of the bore near the shoreline was largely independent of the initial conditions that gave rise to it. For an analogous gas dynamical problem Guderly (1942) found a similarity solution that was shown by Payne (1957) to exhibit similar "forgetfulness". In order to further investigate this forgetfulness Ho and Meyer (1962) found an asymptotic solution for the climb of an initially uniform bore (a bore with constant height and velocity behind the bore front) on a beach and noted that it was a singularity in the governing equations at the shoreline location that

was responsible for the bore "forgetting" its initial conditions. The work of Ho and Meyer (1962) was extended to include the run-up by Shen and Meyer (1963). The authors derived an analytical solution for the entire run-up and part of the backwash, by the hodograph transformation of Carrier and Greenspan (1958), using only seaward boundary data from the domain of dependence of the shoreline singularity, i.e. the region between the bore path and limiting characteristic (refer to Figure 1 of Shen and Meyer (1963)). As such the solution is strictly only valid in the region close to the moving shoreline although it is a legitimate explicit solution to the non linear shallow water equations throughout the entire swash zone. In dimensional form the Shen and Meyer (1963) solution is:

$$h(x, t) = \frac{(U_b t - \frac{1}{2} g t^2 \tan \beta - x)^2}{9 g t^2}, \quad (2.1.4)$$

with the maximim run-up x_{max} given by:

$$x_{max} = \frac{U_b^2}{2 g \tan \beta}, \quad (2.1.5)$$

where U_b is the bore velocity at the initial shoreline position. Shen and Meyer (1963) gave no explicit expression for the flow velocity, however, Peregrine and Williams (2001) derived the solution for flow velocity corresponding to (2.1.4). In dimensional variables this expression is:

$$u(x, t) = \frac{(U_b t - 2 g t^2 \tan \beta + 2x)}{3t}. \quad (2.1.6)$$

The flow field in a large proportion of the interior of the swash lens is dependent on specific seaward boundary conditions; this was alluded to by Shen and Meyer (1963) and later by Peregrine and Williams (2001). The Shen and Meyer (1963) solution implies that when bore-driven swash is modelled using a fixed bed approach then virtually the entire motion of the swash event close to the (moving) shoreline is determined by

conditions at the point of bore collapse. In particular a single free parameter, the bore velocity at the initial shoreline position, is responsible for determining the maximum extent of the run-up in accordance with elementary energy (ballistics) concepts. The theory indicates that throughout the run-up the leading edge is subject only to gravity forces and, thus, the maximum potential energy gained by the particle at the leading edge must be equal to its initial kinetic energy at the original shoreline position. One of the last significant breakthrough in the mathematical analysis of bores was made by Barker and Whitham (1980) who were able to obtain a similarity solution for the climb of a bore on a beach using the method Guderly had employed in his gas dynamical problem almost forty years earlier. The work confirmed the findings of Ho and Meyer (1962) and provided algebraic expressions for the bore height (h_b) and velocity (W) in terms of terminal bore velocity at the original shoreline (U_b) and the still water depth in front of the bore ($h_i(x)$). In dimensional form these expressions are:

$$W = U_b - 2^{\frac{5}{4}} U_b^{\frac{1}{2}} \{g h_i(x)\}^{\frac{1}{4}} \quad (2.1.7)$$

and:

$$h_b = W \{2g^{-1} h_i(x)\}^{\frac{1}{2}}. \quad (2.1.8)$$

Most recently, Pritchard et al. (2008) have provided a quasi-analytical solution for swash flows that is valid for a large range of incident bore conditions. The solution, based on the hodograph transformation, is somewhat involved and breaks down at the point of inception of a secondary bore. Interestingly, the work extends the findings of Shen and Meyer (1963) showing that secondary bore formation does not necessarily always occur in the backwash. Pritchard et al. (2008) illustrate certain cases for which the shallow water theory appears to predict the formation of secondary bores in the run-up. Though relatively complex, the solution should provide an important valida-

tion tool for numerical solvers employed in swash zone modelling.

2.2 Numerical modelling of bore-driven swash

While Keller et al. (1960) provided a numerical solution for the climb of a bore over a plane sloping beach, computation was terminated at the initial shoreline location. It appears that the first numerical solution of swash zone run-up was implemented by Freeman and LeMéhauté (1964), who developed a numerical solution to the run-up of a limiting solitary wave. Although Freeman and LeMéhauté (1964) describe an additional term in the momentum equation that allowed for a linear distribution of the vertical velocity component this was not incorporated in the numerical computations; consequently a bore formed at the front of the wave shortly after computation began. Friction was included using the Chézy law, a relation derived empirically from steady flow conditions (see §1). The numerical scheme employed was based on the method of characteristics (MOC) in specified time interval (STI) form (see §4.2.1). Owing to the Chézy friction term approaching infinity at the wave tip, as $h \rightarrow 0$ there, the shoreline (wet-dry) boundary was determined using a minimum cut-off depth. Water velocity at the tip was found using a stability criterion based on dimensional equivalence as proposed by Abbott (1961). The model did not run as far as the backwash stage and, although a paper on backwash was promised, it appears that it was never published. Amein (1964) also presented solutions to the run-up of various long waves. The numerical model employed was again a variant of the MOC but this time in the more accurate grid of characteristics (GC) form (see §4.1.2). Interestingly, Amein (1964) used a bore classification system, involving two types of bore, that determined how the run-up was computed. The first type of bore, the "*major bore*", was defined as one in

which *"a major portion of the wave profile has caught up with the bore and has taken part in its development"*; the run-up was computed by feeding the bore velocity, obtained from the numerical MOC solution, into the analytical solution of Shen and Meyer (1963). The second bore type, the *"minor bore"*, was defined as one in which, because of the very long wavelengths, *"only small portions of their wave profiles take part in the bore development"*. For minor bores the run-up was computed numerically using the MOC scheme. Due to the fact that Amein (1964) used the GC variant of the MOC the shoreline boundary was dealt with implicitly within the model (see §4.1.2). As the schemes of Freeman and LeMéhauté (1964) and Amein (1964) were characteristics based they utilised the primitive variable form of the shallow water equations and it was therefore necessary to treat discontinuities explicitly using shock-fitting procedures (see §5.2). Mader (1974) used the marker and cell (MAC) method developed at Los Alamos (see e.g. Harlow and Amsden (1970)) to solve the full Navier Stokes equations in order to compute the run-up of a tsunami on a vertical cliff. The results were compared with those obtained using the shallow water theory, with solutions provided by the MOC, and it was noted that for long wave tsunamis the two models were in very close agreement.

A major breakthrough in numerical modelling of the swash zone came with the work of Hibberd and Peregrine (1979) who used a Lax Wendroff explicit finite difference scheme to compute the run-up and backwash of a uniform bore. The equations were cast in conservation form, meaning that the scheme was shock-capturing. The work was motivated by that of Houghton and Kasahara (1968) who had used the Lax Wendroff scheme and a conservation form of the shallow water equations to successfully model trans-critical flow over a mountain ridge. In shock-capturing schemes disconti-

nities are represented by a steep gradient of the dependent variables over a few mesh points rather than a moving internal boundary as in shock-fitting schemes. Depending on their order of accuracy shock-capturing schemes either suffer from a large amount of numerical diffusion or spurious numerical oscillations in the presence of discontinuities (see §5.1 for further details). The Lax Wendroff scheme is second-order accurate and therefore suffers from parasitic oscillations close to shocks, these oscillations can very quickly threaten the overall stability of the solver. In their work Hibberd and Peregrine (1979) were forced to employ the artificial diffusion term detailed by Lax and Wendroff (1960) to overcome this problem. A major difficulty addressed by Hibberd and Peregrine (1979) was the numerical treatment of the shoreline boundary. A rather intricate procedure based on linear extrapolation, the Lax Wendroff scheme, a centred difference scheme for both the mass and momentum equations and a minimum cut-off depth was devised. Hibberd and Peregrine's work was seminal as, for the first time, a quantitative description of the landward facing backwash bore predicted qualitatively by Shen and Meyer (1963) was made available. The scheme pioneered by Hibberd and Peregrine (1979) influenced the development of swash zone modelling throughout the 1980s, with the model further developed to include the effect of bed friction by Packwood (1980) who also simplified and improved the shoreline algorithm, which was subject to numerical instability (Synolakis, 1986). Ryrie (1983) extended the code in order to simulate the longshore currents generated by oblique bores. Kobayashi and co-workers applied a similar model in a series of studies looking at the run-up and reflection on steep rough slopes and structures, see Kobayashi et al. (1987, 1989). By the early 1990s numerical modelling of the swash zone had begun to utilise solvers based on Riemann-type schemes that used both exact and approximate Riemann solvers; an early example being the code developed by Watson et al. (1992). However, although

Model	$x_{s,max}$	T_{swash}	$h_{min}[m]$
PW01	2.00	4.00	
<i>Option 1</i>	1.767	3.936	10^{-6}
<i>Option 2a</i>	1.749	3.873	10^{-6}
<i>Option 2b</i>	1.749	3.878	10^{-6}
<i>Option 2d</i>	1.749	3.875	10^{-6}
<i>Option 2ea</i>	1.749	3.875	10^{-6}
<i>Option 2ea</i>	1.731	3.804	10^{-5}
<i>Option 2eb</i>	1.767	3.875	10^{-6}
<i>Option 3</i>	1.740	3.900	10^{-6}
<i>Option 4a</i>	1.722	3.856	10^{-6}
<i>Option 4b</i>	1.749	3.865	10^{-6}
<i>Option 5a</i>	1.722	3.91	10^{-6}
<i>Option 5b</i>	1.731	3.852	10^{-6}
<i>Option 6</i>	1.731	3.807	10^{-5}

Table 2.1: Results of several different shoreline boundary treatments for a Riemann-type scheme. The table shows the maximum computed run-up $x_{s,max}$ and swash period T_{swash} . Model PW01 gives the analytical results of Shen and Meyer (1963) ($\Delta x = 0.09m$). From Briganti and Dodd (2008) with permission of the authors.

treatment of the shoreline boundary in Riemann-type schemes is relatively simple such schemes have a tendency to under estimate the maximum run-up: see Briganti and Dodd (2008), Table 2.1. Although Riemann-type solvers have dominated the literature for the last fifteen years there have been some interesting departures. The work of Titov and Synolakis (1995) on solitary wave run-up is particularly important as it details a simple, robust and reliable algorithm for the treatment of the shoreline boundary for non-Riemann-type solvers (see §4.3.2 on this). Classical finite difference schemes are also still in use. In particular, the explicit second-order accurate scheme developed by MacCormack (1969) appears to be particularly well disposed for modelling flow in the swash zone when suitable artificial diffusion is applied (Vincent et al., 2001). The primary reason for this is that MacCormack's scheme uses a predictor-corrector approach, this facilitates the inclusion of source terms when compared with one-step schemes such as that of Lax and Wendroff (1960), see §4.2.3 for further details on this.

2.3 Modelling beach face evolution in the swash zone

Pritchard and Hogg (2005) developed an analytical model to predict beachface evolution over a single swash event, namely that of Shen and Meyer (1963). Several different sediment transport formulae were investigated. Initially, an equilibrium transport model is employed in which it is assumed that the same number of sediment particles are deposited on the bed as are entrained from it, i.e. no sediment remains suspended in the water column. Pritchard and Hogg (2005) noted that for an equilibrium model, due to the inherent asymmetry of the flow field, all swash models that use power-law-based sediment transport formulae in which the hydro- and morphodynamics are decoupled predict the net offshore transport of sediment everywhere on a beach.

The inclusion of representative terms for advection and settling lag effects led to the possibility of local onshore transport of sediment. Interestingly, the most important factor was found to be the amount of sediment brought into suspension at initial bore collapse rather than settling lag time.

Numerical modelling of beach change in the swash zone has a relatively short history. Beach evolution in the swash zone has been predicted both by using uncoupled models, i.e. models that assume that changes in bed height have a negligible effect on the flow over a swash event, and fully coupled morphodynamic models, which update the hydrodynamic variables and beach profile simultaneously. Masselink and Li (2001) used an uncoupled numerical model in order to study the effect of infiltration on beachface gradient in the swash zone. The sediment fluxes were computed using the transport formula of Bagnold (1966) calibrated for bedload only; however, the authors noted that validation of bedload formulas against total load field measurements gave sufficient confidence in the Bagnold model to predict the total load transport. In passing it should be noted that although Bagnold type models do give realistic sediment fluxes for various flow conditions such models require careful calibration as calibration error is especially sensitive to the signal-to-noise ratio of the empirical data (Puleo et al., 2005). The numerical solution was effected using a Lax Wendroff finite difference scheme with artificial diffusion and the Hibberd and Peregrine (1979) shoreline boundary treatment. Interestingly, Masselink and Li (2001) concluded that while swash infiltration was important on gravel beaches it had a negligible effect on the morphological evolution of sandy beaches. Karambas and Koutitas (2002) used a decoupled model, which employed a Bousinesq type approach for the hydrodynamics, to model beachface evolution in the surf and swash zones under periodic wave action. The sediment flux was computed using different transport formulae in the surf and

swash zones. For the swash zone a pure bed load type sheet-flow formula was used. The mathematical model incorporated representative terms for modelling both infiltration and exfiltration. The numerical solution employed a fourth-order accurate predictor corrector scheme as the Boussinesq equations contain third-order derivatives. The shoreline boundary was treated using a "dry bed" approach; this approach is straight forward, using a cut-off depth to determine the shoreline location. If the calculated value of h at a mesh point falls below this cut-off depth, Karambas and Koutitas (2002) used $1 \times 10^{-5}\text{m}$, then both h and u are set equal to zero at that mesh point. Both the Masselink and Li (2001) and Karambas and Koutitas (2002) models appeared to be able to simulate erosion and accretion of the beach in the swash zone over relatively long periods.

Numerical models in which the hydro- and morphodynamics are directly coupled are extremely rare in swash modelling. In a recent paper Dodd et al. (2008) describe the development of a fully coupled 2D wave-resolving model based on the shallow water theory with equilibrium sediment transport. The numerical scheme was of the Riemann-type utilising Roe's approximate Riemann solver (Roe, 1981). Due to the fact that cusps tend to form on gravel beaches provision was made for beach infiltration using Darcy's law (see Dicker (1969)). The solver was successfully applied to model the formation and development of beach cusps. This work utilised "tolerance depth" approach to treat the shoreline boundary. The tolerance depth technique works by searching for dry cells that will flood at the next time step and then wetting these cells with the tolerance depth so that the Roe scheme can be applied without modification at the shoreline (see §4.3.2 for details of various other shoreline boundary treatments).

2.4 Fixed bed dam-break problem

The analytical solution to the so called "classical" dam-break problem, i.e. the instantaneous failure of a dam with a dry bed downstream (wet-dry dam-break) and no friction, was provided, in the framework of the shallow water theory, by Ritter (1892). Further analytical solutions have been found for differing dam-break problems some exact and some approximate. Stoker (1948) gives an implicit analytical solution for the inviscid case when there is water on the downstream side of the dam (wet-wet dam-break) using a method of characteristics (MOC) based analysis (details of the MOC are given in §3.4). Both Dressler (1952) and Whitham (1955) give analytical solutions that incorporate friction for wet-dry dam-break waves on a horizontal bed. Dressler (1952) used a perturbation technique to solve the Saint Venant equations approximately. In the vicinity of the tip, Dressler noted that his solution broke down due to the fact that it predicted that rate of change of water height, and consequently wave celerity, increased without bound as the tip was approached. To rectify this Dressler (1952) suggested that the tip region be treated as a boundary layer. Whitham (1955) assumed that friction only became a significant factor within the tip region of the dam-break wave. Following Dressler's suggestion the tip region was treated as a boundary layer¹ separate from the main body of flow, which was presumed to obey the Ritter solution. Friction in the tip region was assumed constant and the whole tip region taken to have a constant velocity. Differential equations for the tip region were then formulated and solved using a Taylor series expansion. Although arrived at by different means, the solutions of Dressler (1952) and Whitham (1955) were compared by Whitham (1955)

¹Although Whitham calls the tip region a boundary layer this is not true in the strict sense. In a genuine boundary layer there exists some form of velocity distribution. Whitham assumes a constant velocity for the entire tip region.

and found to give very similar results. Agreement was within 12% for the time range of the data presented. It is interesting to note that using the simple coordinate transformation proposed by Watson et al. (1992) the analytical solutions of Ritter (1892), Dressler (1952) and Whitham (1955) can be applied to the dam-break on a slope. Hunt (1982, 1984) gave analytical solutions for dam-break waves in sloping prismatic channels, i.e. channels in which both the cross-sectional shape and size are constant, based on the simplifying assumptions of kinematic wave theory (see for example Henderson (1966)). Chanson (2005) has given approximate MOC based analytical solutions that include both friction and slope terms. However, these solutions are founded on the rather unrealistic assumption that the initial outgoing, or backward, characteristic behaves as though it were moving into water of constant depth. Recently, the hodograph transformation (see §2.1) has been applied to the Saint Venant equations along with suitable boundary conditions to provide exact analytical solutions for the instantaneous release of a finite length reservoir of water behind a lock (Hogg, 2006) and a triangular reservoir of water on a slope (Ancey and Rentschler, 2008).

Ré (1946) provided the first numerical solution to the one-dimensional dam-break problem in order to determine flow that would result from enemy sabotage of a dam on the river Rhine. Friction was included in the scheme using the Chézy law formulation, and there was also a body of water present downstream of the dam. Computations for the numerical MOC based scheme were carried out by hand. The ground-breaking work of Ré (1946) was followed by that of Faure and Nahas (1961). This study dealt with both wet-wet and wet-dry dam-break problems incorporating both slope and friction terms. Solution was by numerical MOC, using a GC based model (see §4.1.2); computation was carried out on an IBM 7090 supercomputer. The results compared well with experiments executed by the authors. A similar method was used by Dra-

cos (1970) to examine surge waves in open channels of any geometry; interestingly, this scheme obtained second order accuracy through the use of a predictor corrector method. Sakkas and Strelkoff (1973) solved the problem for a dam-break with a dry downstream region, again utilising a predictor corrector MOC GC scheme for second order accuracy. Unusually, the tip region was treated separately using Whitham's analytical solution. The analytical solution was employed when it became impractical to further reduce step size through the insertion of additional advancing characteristics. Rajar (1978) looked at results for dam-break flow in a prismatic channel that included the formation and propagation of shocks. Both the Lax Wendroff scheme and the first-order dissipative scheme proposed by Cunge (1970) were used in the study. Rajar (1978) found certain expected conclusions such as the fact that Cunge scheme could only very approximately simulate shocks due to a large amount of smearing and the Lax Wendroff scheme being overpowered by instabilities after the formation of shocks. Far more interesting was that introducing a dissipative term into the Lax Wendroff scheme gave the scheme stability but spoiled the accurate simulation of shocks. Shock velocities were in fact found to be too low by around 20%, and Rajar (1978) concluded that the only truly accurate way to represent shocks in highly unsteady flow, such as that due to dam failure, was via shock-fitting.

Recently, as is the case for swash modelling, Riemann-type schemes have become standard for solution of hydrodynamical dam-break type flow. A comparison between various state-of-the-art numerical schemes was undertaken by Zoppou and Roberts (2003) for the one-dimensional dam-break problem. A recent, and interesting, departure is the work of Mohammadian et al. (2007) who have developed a 1D conservative STI MOC solver that is capable propagating shocks at the correct strengths and speeds. The scheme works by ensuring that the interpolation step is performed in terms of con-

served variables based on a finite volume approach (see e.g. LeVeque (1992)). Mohamadian et al. (2007) successfully apply the scheme to fixed bed wet-wet dam-break problems and dam-break problems that involve shock-shock interactions.

2.5 Mobile bed dam-break problem

Although experimental work on mobile bed dam-break flow dates back almost thirty years (Chen and Simons, 1979), the theoretical literature is very recent. Moreover, very few laboratory experiments involving dam-break flows with mobile beds have been conducted. It would appear that, other than the pioneering work of Chen and Simons (1979), the only published results are the experiments of Capart and Young (1998) and those presented in Fraccarollo and Capart (2002). Contrary to the modelling of mobile bed swash flow the majority of numerical mobile bed dam-break have the hydrodynamical and bed evolution equations fully coupled. In an early attempt, Capart and Young (1998) used a shock-capturing upwind scheme to model dam-break flow over a mobile bed comprising relatively large grained, low density sediment. The mathematical model developed was one of two-layer, two-phase flow. The model coupled the shallow water equations to a bed evolution equation which was split into two components: an advection-reaction equation that governed the evolution of bed particles moving with the flow and a fourth equation governing the evolution of the non-moving bed particles. Sediment load was treated in a non-equilibrium manner, i.e. the rate of sediment exchange between the bed and the flow was assumed to be proportional to the difference between the unsteady instantaneous sediment load and the equilibrium load obtained under steady flow. The results from the numerical scheme were compared with experimental data that utilised digital image analysis to trace both

the free surface evolution and the motion of individual sediment grains. In order to facilitate analysis Capart and Young (1998) plotted curves of $u \pm c$ in the physical (x, t) plane and interpreted these as being the hydrodynamic characteristics of the flow. It is noted here that this interpretation is incorrect, as the hydrodynamic characteristic velocities of sediment laden flow are not given simply by $u \pm c$, but are in fact more complex (see §3.4.2). The results of Capart and Young (1998) have important implications; in both the numerical model and the experimental results a shock was observed to form virtually instantaneously upon dam failure. The shock then remained stationary for a short period of time before propagating upstream of the original dam site with increasing speed. Overall the numerical results compared well with the experimental data. Capart and Young (1998) noted that the main differences were in the region of the shock, claiming that the physical limitations of the governing equations were responsible for any discrepancies. Fraccarollo and Capart (2002) readdressed the mobile bed problem employing a sheet flow model² that considered the bed boundary as a phase interface between solid- and fluid-like behaviour. This idea of a boundary being a transition interface between solid- and fluid-like behaviour comes from granular flow theory (e.g Jenkins and Askari (1991); Takahashi (1991)). The approach differs from the technique typically used in alluvial hydraulics (e.g Hsu and Chu (1965); Lai (1991)) primarily because it does not neglect the thickness of the sediment transport layer or the associated inertial effects. Flow in the vertical plane was discretised as a set of three homogenous regions separated by sharp interfaces after the work of Abbott and Minns (1979). Here, the velocity in the sediment layer was assumed to be equal to that of the clear water layer above, an assumption that would appear to be

²Sheetflow refers to multiple layer bedload type flow (see §3.3) in which the bedload is made up from a number of adjacent layers of moving particles each in contact with one another.

valid for such high Froude number flow. Under these conditions a system of equations was derived that coupled the hydro- and morphodynamics. The characteristic form of these equations was then solved using an exact Riemann solver (see Chapter 6 for a detailed description of this solution technique). Characteristic curves were again plotted (this time incorporating all relevant terms) and used for analysis. On top of the conclusions reached by Capart and Young (1998) there was an extra observation resulting from the inertial effect of the sediment. At the tip region the model predicted bulking and subsequent deceleration of the flow leading to the formation of a sediment bore at the wave tip. When compared against experimental evidence Fraccarollo and Capart (2002) concluded that results were very favourable within a limited time window. Beyond this window, however, agreement was poor and long term evolution was deemed a fruitful avenue for further work. Ferreira and Leal (2003) developed a mathematical model of both wet-wet and wet-dry mobile bed dam-break flow based on the shallow water and Exner equations. Closure of the system was obtained using the total load equilibrium formula of Ackers and White (1973) for the sediment flux. The equation system was solved numerically using the MacCormack scheme with an additional total variation diminishing (TVD) step; effectively using self-adaptive artificial viscosity to inhibit parasitic numerical oscillations. The TVD algorithm requires a Roe (1981) approximation to the Jacobian matrix; somewhat peculiarly in their TVD step Ferreira and Leal (2003) only derived the Roe approximation for the shallow water equations as opposed to the full shallow water Exner system. The results of the numerical model were compared with laboratory data and it was observed that while the model gave a good qualitative description of the flow the Ackers and White formula underestimated the total sediment load. In particular, the model predicted less scour than was actually observed in the vicinity of the original dam location.

Cao et al. (2004) used an approximate Riemann solver to solve a set of equations, comprising the continuity of flow containing sediment, conservation of momentum for sediment-laden flow and continuity of sediment discharge. In their system Cao et al. (2004) included all terms in the momentum equation, even those typically neglected in alluvial channel work (see Hsu and Chu (1965) for details). The results obtained were similar to those of Fraccarollo and Capart (2002) with one principle difference: at the front of the wave, two distinct drops in water surface elevation were predicted, the first at the tip and the second further back. The second fall in free surface elevation was shown to be directly accountable to inclusion of all terms in the momentum equation and was directly in line with a contact discontinuity (see §5.3.3) relating to the sediment concentration, i.e. the line separating the flow that is saturated with sediment from that flow which is not.

CHAPTER 3

1 D Mathematical Model

3.1 Introduction

It is widely accepted that water motion in the swash zone is well represented by the shallow water or long wave model (Peregrine, 1972). In the shallow water model wavelength is considered to be much greater than water depth. The nonlinear shallow water equations can be derived from the principles of conservation of fluid mass and momentum using certain simplifying assumptions. In particular, it is assumed that the flow is inviscid and irrotational (i.e. there is no vorticity in the flow). Clearly, the condition of zero vorticity ceases to hold when waves break and collapse in onto themselves. A second assumption is that the vertical accelerations in the fluid are negligible and the pressure distribution is purely hydrostatic. The assumption of hydrostatic pressure allows the horizontal flow velocity to be considered depth uniform. Although the pressure is clearly not hydrostatic at the point where a bore collapses, due to large vertical accelerations in the fluid, the time for which this assumption fails to hold is very small when compared with the duration of a swash event (Freeman and LeMéhauté, 1964).

3.2 Governing Equations

3.2.1 Nonlinear Shallow Water Equations (NLSWE)

Assuming that the water is incompressible and of constant density ρ , then for flow with a depth uniform velocity the 1D continuity equation can be derived relatively simply. To aid the derivation of the differential form of the governing equations frequent use is made of the following notation:

$$\int_{x_1}^{x_2} \frac{\partial(\cdot)}{\partial x} dx \equiv [\cdot]_{x_1}^{x_2}. \quad (3.2.1)$$

Considering the element of water of unit width between x_1 and x_2 in Figure 3.1, the total mass of water in the element is given by:

$$\int_{x_1}^{x_2} \int_B^{h+B} \rho dz dx = \int_{x_1}^{x_2} \rho h dx, \quad (3.2.2)$$

where subscripts 1 and 2 denote the value of flow variables at those respective locations. From the law of conservation of mass (continuity) it follows that the rate of change of mass of water in the element between x_1 and x_2 is equal to the net flux of water mass into (or out of) the element, i.e:

$$\frac{\partial}{\partial t} \int_{x_1}^{x_2} \rho h dx = [\rho u h]_{x_2}^{x_1}. \quad (3.2.3)$$

Thus we have:

$$\frac{\partial}{\partial t} \int_{x_1}^{x_2} h dx + [uh]_{x_1}^{x_2} = 0. \quad (3.2.4)$$

To obtain the differential form of the continuity equation it is easiest to proceed by integrating (3.2.4) over an arbitrary time interval t_1 to t_2 , where $t_1 < t_2$, giving:

$$\int_{t_1}^{t_2} \int_{x_1}^{x_2} \frac{\partial h}{\partial t} + \frac{\partial(uh)}{\partial x} dx dt = 0 \quad (3.2.5)$$

which follows from (3.2.1) and the fact that:

$$\left[\int_{x_1}^{x_2} h dx \right]_{t_1}^{t_2} \equiv \int_{t_1}^{t_2} \int_{x_1}^{x_2} \frac{\partial h}{\partial t} dx dt. \quad (3.2.6)$$

Because the independent variables were defined arbitrarily and x_1 and x_2 are independent of time, (3.2.5) can be generalised to give:

$$\frac{\partial h}{\partial t} + \frac{\partial(uh)}{\partial x} = 0. \quad (3.2.7)$$

This is the so-called conservation form of the continuity equation as it is written in terms of the conserved variables mass and momentum. It is possible to obtain another form of the continuity equation, known as the primitive variable form, by applying the chain rule to (3.2.7) giving:

$$\frac{\partial h}{\partial t} + u \frac{\partial h}{\partial x} + h \frac{\partial u}{\partial x} = 0. \quad (3.2.8)$$

The momentum equation comes from Newton's second law, i.e. that force is equal to rate of change of momentum. For the element of fluid of unit width between x_1 and x_2 it follows that, if the difference in the pressure on the ends of the element is purely hydrostatic, it is given by:

$$\left[\rho g \int_B^{h+B} \{(h+B) - z\} dz \right]_{x_1}^{x_2} = \left[\frac{\rho g h^2}{2} \right]_{x_2}^{x_1}. \quad (3.2.9)$$

Variation in the bed height between x_1 and x_2 gives rise to additional forces at the ends. For a continuous bed¹ it follows that the net additional force due to bed slope is given by:

$$\int_{x_2}^{x_1} \rho g h \frac{dB}{dx} dx. \quad (3.2.10)$$

In the x -direction the momentum flux across x_1 is:

$$(\rho h u^2)|_{x_1}, \quad (3.2.11)$$

¹The case of a discontinuous bed is more complex. A solution to this problem was given by Needham and Hey (1991) and is detailed in §5.3.1

and across x_2 is:

$$(\rho hu^2)|_{x_2}. \quad (3.2.12)$$

The rate of change of momentum in the element of fluid between x_1 and x_2 is:

$$\frac{\partial}{\partial t} \int_{x_1}^{x_2} \rho uh \, dx. \quad (3.2.13)$$

Thus, the net momentum flux in the x -direction is:

$$\frac{\partial}{\partial t} \int_{x_1}^{x_2} \rho uh \, dx + \rho [hu^2]_{x_1}^{x_2}. \quad (3.2.14)$$

Equating the force to the rate of change of momentum gives:

$$\frac{\partial}{\partial t} \int_{x_1}^{x_2} uh \, dx + \left[hu^2 + \frac{1}{2}gh^2 \right]_{x_1}^{x_2} + \int_{x_1}^{x_2} gh \frac{dB}{dx} \, dx = 0. \quad (3.2.15)$$

To obtain the differential form (3.2.15) is integrated over an arbitrary period of time, t_1 to t_2 , where $t_1 < t_2$:

$$\int_{t_1}^{t_2} \int_{x_1}^{x_2} \left(\frac{\partial(uh)}{\partial t} + \frac{\partial(u^2h + \frac{1}{2}gh^2)}{\partial x} + gh \frac{\partial B}{\partial x} \right) dx dt = 0. \quad (3.2.16)$$

Again, because the independent variables were defined arbitrarily the general form of (3.2.16) is:

$$\frac{\partial(uh)}{\partial t} + \frac{\partial(u^2h + \frac{1}{2}gh^2)}{\partial x} + gh \frac{\partial B}{\partial x} = 0. \quad (3.2.17)$$

Employing the chain rule and (3.2.7), (3.2.17) can be written in primitive variable form as:

$$\frac{\partial u}{\partial t} + u \frac{\partial u}{\partial x} + g \frac{\partial(h + B)}{\partial x} = 0 \quad (3.2.18)$$

3.2.2 Bed Evolution (Exner) Equation

The total volumetric sediment transport rate (see §3.3) in the x direction is q . Assuming that q is proportional to the volume rate of flow, then $q = q(u, h)$. Referring to Figure

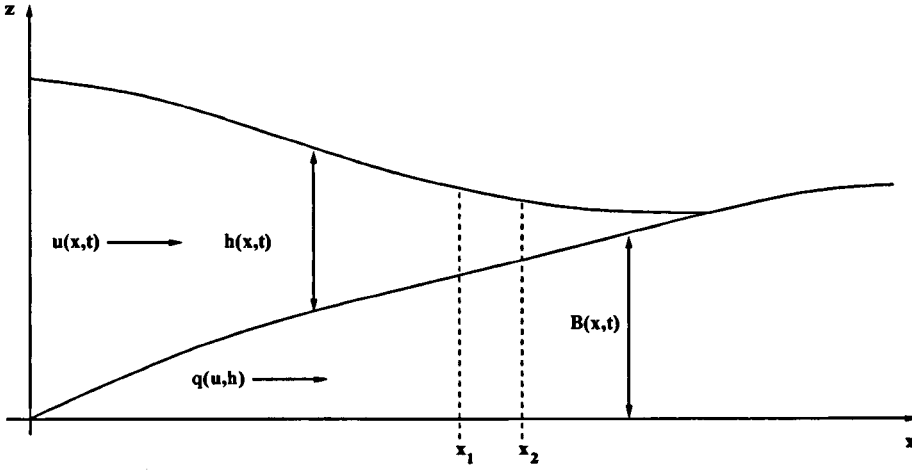


Figure 3.1: Definition sketch for mobile bed flow in the swash zone

3.1 the total volume of sediment entering a region at x_1 is:

$$\zeta q|_{x_1}, \quad (3.2.19)$$

and the total volume of sediment leaving the region at x_2 is:

$$\zeta q|_{x_2}, \quad (3.2.20)$$

where $\zeta = \frac{1}{1-p_o}$ is constant, with p_o being the porosity of the bed material. The total volume of sediment in the region x_1 to x_2 is:

$$\int_{x_1}^{x_2} \int_0^B dz dx = \int_{x_1}^{x_2} B dx. \quad (3.2.21)$$

Using the law of conservation of mass it follows that the rate of change of mass of sediment in the region x_1 to x_2 is equal to the net flux of sediment mass into (or out of) this region, i.e:

$$\frac{\partial}{\partial t} \int_{x_1}^{x_2} B dx = -\zeta [q]_{x_1}^{x_2}. \quad (3.2.22)$$

Again integrating over an arbitrary time interval t_1 to t_2 , where $t_1 < t_2$, gives:

$$\int_{t_1}^{t_2} \int_{x_1}^{x_2} \frac{\partial B}{\partial t} + \zeta \frac{\partial q}{\partial x} dx dt = 0. \quad (3.2.23)$$

By the same reasoning as above this gives us the differential form of (3.2.23) as:

$$\frac{\partial B}{\partial t} + \zeta \frac{\partial q}{\partial x} = 0. \quad (3.2.24)$$

Equation (3.2.24) is referred to in the literature as the bed evolution or Exner equation.

Closure of (3.2.24) is obtained by specifying a particular form for q . The forms for q employed in this thesis are discussed below.

3.3 Sediment Transport Processes and Formulae

Sediment can be transported by water in four principal modes: sliding, rolling, saltating ("jumping") and in suspension. If sediment either slides or rolls it remains in constant contact with the bed; hence, these modes of sediment transport are referred to collectively as bed load transport. It is also usual to consider saltating sediment as being part of the bed load. Suspended sediment particles follow irregular paths often spending long periods of time suspended in the water; hence, this mode of sediment transport is referred to as suspended load transport. Bed load transport is driven by intergranular interaction whereas the principle mechanism behind suspended load transport is fluid turbulence (Fredsoe and Deigaard, 1994). Generally suspended load transport dominates in faster flows and bed load transport dominates in slower flows; however, other factors such as sediment grain size and flow depth also contribute to the dominant type of transport. It is rare for either type of transport to act in isolation, instead bed load and suspended load transport tend to act together to give the total load sediment transport.

Sediment transport in the swash is complex, and although it is generally agreed that bed load is the predominant form of transport in the backwash, a large amount of sediment is brought into suspension at bore collapse, leading to a considerable amount of

suspended load in the run-up particularly on fine grained beaches (Butt et al., 2004). Field data obtained by Masselink and Hughes (1998), from the swash zone of a medium sand beach, indicated that sediment was transported primarily as bed load, and it is accepted that bed load is the dominant mode of transport under normal conditions on gravel beaches (Horn and Mason, 1994).

The variation in sediment transport modes over a single swash event presents considerable difficulty when formulating a mathematical model of the swash. Deciding which type of transport to use, and when, is still the topic of considerable uncertainty and debate (Masselink and Puleo, 2006). Indeed, it has been postulated that the traditional separation of sediment transport modes into bed load and suspended load is not applicable in the swash (Butt and Russell, 2000). In light of this uncertainty it seems justifiable to use a total load approach for transport in the swash zone. Thus, following Hudson and Sweby (2003) this work primarily uses a simple power-law-formulation for total load transport (see Grass (1981) for a derivation) of the form

$$q = Au^3, \quad (3.3.1)$$

where A is a dimensional constant with units s^2m^{-1} . The value of A is determined by the bed material and type of flow under consideration.

3.3.1 Relating A to physical parameters

Suitable values for A can be found from specific empirical data or alternatively can be computed from a simplification of standard sediment transport formulae such as those of Meyer-Peter and Müller or van Rijn. There are numerous sediment transport formulae employed by Engineers in the coastal zone and an excellent description of many can be found in Soulsby (1997). Here the relation between (3.3.1) and the Meyer-

Peter and Müller (MPM) formula is made explicit. The same approach can be used with any of the bed load formulae given in Soulsby (1997). The MPM formula may be written as:

$$q = 8.0(\vartheta - \vartheta_{cr})^{\frac{3}{2}} \{g(\rho_{rel} - 1)D_{50}^3\}^{\frac{1}{2}}, \quad (3.3.2)$$

where D_{50} is the median grain diameter, ρ_{rel} is the ratio of densities of sediment and water, $\vartheta = \frac{f_R u^2}{2g(\rho_{rel} - 1)D_{50}}$ and ϑ_{cr} is the value of ϑ at the threshold of motion, f_R being the coefficient of friction. Setting $\vartheta_{cr} = 0$ and equating (3.3.1) and (3.3.2) gives:

$$A \equiv \frac{8}{g(\rho_{rel} - 1)} \left(\frac{f_R}{2} \right)^{\frac{3}{2}}. \quad (3.3.3)$$

3.3.2 Closing the Exner equation

Owing to its rôle in the model, A will be referred to as a sediment mobility parameter throughout this thesis. The sediment transport formulae discussed above are derived from steady flow conditions and swash zone flows are inherently unsteady. However, a simple cubic velocity power-law-formula for q has been shown to be a good descriptor of sediment transport in the swash (see e.g. Masselink and Hughes (1998); Butt et al. (2004); Hsu and Raubenheimer (2006)). It is the absence of any other commonly used swash zone sediment transport formulae that motivates the use of velocity power-law-formulae in this thesis. Closure of (3.2.24) can be obtained by inserting (3.3.1) to give the conservation form of the Exner equation:

$$\frac{\partial B}{\partial t} + \frac{\partial(A\zeta u^3)}{\partial x} = 0. \quad (3.3.4)$$

Application of the chain rule provides the primitive variable form of (3.3.4) as:

$$\frac{\partial B}{\partial t} + 3A\zeta u^2 \frac{\partial u}{\partial x} = 0, \quad (3.3.5)$$

which can be used to determine bed evolution. Power-law based sediment transport formulae, such as (3.3.1), are based on the underlying premise that a portion of the fluid power delivered to the bed is able to initiate mobilisation and transport sediment as both bed load and suspended load. As such, such transport formulae are often referred to in the literature as being "energetics-based" (Bagnold, 1966). Energetics-based transport models where q is of the form given by (3.3.1) have been criticised because a vanishingly thin film of water can still transport a finite amount of sediment. Pritchard and Hogg (2005) have shown that use of a model in which $q = q(u, h)$ has little effect on the overall sediment transport pattern in the swash zone. The principal contribution of the h term is a reduction in the onshore/offshore transport at the landward limit of the swash due to the very small water depth there. In this thesis a simplified total load formula that takes water depth into account is also employed to obtain closure of (3.2.24). This sediment transport relation is of the form:

$$q = \bar{A}u^3h, \quad (3.3.6)$$

where \bar{A} is a dimensional constant with units s^2m^{-2} . Putting (3.3.6) into (3.2.24) gives:

$$\frac{\partial B}{\partial t} + \frac{\partial(\bar{A}\zeta u^3h)}{\partial x} = 0. \quad (3.3.7)$$

Again, application of the chain rule allows (3.3.7) to be recast in primitive variable form as:

$$\frac{\partial B}{\partial t} + \bar{A}\zeta u^3 \frac{\partial h}{\partial x} + 3\bar{A}\zeta u^2 h \frac{\partial u}{\partial x} = 0. \quad (3.3.8)$$

3.3.3 Values for sediment mobility parameters from field data

Determining suitable sizes for the sediment mobility parameters in (3.3.1) or (3.3.6) is difficult; for representative values this work utilises the field data of Masselink et al. (2005)

collected in the swash zone of a medium sand ($D_{50}=0.27-0.29$ mm) dissipative beach to compute order of magnitude estimates. Masselink et al. (2005) present measured values of total sediment flux, water height and water velocity for a typical swash event. The total suspended sediment flux presented in their paper with units $\text{Kgm}^{-1}\text{s}^{-1}$, and denoted here by q_t , can be converted into a volumetric flux q by dividing through by sediment density ρ_s , i.e.:

$$q = q_t \rho_s^{-1}. \quad (3.3.9)$$

In this work a value of 2650kgm^{-3} was used for ρ_s , cf. Soulsby (1997). Using values of q computed like this, as well as the Masselink et al. (2005) data for h and u in the middle of the run-up and again in the middle of the backwash for a fixed cross-shore location, average values of $A=0.004\text{s}^2\text{m}^{-1}$ and $\bar{A}=0.015\text{s}^2\text{m}^{-2}$ were obtained. Although these are clearly "ball park" figures it seems reasonable to assume that they are at least characteristic of values found on sand beaches.

3.4 Characteristic Decomposition

In order to facilitate notation, the subscripts $,x$ and $,t$ are used in this section to denote partial derivatives with respect to space and time.

3.4.1 Shallow water system: fixed bed case

In this decomposition a combination of equations (3.2.8) and (3.2.18) is sought such that derivatives of the two dependent variables can be combined into ordinary derivatives in a single direction. For the system of governing equations comprising only (3.2.8) and (3.2.18) two such directions exist; these new directions are known as characteristic directions (Courant and Friedrichs, 1976). There are two approaches to transform the

system of equations comprising (3.2.8) and (3.2.18) into characteristic form: the matrix approach and the direct combination approach (Lai, 1986). Although mathematically more elegant (Jeffrey, 1976), the matrix approach is not as intuitive as direct linear combination; for this reason the latter method is employed here. It should also be noted that, as the bed is fixed, for a plane sloping beach $B_{,x}$ is constant. Combining (3.2.8) and (3.2.18) in the following manner $(3.2.8) + \mu(3.2.18)$ and factorising gives:

$$h_{,t} + (u + \mu g)h_{,x} + \mu u_{,t} + (h + \mu u)u_{,x} + \mu g B_{,x} = 0. \quad (3.4.1)$$

Introducing the total derivative² $\frac{d(\)}{dt}$ where:

$$\frac{d(\)}{dt} = \frac{\partial(\)}{\partial t} + \frac{dx}{dt} \frac{\partial(\)}{\partial x}, \quad (3.4.2)$$

letting $\frac{dx}{dt} = \lambda$ reduces (3.4.1) to:

$$\frac{dh}{dt} + \mu \frac{du}{dt} + \mu g B_{,x} = 0, \quad (3.4.3)$$

with:

$$\lambda = (u + \mu g) = \frac{(h + \mu u)}{\mu}. \quad (3.4.4)$$

It follows from $\lambda = (u + \mu g)$ that:

$$\mu = \frac{\lambda - u}{g}. \quad (3.4.5)$$

Using (3.4.5) the relation $\lambda = \frac{(h + \mu u)}{\mu}$ can be re-arranged to give a quadratic in λ of the form:

$$\lambda^2 - 2u\lambda + u^2 - hg = 0. \quad (3.4.6)$$

This is the characteristic (quadratic) polynomial and is solved to give the roots:

$$\lambda = \frac{dx}{dt} = u \pm (gh)^{\frac{1}{2}} = u \pm c. \quad (3.4.7)$$

² $\frac{d(\)}{dt} = \frac{\partial}{\partial t} + \frac{dx}{dt} \frac{\partial}{\partial x}$, i.e. the time rate of change following a fluid particle.

From (3.4.7) and (3.4.3) it follows that:

$$\frac{dh}{dt} + \frac{c}{g} \frac{du}{dt} + \mu g B_{,x} = 0, \text{ for } \frac{dx}{dt} = u + c \quad (3.4.8)$$

and:

$$\frac{dh}{dt} - \frac{c}{g} \frac{du}{dt} + \mu g B_{,x} = 0, \text{ for } \frac{dx}{dt} = u - c. \quad (3.4.9)$$

Recalling that $c = (gh)^{\frac{1}{2}}$ then $h = \frac{c^2}{g}$. Using this to replace h in (3.4.8) and (3.4.9), and dividing through by $\frac{c}{g}$ yields:

$$2 \frac{dc}{dt} \pm \frac{du}{dt} + g B_{,x} = 0 \quad (3.4.10)$$

as $\mu = \frac{c}{g}$ from the relations given by (3.4.4). Hence, from this it can be seen that:

$$\frac{d(u + 2c + g B_{,x} t)}{dt} = 0, \text{ for } \frac{dx}{dt} = u + c \quad (3.4.11)$$

and:

$$\frac{d(u - 2c + g B_{,x} t)}{dt} = 0, \text{ for } \frac{dx}{dt} = u - c. \quad (3.4.12)$$

(3.4.11) and (3.4.12) are the compatibility, or Riemann, equations for the characteristic equations (3.4.7). Characteristic equations thus describe the propagation paths of infinitesimally small disturbances, or wavefronts, whereas compatibility (Riemann) equations describe the signal, or relationship between dependent variables, which is carried by a particular wavefront. (3.4.11) and (3.4.12) therefore state that the quantity $u \pm 2c + g B_{,x} t$ remains constant along a characteristic curve moving with the velocity $u \pm c$ relative to a stationary frame of reference.

3.4.2 Shallow water-Exner system: mobile bed case

Sediment flux given by $q = Au^3$

For the system of governing equations comprising (3.2.8), (3.2.18) and (3.3.5) to be hyperbolic, three characteristic directions should exist. To find these directions we again

employ the direct combination approach. Combining (3.2.8), (3.2.18) and (3.3.5) with the combination factors μ and ω in the following manner:

$$\Re = \mu(3.2.8) + (3.2.18) + \omega(3.3.5), \quad (3.4.13)$$

gives:

$$\Re = \mu h_{,t} + \mu u h_{,x} + \mu h u_{,x} + g h_{,x} + u_{,t} + u u_{,x} + g B_{,x} + 3A\xi\omega u^2 u_{,x} + \omega B_{,t} = 0. \quad (3.4.14)$$

Simplifying (3.4.14) with the aim of obtaining the total (material) derivative:

$$\Re = \mu h_{,t} + (\mu u + g)h_{,x} + u_{,t} + (\mu h + u + 3A\xi\omega u^2)u_{,x} + \omega B_{,t} + g B_{,x} = 0. \quad (3.4.15)$$

Introducing the total derivative (3.4.15) reduces to:

$$\Re = \mu \frac{dh}{dt} + \frac{du}{dt} + \omega \frac{dB}{dt} = 0. \quad (3.4.16)$$

Putting:

$$\lambda = \frac{dx}{dt} = \frac{\mu u + g}{\mu} = \mu h + u + 3A\xi\omega u^2 = \frac{g}{\omega}, \quad (3.4.17)$$

gives:

$$\lambda = \frac{\mu u + g}{\mu} = u + \frac{g}{\mu}, \quad (3.4.18)$$

$$\lambda = \mu h + u + 3A\xi\omega u^2, \quad (3.4.19)$$

$$\lambda = \frac{g}{\omega}, \quad (3.4.20)$$

so that, from (3.4.17):

$$\mu = \frac{g}{\lambda - u} \quad (3.4.21)$$

and:

$$\omega = \frac{g}{\lambda}. \quad (3.4.22)$$

Using (3.4.21), (3.4.22) and (3.4.16) the Riemann equations are:

$$\Re^k = \frac{du}{dt} + \frac{g}{(\lambda_k - u)} \frac{dh}{dt} + \frac{g}{\lambda_k} \frac{dB}{dt} = 0, \quad (3.4.23)$$

where $k = 1, 2, 3$ denotes each of the characteristic families. Next, putting (3.4.21) and (3.4.22) into (3.4.17) gives:

$$\lambda = \frac{gh}{(\lambda - u)} + u + \frac{3A\xi gu^2}{\lambda}. \quad (3.4.24)$$

Rearranging (3.4.24) and simplifying gives the characteristic (cubic) polynomial:

$$\lambda^3 - 2u\lambda^2 + [u^2 - g(h + 3A\xi u^2)]\lambda + 3A\xi gu^3 = 0, \quad (3.4.25)$$

the discriminant of which is:

$$D = \Gamma^3 + R^2, \quad (3.4.26)$$

where:

$$\Gamma = -\frac{1}{9}[u^2 + 3g(h + 3A\xi u^2)] \quad (3.4.27)$$

and:

$$R = \frac{u}{54}[9g(2h - 3A\xi u^2) - 2u^2]. \quad (3.4.28)$$

For the system of governing equations to be hyperbolic, then $D < 0$; this implies that the roots of the cubic, and consequently the characteristic wave speeds, are all real and distinct (Courant and Friedrichs, 1976). If $D = 0$ then the system of governing equations is parabolic and only two distinct families of characteristics exist. For values of $D > 0$ only one of the roots is real, the other two being complex, and the system is elliptic. For physically realistic situations where $h \geq 0$ it can be shown that for (3.4.25), $D < 0$. The governing equations are therefore hyperbolic with wave speeds found directly from (3.4.25) using Cardano's formula (see Spiegel and Liu (1999)):

$$\lambda_1 = 2(-\Gamma)^{\frac{1}{2}} \cos\left(\frac{\Theta}{3}\right) + \frac{2u}{3}, \quad (3.4.29)$$

$$\lambda_2 = 2(-\Gamma)^{\frac{1}{2}} \cos\left(\frac{\Theta + 2\pi}{3}\right) + \frac{2u}{3}, \quad (3.4.30)$$

$$\lambda_3 = 2(-\Gamma)^{\frac{1}{2}} \cos\left(\frac{\Theta + 4\pi}{3}\right) + \frac{2u}{3}, \quad (3.4.31)$$

where:

$$\Theta = \cos^{-1} \left(\frac{R}{(-\Gamma)^{\frac{3}{2}}} \right). \quad (3.4.32)$$

The characteristic equations are given by (3.4.17) as:

$$\frac{dx}{dt} = \lambda_k. \quad (3.4.33)$$

Letting $A \rightarrow 0$ leads to recovery of the well known hydrodynamic C^- and C^+ wave speeds with C^- corresponding to $\lambda_1 = u - (gh)^{\frac{1}{2}}$ and C^+ to $\lambda_2 = u + (gh)^{\frac{1}{2}}$. The bed deformation speed C_b , λ_3 , then becomes zero.

Sediment flux given by $q = \bar{A}u^3h$

The approach employed above can be used for the system of governing equations comprising (3.2.8), (3.2.18) and (3.3.8). Combining (3.2.8), (3.2.18) and (3.3.8):

$$\Re = \mu(3.2.8) + (3.2.18) + \omega(3.3.8) = 0, \quad (3.4.34)$$

and simplifying, again with the aim of obtaining the total derivative:

$$\Re = \mu h_{,t} + (\mu u + g + \omega \bar{A} \zeta u^3) h_{,x} + u_{,t} + (\mu h + u + 3\omega \bar{A} \zeta u^2 h) u_{,x} + \omega B_{,t} + g B_{,x} = 0. \quad (3.4.35)$$

Thus, (3.4.35) reduces to:

$$\Re = \mu \frac{dh}{dt} + \frac{du}{dt} + \omega \frac{dB}{dt} = 0, \quad (3.4.36)$$

with:

$$\lambda = \frac{dx}{dt} = \frac{\mu u + g + \omega \bar{A} \zeta u^3}{\mu} = \mu h + u + 3\omega \bar{A} \zeta u^2 h = \frac{g}{\omega}. \quad (3.4.37)$$

Hence:

$$\omega = \frac{g}{\lambda} \quad (3.4.38)$$

and:

$$\mu = \frac{\lambda - u - 3\bar{A}\zeta g \lambda^{-1} u^2 h}{h}, \quad (3.4.39)$$

so that:

$$\mu = \frac{\lambda - u}{h} - \frac{3\bar{A}\zeta gu^2}{\lambda}. \quad (3.4.40)$$

Hence, from (3.4.36), the Riemann equations are:

$$\Re^k = \frac{du}{dt} + \left(\frac{\lambda_k - u}{h} - \frac{3\bar{A}\zeta gu^2}{\lambda_k} \right) \frac{dh}{dt} + \frac{g}{\lambda_k} \frac{dB}{dt} = 0. \quad (3.4.41)$$

As is the case above, $k = 1, 2, 3$ denotes the respective characteristic families. Next, the characteristic polynomial can be derived from equation (3.4.37):

$$\lambda = u + \frac{(g\lambda^{-1}\bar{A}\zeta u^3 + g)h}{\lambda - u - 3\bar{A}\zeta g\lambda^{-1}u^2h}. \quad (3.4.42)$$

Rearranging (3.4.42) and simplifying gives the cubic characteristic polynomial:

$$\lambda^3 - 2u\lambda^2 + (u^2 - gh - 3\bar{A}\zeta gu^2h)\lambda + 2\bar{A}\zeta gu^3h = 0. \quad (3.4.43)$$

As is the case when $q = Au^3$, the roots of (3.4.43) can be shown to be both real and distinct and are given by (3.4.29), (3.4.30) and (3.4.31) where:

$$\Theta = \cos^{-1} \left(\frac{R}{\sqrt{-\Gamma^3}} \right), \quad (3.4.44)$$

$$\Gamma = \frac{3(u^2 - gh - 3\bar{A}\zeta gu^2h) - 4u^2}{9}, \quad (3.4.45)$$

$$R = \frac{-18u(u^2 - gh - 3\bar{A}\zeta gu^2h) - 54\bar{A}\zeta gu^3h + 16u^3}{54}. \quad (3.4.46)$$

Equation (3.4.46) can be simplified to show that R is independent of \bar{A} giving:

$$R = \frac{u^3}{27} + \frac{ghu}{3}. \quad (3.4.47)$$

3.4.3 Variation of eigenvalues with Froude number

In Figure 3.2 the three eigenvalues (wave speeds) associated with the shallow water-Exner equations, with $q = Au^3$, are given as a function of Froude number; also plotted on the figure, for comparative reasons, are the two wave speeds associated with

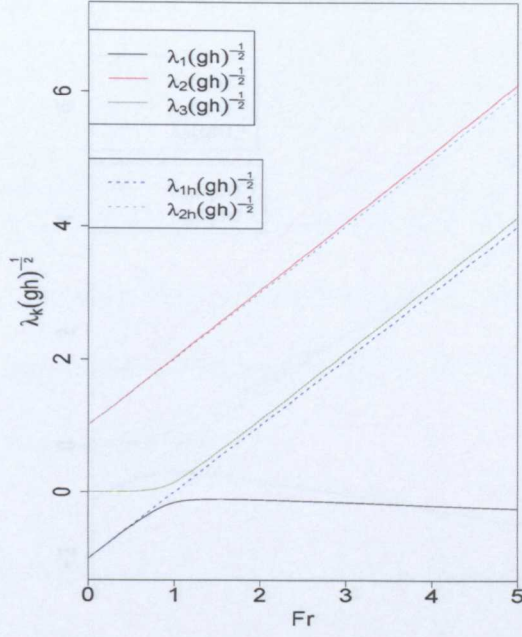


Figure 3.2: Variation of dimensionless wave speeds with Froude number (Fr) for $q = Au^3$ transport ($A = 0.001 \text{ s}^2\text{m}^{-1}$, $p = 0.4$).

purely hydrodynamical (fixed bed) flow (denoted by subscript h). To provide representative values of the wave speeds h is fixed at 1m and u increased from 0 to 15.66 ms^{-1} , values of $A = 0.001 \text{ s}^2\text{m}^{-1}$ and $p = 0.4$ are used. When the wave speeds are examined the value of λ_2 is least effected by the bed mobility and corresponds closely to the purely hydrodynamical incoming wave speed (λ_{2h}). The behaviour of the λ_1 and λ_3 wave speeds is intriguing. For subcritical flow the λ_1 wave speed is in relatively close agreement with the purely hydrodynamical outgoing wave speed (λ_{1h}). However, as $(gh)^{\frac{1}{2}} \rightarrow u$, i.e. as the Froude number (Fr) approaches unity, the agreement begins to deteriorate. Once the flow has become supercritical ($Fr > 1$) the λ_3 wave speed begins to assume similar values to λ_{1h} . The results for the $q = \bar{A}u^3h$ case are very similar, although the agreement between hydro- and morphodynamic wave speeds deteriorates more rapidly for supercritical flow as the Froude number increases (cf. Figure 3.3). Interestingly, similar behaviour has been noted for the shallow water-

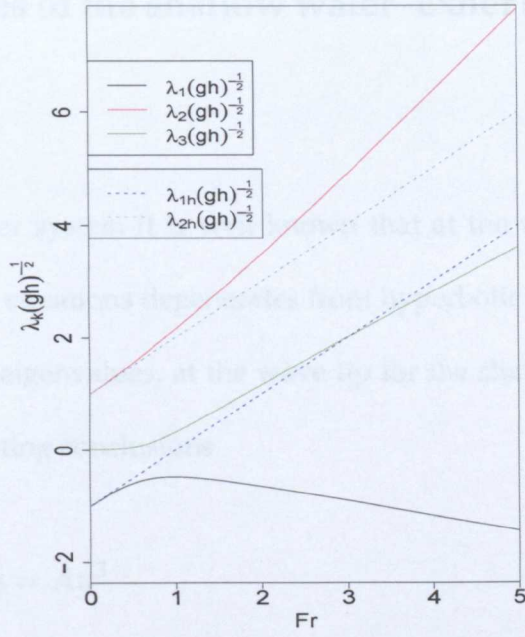


Figure 3.3: Variation of dimensionless wave speeds with Froude number (Fr) for $q = \bar{A}u^3h$ transport ($\bar{A} = 0.01 \text{ s}^2\text{m}^{-2}$, $p=0.4$)

Exner system with closure provided by the Meyer–Peter–Müller sediment transport formula (Savary, 2007). It is worth noting that, for both the $q = Au^3$ and $q = \bar{A}u^3h$ sediment transport formulae, as $A, \bar{A} \rightarrow 0$ the value of $(\lambda_1 \rightarrow \lambda_{1h})$ for $Fr < 0$ and $(\lambda_3 \rightarrow \lambda_{1h})$ for $Fr > 0$. By analogy to the fixed bed case, Savary (2007) reasons that for subcritical flow the essential information about hydrodynamical variables is propagated along characteristics whose wave speeds are given by λ_1 and λ_2 whereas for supercritical flow this information is carried by characteristics with wave speeds given by λ_2 and λ_3 . Savary (2007) concludes that information concerning sediment thus propagates primarily along characteristics with wave speeds given by λ_3 and λ_1 for sub- and supercritical flow respectively. Results concerning the wave structure of a mobile bed dam-break obtained in Chapter 6 appear to support this hypothesis.

3.5 Eigenvalues of the shallow water–Exner system at the wave tip

For the shallow water system it is well known that at the wave tip $h \rightarrow 0$ and the system of governing equations degenerates from hyperbolic to parabolic. Analysis of the wave speeds, or eigenvalues, at the wave tip for the shallow water–Exner system leads to some interesting conclusions.

Closure given by $q = Au^3$

Evidence from the Riemann wave solution developed in Chapter 6 and the work of Dodd et al. (2008), using the same set of equations solved via a Riemann–type scheme, suggests that the water depth at the wave tip tends to zero. Assuming that $h \rightarrow 0$ at the tip, evaluating the wave speeds analytically at $h = 0$ gives:

$$\lambda_3 = u, \quad (3.5.1)$$

$$\lambda_1 = u - \frac{(12A\zeta g + 1)^{\frac{1}{2}}u + u}{2}, \quad (3.5.2)$$

$$\lambda_2 = \frac{(12A\zeta g + 1)^{\frac{1}{2}}u + u}{2}, \quad (3.5.3)$$

giving the relationship:

$$\lambda_3 = \lambda_1 + \lambda_2. \quad (3.5.4)$$

Thus, it follows that, unlike the shallow water system, with $q = Au^3$ the shallow water–Exner system remains hyperbolic at the wave tip. If the Riemann equation (3.4.23) for the third characteristic family ($k = 3$) is considered at $h = 0$, the implication of (3.5.1) is that (3.4.23) is undefined there. This finding may have important implications for the solution of the shallow water–Exner system close to the shoreline.

Closure given by $q = \bar{A}u^3h$

Evidence from the Riemann wave solution developed in Chapter 6 again suggests that $h \rightarrow 0$ at the wave tip when $q = \bar{A}u^3h$. Thus, evaluating the wave speeds analytically at $h = 0$ gives:

$$\lambda_3 = u, \quad (3.5.5)$$

$$\lambda_1 = 0, \quad (3.5.6)$$

$$\lambda_2 = u, \quad (3.5.7)$$

giving the relationship:

$$\lambda_3 = \lambda_2. \quad (3.5.8)$$

Like the shallow water system, the shallow water–Exner system with $q = \bar{A}u^3h$ therefore becomes parabolic at the wave tip.

3.6 Eigenvectors of the shallow water–Exner system

The roots of the characteristic polynomial give the eigenvalues for the respective shallow water and shallow water–Exner systems. The eigenvectors for the shallow water system are well known and can be found in many text books, e.g. Toro (2001). Here the right eigenvectors are derived for the primitive variable form of the shallow water–Exner system with closure given by either $q = Au^3$ or $q = \bar{A}u^3h$. It is necessary to use these eigenvectors when constructing the Riemann wave solution in Chapter 6.

3.6.1 Closure given by $q = Au^3$

Putting the shallow water–Exner system into vector form:

$$\mathbf{f}_t + \mathcal{A}(\mathbf{f})\mathbf{f}_{,x} = 0, \quad (3.6.1)$$

where:

$$\mathbf{f} = \begin{pmatrix} h \\ u \\ B \end{pmatrix},$$

and:

$$\mathcal{A}(\mathbf{f}) = \begin{pmatrix} u & h & 0 \\ g & u & g \\ 0 & 3A\xi u^2 & 0 \end{pmatrix}.$$

The right eigenvectors \mathbf{R}^k are found using:

$$\mathcal{A}(\mathbf{f})\mathbf{R}^k = \lambda_k\mathbf{R}^k, \quad (3.6.2)$$

where $k = 1, 2, 3$ denotes each of the characteristic families, and:

$$\mathbf{R}^k = \begin{pmatrix} r_1^k \\ r_2^k \\ r_3^k \end{pmatrix},$$

to give:

$$\begin{pmatrix} u & h & 0 \\ g & u & g \\ 0 & 3A\xi u^2 & 0 \end{pmatrix} \begin{pmatrix} r_1^k \\ r_2^k \\ r_3^k \end{pmatrix} = \lambda_k \begin{pmatrix} r_1^k \\ r_2^k \\ r_3^k \end{pmatrix}.$$

Multiplying out and setting $r_1^k = 1$ gives the right eigenvectors of the system as:

$$\mathbf{R}^k = \begin{pmatrix} 1 \\ \frac{\lambda_k - u}{h} \\ \frac{3A\xi u^2(\lambda_k - u)}{\lambda_k h} \end{pmatrix}.$$

3.6.2 Closure given by $q = \bar{A}u^3h$

Again, putting the shallow water–Exner system into vector form:

$$\mathbf{f}_{,t} + \mathcal{A}(\mathbf{f})\mathbf{f}_{,x} = 0, \quad (3.6.3)$$

where:

$$\mathbf{f} = \begin{pmatrix} h \\ u \\ B \end{pmatrix},$$

and:

$$\mathcal{A}(\mathbf{f}) = \begin{pmatrix} u & h & 0 \\ g & u & g \\ \bar{A}\bar{\zeta}u^3 & 3\bar{A}\bar{\zeta}u^2h & 0 \end{pmatrix}.$$

Generic right eigenvectors \mathbf{R}^k are found as above, giving:

$$\begin{pmatrix} u & h & 0 \\ g & u & g \\ \bar{A}\bar{\zeta}u^3 & 3\bar{A}\bar{\zeta}u^2h & 0 \end{pmatrix} \begin{pmatrix} r_1^k \\ r_2^k \\ r_3^k \end{pmatrix} = \lambda_k \begin{pmatrix} r_1^k \\ r_2^k \\ r_3^k \end{pmatrix}.$$

Multiplying out and setting $r_1^k = 1$ gives the right eigenvectors of the system as:

$$\mathbf{R}^k = \begin{pmatrix} 1 \\ \frac{\lambda_k - u}{h} \\ \frac{\bar{A}\bar{\zeta}u^2(3\lambda_k - 2u)}{\lambda_k} \end{pmatrix}.$$

3.6.3 A note on the sediment flux formulation used for closure

Throughout this work the main form of the sediment flux used for closure of the shallow water–Exner system is of the form $q = Au^3$. Some additional work is also presented for the shallow water–Exner system closed using a sediment flux of the form

$q = \bar{A}u^3h$; however, it should be made clear that the analysis for this sediment flux is by no means as detailed as the analysis undertaken for the $q = Au^3$ case.

Numerical Methods

4.1 Hydrodynamic (fixed bed) solver

A key component of this research is the comparison between uncoupled and fully coupled modelling of beach face evolution in the swash zone. It is therefore necessary to have an accurate and robust means of modelling swash zone hydrodynamics. The floating grid method of characteristics, often referred to as the grid of characteristics (MOC GC) method, is widely regarded as being the most accurate numerical scheme for solution of the shallow water equations (Cunge et al., 1980). MOC GC methods are also attractive for modelling swash zone flows as the downstream (shoreline) boundary requires no explicit treatment. Additionally, when using MOC GC schemes it is possible to prescribe time varying seaward boundary conditions using the incoming Riemann invariants. It is for these reasons that this research focuses purely on a MOC based solver for uncoupled swash zone hydrodynamical modelling.

4.1.1 The method of characteristics

In a recent paper Guard and Baldock (2007) outline a first-order accurate MOC GC method for use in the swash zone; this method is the same as that detailed by Amein (1964). Neither Amein (1964) nor Guard and Baldock (2007) provide any technique for dealing with the embedded shocks that often arise in the backwash of bore-driven swash. Both of these models are thus of limited use in terms of application to bore-driven swash; moreover, they are formally only first-order accurate. Part of the work undertaken in this thesis was to improve the simple MOC GC schemes of Amein (1964) and Guard and Baldock (2007). Consequently, a new second-order accurate MOC GC scheme was developed that is capable of detecting and evolving embedded shocks such as those found in the backwash of swash due to a uniform bore. A description of the scheme in the absence of shocks is provided below, details of the shock detection and fitting procedures are given in §§5.4.2 and 5.4.4 respectively.

4.1.2 MOC GC technique

Notation

Throughout this section a subscript notation of the form (n, s) will be used in order to identify individual incoming (C^+) and outgoing (C^-) characteristics, as well as mesh points on the characteristic grid. Outgoing (C^-) characteristics are determined by the s subscript, with the first C^- characteristic (i.e. the seaward boundary) taking the value $s = 1$. Subsequent C^- characteristics are denoted by uniform increments of s , so that along the second C^- characteristic $s = 2$ etc. It then follows that the value of n determines the number of the incoming (C^+) characteristic under consideration. This notation allows for easy identification of mesh points within the characteristic grid.

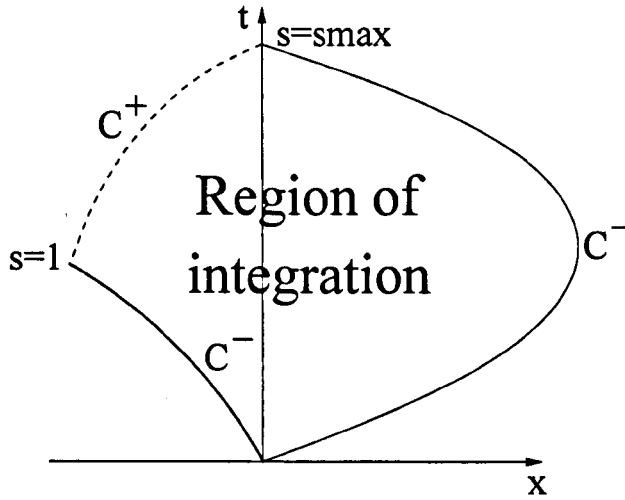


Figure 4.1: The region of integration for a single swash event showing the limiting characteristics, i.e. the seaward boundary characteristic (bold solid line) the shoreline boundary C^- characteristic (solid line) and the last C^+ characteristic (dashed line).

For example, the intersection of the first incoming (C^+) characteristic with the third outgoing (C^-) characteristic would occur at point (1,3). Refer to Figures 4.1 – 4.3 for a schematic representation of this system.

Initial and boundary conditions

When treated as an initial value problem a swash event is governed by the singularity at the instant of its initiation (i.e. the moment of bore collapse). Thus, the MOC GC model begins with initial conditions at the origin of the coordinate system (that is the point $x = 0, t = 0$). It is important to note that at the coordinate origin water depth (h) assumes all values between an upper and lower limit. Seaward boundary conditions are established through integration along a suitable outgoing (C^-) characteristic in accordance with the following procedure. As a consequence of the singular nature of a swash event it is necessary to specify the value of R^- on all outgoing (C^-)

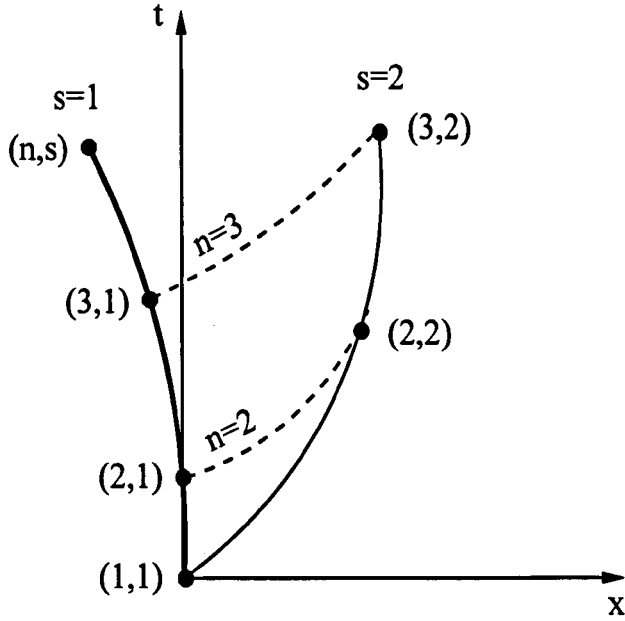


Figure 4.2: Close-up of the initial, seaward boundary, characteristic (bold solid line) and the adjacent C^- characteristic illustrating the notation employed to describe the MOC GC scheme.

characteristics between an upper and lower limit. The lower limit for R^- determines the characteristic that will represent the seaward boundary (i.e. $s = 1$) and the upper limit, alongside other factors, determines how close the model gets to the actual shoreline. Therefore, in choosing a lower bound for R^- it is necessary to ensure that it will furnish information for the entire region of integration under study. In this case the region of integration lies between the seaward boundary characteristic and the C^- characteristic representing the position of the run-up tip where $h \rightarrow 0$, see Figure 4.1. The first outgoing (C^-) characteristic that fulfils these criteria is the one that is initially coincidental with the t axis in the $x - t$ plane; again, refer to Figure 4.2 and the C^- characteristic denoted by $s = 1$ for clarification. Along this characteristic $\frac{dx}{dt}$ is initially zero, hence $u = c$, and therefore recalling that $R^- = u - 2c + B_{,x}gt$, and that $t = 0$ at this point, it follows that this is satisfied when $u = c = \frac{2}{3}c_0$ where $c_0 = (gh_0)^{\frac{1}{2}}$. Hence

$R^- = -\frac{2}{3}c_0$ for all time on this seaward boundary characteristic. Specification of R^+ at the seaward boundary completes the information required to determine both the independent (x and t) and dependent (u and c) variables in the manner detailed later on in this section.

Determining the number of incoming (C^+) characteristics

It should be immediately obvious from the above that the size of the timestep, as well as the upper time limit on the seaward boundary, will directly determine the number of incoming (C^+) characteristics. Thus, if the time step on the seaward boundary is fixed at 1×10^{-6} s, and the upper time limit is set to 4s, then the model will require 4×10^6 incoming (C^+) characteristics and the maximum value of n will be $n_{max} = 4 \times 10^6$. In order to conserve memory the model employs a variable timestep on the seaward boundary; this is set up such that there is a large density of C^+ characteristics at earlier times.

Determining the number of outgoing (C^-) characteristics

The maximum number of outgoing (C^-) characteristics, s_{max} , is set as a parameter in the following manner. As described above, the value of R^- on outgoing characteristics lies within the range $-\frac{2}{3}c_0 \leq R^- < 2c_0$, and so the value of R^- on each of the s_{max} C^- characteristics is assigned by incrementing the initial value of $-\frac{2}{3}c_0$ by the amount $\frac{(\frac{8}{3}c_0)}{s_{max}}$ on each subsequent C^- characteristic. This continues until the shoreline boundary double characteristic, on which $R^- = 2c_0$, is approached with the last C^- characteristic being prescribed as that on which $R^- = 2c_0 - \frac{(\frac{8}{3}c_0)}{s_{max}}$. It can be seen from this that the number s_{max} of outgoing (C^-) characteristics has a direct bearing on how

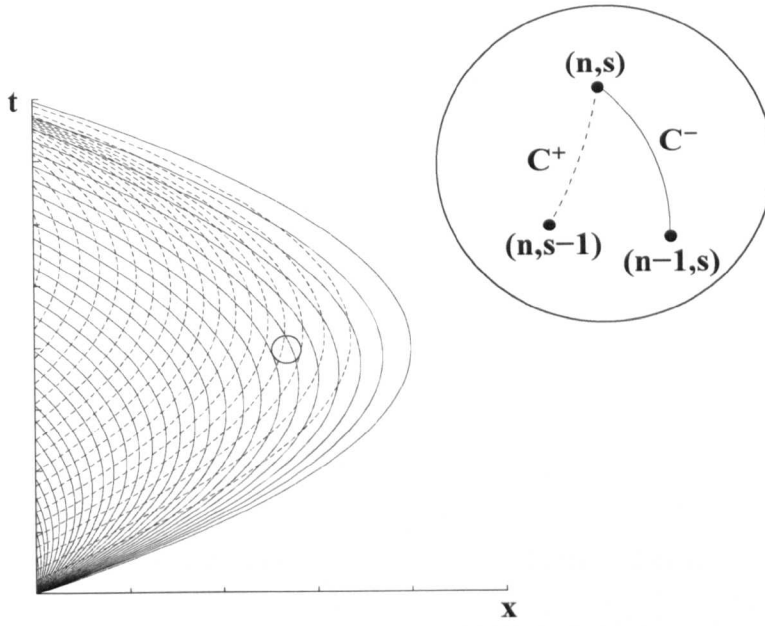


Figure 4.3: Computational mesh for MOC GC fixed bed scheme showing close-up of a typical (subcritical) cell.

close to the run-up tip the solution proceeds.

Formally defining the seaward boundary characteristic

The solution is systematically advanced along subsequent outgoing (C^-) characteristics one at a time, starting with the seaward boundary. The seaward boundary (SB) is taken to be an outgoing (C^-) characteristic; in this section values on this characteristic are denoted by the subscript $s = 1$. A requirement of the MOC GC technique detailed here is that the value of R^+ is known for all time on the SB characteristic. Due to the fact that R^+ is specified on the SB characteristic, and the fact that R^- is known for all time along the SB characteristic, all that is required is to solve the following system of equations in order to determine values for u and c at any prescribed point in time $t_{n,1}$:

$$R^+ = u_{n,1} + 2c_{n,1} + B_{,x}gt_{n,1}, \quad (4.1.1)$$

$$R^- = u_{n,1} - 2c_{n,1} + B_{,x}gt_{n,1}. \quad (4.1.2)$$

As the system comprises a set of two simultaneous equations with two unknowns, u and c , it is readily solved yielding:

$$c_{n,1} = \frac{(R_{n,1}^+ - R_{n,1}^-)}{4}, \quad (4.1.3)$$

and:

$$u_{n,1} = \frac{(R_{n,1}^+ + R_{n,1}^-)}{2} - B_{,x}gt_{n,1}. \quad (4.1.4)$$

On the seaward boundary characteristic it has been established that $R_{n,1}^- = -\frac{2}{3}c_0$. From this the value of u and c at any point $(n, 1)$ can be computed if the R^+ value is specified on the seaward boundary characteristic. Using this information, along with the size of the timestep Δt , an approximation to the location x of point $(n, 1)$ (second-order accurate in time) is made using:

$$x_{n,1} = x_{n-1,1} + \frac{\Delta t}{2} (u_{n-1,1} - c_{n-1,1} + u_{n,1} - c_{n,1}). \quad (4.1.5)$$

The scheme assumes that the value of x , u and c are known at the initial time step. The scheme then increments n by 1 and t by the prescribed amount, values of $u_{n+1,1}$ and $c_{n+1,1}$ are then determined using (4.1.4) and (4.1.3). The next point on the seaward boundary $x_{n+1,1}$ can now be located in an identical fashion to that described above. This process continues until the time limit (set as a parameter) is reached.

Creating the grid of characteristics

The first point on each of the outgoing (C^-) characteristics lies at the origin, with each C^- characteristic being distinguished by its unique value of R^- , where $\frac{2}{3}c_0 \leq R^- \leq 2c_0$. It follows from this that the initial location (i.e. $x_{1,s} = 0, s = 1 \dots s_{max}$) of each C^- characteristic is known. The scheme also requires that the value of u and c are known

at the origin. These values are determined from values of R^+ and R^- through relations derived from (3.4.11) and (3.4.12) as being:

$$c_{1,s} = \frac{(R_{1,1}^+ - R_{1,s}^-)}{4} \quad (4.1.6)$$

and:

$$u_{1,s} = \frac{(R_{1,1}^+ + R_{1,s}^-)}{2}. \quad (4.1.7)$$

Note that the time dependent $B_{,x}gt$ term has dropped out as we are at the origin and $t = 0$. Although the value of R^- is prescribed, and therefore presents no problems, the value of R^+ at the origin, point $(1, 1)$, is generally constant at $2c_o$; it can vary depending on initial conditions. The scheme now begins work on the first outgoing (C^-) characteristic shoreward of the seaward boundary. Conditions are known on the $(s-1)^{th}$ C^- characteristic, and now that conditions have also been established at point $(1, s)$ the scheme proceeds as follows. The difference forms of (3.4.11) and (3.4.12) are:

$$u_{n,s} + 2c_{n,s} = u_{n,s-1} + 2c_{n,s-1} - (t_{n,s} - t_{n,s-1})B_{,x}g \quad (4.1.8)$$

and:

$$u_{n,s} - 2c_{n,s} = u_{n-1,s} - 2c_{n-1,s} - (t_{n,s} - t_{n-1,s})B_{,x}g. \quad (4.1.9)$$

It is possible to construct second-order difference approximations for the characteristic equations (3.4.7):

$$x_{n,s} = x_{n-1,s} + \frac{1}{2} \left((u_{n,s} - c_{n,s} + u_{n-1,s} - c_{n-1,s})(t_{n,s} - t_{n-1,s}) \right) \quad (4.1.10)$$

and:

$$x_{n,s} = x_{n,s-1} + \frac{1}{2} \left((u_{n,s} + c_{n,s} + u_{n,s-1} + c_{n,s-1})(t_{n,s} - t_{n,s-1}) \right). \quad (4.1.11)$$

It follows that (4.1.8) and (4.1.9) can be combined to give:

$$c_{n,s} = \frac{1}{4} \left\{ u_{n,s-1} - u_{n-1,s} + 2(c_{n,s-1} + c_{n-1,s}) + (t_{n,s-1} - t_{n-1,s})B_{,x}g \right\}. \quad (4.1.12)$$

To compute $t_{n,s}$ an expression for $u_{n,s}$ is obtained from (4.1.9) and inserted into (4.1.10) and (4.1.11) to provide two expressions for $x_{n,s}$ which are then equated, rearranged and simplified to give:

$$\begin{aligned}
 t_{n,s} = & \left\{ t_{n,s-1}(3c_{n,s} + c_{n,s-1} - 2c_{n-1,s} + u_{n-1,s} + u_{n,s-1} + t_{n-1,s}B_{,x}g) - \right. \\
 & \left. t_{n-1,s}(c_{n,s} - 3c_{n-1,s} + 2u_{n-1,s} + t_{n-1,s}B_{,x}g) + 2(x_{n-1,s} - x_{s-1,n}) \right\} \times \\
 & \left\{ -2c_{n,s} - c_{n-1,s} + u_{n-1,s} - c_{n,s-1} - \right. \\
 & \left. u_{n,s-1} + t_{n-1,s}B_{,x}g - t_{n,s-1}B_{,x}g \right\}^{-1}, \quad (4.1.13)
 \end{aligned}$$

with $c_{n,s}$ given by (4.1.12). The value of $c_{n,s}$ is substituted, along with the value of $t_{n,s}$, into (4.1.8) or (4.1.9) to yield up $u_{n,s}$. Finally, from (4.1.10) or (4.1.11) $x_{n,s}$ can be obtained. Next n is incremented and the scheme then moves onto the next point on this particular outgoing (C^-) characteristic. The scheme proceeds like this until n reaches a maximum value. This maximum value for n is equal to the number of incoming (C^+) characteristics for the reasons described above.

4.1.3 A note on the formal accuracy of MOC GC schemes

The scheme employed by both Amein (1964) and Guard and Baldock (2007) uses a linear approximation for the characteristic slopes based on known values at the previous time step. The scheme outlined here uses an averaging of the characteristic slopes between their old and new values. By analogy with the rectangular rule of quadrature Lister and Roberts (1956); Lister (1960) have shown that MOC GC schemes employing linear slopes are formally first-order accurate. Lister and Roberts (1956); Lister (1960) have also shown that MOC GC schemes using characteristic slopes based on wave speed averages are formally second-order accurate using the trapezoidal rule of quadrature.

4.2 Morphodynamic (mobile bed) solvers

In the course of this research two numerical solvers were developed successfully to model single swash events on a mobile beach. Initially, an attempt was made to extend the MOC GC scheme to solve the full shallow water–Exner system. This was only successful for certain flow problems. The MOC GC method and results for both dam-break and tidal flow over a sand dune are described in the paper of Kelly and Dodd (2008). The MOC GC scheme proved unsuitable for simulating mobile bed swash flow. In particular, the wave structure is such that the use of a characteristics grid becomes prohibitively difficult especially when embedded shocks develop in the flow. Instead, a specified time interval (STI) MOC scheme with explicit shock fitting was developed alongside two more conventional finite difference shock capturing solvers based on the scheme of MacCormack (1969). The principle motivation for developing a MOC scheme with shock fitting is that such a scheme inherently reveals the underlying flow (morpho)dynamics as it is based on the characteristics of wave propagation. The reason for simultaneously developing a shock capturing type scheme is that it can be used for comparative reasons. Moreover, shock capturing schemes can start from discontinuous initial conditions and thus be used to give some insight into the wave structure of the mobile bed dam-break problems examined in Chapter 6. Finally, it should be relatively easy to extend such a shock capturing finite difference solver in order to model multiple swash events on a mobile beach.

4.2.1 Specified time interval (STI) method of characteristics

The primitive variable form of the shallow water–Exner equations (3.2.8), (3.2.18) and (3.3.5) describing both the water and sediment motion can be solved simultaneously

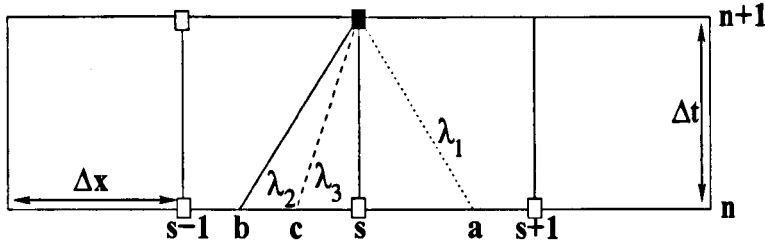


Figure 4.4: Characteristics attending to an ordinary mesh point for the mobile bed MOC STI scheme (sub-critical flow).

using a MOC based numerical scheme. The solution technique employed here belongs to the specified time interval (STI) class of MOC schemes first outlined for unsteady mobile bed flow by Wu (1973) and discussed in more detail by Lai (1986). Such a scheme has not before been used to successfully simulate highly unsteady transcritical flow such as that found in the swash zone. The Riemann equations (3.4.23) are put into Euler difference form and integrated numerically on a regular $x - t$ grid with spatial increments of Δx and time step Δt . Referring to Figure 4.4 the difference equations used are:

$$(u_{s,n+1} - u_i) + \frac{g}{(\lambda_{k,i} - u_i)}(h_{s,n+1} - h_i) + \frac{g}{\lambda_{k,i}}(B_{s,n+1} - B_i) = 0, \quad (4.2.1)$$

where $i = a, b, c$ and $k = 1, 2, 3$ respectively. Equations (4.2.1) can be rewritten as a linear system of equations of the form:

$$u_{s,n+1} + \frac{g}{(\lambda_{k,i} - u_i)}h_{s,n+1} + \frac{g}{\lambda_{k,i}}B_{s,n+1} = L_{k,i}^*, \quad (4.2.2)$$

with:

$$L_{k,i}^* = u_i + \frac{gh_i}{(\lambda_{k,i} - u_i)} + \frac{gB_i}{\lambda_{k,i}}. \quad (4.2.3)$$

The linear system (4.2.2) can then be solved simultaneously in order to provide explicit expression for $h_{s,n+1}$, $u_{s,n+1}$ and $B_{s,n+1}$. Written in the notation of Figure 4.4 these are:

$$B_{s,n+1} = \frac{L_{3c}^* - L_{1a}^* + N^*(L_{2b}^* - L_{1a}^*)}{\frac{u_1}{\lambda_{1a}} - \frac{u_3}{\lambda_{3c}} - N^*\left(\frac{u_2}{\lambda_{2b}} - \frac{u_1}{\lambda_{1a}}\right)}, \quad (4.2.4)$$

$$u_{s,n+1} = \frac{g\{L_{2b}^* - L_{1a}^* + (\frac{u_2}{\lambda_{2b}} - \frac{u_1}{\lambda_{1a}})\}B_{s,n+1}}{(\lambda_{2b} - u_2 - \lambda_{1a} + u_1)}, \quad (4.2.5)$$

$$h_{s,n+1} = L_{1a}^* - \frac{(\lambda_{1a} - u_1)}{g}u_{s,n+1} + \left(\frac{u_1}{\lambda_{1a}} - 1\right)B_{s,n+1}, \quad (4.2.6)$$

where:

$$N^* = \frac{\lambda_{1a} - u_1 - \lambda_{3c} + u_3}{\lambda_{2b} - u_2 - \lambda_{1a} + u_1}. \quad (4.2.7)$$

It is now possible to detail the STI MOC scheme developed as part of this research. Schemes that are both first- and second-order accurate in both space and time are presented. The formal accuracy of the STI MOC schemes is not discussed further here as the proof is somewhat involved. The interested reader is referred to Gustafsson et al. (1992) in which the formal accuracy of STI MOC schemes with space line interpolation is rigorously proved for generic systems of conservation laws.

In the main body of the flow the solution procedure is as follows:

1. Assume the slope of each of the three characteristic families at $(s, n + 1)$ is equal to that at (s, n) .
2. The locations of a , b and c can then be found using extrapolation backwards in time.
3. First approximations for the dependent variables (h , u and B) at $(s, n + 1)$ are then computed using interpolated values of h , u and B at a , b and c in (4.2.4)–(4.2.6). The order of accuracy in space depends on the interpolation procedure used to find values at a , b and c . If the order is > 1 the solution becomes prone to parasitic oscillations around gradient discontinuities (Gibbs phenomenon). These oscillations can be removed by employing the Engquist et al. (1989) filter detailed in §5.1.4¹ For second-order accuracy in time an average of the h_i , u_i , B_i and λ_k

¹It is worth noting that shock capturing finite difference and finite volume solvers also suffer from the

values at (s, n) and $(s, n + 1)$ for $i = a, b, c, k = 1, 2, 3$ is made and used in (4.2.4)–(4.2.6).

4. These new values for h and u are used in (3.4.29), (3.4.30) and (3.4.31) to recalculate the slope at $(s, n + 1)$.
5. Steps 2–4 are repeated until successive values of dependent variables at $(s, n + 1)$ agree within a specified error limit.

In this scheme any order of accuracy can be obtained in space by selecting the appropriate interpolating polynomial. Note that, unlike the MOC GC scheme which does so implicitly, the scheme must satisfy the CFL stability criterion so that

$$\left| \frac{\Delta t}{\Delta x} \right| \leq \frac{1}{|\lambda_{max}|} \quad (4.2.8)$$

where λ_{max} is the maximum wave speed found. Solution of the three-equation system is simultaneous so there is no iteration to a steady state or morphodynamical time-stepping. At the flow boundaries special procedures are required and these are detailed in §4.3.

4.2.2 Initial time step for dam-break IC

For the dam-break initial conditions equivalent to an SM63 swash event, or indeed for any dam-break initial conditions, all of the dependent variables are multivalued at $t = 0$. The MOC solution is therefore started at an initially small time (t_I). Values of the dependent variables at t_I are provided by a Riemann wave solution procedure; Gibbs phenomenon when steep gradients in the dependent variables are present. Whilst a filter is used here to remove Gibbs type oscillations, such oscillations are usually cured in shock capturing schemes by the use of a flux limiter (LeVeque, 1992).

details of this procedure are given in Chapter 6. This practice of starting at a finite time is always necessary when MOC schemes are used to solve dam-break type problems. In the case of wet-dry rigid bed MOC numerical solvers the values of the dependent variables at the start time are typically provided by the Ritter analytical solution (see for example Sakkas and Strelkoff (1973)).

4.2.3 Finite difference method – MacCormack’s scheme

It was mentioned in the introduction that the scheme developed by MacCormack (1969) is particularly suitable for application to swash flow, as source terms are easily treated. Another reason for choosing the MacCormack scheme is that a numerical approximation of the Jacobian matrix is not necessary. The MacCormack scheme is a finite difference predictor corrector scheme with second-order accuracy in both space and time. The scheme is a variant of the Lax and Wendroff (1960) scheme, as are all second-order space centred explicit schemes (Hirsch, 1988). The basic idea behind such schemes can be summarised as follows:

- Approximate the dependent variables (f) at time $t + \Delta t$ by a Taylor series expansion truncated at the second order term, i.e.:

$$f(t + \Delta t) = f(t) + f_{,t}\Delta t + \frac{1}{2}f_{,t,t}\Delta t^2 + O(\Delta t^3) \quad (4.2.9)$$

- Express the time derivatives in terms of the space derivatives, obtained from the governing equations
- Approximate the space derivatives using central differences

The MacCormack predictor corrector sequence is:

$$\text{predictor step: } \bar{f}_s = f_s^n - \frac{\Delta t}{\Delta x} (f_{s+1-\epsilon}^n - f_{s-\epsilon}^n) + \Delta t S_s^n, \quad (4.2.10)$$

$$\text{corrector step: } \tilde{f}_s = f_s^n - \frac{\Delta t}{\Delta x} (\bar{f}_{s+\epsilon} - \bar{f}_{s-1+\epsilon}) + \Delta t \bar{S}_s, \quad (4.2.11)$$

$$\text{update step: } f_s^{n+1} = \frac{(\bar{f}_s + \tilde{f}_s)}{2}, \quad (4.2.12)$$

where S represents the source terms with \bar{S} being the value of S computed using the values of the dependent variables obtained by the predictor step. The parameter ϵ can be either 0 or 1. The predictor step is a first-order forward ($\epsilon = 0$) or backward ($\epsilon = 1$) difference in space. The corrector step is a first-order backward ($\epsilon = 0$) or forward ($\epsilon = 1$) difference in space. The scheme obtains second-order accuracy as a consequence of the cancelling out of the first-order truncation errors in the update step. The computational stencil for the MacCormack scheme is given in Figure 4.5. A problem with the scheme arises when shocks are present in the flow as the exact solution ceases to be Taylor expandable, thus the truncation errors no longer cancel out exactly (Moretti, 1971). The MacCormack scheme is particularly sensitive to the direction of shock propagation, much more so than any other Lax Wendroff variant. An analysis by Lerat and Peyret (1974) illustrates that the choice of the direction for predictor corrector steps is key to minimising parasitic oscillations around shocks. Indeed, it can be shown that the choice of ϵ for a particular shock direction is crucial in deciding if the scheme is dissipative or not. This feature can be beneficial, as choosing the correct direction for the predictor and corrector steps has a stabilising influence on oscillations. The predictor corrector direction is particularly important when dealing with very strong shocks such as backwash bores. Moreover, the instabilities inherent in the MacCormack scheme around such strong shocks tend to cause the scheme to blow up after relatively few time steps. Thus, the instabilities around shocks require special

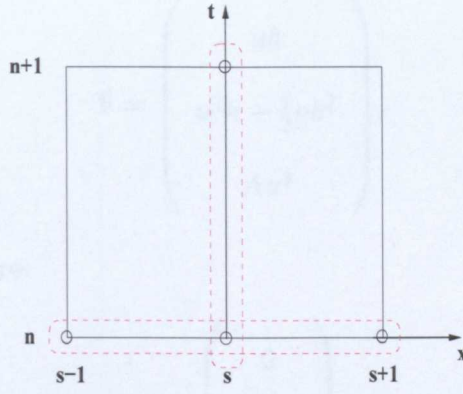


Figure 4.5: Computational stencil for the MacCormack predictor-corrector scheme.

treatment. An in depth discussion of the techniques, merits and drawbacks of shock capturing schemes is postponed until the following Chapter.

4.2.4 Conservation form

MacCormack's scheme is used in the context of this work as a shock capturing scheme. In shock capturing schemes the governing equations must be in conservation form for the shock development to be correctly approximated, see §5.1. In conservation form the MacCormack scheme can be written:

$$\text{predictor step: } \bar{\mathbf{f}}_s = \mathbf{f}_s^n - \frac{\Delta t}{\Delta x} (\mathbf{F}_{s+1-\epsilon}^n - \mathbf{F}_{s-\epsilon}^n) + \Delta t \mathbf{S}_s^n, \quad (4.2.13)$$

$$\text{corrector step: } \tilde{\mathbf{f}}_s = \mathbf{f}_s^n - \frac{\Delta t}{\Delta x} (\bar{\mathbf{F}}_{s+\epsilon} - \bar{\mathbf{F}}_{s-1+\epsilon}) + \Delta t \tilde{\mathbf{S}}_s, \quad (4.2.14)$$

$$\text{update step: } \mathbf{f}_s^{n+1} = \frac{(\bar{\mathbf{f}}_s + \tilde{\mathbf{f}}_s)}{2}, \quad (4.2.15)$$

where \mathbf{f} represents the vector of conserved variables i.e.:

$$\mathbf{f} = \begin{pmatrix} h \\ uh \\ B \end{pmatrix},$$

and \mathbf{F} represents the vector of flux conservative variables, i.e.:

$$\mathbf{F} = \begin{pmatrix} uh \\ u^2h + \frac{1}{2}gh^2 \\ Au^3 \end{pmatrix},$$

and the source terms \mathbf{S} are:

$$\mathbf{S} = \begin{pmatrix} 0 \\ gh \frac{\partial B}{\partial x} \\ 0 \end{pmatrix}.$$

4.2.5 Treatment of source terms for the conservation form

For purely hydrodynamical (fixed bed) swash events the non-dimensionalisation of Hibberd and Peregrine (1979) allows the shallow water equations to be re-written without the beach slope term. This approach is ingenious as, for frictionless flow, it obviates the need to treat any source terms when using a numerical solver. Unfortunately, for fully coupled morphodynamical flow it is impossible to remove the source terms. Thus, when the governing equations are written in conservation form the issue of source terms must be addressed. When using a MacCormack scheme source terms have traditionally been approximated using a pointwise approach i.e.:

$$gh \frac{\partial B}{\partial x} \approx \frac{g(h_{s+1}^n + h_{s-1}^n)(B_{s+1}^n - B_{s-1}^n)}{4\Delta x}. \quad (4.2.16)$$

It is known, however, that such an approximation is unstable in the presence of an irregular bottom topography (Hubbard and Garcia-Navarro, 2000). The instabilities generated by a pointwise approach often lead to the failure of a scheme to conserve mass. For this reason it has been suggested by certain researchers, e.g. Hubbard and Garcia-Navarro (2000); Vincent et al. (2001); LeVeque (2002), that source terms be approximated in the same manner as the flux gradient terms. Thus, in this work the

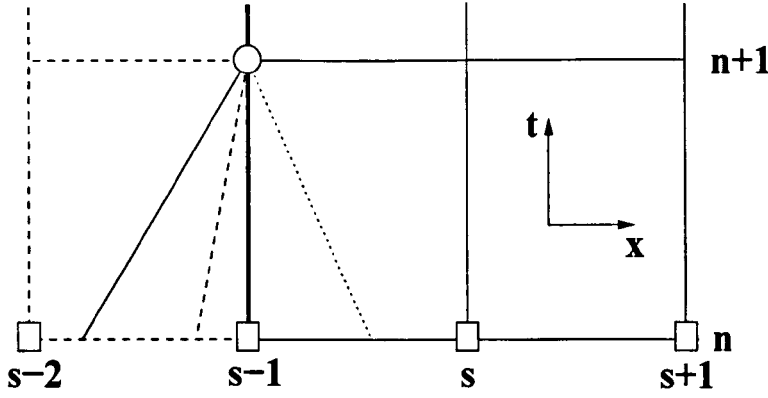


Figure 4.6: Characteristics based treatment of the upstream (seaward) boundary for mobile bed flow

source terms are discretised at each step using forward or backward differences, i.e.:

$$gh \frac{\partial B}{\partial x} \approx \frac{g(h_{s+1-\epsilon}^n + h_{s-\epsilon}^n)(B_{s+1-\epsilon}^n - B_{s-\epsilon}^n)}{2\Delta x} \quad (4.2.17)$$

where $\epsilon = 0$ for forward differences and $\epsilon = 1$ for backward differences. Such an approach has proven extremely stable throughout the course of this research.

4.3 Boundary conditions for non-GC schemes

With the exception of the MOC GC scheme, described in §4.1.1, which treats boundaries implicitly, all the schemes described above make use of the following boundary treatments.

4.3.1 Upstream (seaward) transmissive boundary

A characteristics based method, developed from that outlined by Sieben (1997), for treating the upstream boundary that allows for a limited spatial domain is presented here. Referring to Figure 4.6, the boundary is fixed in space at x_{s-1} ; this is denoted by the bold line in the figure. An additional "ghost" cell, x_{s-2} , is introduced on the n^{th} time

level. The point x_{s-2}^n is located at a distance of Δx to the left of the upstream boundary. Values of all the dependent variables (h, u and B) are computed at x_{s-2}^n using linear extrapolation from values at x_{s-1}^n and x_s^n . Next, the STI MOC procedure described in §4.2.1 is used to compute values of h, u and B at x_{s-1}^{n+1} . This procedure is applied at the end of each time step in order to obtain boundary data for the next time. This type of treatment allows waves to exit the computational domain, i.e. is transmissive, and has been successfully employed in the STI MOC solver.

As the work here involves only one spatial dimension it is possible to simplify handling of the upstream boundary. By ensuring that the upstream domain is sufficiently long, the tail of the rarefaction wave is allowed to move unhindered until the computation has finished. An approach such as this requires no explicit treatment of the upstream boundary and was used with the STI MOC and MacCormack based finite difference schemes.

4.3.2 Downstream (shoreline) boundary

Background

The downstream shoreline boundary represents the interface of land and water and, as such, the boundary is of a wet-dry type. Wet-dry boundaries, like the analogous gas-vacuum boundaries of gas dynamics, are particularly difficult to treat numerically. When using MOC GC schemes the shoreline boundary is dealt with implicitly; however, as the wave tip is approached certain problems become apparent. In the fixed bed case close to the shoreline boundary, incoming and outgoing characteristics have very similar slopes as $h \rightarrow 0$ and in fact $\frac{dx}{dt} \rightarrow u$ for both characteristic families. Thus, the intersection of opposing families of characteristics can become infrequent, leading to

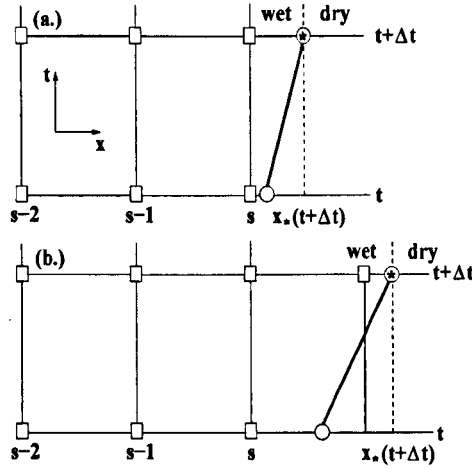


Figure 4.7: Downstream (shoreline) boundary treatment using a time dependent space step for mobile bed flow

poor definition close to the tip. For frictionless flow the shoreline comprises a double characteristic as $h = 0$ there, therefore $\frac{dx}{dt}$ is identical for both C^+ and C^- characteristics. Consequently, under these conditions, it is impossible to define the actual tip using a MOC GC scheme. It is, however, possible to get ever closer to the tip with the inclusion of additional advancing (C^+) characteristics. Furthermore, it is theoretically possible to reach the tip when friction is included in the model (Sakkas, 1972). In a paper concerning fixed bed dam-break type flows, Abbott (1961) argued that letting $h \rightarrow 0$ at the tip is physically unrealistic. Instead, he suggested that, even in the absence of friction, the tip represented a "wall" of water moving over the dry bed; for flow with depth averaged velocity Abbott stated that the structure of the wall was irrelevant. What was important was to establish relations between the height of the wall h_* and its velocity u_* . For dimensional equivalence Abbott suggested a simple relationship between h_* and u_* of the form:

$$u_* = \kappa (gh_*)^{\frac{1}{2}}, \quad (4.3.1)$$

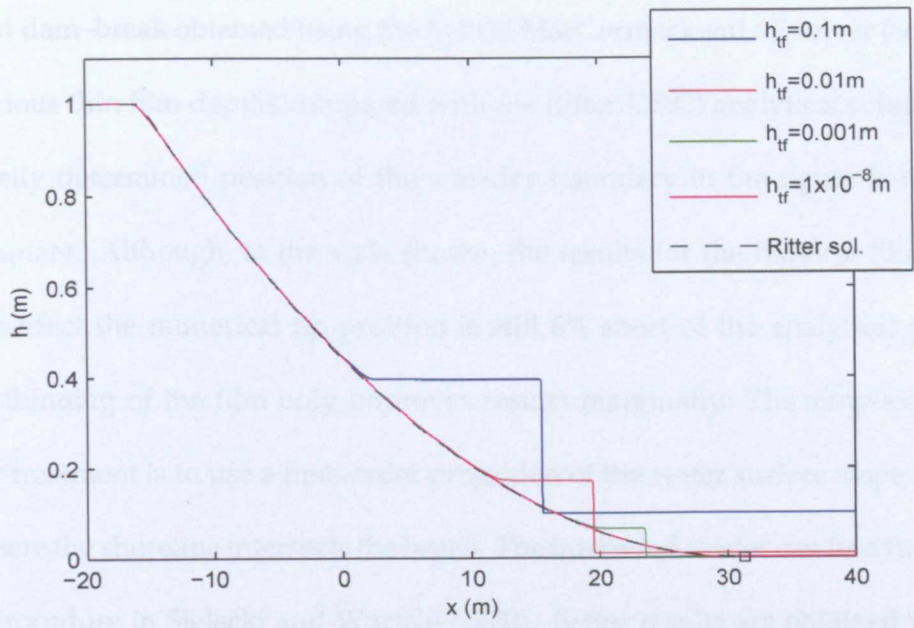


Figure 4.8: Snapshots of water height at $t=5s$ for a fixed bed wet-dry dam-break showing the effect of thin film depth (h_{tf}) on wave profile and tip velocity.

where κ is the constant of proportionality. Experimental results can be used to determine a suitable value for κ , and Abbott illustrated that his "stability criterion" approach gave a better approximation for actual physical dam-break flows than the Ritter solution. Abbott's approach is particularly suitable for cases when bed friction is included and Freeman and LeMéhauté (1964) used this technique in their STI MOC computation of limiting solitary wave run-up.

There appear to be four primary methods of attack when treating a wet-dry boundary using a classical hyperbolic solver such as the MacCormack scheme. The simplest, in coding terms, is to employ the so-called "thin film" technique; indeed, this is the only method discussed here that does not require explicit tracking of the wet-dry boundary. When using the thin film technique conditions are set up such that a thin film of water covers the "dry" region. If the film is made thin enough then the solution replicates the actual wet-dry case reasonably well. Figure 4.8 illustrates water depth profiles for a

fixed bed dam-break obtained using the hybrid MacCormack–mLxF solver (see §5.1.5) with various thin film depths compared with the Ritter (1892) analytical solution. The analytically determined position of the wet–dry boundary in the figure is indicated by the square. Although, at the scale shown, the results for the thinnest film appear almost perfect the numerical tip position is still 6% short of the analytical position. Further thinning of the film only improves results marginally. The simplest *genuine* wet–dry treatment is to use a first–order projection of the water surface slope to determine where the shoreline intersects the beach. The interested reader can find full details of this procedure in Sielecki and Wurtele (1970). Better results are obtained using an extrapolative predictor step followed by a corrector step based on a time centred difference scheme; this technique was pioneered by Hibberd and Peregrine (1979) and from here on in this technique is referred to as the HP79 algorithm. Another, rather ingenious, approach is to use a transformation of the independent variables that effectively fixes the position of the shoreline. This approach was initially employed by L’atkher and Shkol’nikov (1978) and Takeda (1984); more recently the technique was used to successfully model the run–up of both non–breaking and breaking solitary waves by Li and Raichlen (2002). The most novel idea is that of Aida (1977) who considered the beach as comprising a ladder of small steps and applied a weir formula to each step. In the course of this research the HP79 algorithm was tried but suffered from severe spurious oscillations when used in the mobile bed model even with the corrections proposed by Packwood (1980). Instead, following Titov and Synolakis (1995) treatment of the shoreline boundary in this work uses a time dependent space step for which $\Delta x = \Delta x(t)$ for the last mesh point (shoreline position). However, the algorithm developed in Titov and Synolakis (1995) requires that the beach slope is known *a priori*, this criterion is not met for the mobile bed problem when the sediment transport formula

$q = q(u)$ only. Therefore, referring to Figure 4.7, the following algorithm is presented for the shoreline boundary. It should be noted that treatment of the bed height at the tip (B_*) depends on the form of q employed for closure. In Chapter 6 quasi-analytical solutions are derived for the mobile bed dam-break for which $q = Au^3$ and $q = \bar{A}u^3h$. These solutions indicate that when $q = Au^3$, B_* is governed by a shock relation derived from the Exner equation and when $q = \bar{A}u^3h$, $B_* \rightarrow 0$. For this reason two distinct treatments for the bed height at the wave tip that depend on the form given to q are presented below.

Run-up

Assuming that at time t the location of the shoreline boundary $x_* = x_*^t$ is known, then, with the subscript s representing the last fixed nodal point on a beach whose slope ($\tan\beta$) is initially constant, the algorithm is summarised as follows:

1. At time t the velocity at the shoreline boundary $\frac{dx_*}{dt} = u_*$ is set equal to that at the previous fixed node ($u_* = u_s$). Or, u_* is obtained by (linear) extrapolation from the previous two (s and $s - 1$) or (quadratic) extrapolation from the previous three ($s, s - 1$ and $s - 2$) fixed nodes.
2. An initial guess for $x_*^{t+\Delta t}$ is made using the formula $x_*^{t+\Delta t} = x_*^t + u_*^t \Delta t$.
3. $u_*^{t+\Delta t}$ is set equal to that at the previous fixed node, i.e. $u_*^{t+\Delta t} = u_s^{t+\Delta t}$ or computed using either linear or quadratic extrapolation.
4. $x_*^{t+\Delta t}$ is re-computed using the formula $x_*^{t+\Delta t} = x_*^t + \left\{ \frac{(u_*^{t+\Delta t} + u_*^t)}{2} \Delta t \right\}$
5. If extrapolation is used to find $u_*^{t+\Delta t}$, steps 3 and 4 are repeated until values of $x_*^{t+\Delta t}$ agree to within a specified error limit.

6. The water depth at the shoreline boundary h_* is set equal to zero.
7. (a.) If sediment flux is given by $q = Au^3$ the value of the bed height is set using the beach slope ($\tan \beta$) and the shock relation at the shoreline boundary i.e:

$$B_* = A\zeta u_*^2 + x_*(t + \Delta t) \tan \beta. \quad (4.3.2)$$

- (b.) If sediment flux is given by $q = \bar{A}u^3h$ the value of the bed height is set using the beach slope only i.e. $B_* = x_*(t + \Delta t) \tan \beta$.
8. If, at time $t + \Delta t$, the shoreline boundary position x_* exceeds the next fixed mesh point ($s + 1$) the value of s is incremented by 1 and this fixed mesh point is introduced. The dependent variables here are determined by an interpolation from the values at the previous fixed mesh point (x_{s-1}) and those at x_* .

Backwash

Treatment of the backwash is much the same as the run-up; the differences being that in step 4 the bed level at the tip is computed using an extrapolation procedure employing data from the previous two mesh points. In step 5 if the shoreline has receded beyond a fixed mesh point then that mesh point is no longer used in the computational procedure.

This approach differs from that of Titov and Synolakis (1995) as here the shoreline position is tracked explicitly through time using an extrapolative procedure. Titov and Synolakis (1995) use a horizontal projection of the free surface and specify the shoreline position as being where this line intercepts the beach, cf. Figure 2 of their paper. The algorithm presented here has proven to be extremely robust when used with both conventional finite difference (MacCormack) and STI MOC type schemes.

4.3.3 Stencil for the penultimate mesh point when using MacCormack based schemes

For MacCormack based solvers treatment of the penultimate meshpoint is slightly different to that of meshpoints in the main body of flow. The reason for this is that Δx is variable between mesh points s and $s + 1$ at time level n when point $s + 1$ corresponds to the shoreline boundary. Thus, with $\epsilon=0$, $\Delta x = r(t)$ for the forward difference step or, with $\epsilon=1$, $\Delta x = r(t)$ for the backward difference step. No special treatment of the penultimate mesh point is necessary when using the STI MOC solver.

4.3.4 Treatment of the penultimate mesh point in shock capturing schemes

If a shock capturing scheme is to be employed it is necessary to use the conservation form of the governing equations. Casting the equations in conservation form can generate problems for numerical solvers as the tip is approached. This occurs because $h \rightarrow 0$ whilst u tends towards some finite limiting value u_* and u is necessarily computed using:

$$u = \frac{uh}{h}, \quad (4.3.3)$$

meaning that any small errors in the computation are amplified. This can lead to numerical instability and even code failure. A suitable solution to this problem is to employ the primitive variable form of the governing equations in the vicinity of the tip such that a value for u is obtained directly. Numerical experiments using the shock capturing schemes described above have shown that it is sufficient to employ primitive variables only when computing values of the dependent variables at the penultimate mesh point before the tip.

4.4 Model verification

It is essential to check that the numerical schemes described above are capable of reproducing analytical solutions obtained for the same equation set. The system of partial differential equations comprising (3.2.8), (3.2.18) and (3.3.5) reduces to a system comprising only the shallow water equations (3.2.8) and (3.2.18) if A is set equal to zero. There are a number of known analytical solutions to the shallow water equations (Carrier and Greenspan, 1958; Shen and Meyer, 1963; Spielvogel, 1976; Synolakis, 1986) but, as was discussed in §2.1, only the Shen and Meyer (1963) SM63 is representative of bore-driven swash. For this reason the SM63 solution is used to verify the numerical schemes described in this thesis. Thus, in order to test the validity of the STI MOC and MacCormack based schemes, as well as the shoreline boundary treatment, A is set at $A = 1 \times 10^{-12} \text{s}^2 \text{m}^{-1}$ in order to 'fix' the bed and the following initial conditions used:

$$\left. \begin{aligned} h(x, 0) &= h_o \\ u(x, 0) &= 0 \end{aligned} \right\} \forall x \leq 0 \quad (4.4.1)$$

and:

$$\left. \begin{aligned} h(x, 0) &= 0 \\ u(x, 0) &= 0 \end{aligned} \right\} \forall x > 0, \quad (4.4.2)$$

with:

$$B(x, 0) = 0.1x. \quad (4.4.3)$$

Computational parameters employed are given in table 4.4. Two solvers based on the MacCormack scheme are developed in Chapter 5; for reasons given in that chapter only results obtained using the MacCormack-modified Lax Friedrichs (mLxF) hybrid scheme are presented here. Results of both the STI MOC and MacCormack numerical schemes are compared with the SM63 analytical solution in Figures 4.9 to 4.11. In

Parameter	Value used
Δx	$1 \times 10^{-2} \text{ m}$
Δt	$1 \times 10^{-3} \text{ s}$
Courant N ^o .	Variable
θ_B	1×10^{-12}
h_{tol}	$1 \times 10^{-6} \text{ m}$
t_I	$1 \times 10^{-2} \text{ s}$

Table 4.1: Computational parameters used for the verification of both STI MOC and MacCormack based numerical schemes.

Figure 4.9 predictions were made using the MacCormack–mLxF hybrid scheme with a value of $\Delta x = 1 \times 10^{-2}\text{m}$. Results shown in Figure 4.10 were obtained using the second–order accurate (in space and time) STI MOC solver. For both solvers the initial data was provided by the Riemann wave solution where the value of t_I (see Chapter 6 for details on t_I and the Riemann wave solution) was set equal to the value of Δx . By employing the Riemann wave solution in this way an excellent approximation of the initial tip velocity is achieved. Note that for the last two times $t = 8$ and $t = 10 \text{ s}$ shown the water is retreating off the beach, i.e. the backwash has begun. Maximum discrepancy of both numerical schemes from the SM63 solution is found closest to the original dam/shoreline location at all the times shown. For both schemes the maximum discrepancy between analytical and numerical solutions is less than 2.5% in the figures provided. The most likely cause of this discrepancy is the small amount of bed mobility required by both schemes; scour is at a maximum at the original dam/shoreline location for the mobile bed problem. It should also be noted that the MacCormack–mLxF

hybrid scheme does not perform as well as the STI MOC scheme. The cause of this is likely to be the inaccuracy introduced at the gradient discontinuity corresponding to the tail of the upstream rarefaction. The inaccuracy is a consequence of numerical diffusion; details of this are given in §5.1.5. The fact that the error decreases as distance from the gradient discontinuity increases appears to substantiate this assumption.

Figure 4.11 illustrates shoreline evolution according to the SM63 analytical solution, STI MOC and MacCormack–mLxF numerical schemes. For this test a value of $\Delta x = 5 \times 10^{-3}\text{m}$ was used and quadratic extrapolation used to determine u at the shoreline. Clearly the agreement between analytical and numerical results, from both STI MOC and MacCormack–mLxF schemes, is excellent. The maximum discrepancy between the numerical and analytical solutions is within 1.25%. Interestingly, the numerical scheme slightly over predicts the run-up. From this it can be concluded that the shoreline boundary treatment introduced in §4.3.2 works exceedingly well for the fixed bed case. Note that the results presented in Figure 4.11 are dimensionless but retain a dependence on the beach slope ($\tan\beta = 0.1$). Typically, in the literature, results are presented in dimensionless form with the beach slope scaled to unity, see e.g. Hibberd and Peregrine (1979). In Chapter 7 suitable non-dimensional variables are derived for the shallow water–Exner equations and used for the presentation of results thereafter; however, beach slope is not scaled out as, for a mobile bed, it is no longer time independent. Further validation is carried out in Appendix D, where results of the STI MOC and MacCormack finite difference schemes are compared with the morphodynamic dam-break solutions developed in Chapter 6. In Appendix D, results obtained using the MOC GC scheme detailed in §4.1.1 are also validated for test cases that include a comparison with the SM63 analytical solution. In all the cases considered all schemes are found to perform very well.

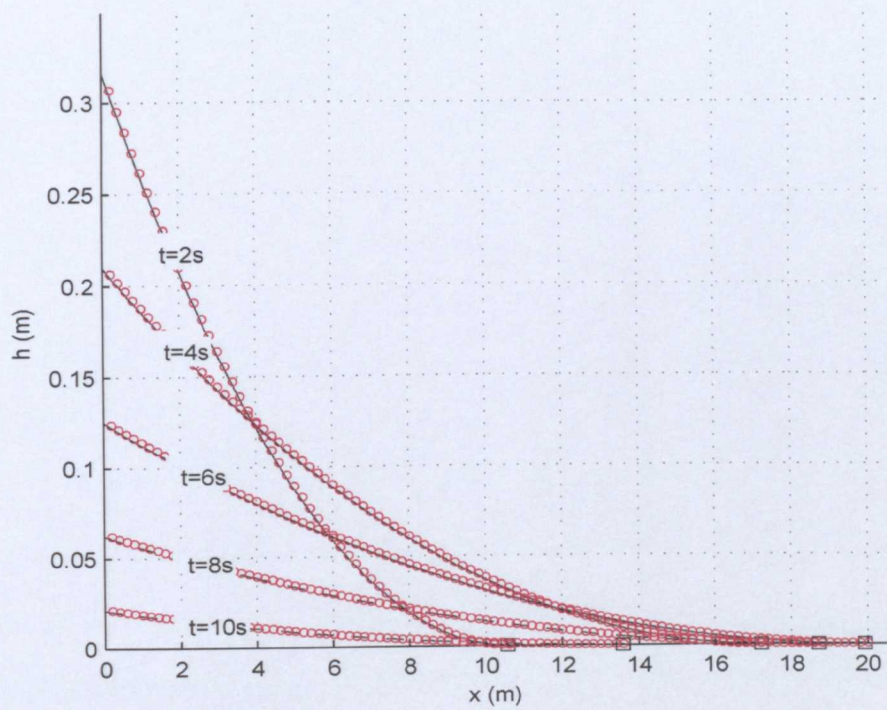


Figure 4.9: Comparison of analytical (lines) and Mac-mLxF numerical (circles) predictions of the water height h at times shown for SM63 swash with $A = 1 \times 10^{-10} \text{ s}^2 \text{ m}^{-1}$

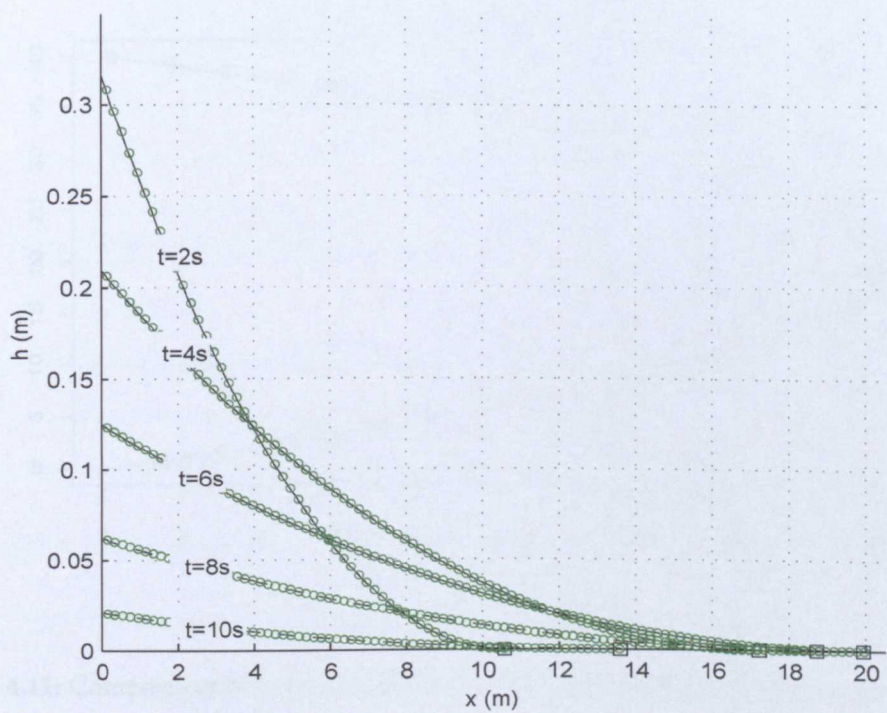


Figure 4.10: Comparison of analytical (lines) and STI MOC numerical (circles) predictions of the water height h at times shown for SM63 swash with $A = 1 \times 10^{-10} \text{s}^2 \text{m}^{-1}$.

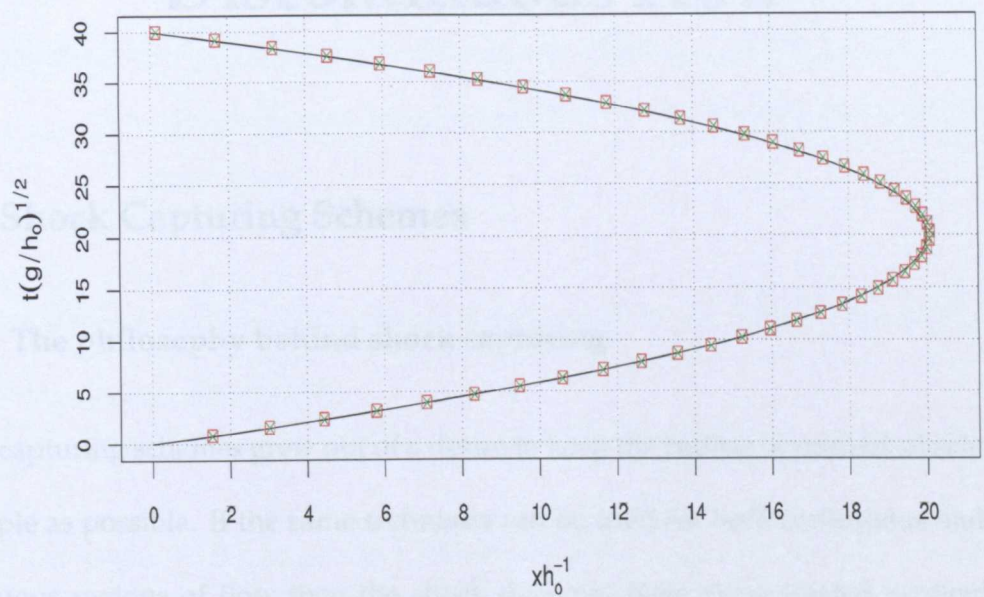


Figure 4.11: Comparison of analytical and numerical predictions of the instantaneous shoreline position for SM63 swash with $A = 1 \times 10^{-10} \text{s}^2 \text{m}^{-1}$ here $\Delta x = 5 \times 10^{-3} \text{m}$.

Discontinuous Flow

5.1 Shock Capturing Schemes

5.1.1 The philosophy behind shock capturing

Shock capturing schemes grew out of a desire to keep the coding of numerical schemes as simple as possible. If the same technique can be used for both continuous and discontinuous regions of flow then the shock does not have to be treated explicitly as a moving internal boundary. The principle idea behind shock capturing schemes is therefore that discontinuous regions can be thought of as continuous regions in which the dependent variables change rapidly. In a preliminary look at devising a numerical scheme for discontinuous gas dynamical flow, von Neumann and Richtmyer (1950) found inspiration from the physical problem where viscous effects in a gas act to smear out any shocks between discontinuous regions. Thus, von Neumann and Richtmyer (1950) proposed introducing artificial viscosity (dissipation) into the Euler equations of gas dynamics. This artificial dissipation is formulated such that its value is very low in continuous regions but increases dramatically in regions where the dependent variables change rapidly in space. Lax (1954) was the first to note, what is now a fun-

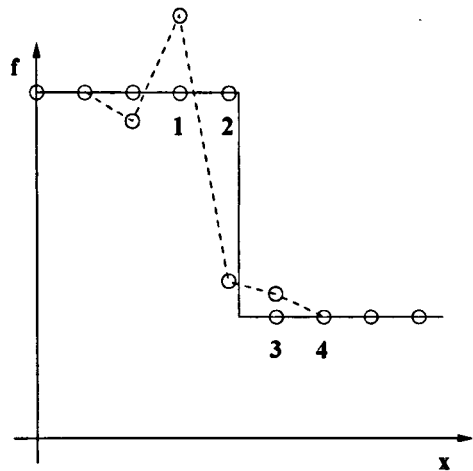


Figure 5.1: Formation of parasitic oscillations near a shock. Initial configuration (solid line) and profile after two time steps (dashed line) following the argument of Moretti (1969).

damental premise, that for shock capturing schemes the equations of motion should be cast in conservation form so that:

$$\mathbf{f}_{,t} = -\mathbf{F}_{,x}, \tag{5.1.1}$$

where \mathbf{f} is a vector of the variables conserved in time, such as mass and momentum in shallow water flow, and \mathbf{F} a vector of the flux conservative variables (see §4.2.4). Note that for discontinuous flow the variables represented by \mathbf{F} are only conserved in a frame of reference for which the discontinuity remains stationary.

5.1.2 On the instability of shock capturing schemes

Inevitably in shock capturing schemes the width of a shock will be grid dependent and scaled according to the mesh spacing. Ideally, shock capturing schemes should resolve the shock over 2 mesh points; however, this is not possible due to the development of parasitic oscillations on the high side of the shock. Many researchers have acknowledged that instabilities are always present in shock capturing schemes based

on finite-differences and attribute them to second-order effects (see for example Lax and Wendroff (1960); Hirsch (1988)). Moretti (1969) has demonstrated succinctly that the inception and development of parasitic oscillations is actually a first-order effect. Moretti's explanation does not appear to be widely known within the hydraulic modelling community and it is therefore summarised here.

The argument is based on an underlying supposition of shock capturing schemes that there is a continuous transition of dependent variables across a shock rather than a jump; thus, the Taylor expansion (4.2.9) remains valid across the shock. The simplest, non-stationary shock is one moving with constant velocity separating two uniform regions as depicted in Figure 5.1. At the initial time it is assumed that the shock is bracketed by mesh points 2 and 3; also, all the dependent variables (f) are higher on the left side of the shock than the right side (always true for an unsteady shock moving from left to right). For the numerical scheme the condition:

$$\left| \frac{1}{2} f_{,t,t} \Delta t^2 \right| < |f_{,t} \Delta t|, \quad (5.1.2)$$

is assumed to hold, and is obviously the case if Δt is small enough. While (5.1.2) is true it follows that first-order effects will dominate over second-order effects. Now consider the first computational step. Using a centred difference scheme the approximation to the x -derivatives at points 2 and 3 will be negative. Consequently, according to (5.1.1), over this time step all the dependent variables will increase at points 2 and 3. At the next time step the numerical x -derivatives are negative at 1, 2 and 4 and positive at 3. It follows from (5.1.1) that the value of all dependent variables increase at 1, 2 and 4 and decrease at 3; the profile of f is now the same as that shown in Figure 5.1. Parasitic oscillations are beginning to develop on the high side of the shock and the solution is already becoming disassociated from the physical problem. The behaviour

illustrated in Figure 5.1 is independent of the growth of f with respect to the initial shock strength. In the words of Moretti (1969):

"This is a common, typical situation, due to a bold, but hardly justifiable attempt to compute derivatives across a discontinuity; and it is a first-order effect. The introduction of higher order terms, as in the Lax Wendroff technique, is irrelevant as far as this effect is concerned."

Interestingly, the relatively large truncation error associated with first-order schemes acts like artificial dissipation. This means that for reasonable mesh spacings first-order schemes smear shocks over several mesh intervals. Thus, first-order methods limit the problem of parasitic oscillations without recourse to additional artificial dissipation terms. Unfortunately, a typical consequence of this first-order dissipation is the spreading of the shock far from its original location. Use of extremely fine mesh spacing reduces smearing but increases computation time and, if fine enough, causes oscillations as predicted by Moretti. The existence of oscillations around data extrema, such as shocks, in first-order schemes is investigated mathematically by Breuss (2005). Second-order schemes suffer oscillations in the vicinity of strong shocks due to the Gibbs phenomenon (Moretti, 1987). Artificial dissipation can be used to reduce the amplitude of these oscillations in second-order schemes and many ingenious methods employing adaptive dissipation terms have been derived; for details of many see Hirsch (1988). The majority of these methods, such as the common total variation diminishing (TVD) schemes, apply dissipation locally in the vicinity of the shock by reducing the scheme to first-order accuracy there, thus ensuring that the scheme remains monotone. Another popular approach to the treatment of shocked flow is to use the essentially non-oscillatory (ENO) family of shock capturing schemes. These methods tend to employ a high n^{th} order difference scheme, typically third-order or higher, which reduces to $(n-1)^{\text{th}}$ order in the vicinity of a shock. Such schemes, by definition,

allow small oscillations near shocks; the magnitude of these oscillations must be controlled using some form of limiter. As there is an entire literature dedicated to limiters to keep the numerics as simple as possible it was decided to use a simple second-order Lax Wendroff type scheme in this work. An unavoidable side effect of using artificial dissipation in second-order schemes is the smearing of shocks over additional mesh points. Thus, it becomes apparent that resolving the shock over two mesh points does not appear practical using such techniques. Another possibility is to filter out any high frequency oscillations at the end of each time step. If implemented correctly such filtering has the advantage of allowing the shock to be resolved over two or three mesh points; the flow is also allowed to remain completely inviscid throughout the computational region. Details and limitations of this type of filtering technique for swash modelling are discussed in §5.1.4 below.

5.1.3 Entropy violating shocks

It is well known that many finite difference schemes, including MacCormack's scheme, allow for the formation of stationary "expansion shocks" within transcritical (sonic) rarefactions, see e.g. Harten (1989). Expansion shocks do not satisfy the entropy condition, which states that entropy has to increase across discontinuities, i.e.:

$$\lambda_L > W > \lambda_R, \quad (5.1.3)$$

where W is the shock velocity. That is, characteristics of one family must converge to the Hugoniot locus (shock path). If (5.1.3) does not hold then characteristics diverge from the Hugoniot locus and an expansion shock forms. Expansion shocks are unstable and the addition of any amount of viscosity smears this type of shock into a rarefaction fan. A transcritical rarefaction wave contains a "sonic point" where $u = (gh)^{\frac{1}{2}}$ leading

to a vertical characteristic, i.e. zero wave speed. For the Lax Wendroff family of difference schemes the numerical dissipation increases with the local Courant number (see Hirsch (1988) for a full explanation of this). At a sonic point the local Courant number is zero and the artificial dissipation is at a minimum, thus the solution is not smeared into a rarefaction wave and the expansion shock remains.

5.1.4 Classic filtering

By the late 1980s finite-difference schemes had largely become redundant for modelling gas dynamical flow, with Riemann-type schemes taking over (this happened in hydraulic modelling a few years later). However, when compared to traditional finite-difference schemes Riemann-type schemes are computationally expensive, particularly for multi-dimensional flow. This led Engquist et al. (1989) to investigate the possibility of stabilising the Lax Wendroff family of difference schemes using non-linear conservation law filters. The filters developed by Engquist et al. (1989) are discrete filters based on certain premises, in particular the filter must:

- be able to effectively locate meshpoints where the solution oscillates and leave smooth regions of flow alone
- be able to determine if the oscillation is a local maximum or minimum and thus whether the dependent variable requires decreasing or increasing
- be conservative, i.e. a reduction at one mesh point must be balanced by an addition at an adjacent mesh point and vice-versa

If there is a local extremum in the conserved quantity f at point s on the mesh then the simplest filter given by Engquist et al. (1989) is

$$f_s^F = f_s + \text{signum}(\Delta_+ f_s) \cdot \min\left(|\Delta_+ f_s|, \frac{|\Delta_- f_s|}{2}\right), \quad (5.1.4)$$

where f_s^F is the filtered value and Δ_+ , Δ_- are forward and backward differences respectively. The results obtained by Engquist et al. (1989) illustrated that the introduction of a filter improved the accuracy of a classical Lax Wendroff solver to such an extent that it was now in line with Riemann-type schemes. Moreover, the filter is a post processing device and, as such, it should be possible to use it with any numerical scheme including those based on the MOC.

There are two ways of implementing the Engquist non-linear filter; the dependent variables can be filtered directly, or a field by field decomposition can be undertaken in the spirit of Roe (1981) and the local characteristic variables filtered instead. Even if the filter is applied to the characteristic variables the eigenvectors and wave strengths need only be computed when a correction is necessary. For Riemann-type solvers the eigenvectors and wave strengths must be computed for every mesh point, increasing the computational cost considerably. The CPU time for the classical schemes employing a filter is therefore a fraction of the CPU time of Riemann-type solvers; unfortunately, Engquist et al. (1989) do not provide a quantitative measure of the difference in this computational cost.

In this work the simplest algorithm presented in Engquist et al. (1989) was adapted and coded for use with the MacCormack scheme to solve the shallow water-Exner system in conservation form. The scheme was found to work very well with moderately strong shocks, such as an incident uniform bore, and results compared with the standard MacCormack scheme, and the STI MOC scheme with shock fitting, are

illustrated in Figures 5.8 and 5.9. However, a major problem became apparent when using the filtered MacCormack scheme in order to simulate swash zone flows. When the solver was used to simulate fixed, or mobile, bed swash driven by a uniform incident bore the scheme broke down during the backwash phase. Breakdown occurred when the backwash bore was in the final stages of existence. The reason apparently being the very high strength of this bore caused by the extremely thin water in front of it. It is possible that this problem could be alleviated by employing the more complex filter described in Engquist et al. (1989) based on field by field decomposition of the governing equations. However, the motivation for employing a shock capturing scheme within the framework of this thesis is to develop a simple, robust and computationally cheap solver; undertaking complex decompositions obviously defeats this purpose. Moreover, when tested for certain wet-dry dam-break type problems, the filtered MacCormack scheme exhibited a stationary expansion shock in the rarefaction fan. These two problems motivated the development of the hybrid scheme outlined below.

5.1.5 Hybrid scheme

The accuracy of second-order schemes and the numerical dissipation of first-order schemes can be combined to good effect. This was first realised by Harten and Zwas (1972) who pioneered the development of self-adjusting hybrid schemes. Such schemes provide accurate solutions in regions of continuous flow and non-oscillatory, smeared, shock profiles in regions where the flow variables are discontinuous. The simplest self-adjusting hybrid methods comprise a weighted average of low-order and high-order schemes such that:

¹ Bore strength, as referred to here, is the ratio of high side to low side values of the dependent variables.

$$F(f, s) = \theta(f, s)F_L(f, s) + \{1 - \theta(f, s)\}F_H(f, s),$$

where F_L and F_H represent the lower and higher order fluxes respectively. The function $\theta(f, s)$, sometimes referred to as the "switch function", must be chosen such that it is close to zero when f is smooth and approaches a value of unity at discontinuities. An appropriate form for θ is given by Holden and Risebro (2002) as being:

$$\theta(f, s) = 1 - \frac{1}{1 + |f_{,x,x}|}, \quad (5.1.5)$$

where $f_{,x,x}$ is approximated numerically by:

$$f_{,x,x} \approx \frac{f_{s+1} - 2f_s + f_{s-1}}{(\Delta x)^2}. \quad (5.1.6)$$

Clearly the value of θ given by (5.1.5) is ≈ 0 in continuous regions where $f_{,x,x}$ is small. Around a shock $f_{,x,x}$ becomes large, thus $\theta \rightarrow 1$ and the scheme becomes first-order. When the MacCormack scheme is used to provide the high-order fluxes careful consideration must be given the choice of a suitable first-order scheme. At first glance the Cole-Murman (1974) scheme seems appropriate as this is known to be the least dissipative first-order finite difference scheme in existence (Harten, 1989). However, like the MacCormack scheme, the Cole-Murman scheme admits expansion shocks; such a hybrid scheme would therefore require some form of entropy fix (see LeVeque (2002)). In order to keep the code for the hybrid scheme as simple as possible, a first-order scheme that gives the unique physical solution is required. One of the few finite-difference schemes known to give the correct physical solution at sonic points is the Lax Friedrichs (LxF) scheme. A modified LxF (mLxF) scheme having only half the numerical dissipation of the original LxF scheme was introduced by Tadmor (1984). As with the original LxF scheme the artificial dissipation within the mLxF scheme does not vanish at sonic points. This property means that the mLxF scheme always gives

the physically valid solution for transonic rarefactions, see e.g. LeVeque (2002). The mLxF scheme, written in the notation of this thesis, is:

$$f_s^{n+1} = f_s^n + \frac{1}{4}(f_{s-1}^n - 2f_s^n + f_{s+1}^n) - \frac{\Delta t}{2\Delta x}(F_{s+1}^n - F_{s-1}^n).$$

It is important to note that, for dimensional consistency, all variables used for computations in the hybrid scheme should be dimensionless. During the course of this work, the MacCormack–mLxF hybrid scheme has been found to be extremely rapid and robust when computing mobile bed swash flow. The only apparent downside to the scheme is the smearing of shocks over a relatively large number of mesh points. For the problems considered here shocks can be smeared over between 4 and 10 mesh points. In order to validate the MacCormack–mLxF hybrid solver the numerical results are compared with the Stoker (1948) analytical solution for the wet–wet dam-break problem. The test case is challenging as it contains both a shock and transonic rarefaction. Results are presented in Figure 5.2 and were obtained using a mesh spacing of $\Delta x=0.01\text{m}$. As the Stoker solution is for an immobile bed, the bed was fixed in the MacCormack–mLxF solver by setting $A=1\times 10^{-10}\text{s}^2\text{m}^{-1}$. Although the shock is smeared the strength and position are extremely well predicted by the numerical scheme. For the test case considered in Figure 5.2 the relative error between the numerical and analytical shock strength is $< 0.5\%$. Only visual comparisons are made for the shock position. Quantitative comparisons of the numerical prediction of the shock location and the exact shock location are difficult because the numerical schemes smear the shock over several mesh points. Application of the Breuss filter described in §5.1.6 below removes smearing and provides results that are clearly in excellent agreement with the analytical solution, the relative error between the numerical and analytical shock strength remains $< 0.5\%$. Moreover, as predicted, the hybrid solution does not

exhibit a stationary expansion shock at the sonic point. There is some rounding of the gradient discontinuities at the beginning and end of the rarefaction region. This could almost certainly be minimised by a more careful consideration regarding the form of the switch function θ .

5.1.6 Breuss Filter

In a recent paper and report (Breuss and Welk, 2006; Breuss, 2006) Breuss provides details of a new conservative non-linear filter that removes the smearing effect around shocks associated with first-order and dissipative second-order schemes for gas dynamical applications. Classical non-linear filters such as that discussed in §5.1.4 apply corrections based on variations in local curvature of the dependent variables and are designed for schemes with second-order or higher accuracy. Such filters are necessarily applied discretely at each time step. The Breuss filter was conceived to work with schemes that deliberately employ dissipation to ensure stability around shocks and is thus an anti-diffusion tool. As long as the finite difference scheme accurately predicts the shock velocity and strength the filter need only be applied at the data output stage and is therefore computationally inexpensive. It is also possible to apply the filter after a preset number of timesteps if the accuracy of the numerical solver is questionable. The results presented by Breuss (2006) show that when used with a conventional second-order TVD scheme the filtered solutions give improved accuracy over ENO type schemes in the vicinity of shocks. Moreover, once filtered the shock is only smeared over a maximum of 3, typically 2, mesh points – the best resolution of a shock possible using a shock capturing scheme. Here a brief overview of the Breuss filter is provided; in depth mathematical analysis and rigorous validation is given in Breuss and Welk (2006). The filter works by first identifying all mesh points belonging to the smeared shock. Identification of such points at time level n is achieved employing the following criteria:

Jump in the conserved variable (f):

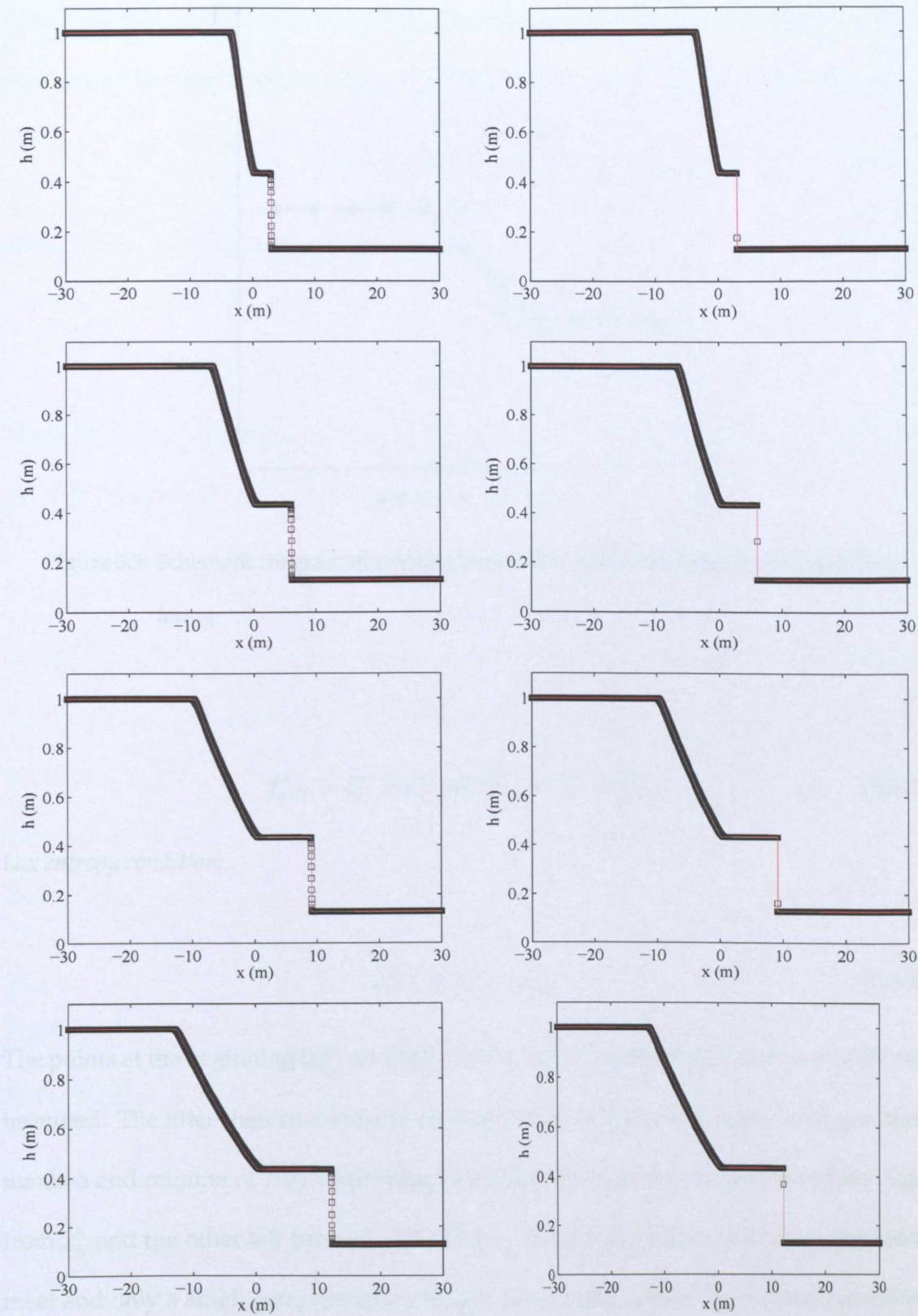


Figure 5.2: Snapshots of Stoker (1948) analytical solution (red line) and solution by MacCormack-mLxF hybrid solver (squares) without (left) and with (right) Breuss filtering at $t=1,2,3$ and 4 s.

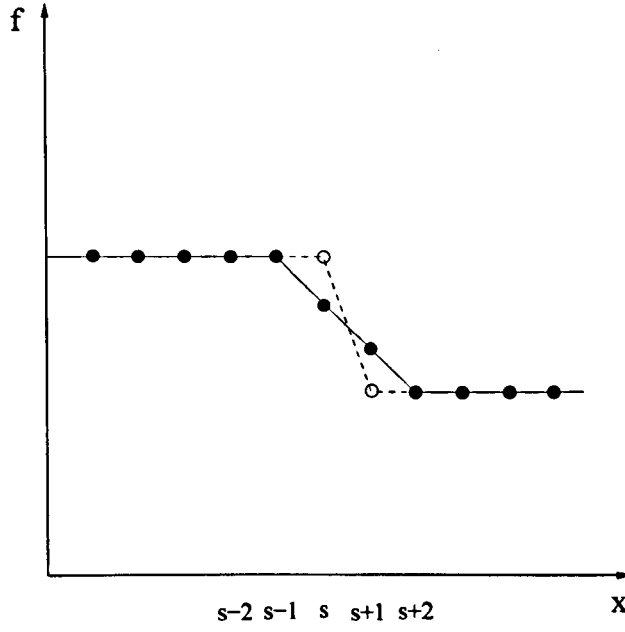


Figure 5.3: Schematic diagram illustrating removal of artificial diffusion by Breuss filtering.

$$f_{s-1}^n > f_s^n > f_{s+1}^n \text{ or } f_{s-1}^n < f_s^n < f_{s+1}^n \quad (5.1.7)$$

Lax entropy condition:

$$u_{s-1}^n > u_s^n > u_{s+1}^n \quad (5.1.8)$$

The points at the beginning ($x_{s_l}^n$) and end ($x_{s_r}^n$) of the smeared shock are thus readily determined. The filter then successively eliminates each decreasing slope linking a local maxima and minima of f by employing two discontinuous waves one travelling right from $x_{s_l}^n$ and the other left from $x_{s_r}^n$. The filter is terminated when both discontinuities meet and only a single jump between the maximum and minimum f values remains. The conserved variables remain conserved as the discontinuous wave moving right increases the integral over f at a constant rate whilst that moving left decreases the integral over f at an equal rate.

Following the explanation given by Breuss (2006) the filter can be better understood by considering the case shown in Figure 5.3. The PDE that describes the Breuss filter is:

$$f_{,\tau}(x, \tau) = G(\text{signum}(f_{,x}(x, \tau))f_{,x}(x, \tau))_{,x} \quad (5.1.9)$$

where $G = G(a)$ is defined as:

$$G(a) = \begin{cases} 0 & \text{if } a \leq 0 \\ 1 & \text{if } a > 0. \end{cases}$$

Thus, as $f_{,x} < 0$ (note that a similar argument can be provided for the case where $f_{,x} > 0$), it follows that (5.1.9) becomes:

$$f_{,\tau} = G(-f_{,x})_{,x}, \quad (5.1.10)$$

as $\text{signum}(f_{,x}) = -1$. To eliminate the smearing of the discontinuity shown in Figure 5.3 it is necessary to remove the amount $f_{s+1} - f_{s+2}$ from f_{s+1} and add it to f_s . According to (5.1.10) there is inflow into cell s as $f_{s+2} - f_{s+1} < 0$ and there can be no outflow from s to $s - 1$ as $f_{s-1} - f_{s-2} = 0$. Equation (5.1.10) can be written in difference form as:

$$f_s^{\tau+1} = f_s^{\tau} + \frac{\Delta\tau}{\Delta x} \left\{ G\left(\frac{f_{s+1}^{\tau} - f_{s+2}^{\tau}}{\Delta x}\right) - G\left(\frac{f_{s-2}^{\tau} - f_{s-1}^{\tau}}{\Delta x}\right) \right\}. \quad (5.1.11)$$

The value of $\Delta\tau$ is chosen to ensure stability such that, if the points at the limits of the smeared shock (points f_s^{τ} and f_{s+1}^{τ} in Figure 5.3) are denoted as f_{sl}^{τ} and f_{sr}^{τ} , then:

$$\Delta\tau = \min\left(f_{sl-1}^{\tau} - f_{sl}^{\tau}, f_{sr}^{\tau} - f_{sr+1}^{\tau}\right) \Delta x. \quad (5.1.12)$$

Considering Figure 5.3 then at point s :

$$G(f_{s-2}^{\tau} - f_{s-1}^{\tau}) = 0 \text{ and } G(f_{s+1}^{\tau} - f_{s+2}^{\tau}) = 1, \quad (5.1.13)$$

hence:

$$f_s^{\tau+1} = f_s^{\tau} + \frac{\Delta\tau}{\Delta x} = f_{sl-1}^{\tau}. \quad (5.1.14)$$

Similarly, at point $s + 1$ in Figure 5.3:

$$G(f_{s-1}^\tau - f_s^\tau) = 1 \text{ and } G(f_{s+2}^\tau - f_{s+3}^\tau) = 0, \quad (5.1.15)$$

hence:

$$f_{s+1}^{\tau+1} = f_{s+1}^\tau - \frac{\Delta\tau}{\Delta x} = f_{sr+1}^\tau. \quad (5.1.16)$$

In summary the procedure is:

- Find $x_{(s_l)}^n$ and $x_{(s_r)}^n$.
- compute $\Delta\tau$, which stabilises the filter, using:

$$\Delta\tau = \Delta x \min(f_{s_l-1}^\tau - f_{s_l}^\tau, f_{s_r}^\tau - f_{s_r+1}^\tau).$$

- update f at these locations using:

$$f_{s_l}^{\tau+1} = f_{s_l}^\tau + \frac{\Delta\tau}{\Delta x} \text{ and } f_{s_r}^{\tau+1} = f_{s_r}^\tau - \frac{\Delta\tau}{\Delta x}.$$

- if $s_l - s_r = 1$ filtering is complete.

Note that τ denotes the filter step with f_s^1 being the original unfiltered variables. Results of the hybrid scheme both with and without Breuss filtering are shown in Figure 5.2. It is clear from the figure that without filtering the shock is smeared over 10 mesh points, whereas the filtered solution smears the shock over 3 mesh points. The location and strength of the shock are accurately predicted both being within 1% of the analytical value for the time window illustrated.

5.2 Shock fitting

5.2.1 The philosophy behind shock fitting

Modern shock fitting schemes for inviscid flow grew out of the desire to treat discontinuities in a mathematically impeccable manner such that numerical schemes remained

stable and shock width was not grid dependent. The differential form of the equations of motion are invalid in regions where it is not possible to differentiate the dependent variables, this is precisely what happens across a shock. Thus, it is correct to use these equations only in smooth regions and to connect smooth regions together across shocks using the Rankine Hugoniot, or jump, conditions. Such an approach alleviates parasitic oscillations and resolves each shock over a single mesh point. Additional benefits include the possibility of using coarser meshes, and therefore faster computation. Unfortunately, the downside is a more complex code. Coding shock fitting schemes for relatively few shocks in one spatial dimension, whilst far more complex than an equivalent capturing scheme, is achievable. However, for flow with many shocks and shock-shock interactions, coding becomes prohibitively complex even in one spatial dimension. Under shock fitting methodologies a shock must be tracked through time as a separate data structure. Thus, a shock acts as a moving internal boundary interacting with, and modifying, the surrounding flow.

5.2.2 Types of fitting procedure

There are two principle methodologies used to fit shocks for one-dimensional flow in state-of-the-art gas dynamical solvers, both stem from the seminal work of Moretti (1971). The simplest of these fitting procedures treats shocks as an internal boundary separating regions of continuous flow; the so-called "shock as a boundary" approach. The shock is treated exactly as any other boundary and the mesh is adjusted such that the position of each shock corresponds to a fixed mesh point. The mesh point denoting the shock location thus corresponds to the downstream boundary of one region and the upstream boundary of the next region. Dependent variables at the boundaries are related to each other via the jump conditions. In unsteady flow the shock bound-

ary moves in time; this approach therefore requires a re-meshing at each time step in accordance with the evolution of the shock boundary. The second, more complex, technique treats the shock as an embedded boundary allowed to wander freely between, and across, fixed mesh points in the original computational region; this approach is known as "floating shock fitting" (Moretti, 1973). This method requires the introduction of special additional data points for each shock that contain information about all the dependent variables on both the high and low sides of that shock. In either procedure all shocks within the flow are dealt with explicitly and are thus resolved at a single point in space. Unfortunately in swash zone flow the presence of a moving shoreline boundary complicates the use of the shock as a boundary method, for this reason the floating shock fitting technique was employed in this work.

5.3 Rankine Hugoniot (jump) conditions

As shock fitting requires the explicit formulation of the Rankine Hugoniot (jump) equations these equations are derived below for the shallow water–Exner system of governing equations. Techniques to fit purely hydrodynamical shocks are also detailed in this chapter. However, as the Rankine Hugoniot equations associated with the shallow water equations are well known, their derivation is relegated to Appendix C where it is also shown that a characteristic path represents the limit of a weak shock.

5.3.1 Rankine Hugoniot conditions for the shallow water–Exner system

The morphodynamic Rankine Hugoniot (jump) conditions may be obtained directly from the integral form of the governing equations which are derived in Chapter 3. If water mass is conserved then the rate of change of the total amount of mass in any

domain $x_2 > x > x_1$ is necessarily balanced by the net inflow across x_2 and x_1 , thus:

$$\frac{d}{dt} \int_{x_1}^{x_2} h dx + [hu]_{x_1}^{x_2} = 0. \quad (5.3.1)$$

Assuming unsteady flow then the shock position ζ will vary in time so that $\zeta = \zeta(t)$.

Here it is assumed that the shock lies between x_1 and x_2 , i.e. $x_2 > \zeta(t) > x_1$. Splitting the range of integration in (5.3.1) either side of the shock using:

$$\int_{x_1}^{x_2} \equiv \int_{x_1}^{\zeta^-(t)} + \int_{\zeta^+(t)}^{x_2}, \quad (5.3.2)$$

and applying Leibnitz's theorem for the differentiation of an integral to the integral terms, (5.3.1) becomes:

$$\begin{aligned} \int_{x_1}^{\zeta^-(t)} \frac{\partial h}{\partial t} dx + h|_{\zeta^-(t)} \frac{d\zeta(t)}{dt} - h|_{x_1} \frac{dx_1}{dt} + \int_{\zeta^+(t)}^{x_2} \frac{\partial h}{\partial t} dx + \\ h|_{x_2} \frac{dx_2}{dt} - h|_{\zeta^+(t)} \frac{d\zeta(t)}{dt} + [hu]_{x_1}^{x_2} = 0. \end{aligned} \quad (5.3.3)$$

Note that $h|_{\zeta^-(t)}$ and $h|_{\zeta^+(t)}$ are the values of $h(x, t)$ as $x \rightarrow \zeta(t)$ from below and above respectively; note also that x_1 and x_2 are time independent hence their derivatives with respect to time are zero. If we let the spatial extent of the shock become very small then $x_1 \rightarrow \zeta^-(t)$ and $x_2 \rightarrow \zeta^+(t)$ hence:

$$\int_{x_1}^{\zeta^-(t)} \frac{\partial h}{\partial t} dx \rightarrow 0 \quad (5.3.4)$$

and:

$$\int_{\zeta^+(t)}^{x_2} \frac{\partial h}{\partial t} dx \rightarrow 0. \quad (5.3.5)$$

Letting $W = \frac{d\zeta}{dt}$ and simplifying (5.3.3) gives:

$$[h(u - W)]_{x_1}^{x_2} = 0. \quad (5.3.6)$$

From the integral form of the momentum equation:

$$\frac{d}{dt} \int_{x_1}^{x_2} uh dx + \left[hu^2 + \frac{gh^2}{2} \right]_{x_1}^{x_2} + \int_{C_{B1,2}} gh dz = 0, \quad (5.3.7)$$

where $C_{B1,2}$ denotes the line integral along the bed. Here \bar{z} is defined such that $\bar{z} = B(x)$, hence $h(\bar{z}) \equiv h(B(x))$; thus, $dz = \frac{dB}{dx} dx$. As long as the bed profile is continuous then the last term on the LHS of (5.3.7) can be expressed as:

$$\int_{C_{B1,2}} gh \, dz \equiv \int_{x_1}^{x_2} gh \frac{dB}{dx} dx. \quad (5.3.8)$$

Clearly the function $h(x, t)$ is not well defined along the face of a bed step. As, at any point, h measures the vertical distance between the bed and the free surface it follows that at the bed step the water surface must itself be discontinuous. In their work on alluvial river flow Needham and Hey (1991) provide a method of overcoming the problem of a bed step; what follows here is a summary of their method:

Firstly, h is defined along the bed step such that:

$$h = d'(\bar{z}), \min(B_{x_1}, B_{x_2}) < \bar{z} < \max(B_{x_1}, B_{x_2}), \quad (5.3.9)$$

where d' is a positive differentiable function, monotone in z , that satisfies the end conditions:

$$d'(B_{x_1}) = h_{x_1}, \quad d'(B_{x_2}) = h_{x_2}. \quad (5.3.10)$$

Hence, at a step discontinuity in the bed:

$$\int_{C_{B1,2}} gh \, dz \equiv [gd(\bar{z})]_{x_1}^{x_2}. \quad (5.3.11)$$

In order to derive the jump conditions associated with the momentum equation it is necessary to have a workable form of $d'(\bar{z})$; this has been provided by Needham and Hey (1991) who used empirical observations to justify that $d'(\bar{z})$ can be considered as a simple linear function of z . The form of $d'(\bar{z})$ is found by ensuring that (5.3.10) is satisfied and is given as:

$$d'(\bar{z}) = h_{x_1} + \frac{(\bar{z} - B_{x_1})(h_{x_2} - h_{x_1})}{(B_{x_2} - B_{x_1})}. \quad (5.3.12)$$

Integration of (5.3.12) with respect to z gives $d(\bar{z})$ as:

$$d(\bar{z}) = h_{x_1} \bar{z} + \frac{(\bar{z} - 2B_{x_1})(h_{x_2} - h_{x_1})\bar{z}}{2(B_{x_2} - B_{x_1})}. \quad (5.3.13)$$

Evaluating $[gd(\bar{z})]_{x_1}^{x_2}$ and simplifying gives:

$$[gd(\bar{z})]_{x_1}^{x_2} = \frac{g}{2}(B_{x_2} - B_{x_1})(h_{x_1} + h_{x_2}). \quad (5.3.14)$$

At a bed discontinuity we can therefore use the relationship:

$$\int_{C_{b12}} gh \, dz \equiv \frac{g}{2}(B_{x_2} - B_{x_1})(h_{x_1} + h_{x_2}) \quad (5.3.15)$$

in equation (5.3.7). Next, splitting the range of integration using:

$$\int_{x_1}^{x_2} \equiv \int_{x_1}^{\zeta^-(t)} + \int_{\zeta^+(t)}^{x_2}, \quad (5.3.16)$$

and applying Leibnitz's theorem for the differentiation of an integral to the integral terms (5.3.7) becomes:

$$\begin{aligned} & \int_{x_1}^{\zeta^-(t)} \frac{\partial uh}{\partial t} dx + (uh)|_{\zeta^-(t)} \frac{d\zeta(t)}{dt} - (uh)|_{x_1} \frac{dx_1}{dt} + \int_{\zeta^+(t)}^{x_2} \frac{\partial uh}{\partial t} dx + \\ & (uh)|_{x_2} \frac{dx_2}{dt} - (uh)|_{\zeta^+(t)} \frac{d\zeta(t)}{dt} + \left[hu^2 + \frac{gh^2}{2} \right]_{x_1}^{x_2} + \\ & \frac{g}{2}(B_{x_2} - B_{x_1})(h_{x_1} + h_{x_2}) = 0. \end{aligned} \quad (5.3.17)$$

If we let the spatial extent of the shock become very small then $x_1 \rightarrow \zeta^-(t)$ and $x_2 \rightarrow \zeta^+(t)$ hence:

$$\int_{x_1}^{\zeta^-(t)} \frac{\partial(uh)}{\partial t} dx \rightarrow 0 \quad (5.3.18)$$

and:

$$\int_{\zeta^+(t)}^{x_2} \frac{\partial(uh)}{\partial t} dx \rightarrow 0. \quad (5.3.19)$$

Simplifying (5.3.17) gives:

$$-W[uh]_{x_1}^{x_2} + \left[hu^2 + \frac{gh^2}{2} \right]_{x_1}^{x_2} + \frac{g}{2}(B_{x_2} - B_{x_1})(h_{x_1} + h_{x_2}) = 0. \quad (5.3.20)$$

Finally, using this approach the integral form of the bed-updating (Exner) equation is:

$$\frac{d}{dt} \int_{x_1}^{x_2} B dx + \zeta[q]_{x_1}^{x_2} = 0 \quad (5.3.21)$$

Splitting the range of integration as above, equation 5.3.21 becomes:

$$\frac{d}{dt} \int_{x_1}^{\zeta^-(t)} B dx + \frac{d}{dt} \int_{\zeta^+(t)}^{x_2} B dx + \zeta[q]_{x_1}^{x_2} = 0. \quad (5.3.22)$$

Application of Leibnitz's theorem for differentiation of an integral to the integral terms in (5.3.22) gives:

$$\begin{aligned} \int_{x_1}^{\zeta^-(t)} \frac{\partial B}{\partial t} dx + B|_{\zeta^-(t)} \frac{d\zeta(t)}{dt} - B|_{x_1} \frac{dx_1}{dt} + \int_{\zeta^+(t)}^{x_2} \frac{\partial B}{\partial t} dx + \\ B|_{x_2} \frac{dx_2}{dt} - B|_{\zeta^+(t)} \frac{d\zeta(t)}{dt} + \zeta[q]_{x_1}^{x_2} = 0. \end{aligned} \quad (5.3.23)$$

Again letting the spatial extent of the shock become very small then $x_1 \rightarrow \zeta^-(t)$ and $x_2 \rightarrow \zeta^+(t)$ hence:

$$\int_{x_1}^{\zeta^-(t)} \frac{\partial B}{\partial t} dx \rightarrow 0 \quad (5.3.24)$$

and:

$$\int_{\zeta^+(t)}^{x_2} \frac{\partial B}{\partial t} dx \rightarrow 0. \quad (5.3.25)$$

Simplification of (5.3.23) therefore gives:

$$[BW - \zeta q]_{x_1}^{x_2} = 0. \quad (5.3.26)$$

Using a sediment transport flux of the form $q = Au^3$ provides the shock relation as:

$$[BW - A\zeta u^3]_{x_1}^{x_2} = 0. \quad (5.3.27)$$

5.3.2 Bore relations for a uniform bore advancing into still water over a mobile bed ($q = Au^3$)

Referring to Figure 5.4, with $u_L = 0$ and $B_L = 0$ the morphodynamic Rankine Hugoniot (jump) condition for the sediment continuity (Exner) equation becomes:

$$B_H = \frac{A\zeta u_H^3}{W}, \quad (5.3.28)$$

and from the Rankine Hugoniot condition associated with continuity equation:

$$u_H = \frac{W(h_H - h_L)}{h_H}. \quad (5.3.29)$$

Finally the Rankine Hugoniot condition associated with the conservation of fluid momentum becomes:

$$Wu_H h_H - \frac{gh_H^2}{2} - u_H^2 h_H + \frac{gh_L^2}{2} - \frac{gB_H}{2}(h_H + h_L) = 0. \quad (5.3.30)$$

Putting (5.3.28) and (5.3.29) into (5.3.30) gives:

$$\left[h_H - h_L - \frac{(h_H - h_L)^2}{h_H} - \frac{A\zeta g(h_H - h_L)^3}{2h_H^2} \left(\frac{h_H + h_L}{h_H} \right) \right] W^2 + \frac{g(h_L^2 - h_H^2)}{2} = 0. \quad (5.3.31)$$

Letting:

$$\psi = h_H - h_L - \frac{(h_H - h_L)^2}{h_H} - \frac{A\zeta g(h_H - h_L)^3}{2h_H^2} \left(\frac{h_H + h_L}{h_H} \right), \quad (5.3.32)$$

gives:

$$W = \pm \left[\frac{g(h_H^2 - h_L^2)}{2\psi} \right]^{\frac{1}{2}}. \quad (5.3.33)$$

We are required to take the positive root if the bore is to move forwards with increasing x , thus:

$$W = \left[\frac{g(h_H^2 - h_L^2)}{2\psi} \right]^{\frac{1}{2}}. \quad (5.3.34)$$

Note that for physically realistic solutions $\psi > 0$ requiring that:

$$h_H > h_L + \frac{(h_H - h_L)^2}{h_H} + \frac{A\zeta g(h_H - h_L)^3}{2h_H^2} \left(\frac{h_H + h_L}{h_H} \right). \quad (5.3.35)$$

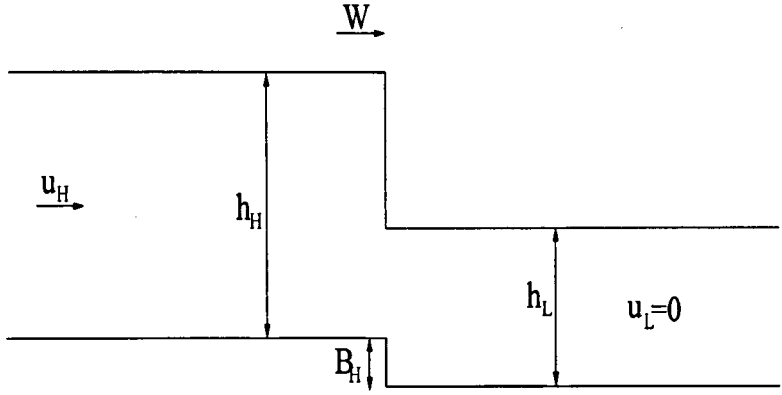


Figure 5.4: Schematic of a uniform bore advancing into still water over a mobile bed

Letting $A \rightarrow 0$ in (5.3.34) means that, as $B_H \rightarrow 0$ from (5.3.28), we recover the expression for a purely hydrodynamical bore moving into still water i.e.

$$W \rightarrow \left[\frac{gh_H(h_H + h_L)}{2h_L} \right]^{\frac{1}{2}}. \quad (5.3.36)$$

5.3.3 Analysis of the wave tip discontinuity when $q = Au^3$

Using the shock relations derived in §5.3.1 Needham and Hey (1991) have shown that, for alluvial flows, it is not possible for the shallow water–Exner system to admit contact discontinuities. Importantly, the case for which $h = 0$ at both sides of the discontinuity was not considered by Needham and Hey (1991), as this is not expected to occur in alluvial flows. The Riemann wave solution developed in Chapter 6, however, indicates that this is precisely the situation that does occur for mobile bed flows with a moving wet–dry boundary. Results for the mobile bed dam–break show that water height does in fact tend to zero at the wave tip while both bed height and water velocity tend to some limiting value. This means that downstream of the tip, at x_1 , values for all dependent variables h, u and B are zero, as the water has not yet reached this point,

whereas immediately upstream u and B have some finite value but h is again zero. It follows that (5.3.27) becomes:

$$B = \frac{A\zeta u^3}{W}. \quad (5.3.37)$$

However, the analysis of §3.5 has shown that tip velocity (corresponding to W) is equal to water particle velocity u at the tip (from (3.5.1)), therefore at the tip (5.3.37) reduces to:

$$B = A\zeta u^2. \quad (5.3.38)$$

The remaining shock relations (5.3.6) and (5.3.20) are satisfied trivially. The properties of contact discontinuities found in gas dynamics are summarised by Chorin and Marsden (1993) as being:

- Some, but not all, of the dependent variables are discontinuous across the contact.
- The contact moves with the local fluid velocity u .
- The contact moves along the trajectory of a characteristic.

The discontinuity found at the wet–dry interface obeys all the above criteria, if h can be considered continuous. On the basis of this analysis it would seem that the "sediment bore" found at the wave tip is best described as a contact discontinuity. However, there is a further criterion required for the rigorous definition of a contact discontinuity (Jeffrey, 1976):

"A degenerate shock with speed W that coincides with an eigenvalue λ_k^j on either side of the shock is known as a contact discontinuity"

i.e., characteristics either side of a contact discontinuity must run parallel with the path of the discontinuity. A discussion of this last point is left until Chapter 6 where the wave structure of a mobile bed dam–break is analysed.

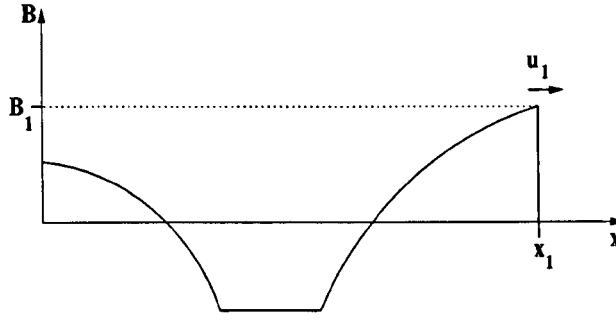


Figure 5.5: Schematic diagram of the sediment bore observed at the wave tip ($x = x_1$) when a transport formula of the form $q = Au^3$ is used

Alternative derivation of the tip relation – $B = A\zeta u^2$

It is possible to arrive at (5.3.38) using a different approach. Here considering conservation of sediment it follows that:

$$q = V_s u, \quad (5.3.39)$$

where V_s is the volume of sediment per unit area. Equation (5.3.39) is based on the assumption that sediment is advected by the flow. For the one dimensional case the volume of sediment per unit area at a specific abscissa is just the bed height there with an allowance made for bed porosity, i.e.:

$$V_s = (1 - p)B. \quad (5.3.40)$$

Thus, from (5.3.39) it follows that:

$$q = u\zeta^{-1}B. \quad (5.3.41)$$

Using the notation of Figure 5.5 then the volume of sediment passing through x_1 is given by $q = Au_1^3$, thus from (5.3.39):

$$B_1 = A\zeta u_1^2. \quad (5.3.42)$$

5.4 Implementation of shock fitting procedure for swash flow

5.4.1 Shock detection

If a shock is present in the initial data its position and velocity at this time tend to be known. In many cases of unsteady flow, however, a shock will not be present initially but will develop at some later time. The GC variant of the MOC is particularly well suited to the detection of embedded shocks. Mesh points in GC schemes are defined at points of characteristic intersection, it is therefore straightforward to modify a GC code to check for the intersection of characteristics of the same family. In theory, such an intersection point is the position of shock inception in the $x-t$ plane. An average value of the two characteristic slopes can be taken to give an estimate for shock velocity at this point. This type of detection scheme was implemented for use with the decoupled MOC GC scheme developed in §4.1.1. There are large drawbacks when using GC schemes with shock fitting, in particular the extremely irregular "floating" mesh. For this reason when treating shocked flow using explicit fitting techniques it is easier to employ MOC STI or traditional finite difference schemes which are based on regularly spaced grids. This necessitates the development of a robust procedure capable of determining the time and place of shock inception and providing a good estimate of the initial shock velocity. Since the mid 1970s the trend in numerical hydraulic modelling has been towards the use of shock capturing schemes; the early work that utilised shock fitting has consequently been buried under over 30 years worth of literature focusing almost uniquely on shock capturing schemes. Moreover, other than those based on the intersection of same-family characteristics, it has proven impossible to trace any procedures for the detection of embedded shocks in the hydraulic literature. Thus, it is necessary to turn to the field of gas dynamics where embedded shocks have been

treated explicitly for over 35 years (Moretti, 2002). A discussion of these techniques and their adaption for swash flows is given in the relevant sections below.

5.4.2 Shock inception on a characteristics grid

In the course of this work a shock detection procedure for the uncoupled MOC GC scheme detailed in §4.1.1 was developed. It is well known that shocks form when characteristics belonging to the same family intersect and values of the dependent variables consequently become multi-valued (Whitham, 1974). For a MOC GC scheme it is logical to determine the point of shock inception by finding the interception point of two adjacent same family characteristics. This approach was suggested for use with MOC STI schemes to detect the inception of tidal bores by Dronkers (1964). A subroutine based on this idea was coded and employed in the MOC GC code to detect the inception of a backwash bore. During the course of numerical experiments it was found that occasionally the routine led to the detection of non-physical shocks. This was almost certainly due to the extremely large number of characteristics present within regions where the flow variables were rapidly changing. A modification to the original routine was therefore made to increase reliability. In the new routine, instead of using directly adjacent characteristics, a prescribed number of characteristics (typically ≤ 5) were missed out before intersection was checked for. This new routine was found to be reliable for the entire range of boundary value problems tested. An estimate for the initial shock velocity W_{in} was found by averaging the wave speeds of the two intersecting characteristics.

5.4.3 Shock inception on a fixed grid

There appear to be two primary techniques for the detection of embedded shocks on a fixed grid currently in use in the field of gas dynamics. One is a variant of crossing characteristics and was pioneered by DiGiacinto and Valorani (1989). In this approach a search is made for all mesh points where wave speeds decrease moving from one mesh point s to the next $s + 1$, i.e. compression regions. At any mesh points where this occurs a shock is deemed to be present at the mid-point $(s + \frac{1}{2})$ between the cells. The Mach number of each of the shocks detected in this way is then computed. What DiGiacinto and Valorani (1989) define as Mach number is best thought of in a hydraulics context as a relative Froude number F_{rel} , given by:

$$F_{rel} = \frac{(u_L - W_{in})}{(gh_L)^{\frac{1}{2}}}, \quad (5.4.1)$$

where the L subscripts denote variables on the low side of the shock. A value for W_{in} is computed by averaging the relevant wave speeds of the mesh points at s and $s + 1$ bracketing the shock, i.e:

$$W_{in} = 0.5(\lambda_{k(s)} + \lambda_{k(s+1)}), \quad (5.4.2)$$

where k denotes the characteristic family. DiGiacinto and Valorani (1989) propose an empirical interpolating formula to find the value of the dependent variables (f) at the low side of the shock of the form:

$$f_L = f_s + \frac{\Delta x}{2(1 + Y)} \left\{ \frac{(f_s - f_{s-1})}{\Delta x} + 2Y \frac{((f_{s+1} - f_s))}{3\Delta x} \right\}. \quad (5.4.3)$$

Here Y is an empirical coefficient that determines how the values are interpolated or extrapolated. Thus, (5.4.3) is based on not only the variable jump within the cell but the trend of flow variables in the adjacent cell. If the Mach number is greater than some prescribed minimum value the shock is assumed to be physical. This technique has the

advantage that it can be calibrated to allow for the early detection of shocks. The other approach, developed by Moretti (1971), is simpler. Moretti's approach consists of, at the end of each time step, identifying the mesh interval $(s, s + 1)$ where the gradient of a chosen dependent variable is greatest. If this maximum gradient then increases in time for a prescribed number of consecutive steps (results presented in this thesis used 5 consecutive steps, however, the shock is detected only marginally later if more steps are used) a shock is placed at the mid-point of the mesh interval $(s + \frac{1}{2})$. The number of consecutive steps is again an empirical parameter Y . The initial shock speed W_{in} is determined using (5.4.2).

In this work both procedures were tested and it was found that not only was Moretti's procedure easier to code it was also much less sensitive to variations in the empirical parameter Y . For this reason the Moretti (1971) detection technique was employed in the shock detection procedure developed for the STI MOC code. Also, following Moretti (1971), it is noted that the early detection of shocks, in which the shock initially moves as a characteristic (i.e. the limit of a weak shock, see Appendix C), is preferable to late detection where the shock has already built up some strength. Numerical experiments indicate that when a shock is detected too late the forbidden act of differentiating across a discontinuity has already occurred. Consequently, parasitic oscillations grow up and propagate into the main body of the flow causing the appearance of wiggles. Such instabilities can, under certain circumstances, cause a catastrophic failure of the code.

5.4.4 Shock evolution on a characteristics grid

The procedure detailed in this section was successfully employed to treat embedded hydrodynamic (fixed-bed) shocks on a characteristics grid. In this section the words

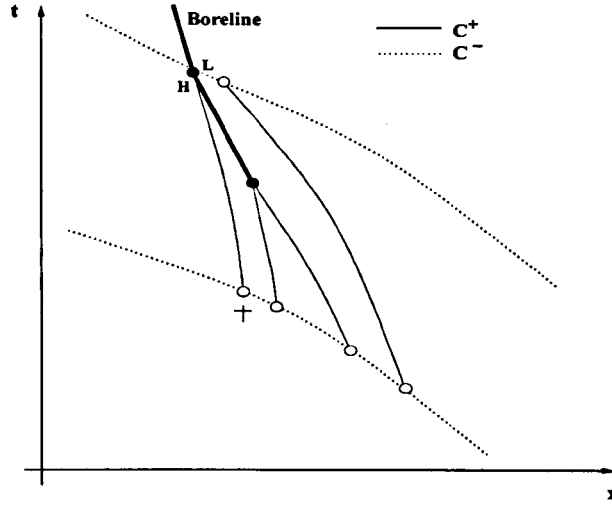


Figure 5.6: Schematic of the characteristics grid illustrating shock development

shock and bore will be used interchangeably. Letting the subscripts H and L denote quantities behind and in front of a shock respectively, then from (C.0.21), and the fact that $h_H > h_L$, we have the following relation:

$$u_L + c_L < W = u_L + (gh_H)^{\frac{1}{2}} \left(\frac{h_H + h_L}{2h_L} \right)^{\frac{1}{2}} < u_H + c_H. \quad (5.4.4)$$

Thus, characteristics on the low side of the shock will meet the shock path as $W > u_L + c_L$. This enables the water velocity and water height on the low side of the shock to be computed by the GC MOC method up until the point of shock arrival. Characteristics on the high side of the shock will reach the bore line as $u_H + c_H > W$. The procedure devised for shock fitting on a characteristics grid therefore proceeds as follows: Firstly, the check detailed in §5.4.2 is made for shock inception. If a shock is present W_{in} is calculated in the manner outlined and a flag set to indicate the presence of the shock. The movement of the shock is now tracked in the $x-t$ plane along a "boreline". The subsequent position of the shock can be determined either when (i) it is intercepted by the next characteristic arriving from the high side or (ii) it intercepts a characteristic on the low side, see Figure 5.6. As the solution proceeds along a C^- characteristic a check

is made for the possibility of this characteristic or any C^+ characteristic attending to it intersecting the boreline. The bore velocity and the water height immediately behind the bore are not constant for unsteady flow. The bore is modified by wave components carried by characteristics overtaking from the high side, and by characteristics on the low side carrying information about the water into which the bore is moving (i.e. the depth variation and water particle velocity). It is, therefore, necessary to update h_H , h_L , u_H , u_L and W when the boreline intercepts a characteristic of either family. Referring to Figure 5.6 and denoting flow variables at \dagger (i.e. the point where this high side C^+ characteristic last crossed a C^- characteristic) by the subscript \dagger , it follows that:

$$u_{\dagger} + 2c_{\dagger} + mgt_{\dagger} = u_H + 2c_H + mgt_H. \quad (5.4.5)$$

Putting (C.0.1) and (C.0.2) into (C.0.7) gives:

$$u_H = W \left(1 - \frac{h_L}{h_H} \right) + \frac{h_L u_L}{h_H}. \quad (5.4.6)$$

Recalling that $c_H = (gh_H)^{\frac{1}{2}}$, and putting this relation and (5.4.6) into (5.4.5) and replacing W with the expression given by (C.0.21), then dividing through by $(gh_L)^{\frac{1}{2}}$ and rearranging gives:

$$\frac{R}{\sqrt{2}}(1 + R^2)^{\frac{1}{2}} - \frac{1}{\sqrt{2}R}(1 + R^2)^{\frac{1}{2}} + 2R = q. \quad (5.4.7)$$

where:

$$R = \frac{c_H}{c_L}. \quad (5.4.8)$$

and:

$$q = \frac{u_{\dagger} + 2c_{\dagger} + mg(t_{\dagger} - t_H) - u_L}{c_L}. \quad (5.4.9)$$

Application of a common denominator $\sqrt{2}R(1 + R^2)^{\frac{1}{2}}$ gives:

$$\frac{R^4 - 1}{\sqrt{2}R(1 + R^2)^{\frac{1}{2}}} + 2R - q = 0. \quad (5.4.10)$$

Equation (5.4.10) was first given by LeMéhauté (1963). A value for q can be computed directly as the variables t_+ , t_H , u_+ , c_+ , u_L and c_L are all known, (5.4.10) is solved using an iterative procedure. In this work the bisection method was employed (see Press et al. (2007)), to yield R . Values for h_H , u_H and W are then found through rearrangement of the relevant equations. The characteristic family whose crossing initiated the shock, in the case of a hydrodynamical backwash bore the C^+ family, are terminated at the boreline and play no further part in the computational procedure. It should be mentioned that modification of the bore by overtaking wave components is a continuous process; Ho and Meyer (1962) give a method that allows for the continued modification of a bore by more expeditious wave components. If the characteristics are close enough together then the development of the bore will be well approximated by the numerical MOC GC scheme detailed here (see Amein (1964)).

The above approach is complicated somewhat by an unstructured grid, in particular the irregular manner in which the GC scheme moves forward through time. When flow with a mobile bed is considered the addition of a third characteristic family means that it is not always possible to compute the flow in front of the shock prior to shock arrival. The reasons for this will become clear when type 2 shocks are discussed in the following section.

5.4.5 Shock evolution on a fixed grid

In shock fitting schemes the position of the shock must be tracked through time. Additionally, for unsteady flow, values of all dependent variables on the high side of the shock, as well as the shock velocity, must be computed at each time step. Morphodynamic shocked flow is more complex than pure hydrodynamic shocked flow as three distinct shock types can exist. Sieben (1997, 1999) has classified the three shock types

for the shallow water–Exner system. Each shock type corresponds to a different characteristic configuration at the shock; the possible characteristic configurations are shown in Figure 5.7. The method used to fit shocks necessarily varies according to the type of shock under consideration. The following text, used in conjunction with Figure 5.7, outlines the fitting procedures developed for use with the MOC STI scheme presented in §5.4.3.

Type 1 or type 3 (hydrodynamic) shock

1. An initial estimate for the new shock location x_w at $n + 1$ is made using the value of the shock speed at n . This is assumed to be known in the case of a pre-existing shock or is computed by the method given in §5.4.3 for the first time step following the detection of an embedded shock.
2. Values of all dependent variables (h , u , and B) more than one mesh point away on the low and high sides of the shock are computed using the MOC technique detailed in §4.2.1.
3. Values of all dependent variables (h , u , and B) at point L on the low side of the shock are computed directly by the MOC technique detailed in §4.2.1.
4. Using high side values from the previous time step an estimate of the C^- characteristic wavespeed (λ_1) is arrived at point H . Using this approximation a linear extrapolation backwards in time made to find the location of the base of this characteristic. Values for the dependent variables at the base point are determined using a linear interpolation in space between values at node points bracketing the base location.

5. The 3 Rankine Hugoniot equations are solved simultaneously with the difference form of the Riemann equation (4.2.1) valid along the C^- characteristic ($k = 1$) arriving from the high side. This set of equations presents a system comprising 4 nonlinear equations in 4 unknowns (h_H, u_H, B_H and W) and is solved numerically using a globally convergent Newton Raphson technique (see Press et al. (2007)). This yields up new values for h_H, u_H and B_H as well as W in typically < 10 iterations.
6. Using an average of W^n and the newly computed value of W a new estimate for the shock location x_w at $n + 1$ is made. Step 4 is then repeated until successive values of h_H, u_H, B_H and W agree within a specified error limit.
7. Values of the independent variables at the meshpoint adjacent to the low side of the shock are computed by linear interpolation between the low side of the shock (point L) and the next supercritical node.
8. Values of the independent variables at the meshpoint adjacent to the high side of the shock are computed by linear interpolation between the high side of the shock (point H) and the next subcritical node.

Type 2 (morphodynamic) shock

1. Computation by the MOC proceeds up until the fixed mesh point immediately preceeding the new shock location values at this mesh point are not computed. An initial estimate for this new shock location x_w at $n + 1$ is made using the value of the shock speed at n . This is assumed to be known in the case of a pre-existing shock or is computed by the method given in §5.4.3 for the first time step following the detection of an embedded shock.

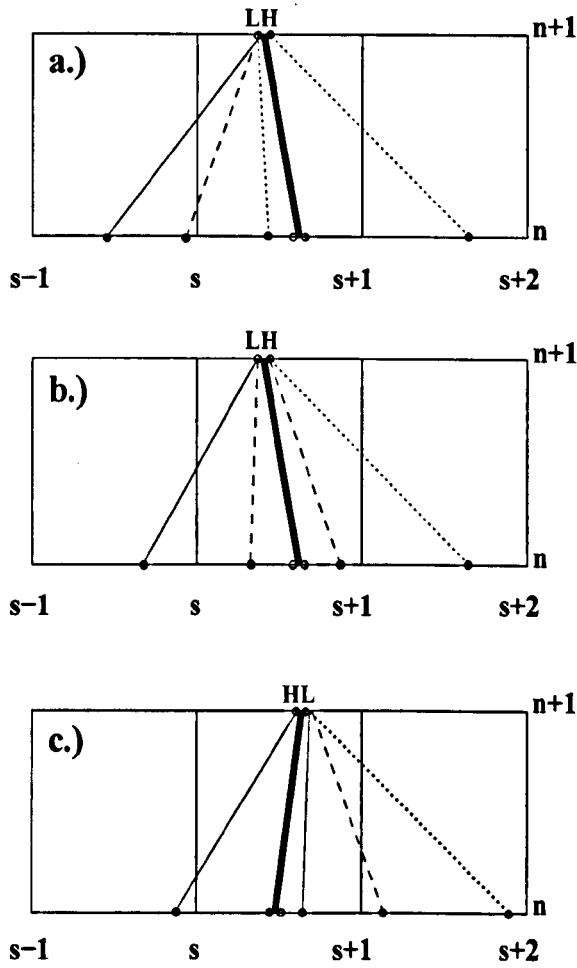


Figure 5.7: Configuration of characteristics in the $x-t$ plane attending to a.) type 1, b.) type 2 and c.) type 3 shocks. The shock path is shown by the thick line whereas C^+ , C^- and C_b characteristics are represented by thinner solid, dotted and dashed lines respectively.

2. Estimates of the C^+ and C_b wave speeds on the low side (at point L) and the C^- and C_b wave speeds on the high side (at point H) of the shock are made using values from the previous time step. The base points of these characteristics are found using linear extrapolation backwards in time. Values for the dependent variables at the base point of each characteristic are determined using a linear interpolation in space between values at node (or shock base) points bracketing the characteristic base locations.
3. The 3 Rankine Hugoniot equations are solved simultaneously with the 2 Riemann difference equations (4.2.1) valid along the C^+ ($k = 2$) and C_b ($k = 3$) characteristics arriving from the low side and the 2 Riemann difference equations (4.2.1) valid along the C^- ($k = 1$) and C_b ($k = 3$) characteristics arriving from the high side. This set of equations presents a system comprising 7 nonlinear equations in 7 unknowns ($h_L, u_L, B_L, h_H, u_H, B_H$ and W) and is again solved numerically using a globally convergent Newton Raphson technique. Again, convergence is usually obtained within 10 iterations.
4. Using an average of W^n and the newly computed value of W a new estimate for the shock location x_w at $n + 1$ is made. Steps 2 and 3 are then repeated until successive values of $h_L, u_L, B_L, h_H, u_H, B_H$ and W agree within a specified error limit.
5. Values of the independent variables at the meshpoint adjacent to the low side of the shock are computed by linear interpolation between the low side of the shock (point L) and the next supercritical node.
6. Values of the independent variables at the meshpoint adjacent to the high side of the shock are computed by linear interpolation between the high side of the

shock (point H) and the next subcritical node.

Note that in both cases interpolation of variables across a shock is prohibited for obvious reasons. Thus, a check is made to determine if the fixed mesh points to be used for interpolation bracket the shock. If this is the case interpolations are made between base values at the appropriate side of the shock and the adjacent mesh point. It should be clear from the descriptions given that at the two mesh points immediately bracketing the shock the overall solver is spatially only first-order accurate, even if the MOC STI solver is second-order accurate in space. This is typically the case in shock fitting schemes and does not adversely affect the global accuracy of the solver (Moretti, 2002). The algorithms developed above have proven robust and capable of dealing with both (pre-existing) incident bores (type 3 shocks) and the embedded backwash bores (type 2 shocks) that develop for SM63 initial conditions on a mobile bed, see Chapter 8.

5.5 Comparison of fitted and captured shocks on a mobile bed

As an example test case the propagation of a uniform bore over a mobile bed is considered. An analytical solution to this problem was derived in §5.3.2. For the results shown in Figures 5.8 and 5.9 a relatively large space step was used ($\Delta x = 5 \times 10^{-2} \text{m}$) and the time step was fixed at $\Delta t = 5 \times 10^{-3} \text{s}$. Figure 5.8 illustrates the results obtained using the standard shock capturing MacCormack scheme. The figure shows that, regardless of filtering, the shock is smeared over 4 mesh points. Parasitic oscillations are present on the high side of the shock for the standard non-filtered MacCormack scheme. Interestingly, these oscillations are found to be (relatively) much worse for the bed height than the water height. The Engquist filter successfully suppresses the oscillations providing a stable solution, albeit a smeared one. The same problem but with

a fitted shock is shown in Figure 5.9. It is important to note that although data is computed at the specific shock location within the code it is only outputted at fixed mesh points. This means that although the shock appears to be spread over two mesh points in Figure 5.9, within the shock fitting code it is actually resolved over a single nodal point. The results for both water and bed height are oscillation free and the shock is computed crisply with no smearing. Predictions for the location of the shock front for both the fitting and capturing schemes are in excellent agreement with the analytical result. In order to compare the shock fitting and hybrid shock capturing schemes the climb of a bore on a mobile beach is considered. Figure 5.10 shows snapshots of water depth at 0.25s intervals as the bore approaches the initial shoreline position, at $xh_i^{-1}=10$ in the figure. This test used $A=0.004\text{s}^2\text{m}^{-1}$, $p=0$ and $\Delta x=0.001\text{m}$. The main figure illustrates results computed using the hybrid MaCormack–mLxF shock capturing scheme and the MOC STI scheme with shock fitting. Inset is a close up of the last two profiles with circles denoting grid points. The plot illustrates excellent agreement between the two schemes both in terms of the shock location and strength. As is to be expected, the hybrid scheme has smeared the shock over a relatively large number of mesh points. Most important is the location and strength of the shock, as the smearing can be almost eliminated using the Breuss filter, cf. Figure 5.12. Results for bed height and water velocity are the same qualitatively and are therefore not presented. A detailed study of this problem that includes snapshots and contour plots of all dependent variables is made in §8.2. Finally, a rigorous test of the shock fitting scheme is to examine the behaviour of h , u and B immediately behind the front (at $x = \zeta(t)$) of a uniform bore as it climbs a mobile beach. This problem was originally studied for a fixed bed by Keller et al. (1960), see §2.1. Here the test was carried out on a mobile bed with an initially uniform bore of strength 1.6. Results for all flow variables are shown in Figure 5.11.

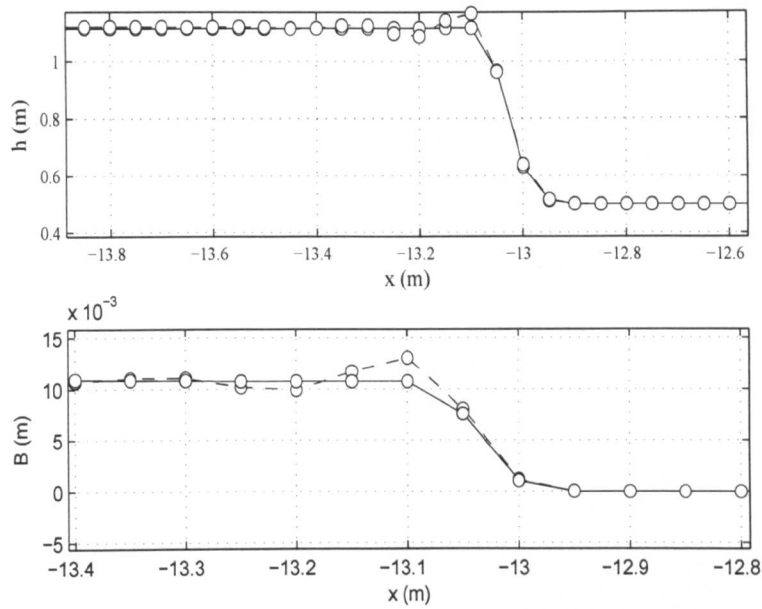


Figure 5.8: Uniform bore moving over a mobile bed ($A=0.004\text{s}^2\text{m}^{-1}$, $p=0$). Snapshots of water and bed elevations after 100 time steps using MacCormack shock capturing scheme with (solid) and without (dashed) the Engquist nonlinear filter.

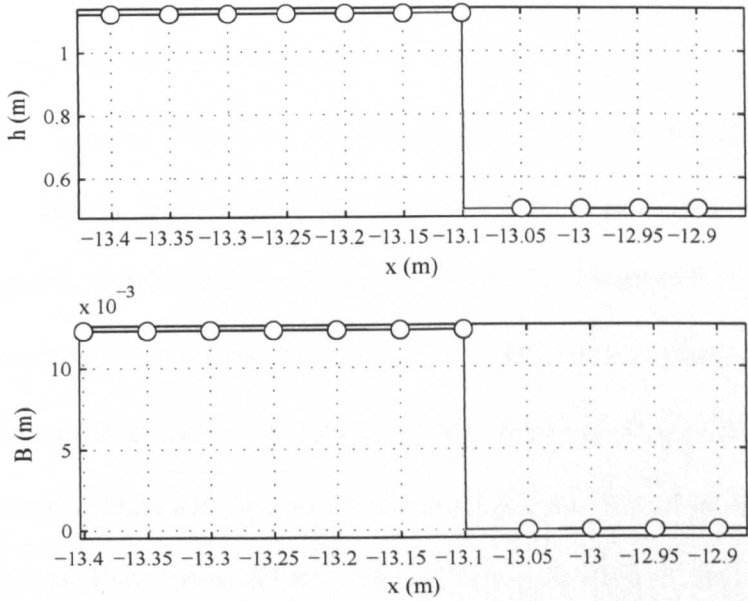


Figure 5.9: As in Figure 5.8 but using STI MOC shock fitting scheme (circles) and analytical solution (solid line).

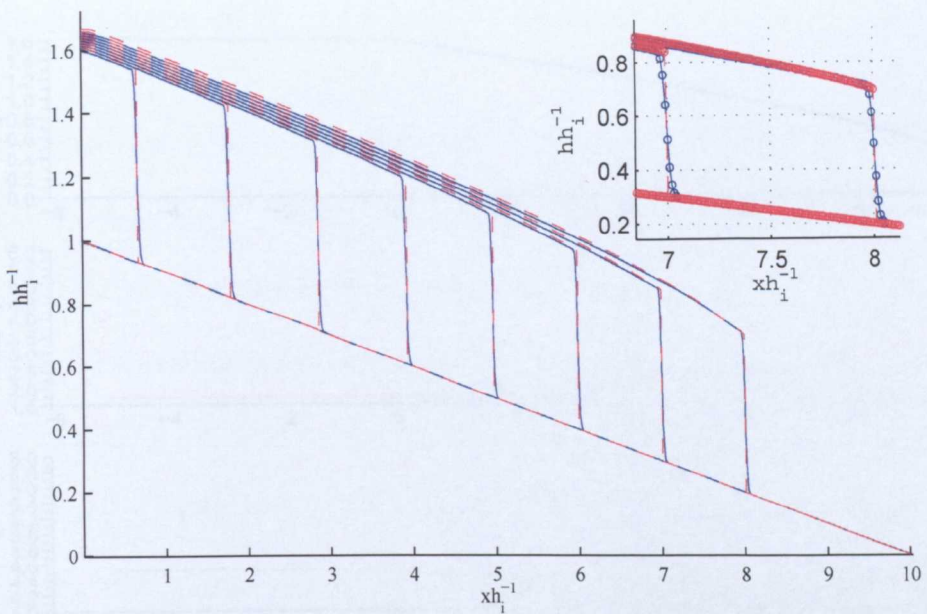


Figure 5.10: Snapshots of water depth for a bore climbing a mobile beach with $A=0.004\text{s}^2\text{m}^{-1}$ and $p=0$. Blue solid line shows hybrid shock capturing solution and red dashed line is MOC solution with shock fitting.

For this test problem there are three distinct phases. The bore first moves through a region of uniform depth before encountering the beach toe (at $\zeta = 0\text{m}$ in the figure). It then climbs the sloping beach and finally it collapses at the initial shoreline position ($\zeta = 10\text{m}$ in the figure). In the region of uniform depth all quantities behind the bore, and the bore speed, should remain constant; Figure 5.11 illustrates that this is clearly the case. As the bore then climbs the beach the water particle velocity behind it initially decreases and then increases rapidly as the shoreline is approached. The bore velocity continues to increase right up until bore collapse. Note that the bore velocity always remains less than the water velocity immediately behind the bore front otherwise the bore would collapse as a rarefaction wave. Water height immediately behind the bore decreases as the bore moves up the beach rapidly decreasing as the shoreline is approached. At the initial shoreline location it can be seen that the water height does

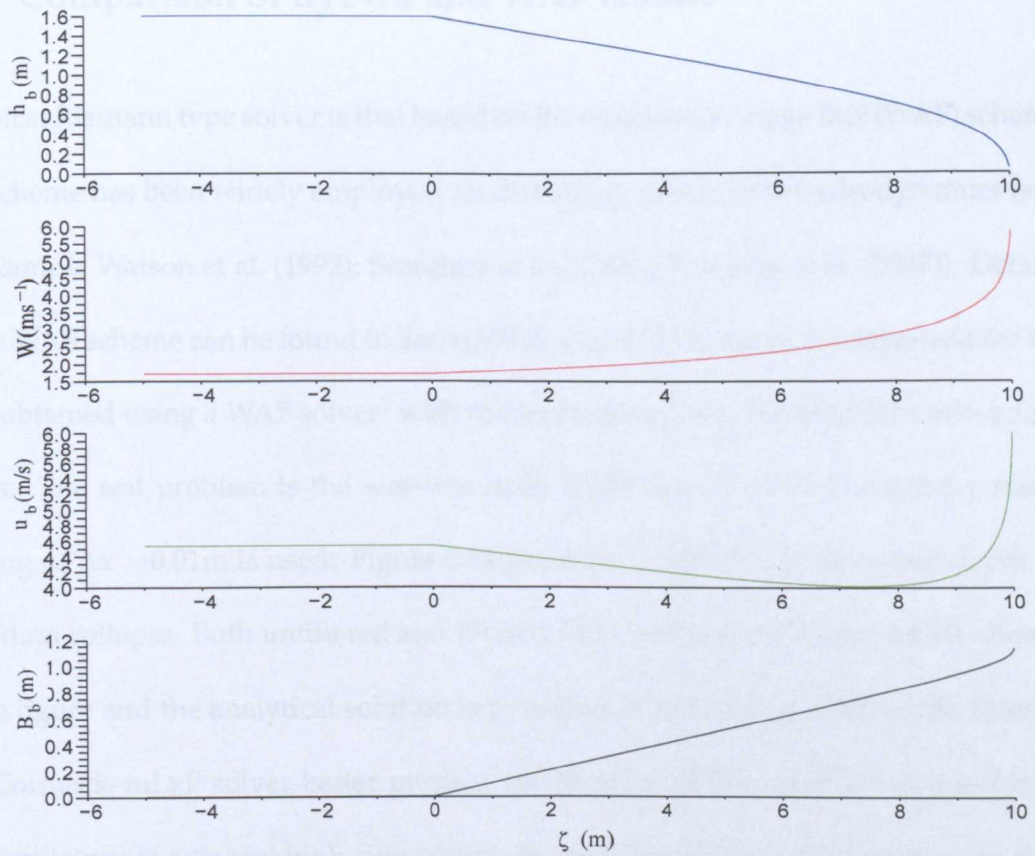


Figure 5.11: Values of dependent variables immediately behind an initially uniform subcritical incident bore as the bore approaches the original shoreline (at $\zeta=10\text{m}$), also shown is the bore velocity (W).

indeed tend to zero while the bore and water particle velocities tend to a finite limit. Interestingly, bed mobility does not appear to have a major effect on the hydrodynamics and the results obtained are qualitatively very similar to those given by Keller et al. (1960) for an initially uniform subcritical bore.

5.6 Comparison of hybrid and WAF results

A typical Riemann type solver is that based on the weighted average flux (WAF) scheme; this scheme has been widely employed for modelling swash zone hydrodynamics (see for example Watson et al. (1992); Brocchini et al. (2001); Antuono et al. (2007)). Details of the WAF scheme can be found in Toro (1999). Figure 5.12 shows a comparison for results obtained using a WAF solver¹ with those obtained using the MacCormack–mLxF solver. The test problem is the wet–wet dam-break described in §5.1.5 and a mesh spacing of $\Delta x = 0.01\text{m}$ is used. Figure 5.12 provides a snapshot of the water depth 3s after dam collapse. Both unfiltered and filtered MacCormack–mLxF results are shown in the figure and the analytical solution is provided as a reference. Clearly, the filtered MacCormack–mLxF solver better predicts the location of the shock as well as being less oscillatory at adjacent high side points. In the bottom close-up it can be seen that the shock is smeared over 4 mesh points for the WAF scheme but only 3 mesh points for the filtered MacCormack–mLxF scheme. Not so clear from the figure is the smearing of the gradient discontinuities at the beginning and end of the rarefaction fan by both schemes. The smearing due to the MacCormack–mLxF scheme is far more severe than that of the WAF scheme. As mentioned in §5.1.5, the excessive smearing of gradient discontinuities by the MacCormack–mLxF scheme is a direct consequence of the simple switch function given by (5.1.5).

¹These results were kindly provided by Dr. R. Briganti and were computed using the WAF–HLL solver detailed in Briganti and Dodd (2008).

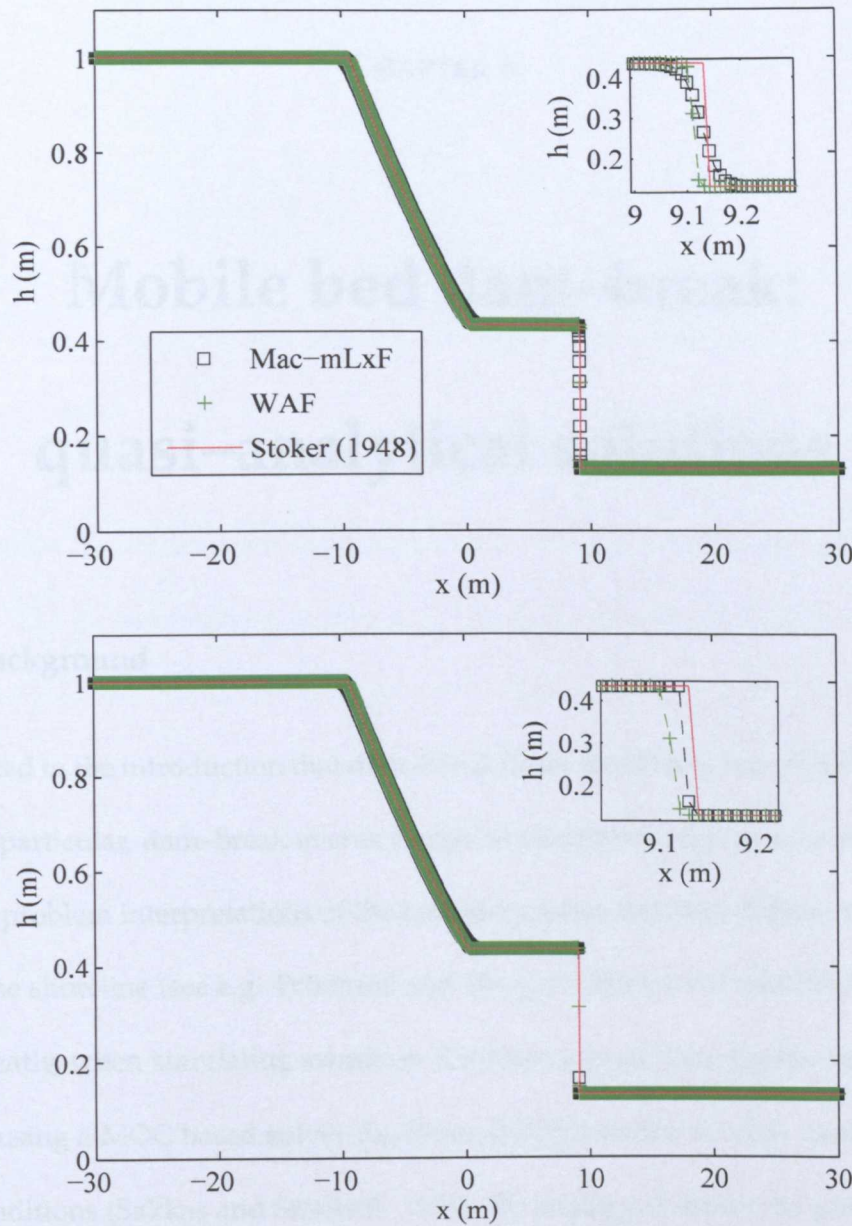


Figure 5.12: Comparison of numerical results at 3000 time-steps with Stoker (1948) analytical solution using WAF-HLL and MacCormack-mLxF hybrid schemes both without (top) and with (bottom) Breuss filter.

Mobile bed dam-break: quasi-analytical solutions

6.0.1 Background

It was stated in the introduction that dam-break flows are closely related to swash zone flows. In particular, dam-break events comprise alternative (and more accessible) initial value problem interpretations of the boundary value problem defined when a bore reaches the shoreline (see e.g. Pritchard and Hogg (2005); Guard and Baldock (2007)). Consequently, when simulating swash on fixed beaches or dam-breaks on fixed sloping beds using a MOC based solver the Ritter (1892) solution is often used to provide initial conditions (Sakkas and Strelkoff, 1973). By analogy it should be possible to use the same approach for mobile bed problems. For this reason quasi-analytical solutions for the shallow water-Exner mobile bed dam-break based on the $q = Au^3$ and $q = \bar{A}u^3h$ sediment flux formulations are constructed here. The validity of using the solution to a flat bed problem to provide initial conditions for a sloping bed problem at some small start time does not appear to have been discussed in the literature. With

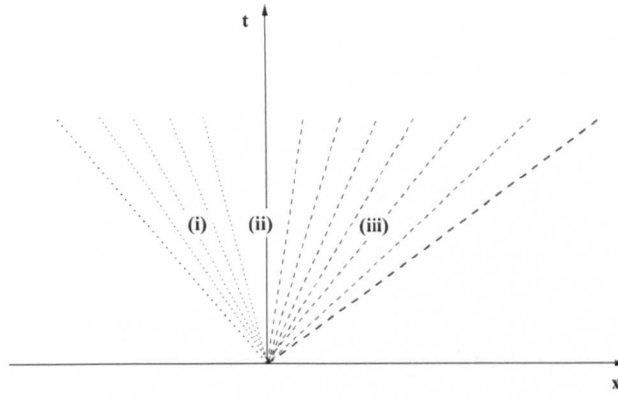


Figure 6.1: Wave structure for the shallow water-Exner mobile bed dam-break for both sediment flux formulations (refer to the accompanying text for details).

this in mind in Appendix A a scaling argument is used to show that this approach is in fact valid. The quasi-analytical mobile bed dam-break solutions are later used to generate initial values of the dependent variables when modelling Shen and Meyer (1963) type swash events, and also provide a valuable check on the accuracy of the other numerical schemes developed to solve the shallow water-Exner equations. Furthermore, an accurate solution for the mobile bed dam-break with a $q = Au^3$ sediment flux formulation will allow for checking of the validity of the shock relation (5.3.38) derived in §5.3.3. The solution technique employed is based on the so-called Riemann wave approach pioneered for use with dam-break flows by Fraccarollo and Capart (2002).

6.0.2 Wave structure

In order to develop Riemann wave solution for the shallow water-Exner mobile bed dam-break a qualitative *a priori* knowledge of the wave structure is necessary. In the appendix of a recent paper, Dodd et al. (2008) give snapshots of h , u and B for the shallow water-Exner mobile bed dam-break problem when $q = Au^3$. This solution was

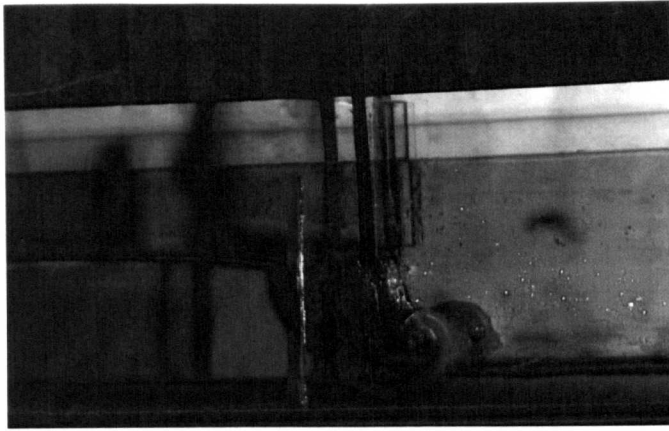


Figure 6.2: Mobile bed dam-break in the flume at the University of Nottingham (Picture courtesy of Dr. R. Munro)

constructed by Dodd et al. (2008) using a Riemann-type numerical solver based on Roe approximations. From these snapshots and the work presented in Fraccarollo and Capart (2002) for the two phase mobile bed dam-break problem, it has been possible to deduce the wave structure that represents the solution of the shallow water-Exner dam-break problem. Initially, in the region $x < 0$ the $\lambda_1 (C^-)$ family of characteristics form a centred simple wave up to the point where a constant state region develops. The λ_1 simple wave is represented by region (i) of Figure 6.1; this corresponds physically to a rarefaction wave. The constant state region, region (ii) of Figure 6.1, is followed further downstream by a $\lambda_3 (C_b)$ centred simple wave – region (iii) of Figure 6.1. From Figure 17 of Dodd et al. (2008), the λ_3 rarefaction fan seems to be terminated by an unusual discontinuity in both bed height and water velocity, the water height apparently tending to zero there. The wave tip thus comprises a wedge of sediment that moves over the dry downstream reach as a kind of "sediment bore". This ties in with the eigenvalue analysis undertaken in §3.6 in which it was shown that for $h = 0$ the water velocity tends to the celerity of the bed deformation, i.e. $u \rightarrow \lambda_3$. Thus, this discontinuity in water velocity and bed height travels as a C_b characteristic. It was postulated in

§3.6 that the sediment bore at $h = 0$ is a kind of contact discontinuity; if so, it is unlike the contact discontinuities found in gas dynamics as the characteristics either side of it certainly do not run parallel to it. Instead, this discontinuity appears to be what, in gas dynamics, is known as an "intermediate discontinuity" (Jeffrey, 1976). An intermediate discontinuity is a discontinuity whose velocity is equal to one of the eigenvalues of the state immediately behind it. A similar wave structure to that described above was observed when the hybrid MacCormack solver described in §5.1.5 was employed to solve the shallow water-Exner equations with $q = \bar{A}u^3h$. The initial conditions there were for a wet-wet dam-break with the upstream depth set at 1m and the downstream depth set at 1×10^{-8} m, i.e. a wet-dry dam-break employing a "thin film" treatment of the wave tip. The primary difference observed when compared with the $q = Au^3$ formulation was that the bed height appeared to tend to zero at the wave tip. Otherwise, apart from a narrower constant state region, the wave structure appeared to be the same.

The wave structure described above contains two centred simple waves each corresponding to a distinct characteristic family. For a centred simple wave comprising the k^{th} characteristic family the eigenvalues of this family are given by $\lambda_k = \frac{x}{t}$. This property and the fact that each of these characteristic families has associated generalised Riemann invariants allows a Riemann wave solution to be constructed, cf. Fraccarollo and Capart (2002).

It appears reasonable to assume that as the sediment becomes less and less mobile, i.e. as $A \rightarrow 0$, the wave structure of the mobile bed problems should get ever closer to the fixed bed solution of Ritter (1892). It is shown later in this chapter that as $A \rightarrow 0$ the width of the constant state region tends to zero for both transport formulae, leaving a single rarefaction wave, thus providing a valuable check on the validity of the models

developed in §6.0.4.

6.0.3 Generalised Riemann invariants

The right eigenvectors for the shallow water–Exner system were derived in §3.6. From the details given by Jeffrey (1976) and deductions made above about the wave structure of a shallow water–Exner morphodynamic dam-break it is to be expected that, in a system comprising two independent and three dependent variables, there will be two generalised Riemann invariants associated with the λ_1 simple wave region and two generalised Riemann invariants associated with the λ_3 simple wave region. Following the procedure outlined in Jeffrey (1976) the generalised Riemann invariants for the shallow water–Exner system are found from the equation:

$$\frac{dh}{r_1^k} = \frac{du}{r_2^k} = \frac{dB}{r_3^k}. \quad (6.0.1)$$

$q = Au^3$ formulation

Inserting the components of the right eigenvectors, found in §3.6.1, into (6.0.1) and rearranging gives:

$$du = \left(\frac{\lambda_k - u}{h} \right) dh \quad (6.0.2)$$

and:

$$dB = \left(\frac{3A\xi u^2(\lambda_k - u)}{\lambda_k h} \right) dh. \quad (6.0.3)$$

Integrating (6.0.2) and (6.0.3) yields the generalised Riemann invariants:

$$u - \int \left(\frac{\lambda_k - u}{h} \right) dh = K_1 \quad (6.0.4)$$

and:

$$B - \int \left(\frac{3A\xi u^2(\lambda_k - u)}{\lambda_k h} \right) dh = K_2, \quad (6.0.5)$$

where K_1 and K_2 are constants of integration. When $k = 1$ the generalised Riemann invariants are associated with the λ_1 rarefaction fan and when $k = 3$ the generalised Riemann invariants are associated with the λ_3 rarefaction fan.

$q = \bar{A}u^3h$ formulation

Inserting the components of the right eigenvectors, found in §3.6.2, into (6.0.1) and rearranging gives:

$$du = \left(\frac{\lambda_k - u}{h} \right) dh \quad (6.0.6)$$

and:

$$dB = \left(\frac{\bar{A}\bar{\zeta}u^2(3\lambda_k - 2u)}{\lambda_k} \right) dh, \quad (6.0.7)$$

Integration of (6.0.6) and (6.0.7) yields the generalised Riemann invariants:

$$u - \int \left(\frac{\lambda_k - u}{h} \right) dh = K_3 \quad (6.0.8)$$

and:

$$B - \int \left(\frac{\bar{A}\bar{\zeta}u^2(3\lambda_k - 2u)}{\lambda_k} \right) dh = K_4, \quad (6.0.9)$$

where K_3 and K_4 are constants of integration. Again, when $k = 1$ the generalised Riemann invariants are associated with the λ_1 rarefaction fan and when $k = 3$ the generalised Riemann invariants are associated with the λ_3 rarefaction fan.

6.0.4 Constructing the solution

$q = Au^3$ formulation

The solver integrates (6.0.4) and (6.0.5) using the Euler difference forms of (6.0.2) and (6.0.3) i.e.:

$$u = u_i + \frac{\lambda_{ki} - u_i}{h_i}(h - h_i) \quad (6.0.10)$$

and:

$$B = B_i + \frac{3A\zeta u_i^2(\lambda_{ki} - u_i)}{\lambda_{ki}h_i}(h - h_i), \quad (6.0.11)$$

where the subscript i refers to values on the previous characteristic. The initial C^- characteristic is defined as that which represents the tail of the first rarefaction fan of the dam-break. It follows that, as this characteristic is moving into still water of constant depth h_o , along this characteristic $u = 0$ and $h = h_o =$ for all time. Hence, the wave speed along this characteristic is given by the relation $\lambda_1 = -(gh_o)^{\frac{1}{2}} = -c_o$. The bed level must be equal to the initial reference level B_{ref} along this characteristic as $q = Au^3$. With this information known the scheme proceeds by incrementing the value of λ_1 by a fixed amount. As we have a centred simple wave then it follows that $\lambda_1 = \frac{x}{t}$ and therefore the abscissa x can be computed from the value of λ_1 and the value of t that is specified. Next, it is necessary to devise a generic scheme that allows us to compute values of the independent variables at this point. To this end (6.0.11) is rearranged to give an expression for h :

$$h = h_i + \frac{(B - B_i)(\lambda_{ki}h_i)}{3A\zeta u_i^2(\lambda_{ki} - u_i)}. \quad (6.0.12)$$

A value for B is chosen using an iterative procedure (e.g. the bisection technique) such that when the corresponding value of h , obtained from (6.0.12), and u , obtained from (6.0.10), are inserted into (3.4.29) to compute λ_1 , this value and the value of $\frac{x}{t}$ agree to the desired level of accuracy. The newly computed dependent variables are then used to update the eigenvalues and right eigenvectors at this point before the solution continues in this fashion, traversing the λ_1 rarefaction fan until $h \leq h_{cs}$ (where h_{cs} is the water height inside the constant state region). It is not possible to use (6.0.12) when computing the value of dependent variables along the first characteristic to the right of the initial C^- characteristic as $u_i = 0$ in this case and consequently (6.0.12) is

undefined. Instead a rearrangement of (6.0.10) is used to compute h from the value of u determined by an iteration technique. Finally, (6.0.11) is used to find B once the correct value of u has been determined.

The value of h_{cs} cannot be known *a priori* as it forms part of the solution, cf. Fraccarollo and Capart (2002). It is therefore necessary to make an initial guess at the value of h_{cs} and then use some criterion to refine this guess. In this work the refinement criterion is that the volume of sediment is conserved to a pre-specified level of accuracy. Once $h \leq h_{cs}$ it is deemed that the λ_1 rarefaction fan has ended and the constant state region begun. The abscissa for the end of the constant state region is found by inserting h_{cs} and u_{cs} into (3.4.31) to find λ_3 and recalling that, as the λ_3 simple wave has begun, $\lambda_3 = \frac{x}{t}$. The scheme then traverses the λ_3 (C_b) rarefaction fan in a manner identical to that detailed for the λ_1 (C^-) fan until the specified cut off depth h_{co} is reached. The final step is to check that sediment mass is conserved as described in §6.0.5.

$q = \bar{A}u^3h$ formulation

The procedure is similar to that detailed above except that (6.0.10) and (6.0.11) are replaced with:

$$h = h_i + \frac{(b - b_i)\lambda_{ki}}{\bar{A}\xi u_i^2(3\lambda_{ki} - 2u_i)} \quad (6.0.13)$$

and:

$$u = u_i + \left(\frac{\lambda_{ki} - u_i}{h_i} \right) (h - h_i) \quad (6.0.14)$$

in the λ_1 fan, and:

$$h = h_i + \frac{(u - u_i)h_i}{\lambda_{ki} - u_i} \quad (6.0.15)$$

and:

$$b = b_i + \left(\frac{\bar{A}\xi u_i^2(3\lambda_{ki} - 2u_i)}{\lambda_{ki}} \right) (h - h_i) \quad (6.0.16)$$

in the λ_3 fan. Note that the same approach as that used for $q = Au^3$ is employed along the first outgoing (C^-) characteristic.

6.0.5 Sediment conservation

In order to check that sediment mass is conserved once the downstream (wave tip) boundary is reached, i.e. $h < h_{co}$, the following procedure is employed:

- The total volume of sediment per unit area scoured out (MB_-) is computed through the numerical integration of the total area below the line B_{ref}
- The total volume of sediment per unit area deposited (MB_+) is computed through the numerical integration of the total area above the line B_{ref}
- The check $|MB_+ - MB_-| < tol$ is made, where tol is a user specified tolerance.

If sediment mass is conserved to the required degree of accuracy the value chosen for h_{cs} is assumed to be correct. If the required accuracy is not met, the scheme increments or decrements the height of water in the constant state region h_{cs} by a prescribed amount and the entire computation procedure is repeated.

6.1 Self-similarity

As is the case for the Ritter (1892) and Stoker (1948) dam-break solutions, the above solutions can be shown to be self-similar. This self-similarity comes about as a direct consequence of the wave structure for both transport formulae comprising a constant state region bordered on either side by centred simple waves. In both simple wave regions the eigenvalues are given simply by $\frac{x}{t}$, thus the characteristics are straight lines

passing through the origin. It follows that values of the dependent variables can therefore be written as a function of $\frac{x}{t}$ as opposed to functions of x and t separately. A corollary of this is that the dependent variables propagate unchanged along the respective characteristics in each rarefaction fan. As one member of each straightline family also borders the constant state region it follows that the entire solution dilates at the rate $\frac{x}{t}$.

6.2 Validation

It was stated above that a good, and currently the only test of the validity of the above solution is to let $A \rightarrow 0$ and see if the Ritter analytical solution is recovered. Figure 6.3 provides snapshots of water height (top) and velocity (bottom) when a value of $1 \times 10^{-8} \text{s}^2 \text{m}^{-1}$ was employed for A . It is not possible to set A equal to zero because (6.0.12) becomes undefined. Initial conditions are given by:

$$h(x, 0) = \begin{cases} h_o & \text{if } x < 0 \\ 0 & \text{if } x > 0 \end{cases} \quad (6.2.1)$$

with:

$$u(x, 0) = 0 \text{ and } B(x, 0) = 0 \quad \forall x,$$

where the initial water height, $h_o = 1\text{m}$. Values of x and h have been made dimensionless by dividing through by h_o and u non-dimensionalised by dividing through by $(gh_o)^{\frac{1}{2}}$. On the plots the Ritter solution is represented by the solid green line and the numerical solution by black circles. The snapshots are presented at 1 second intervals between 0 and 5 seconds inclusive. Values at the tip are denoted by green crosses for the analytical solution and black squares for the numerical solution. It should be noted that for clarity the numerical solution in the main figures are plotted every 5000 data points (all data points are shown on the inset figure). The tip velocity is well approxi-

mated being within 0.4% of the Ritter analytical value. Inset in the top of the figure is a close up of the constant state region at $t = 1s$; it is clear that the width of this region has shrunk considerably as the theory suggests. As would be expected the same constant state region exists in the velocity profile. Computed height values throughout the flow domain are within 0.25% of the Ritter analytical heights at $t = 1s$; this holds for all time as the solution is self-similar. The agreement between numerical and analytical results is exceptional; any discrepancy between results is down to a combination of numerical error and analytical difference due to the small amount of bed mobility that must be introduced in order for the model to remain bounded. The same verification test was also performed using the $q = \bar{A}u^3h$ model and results of comparable accuracy obtained. The relationship between the predicted and computed "sediment bore" height is now investigated in order to prove that the corresponding shock relation derived in §5.3.3 is indeed valid.

6.3 Non-dimensionalisation

Before presenting results for the mobile bed dam-break suitable non-dimensional time and length scales are derived for the system of equations comprising (3.2.8), (3.2.18) and (3.2.24). In this thesis non-dimensional scales are derived purely for the coherent presentation of results, consequently all analysis employs dimensional variables. Subscripts $,x$ and $,t$ are again used to denote partial derivatives with respect to space and time. Representing dimensionless variables with an asterisk and taking

$$x^* = \frac{x}{X_o}, t^* = \frac{t}{T_o}, h^* = \frac{h}{h_o}, u^* = \frac{u}{u_o}, B^* = \frac{B}{B_o} \text{ and } q^* = \frac{q}{q_o}, \quad (6.3.1)$$

suitable non-dimensional variables can be obtained for both flux formulations considered in this thesis. Note that ζ is already dimensionless.

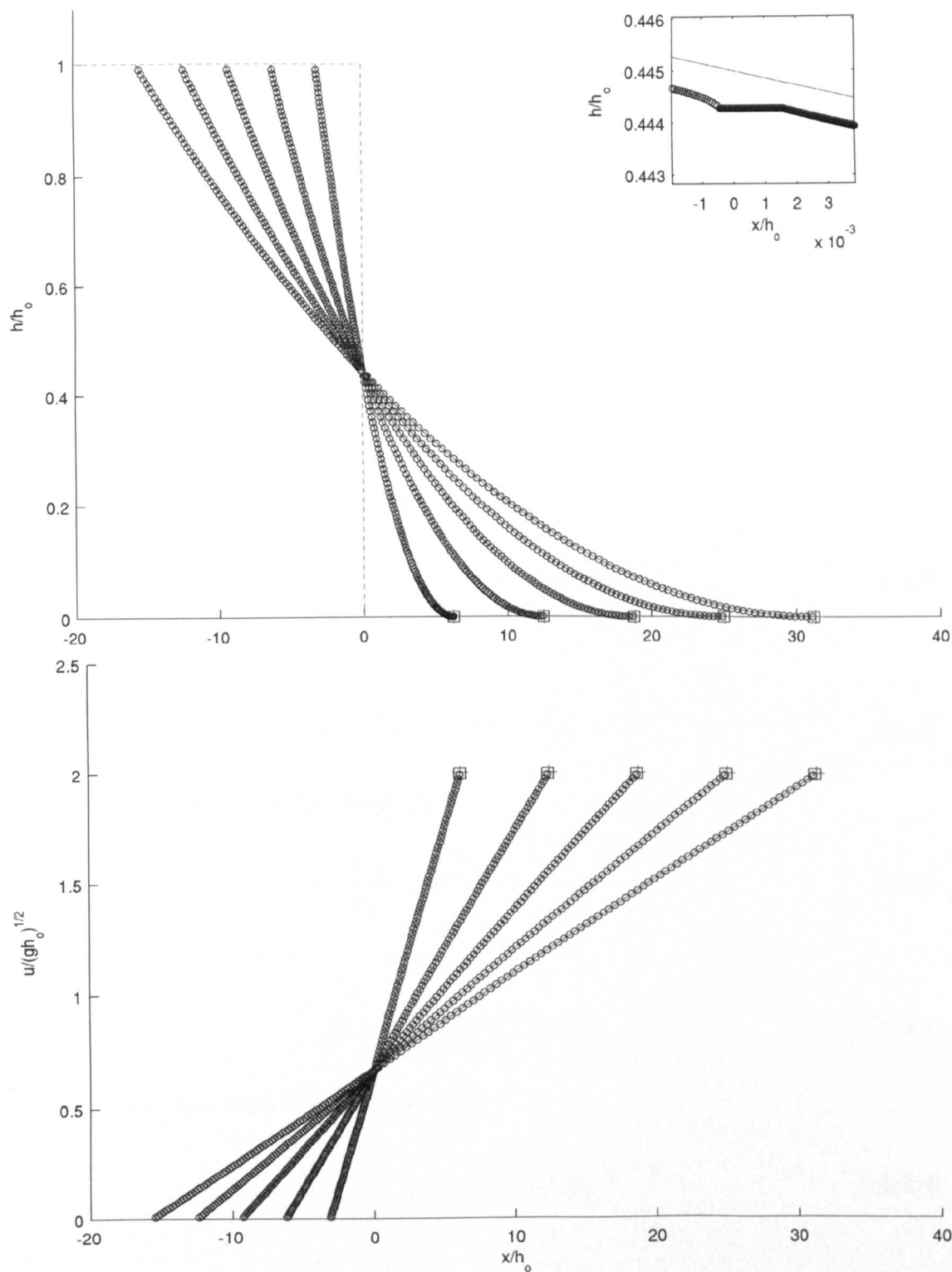


Figure 6.3: Comparison of "fixed bed" numerical solution with the Ritter analytical solution. For plot details see the accompanying text.

6.3.1 Sediment flux given by $q = Au^3$

Substituting (6.3.1) into the governing equations gives:

$$(3.2.8) \rightarrow \frac{h_o}{T_o} h^*_{,t^*} + \frac{u^* u_o h_o}{X_o} h^*_{,x^*} + \frac{h^* h_o u_o}{X_o} u^*_{,x^*} = 0, \quad (6.3.2)$$

$$(3.2.18) \rightarrow \frac{u_o}{T_o} u^*_{,t^*} + \frac{u^* u_o^2}{X_o} u^*_{,x^*} + \frac{g B_o}{X_o} B^*_{,x^*} - \frac{g h_o}{X_o} h^*_{,x^*} = 0, \quad (6.3.3)$$

$$(3.2.24) \rightarrow \frac{B_o}{T_o} B^*_{,t^*} + \frac{3 A_o \zeta u_o^3 u^{*2}}{X_o} u^*_{,x^*} = 0. \quad (6.3.4)$$

When non-dimensionalising it seems sensible to set $B_o = h_o$ and also $X_o = h_o$ and take the Froude scaling of Peregrine (1972), i.e. $T_o = h_o^{\frac{1}{2}} g^{-\frac{1}{2}}$ and $u_o = (g h_o)^{\frac{1}{2}}$. Using these variables in (6.3.2) and (6.3.3) when simplified gives:

$$h^*_{,t^*} + u^* h^*_{,x^*} + h^* u^*_{,x^*} = 0 \quad (6.3.5)$$

and:

$$u^*_{,t^*} + u^* u^*_{,x^*} + B^*_{,x^*} - h^*_{,x^*} = 0. \quad (6.3.6)$$

Considering the generic form of (6.3.4) i.e.:

$$\frac{B_o}{T_o} B^*_{,t^*} + \frac{\zeta q_o}{X_o} q^*_{,x^*} = 0, \quad (6.3.7)$$

then:

$$B^*_{,t^*} + \left(\frac{\zeta q_o T_o}{X_o B_o} \right) q^*_{,x^*} = 0. \quad (6.3.8)$$

For a sediment flux of the form $q = Au^3$ then:

$$q_o = \frac{q}{q^*} = \frac{Au^3}{u^{*3}} = Au_o^3, \quad (6.3.9)$$

so:

$$\left(\frac{\zeta q_o T_o}{X_o B_o} \right) q^*_{,x^*} = A \zeta g q^*_{,x^*}. \quad (6.3.10)$$

Thus, (6.3.8) becomes:

$$B^*_{,t^*} + \sigma u^{*3}_{,x^*} = 0, \quad (6.3.11)$$

where σ is the dimensionless "bed evolution" parameter given by:

$$\sigma = A\zeta g. \quad (6.3.12)$$

The non-dimensional variables then are:

$$x^* = xh_o^{-1}, t^* = tg_o^{\frac{1}{2}}h_o^{-\frac{1}{2}}, h^* = hh_o^{-1}, u^* = u(gh_o)^{-\frac{1}{2}} \text{ and } B^* = Bh_o^{-1}. \quad (6.3.13)$$

6.3.2 Sediment flux given by $q = \bar{A}u^3h$

Applying the same approach as in the $q = Au^3$ case the non-dimensional form of the mass and momentum equations is identical, i.e. (6.3.5) and (6.3.6) respectively. When $q = \bar{A}u^3h$ then (6.3.9) becomes:

$$q_o = \frac{q}{q^*} = \frac{\bar{A}u^3h}{u^{*3}h^*} = \bar{A}u_o^3h_o. \quad (6.3.14)$$

From (6.3.7) it follows that:

$$B^*_{,t^*} + \left(\frac{\zeta q_o T_o}{X_o B_o} \right) q^*_{,x^*} = 0. \quad (6.3.15)$$

The quantity:

$$\frac{\zeta q_o T_o}{X_o B_o} \quad (6.3.16)$$

can be re-written in terms of g and h_o using the Froude scaling employed above to give the dimensionless bed evolution parameter $\bar{\sigma}$ for this form of sediment flux, where:

$$\bar{\sigma} = \bar{A}\zeta h_o g, \quad (6.3.17)$$

meaning that the non-dimensional form of the Exner equation is:

$$B^*_{,t^*} + h^*_{,x^*} + \bar{\sigma} u^{*3}_{,x^*} = 0. \quad (6.3.18)$$

The non-dimensional variables are identical to those given by (6.3.13).

6.3.3 Values for the bed evolution parameters σ and $\bar{\sigma}$

A procedure to determine order of magnitude estimates for A and \bar{A} is given in §3.3.3. The values so obtained can be used along with suitable porosity values to decide on suitable estimates for the dimensionless parameters σ and $\bar{\sigma}$ in the swash. The porosity of varying grain sizes is well understood (Soulsby, 1997) and a reasonable range for sand beaches is:

$$0 \leq p \leq 0.5. \quad (6.3.19)$$

Using the value $A=0.004\text{s}^2\text{m}^{-1}$, obtained in §3.3.3, and assuming a typical value of 0.4 for beach porosity a value of $\sigma = 0.0654$ is found from (6.3.12). Similarly, with $\bar{A}=0.015\text{s}^2\text{m}^{-2}$, again obtained in §3.3.3, $\bar{\sigma} = 0.15$ from (6.3.17). It is also useful to have likely maximum and minimum values for σ in order to compute bed profiles at these extrema. Using field data kindly provided by G. Masselink (personal communication, 2008) for sand beaches the method of §3.3.3 provided the following range for σ :

$$0.001 \leq \sigma \leq 0.2, \quad (6.3.20)$$

and $\bar{\sigma}$:

$$0.075 \leq \bar{\sigma} \leq 0.5. \quad (6.3.21)$$

6.4 Shock relation at the wave tip

The Riemann wave solution detailed above can be employed to check the validity of the shock relation (5.3.38). Using the Riemann wave value of tip velocity, predictions for the height of the sediment bore for a number of different values of $\sigma = A\zeta g$ (corresponding to different combinations of A and p , see §6.3.1) were made using (5.3.38). Agreement between the predicted value and the computed value was checked for dif-

σ	h_{co}	% diff. between predicted and computed B_*
0.01	5×10^{-6}	0.06
0.04	5×10^{-6}	0.02
0.01	1×10^{-6}	0.03
0.04	1×10^{-6}	0.01

Table 6.1: Comparison of bed heights predicted using (5.3.38) and computed by the Riemann wave technique.

ferent values of the minimum cut-off depth h_{co} ; a brief selection of results so obtained is presented in Table 6.4. The agreement between the predicted and observed solutions is excellent and improves as the cut-off depth is decreased. This occurred for all values of σ tested suggesting convergence between predicted and computed values and indicating that the relation (5.3.38) is valid. It is therefore possible to predict bed height at the wave tip as a function of the water velocity there.

6.5 Example results for $q = Au^3$ and $q = \bar{A}u^3h$

The Riemann wave models developed for the $q = Au^3$ and $q = \bar{A}u^3h$ sediment flux formulations have been run with a number of different values of the respective bed evolution parameters. Representative order of magnitude estimates for the bed evolution parameters were computed from field data as described in §3.3.3. Example results that clearly indicate the configuration of dependent variables within the flow field are presented here. Figures 6.4, 6.5 and 6.6 show results from the $q = Au^3$ sediment flux formulation for $\sigma = 0.00981, 0.039$ and 0.2 respectively. The initial conditions for all figures are given by (6.2.1) with $h_o = 1\text{m}$. Snapshots are presented at 1 second intervals

between 0 and 5 seconds inclusive. The figures show that increasing the bed evolution parameter σ has a significant effect on tip velocity and the height of the sediment bore at the wave tip. As would be expected on physical grounds increased sediment mobility magnifies the amount of scour at the initial dam location. Thus, for a higher value of A the water is moving a greater mass of sediment and the tip velocity is consequently reduced. Similar results are found when the $q = \bar{A}u^3h$ sediment flux model is run; however, behaviour at the wave tip is very different. At the tip model results confirm that sediment is conserved to machine accuracy if the water depth and bed height at the tip tend to zero. This would appear to validate the assumption made above concerning water depth and bed height at the tip for this sediment flux formulation. Figures 6.8 and 6.7 illustrate results obtained using a $q = \bar{A}u^3h$ sediment flux.

6.5.1 Bed profile and tip velocity when $q = \bar{A}u^3h$

Figure 6.9 illustrates snapshots of the (dimensionless) instantaneous sediment flux given by $q = \bar{A}u^3h$ where $\bar{A} = 1.5 \times 10^{-2}s^2m^{-2}$ and $p = 0$. It is interesting to note that the maximum flux does not occur at the tip, as in the $q = Au^3$ case, but much further back in the flow. The instantaneous flux at the tip itself is zero. This is clearly a consequence of a transport formula for which $q \propto h$. The low water depths begin to dominate over the water velocity a fair way back into the flow thus reducing transport as the tip is approached. Without a storage term present the effect of this decrease in transport downstream is the accumulation of sediment on the bed.

For the mobile bed cases illustrated here the tip velocities exceed the fixed bed tip velocity predicted by the Ritter (1892) solution. On initial consideration this result seems unusual, but the reason is obvious when Figure 6.10 is examined. The bed gradient, $B_{,x}$, at the tip is negative and therefore provides additional acceleration compared to

the Ritter case where the fixed bed remains horizontal. Physically, this result would appear to be unsound as experimental evidence suggests that mobile bed dam-breaks travel slower than their fixed bed counterparts (Zech et al., 2008). This result challenges the validity of using a $q = \bar{A}u^3h$ sediment transport formula for governing equations without a storage term.

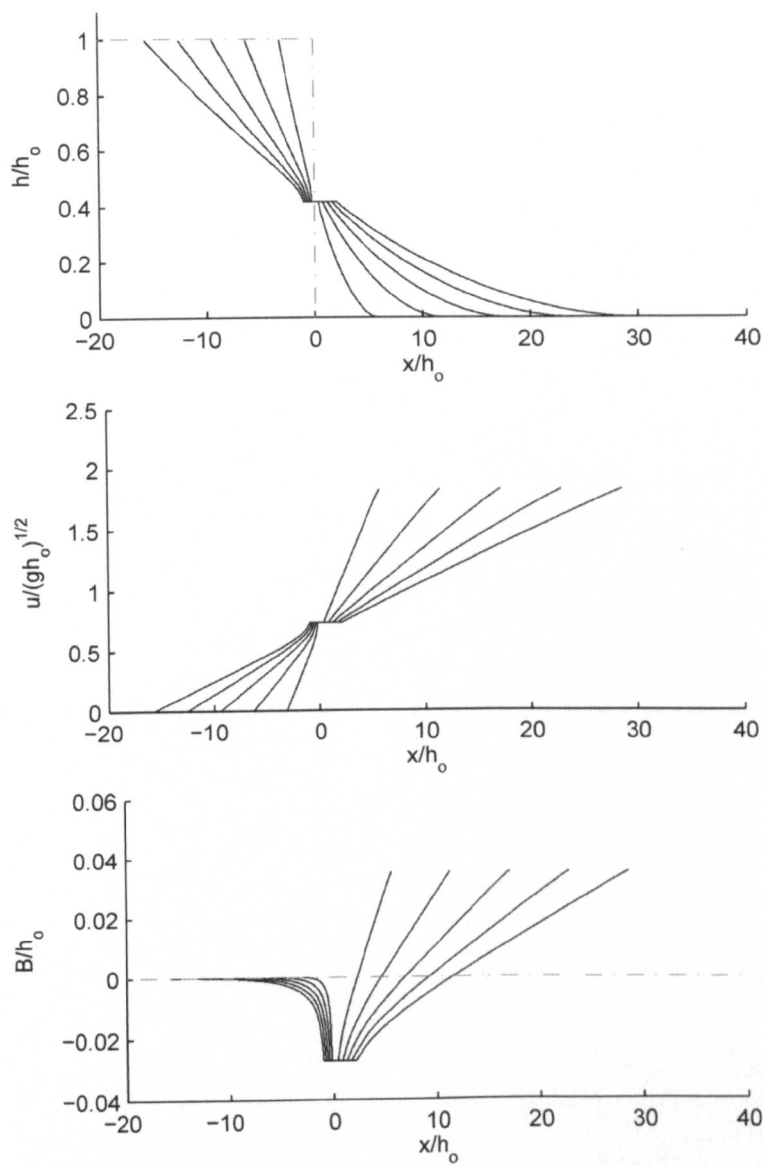


Figure 6.4: Snapshots of dimensionless dependent variables from the quasi-analytical solution for mobile bed dam-break with $q = Au^3$ where $A = 1 \times 10^{-3} \text{s}^2 \text{m}^{-1}$ and porosity is zero (hence $\sigma = 0.00981$).

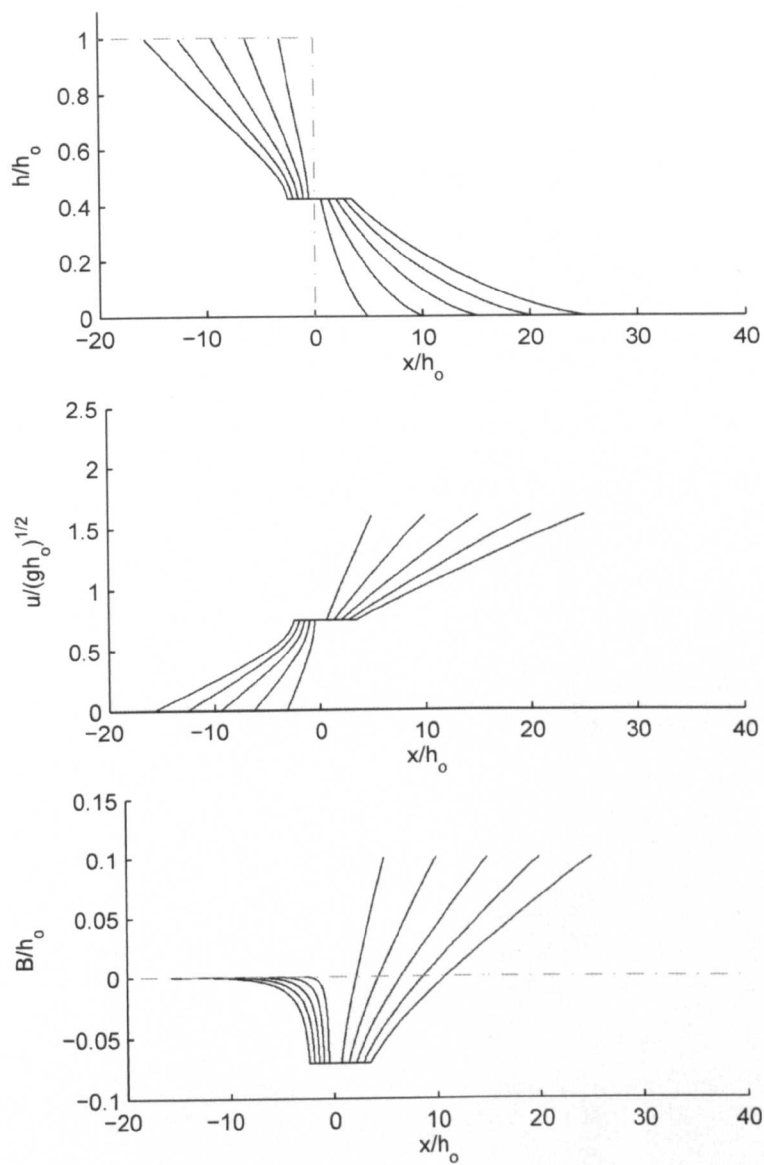


Figure 6.5: Snapshots of dimensionless dependent variables from the quasi-analytical solution for mobile bed dam-break with $q = Au^3$ where $A = 4 \times 10^{-3} \text{s}^2 \text{m}^{-1}$ and porosity is zero (hence $\sigma = 0.039$).

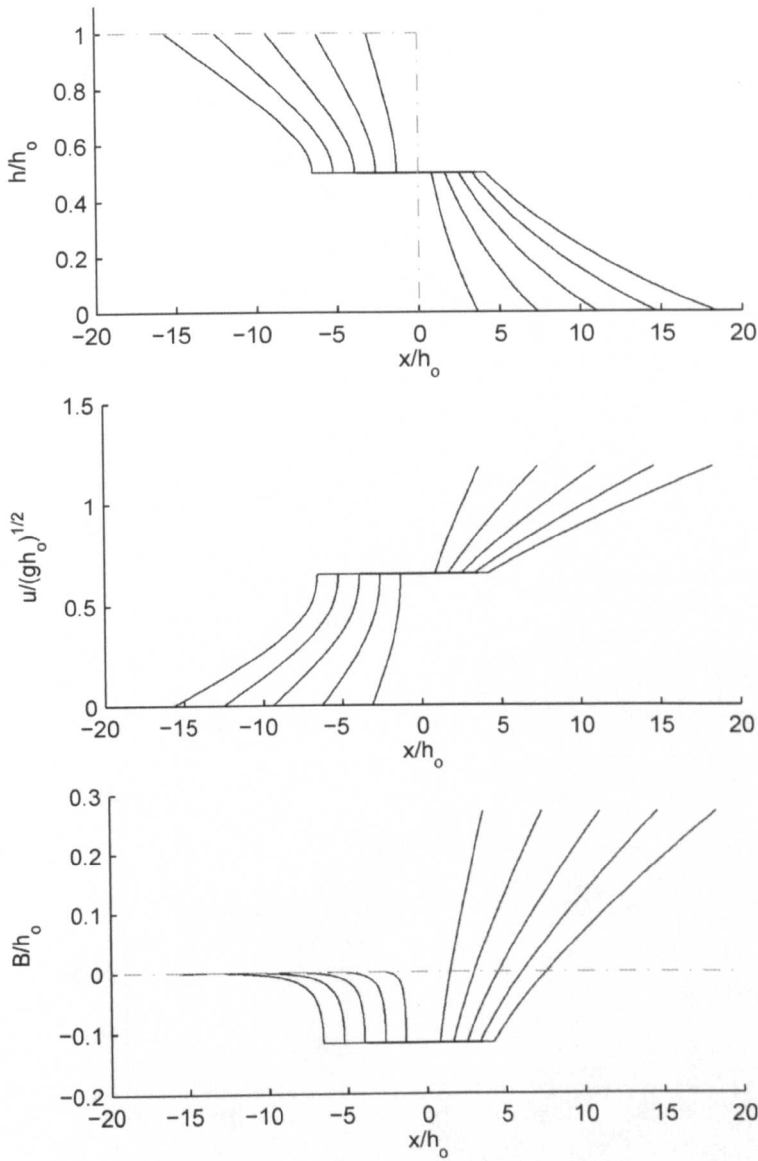


Figure 6.6: Snapshots of dimensionless dependent variables from the quasi-analytical solution for mobile bed dam-break with $q = Au^3$ where $A = 0.02 \times 10^{-3} \text{s}^2 \text{m}^{-1}$ and porosity is zero (hence $\sigma = 0.2$).

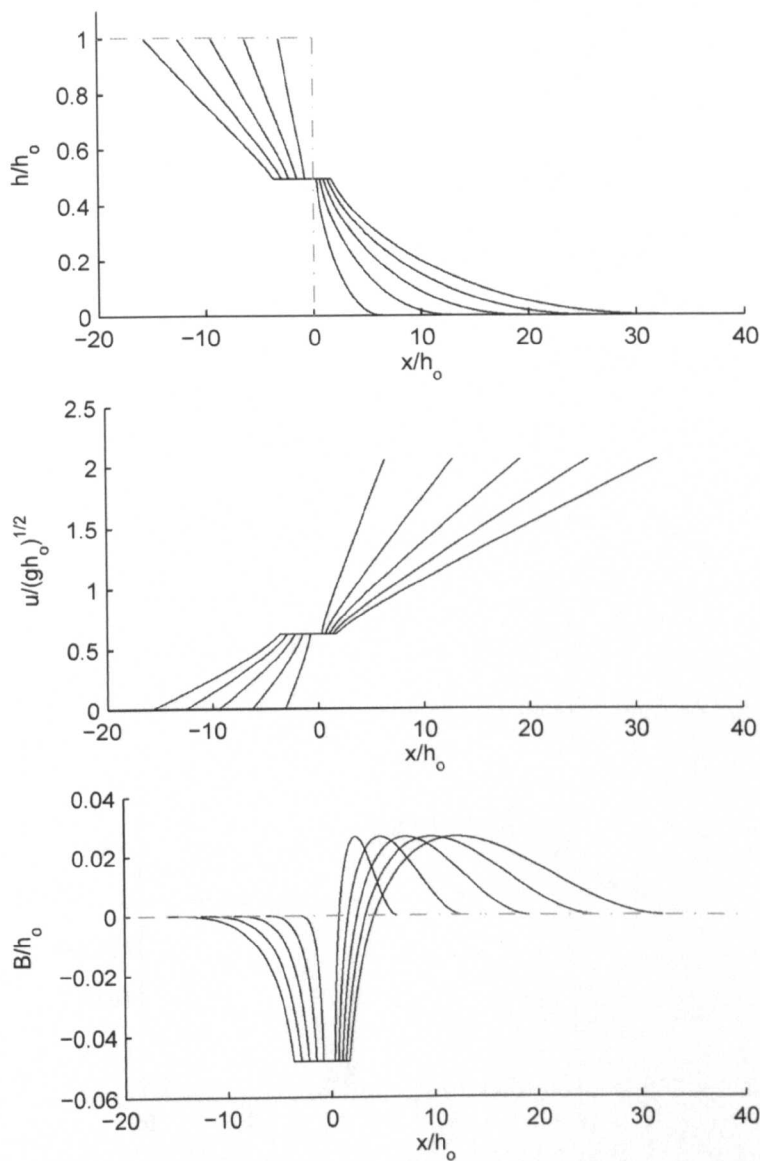


Figure 6.7: Snapshots of dimensionless dependent variables from the quasi-analytical solution for mobile bed dam-break with $q = \bar{A}u^3h$ where $\bar{A} = 1.5 \times 10^{-2}\text{s}^2\text{m}^{-2}$ and porosity is zero (hence $\bar{\sigma} = 0.00981$).

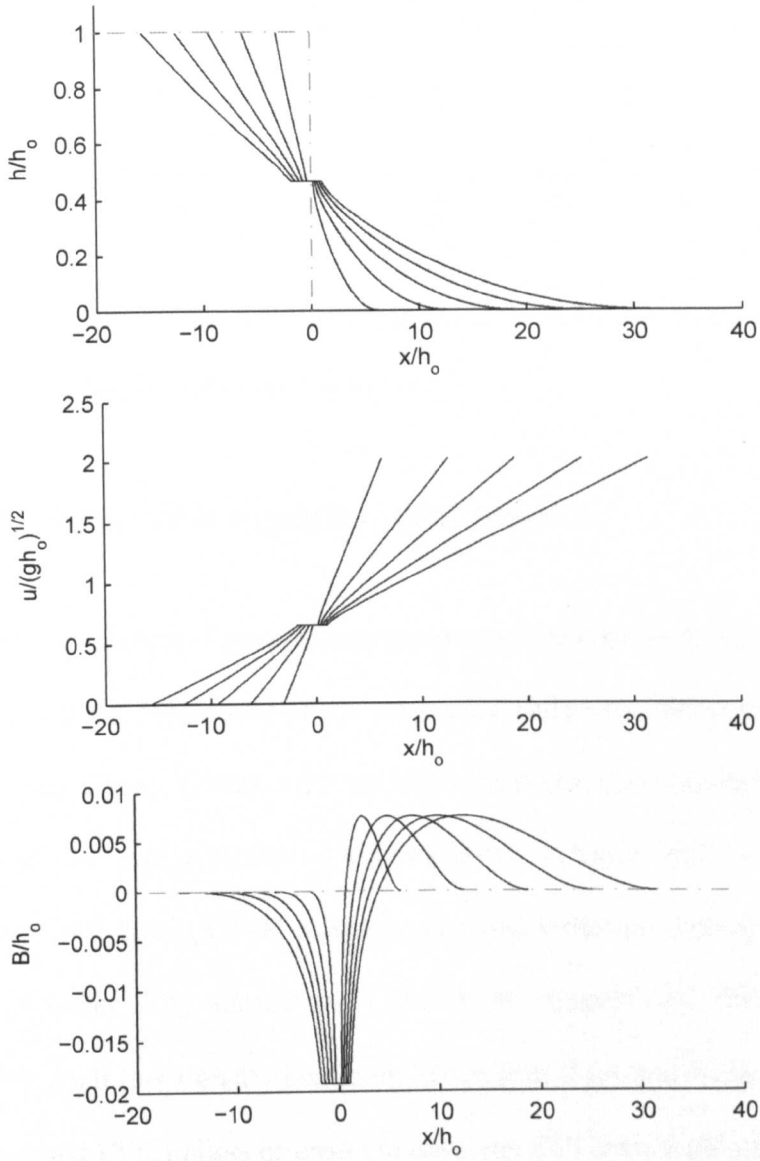


Figure 6.8: Snapshots of dimensionless dependent variables from the quasi-analytical solution for mobile bed dam-break with $q = \bar{A}u^3h$ where $\bar{A} = 4 \times 10^{-3}\text{s}^2\text{m}^{-2}$ and porosity is zero (hence $\bar{\sigma} = 0.039$).

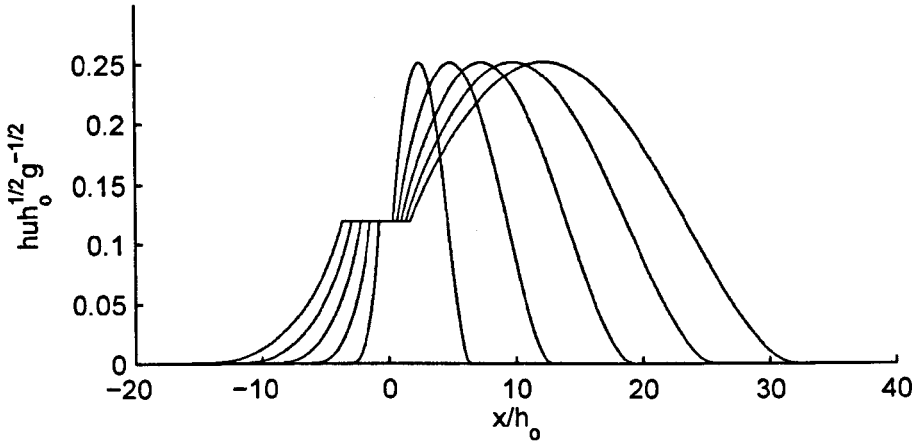


Figure 6.9: Snapshots of dimensionless instantaneous sediment fluxes (with $q = \bar{A}u^3h$) for the dam-break of Figure 6.7.

6.6 Comparison with experimental results

For completeness a brief, and simple, comparison is made between certain measured profiles obtained in the laboratory at the Université catholique de Louvaine, detailed in Fraccarollo and Capart (2002), and the theoretical solution described above with sediment flux of the form $q = Au^3$. No comparison is made with the experimental results of Capart and Young (1998) as these involved sediment with a density almost equal to that of water. The density ratio used in the Capart and Young (1998) tests was $\frac{\rho_s}{\rho} = 1.048$; such low density sediment is not found on real world beaches. The Louvaine tests used PVC pellets of uniform diameter (3.5 mm) with a relative density $\frac{\rho_s}{\rho} = 1.54$. Although the density ratio is still low compared with that of medium grain sand (for which $\frac{\rho_s}{\rho} = 2.65$) the results are clearly presented, thus facilitating a comparison with the theoretical results. Full details of the tests are given in Fraccarollo and Capart (2002) and will not be repeated here.

The results shown in Figures 6.11 and 6.12 are presented in the same self-similar coordinates as used by Fraccarollo and Capart (2002). In Figure 6.11, $\sigma = 0.0164$; this

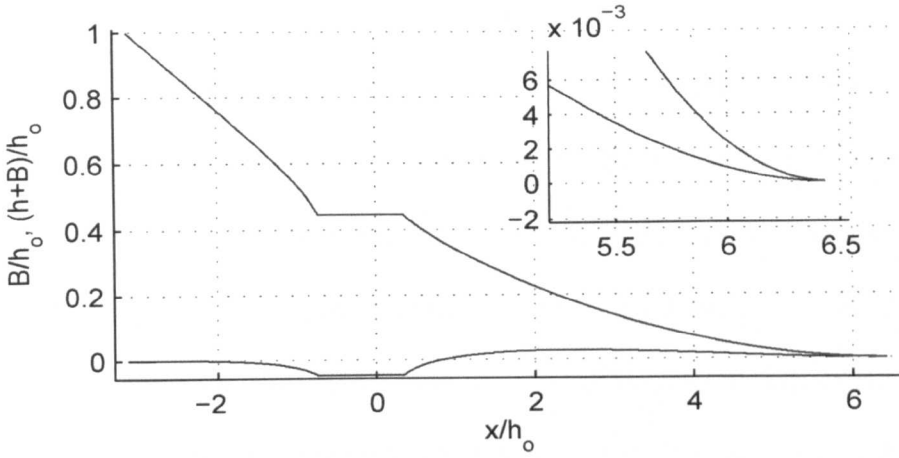


Figure 6.10: Profile at $t=1s$ for the dam-break of Figure 6.7 (with $q = \bar{A}u^3h$); inset: close-up of the tip region.

is obtained by computing A using (3.3.3) with $f_R = 0.014$ as suggested by Fraccarollo and Capart (2002) and taking $p = 0.4$. Clearly, the quantitative agreement between the theoretical result and experimental result is poor for this value of σ . The theoretical result gives the tip location as being almost twice as far downstream as the experimental result. In constructing Figure 6.11 a value of $p = 0.4$ is used for the bed porosity as no value is given in Fraccarollo and Capart (2002); the bed porosity would almost certainly be lower for the PVC pellets used in the experiment. Employing a lower value for p has the effect of increasing the value of σ . In terms of the tip position, sediment bore height and scour depth, numerical experiments have shown that using a larger value for σ increases the level of agreement between the theoretical and experimental results up to a value of $\sigma \approx 0.2$. Following this somewhat *ad hoc* approach a value of $\sigma = 0.2$ is used to obtain the results shown in Figure 6.12. The value of A , and thus f_R , that a σ value of 0.2 corresponds to depends on the value assigned to $p = 1 - \xi^{-1}$ in accordance with (6.3.12) and (3.3.3). In both plots the theoretical solution captures the qualitative features of the flow reasonably well, the experimental results clearly exhibit

both the central region (corresponding to the constant state region of the theoretical model) and the sediment bore at the wave tip. The theoretical solution captures the two simple wave regions, although it over estimates the free surface slope in the first (upstream) region and underestimates it in the second (downstream) region.

It is beyond the scope of this thesis to provide a quantitative analysis of the agreement between experimental and theoretical data. However, to give an idea of the quantitative differences between the experimental data and the Shallow water-Exner theory for the mobile bed dam-break, in Figure 6.12 the tip position is over estimated by approximately 20% in the theoretical model. Such a discrepancy is doubtless due to the simplified nature of the governing equations and sediment transport formula used to obtain the quasi-analytical solution. The inclusion of friction into the governing equations would almost certainly improve the level of agreement between theory and experiment.

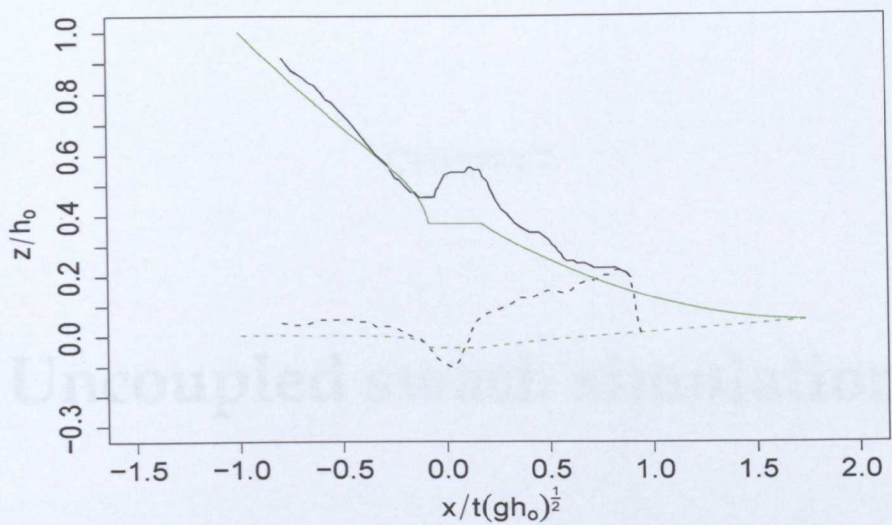


Figure 6.11: Comparison of the theoretical solution with $\sigma = 0.0164$ (green lines) and measured (black lines) profiles for the Louvaine experiment reported in Fraccarollo and Capart (2002) at $t = 0.75\text{s}$.

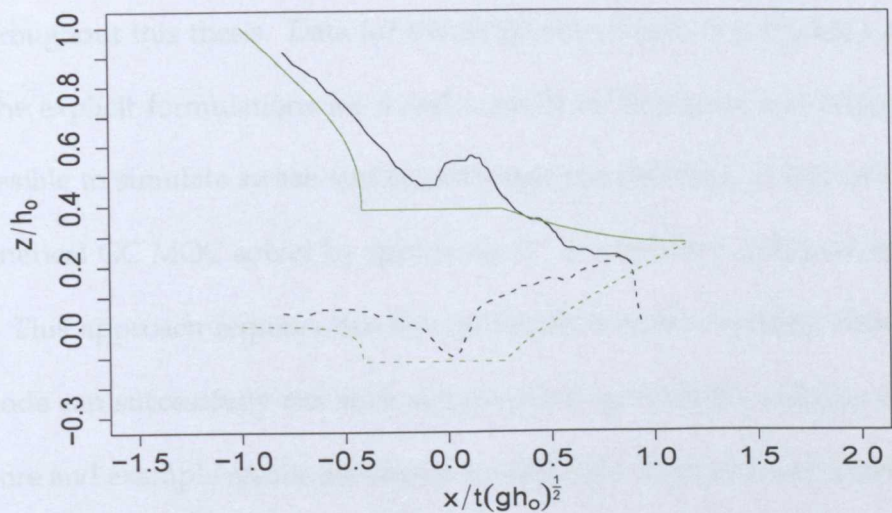


Figure 6.12: Comparison of the theoretical solution with $\sigma = 0.2$ (green lines) and measured (black lines) profiles for the Louvaine experiment reported in Fraccarollo and Capart (2002) at $t = 0.75\text{s}$.

Uncoupled swash simulations

In this chapter results for swash simulations corresponding to SM63 type initial conditions and for swash driven by a uniform bore of the same initial specification as that detailed in HP79 are presented. For these simulations the bed is assumed to be fixed so that the beach profile is only updated at the end of the swash event; i.e. morphodynamical time stepping is adopted. Such an approach is referred to as being uncoupled throughout this thesis. Data for the SM63 simulations are obtained analytically using the explicit formulations for h and u given by Peregrine and Williams (2001). It is possible to simulate swash similar, although not identical, to that of HP79 using the numerical GC MOC solver by specifying R^+ as explained in Guard and Baldock (2007). This approach requires that the backwash bore be explicitly fitted. The GC MOC code can successfully run such swash events up until the collapse of the backwash bore and example results are shown in Appendix D. A problem arises, however, when the backwash bore collapses as the logic of the code dictates the initiation of another dam-break event at this point. Logistically, the GC MOC code becomes prohibitively complex. Consequently, data for the HP79 swash simulations are obtained using the MacCormack–mLxF hybrid shock capturing code described in §5.1.5. The

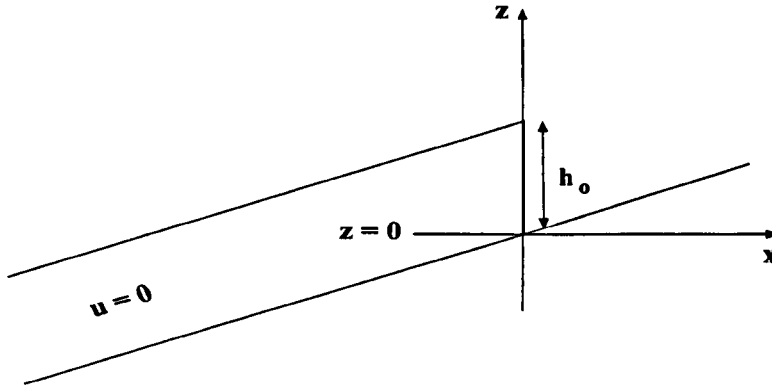


Figure 7.1: Initial conditions for SM63 swash

hybrid solver based around the $q = Au^3$ transport formulation was chosen as it has undergone more rigorous validation than the solver developed for the $q = \bar{A}u^3h$ formulation. For the HP79 simulations, in order to decouple the hydro- and morphodynamics, a value of $A = 1 \times 10^{-10} \text{s}^2 \text{m}^{-1}$ is used and bed porosity is set to zero. To obtain the numerical results the shoreline boundary algorithm developed in §4.3.2 is employed without any modification.

7.1 SM63 swash

7.1.1 Analytical solution for both flux formulations

Pritchard and Hogg (2005) give analytical solutions for net sediment flux in the swash zone based on hydrodynamical information provided by the SM63 solution. In their paper Pritchard and Hogg (2005) develop several total load models based on differing formulations of q including $q = \bar{A}u^3h$. No explicit solution is given for a sediment flux of the form $q = Au^3$. Moreover, as the primary focus of the paper is on the effect of sediment advection and settling lag, details of the solution for the simple transport formulae are not given. This motivates the derivations provided here.

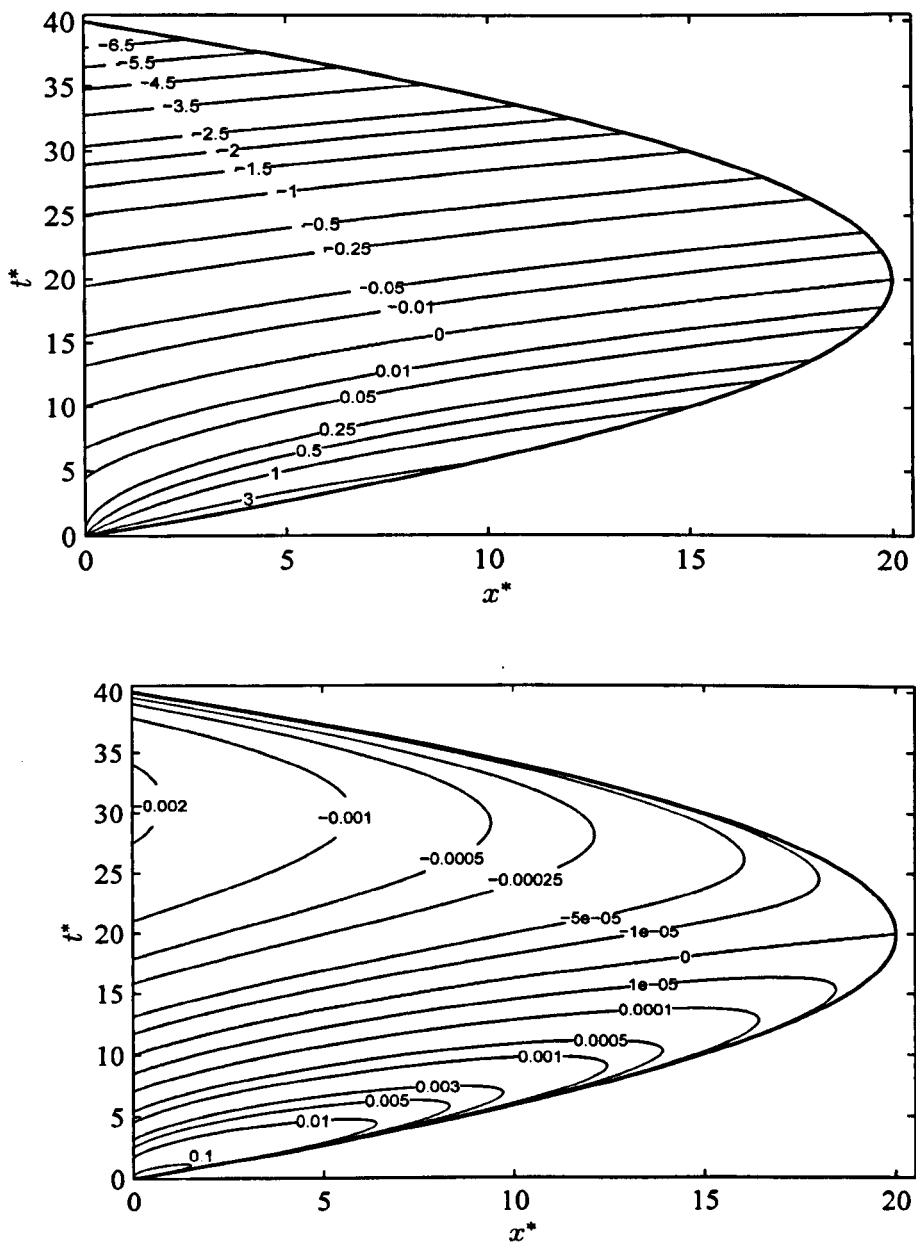


Figure 7.2: Contours of dimensionless instantaneous sediment flux (q^*) where top: $q^* = u^{*3}$. Bottom: $q^* = u^{*3} h^*$; the shoreline is bold and contours are individually labelled.

An analytical expression for the instantaneous sediment flux where $q(x, t) = Au^3(x, t)$ is obtained by substituting (2.1.6) into (3.3.1):

$$q(x, t) = \frac{8A}{27} \frac{\left((gh_o)^{\frac{1}{2}}t - gt^2 \tan \beta + x\right)^3}{t^3}. \quad (7.1.1)$$

Similarly, an analytical expression for the instantaneous sediment flux where $q(x, t) = \bar{A}u^3(x, t)h(x, t)$ is obtained by substituting (2.1.6) and (2.1.4) into (3.3.6):

$$q(x, t) = \frac{2\bar{A}\{-2x - gt^2 \tan \beta + 4(gh_o)^{\frac{1}{2}}t\}(x - gt^2 \tan \beta + (gh_o)^{\frac{1}{2}}t)^3}{243gt^5}. \quad (7.1.2)$$

Figure 7.2 shows contours of instantaneous sediment fluxes according to (7.1.1) and (7.1.2); all variables have been non-dimensionalised using (6.3.13). As the principal focus of this work is on the coupled modelling of beachface evolution, data is only presented here for the representative values of σ and $\bar{\sigma}$ computed in §6.3.3.

7.1.2 Uncoupled beachface evolution for SM63 swash

Following Pritchard and Hogg (2005), respective net fluxes Q over a swash event for each transport formula are given by:

$$Q(x) = \int_{t_i(x)}^{t_d(x)} q(u)dt = A \int_{t_i(x)}^{t_d(x)} u^3 dt, \quad (7.1.3)$$

or:

$$Q(x) = \int_{t_i(x)}^{t_d(x)} q(u, h)dt = \bar{A} \int_{t_i(x)}^{t_d(x)} u^3 h dt, \quad (7.1.4)$$

where $t_i(x)$ is the time of inundation and $t_d(x)$ the time of denudation. Expressions for the inundation and denudation times at a specific cross-shore location x can be obtained by setting (2.1.4) equal to zero and solving the resulting quadratic giving:

$$t_i = \frac{4(gh_o)^{\frac{1}{2}} - (16h_o g - 8gx \tan \beta)^{\frac{1}{2}}}{2g \tan \beta} \quad (7.1.5)$$

and:

$$t_d = \frac{4(gh_o)^{\frac{1}{2}} + (16h_o g - 8gx \tan \beta)^{\frac{1}{2}}}{2g \tan \beta}. \quad (7.1.6)$$

The net fluxes over one swash cycle according to each sediment transport formula can thus be computed analytically by integrating up (7.1.3) and (7.1.4); results so obtained are shown in Figure 7.3. In order to compute the change in bed level at each cross-shore point it is necessary to integrate (3.3.5) with respect to time yielding:

$$-\left[B\right]_{t_i(x)}^{t_d(x)} = \zeta \int_{t_i(x)}^{t_d(x)} \frac{\partial q}{\partial x} dt. \quad (7.1.7)$$

Applying Leibniz's rule to the RHS of (7.1.7):

$$\int_{t_i(x)}^{t_d(x)} \frac{\partial q}{\partial x} dt = \frac{\partial}{\partial x} \int_{t_i(x)}^{t_d(x)} q(x, t) dt + q(x, t_i) \frac{\partial t_i(x)}{\partial x} - q(x, t_d) \frac{\partial t_d(x)}{\partial x}. \quad (7.1.8)$$

Hence:

$$\left[B\right]_{t_i(x)}^{t_d(x)} = -\zeta \left\{ \frac{\partial Q}{\partial x} + q(x, t_i) \frac{\partial t_i(x)}{\partial x} - q(x, t_d) \frac{\partial t_d(x)}{\partial x} \right\}. \quad (7.1.9)$$

Thus, as well as being dependent on Q , the change in bed level at each cross-shore location is also dependent on two additional terms. For the cases considered throughout the duration of this research the contribution due to these additional terms, i.e.:

$$q(x, t_i) \frac{\partial t_i(x)}{\partial x} - q(x, t_d) \frac{\partial t_d(x)}{\partial x}, \quad (7.1.10)$$

was found to be at least an order of magnitude less than the $\frac{\partial Q}{\partial x}$ term. Indeed, $\frac{\partial t_i(x)}{\partial x} \equiv u_*^{-1}$ and $\frac{\partial t_d(x)}{\partial x} \equiv u_*^{-1}$ and $qu_*^{-1} \equiv B_*$. Thus, for flow in which the tip motion is symmetrical, like fixed bed SM63 and HP79 flow (until the formation of a backwash bore), (7.1.10) should be zero.

Figures 7.4 and 7.5 illustrate the final beach profile as predicted using the uncoupled analytical model for each q formulation; results have been non-dimensionalised using the scaling given in Chapter 3. It can be seen that the beach is eroded everywhere;

this is a direct consequence of the velocity asymmetry over the swash cycle caused by the backwash being of a longer duration than the run-up. The principal effect of setting $q = q(u, h)$ is to reduce the impact the swash has on morphology further up the beach due to the very low water depths experienced there. Pritchard and Hogg (2005) have shown that when using a sediment flux which is an increasing function of $|u|$ and driven by SM63 hydrodynamics, offshore transport will always result. However, it is interesting to note that for the case of the HP79 incident bore not all the net transport is offshore. It will also be shown in Chapter 8 that net offshore transport is not the rule for both SM63 and HP79 swash when the hydro- and morphodynamics are directly coupled.

7.2 HP79 swash

The simplest physically realisable bore is the so-called "uniform bore" for which height and velocity everywhere behind the bore front remain constant (Miller, 1968). It was the relative ease of providing boundary conditions for such a bore that motivated the choice of an initially uniform bore for detailed study by HP79. A definition sketch of the variables used in this section for a uniform bore approaching a plane sloping beach is given by Figure 7.6. Bores in the nearshore are usually subcritical, supercritical bores are uncommon on real beaches (Packwood, 1980), with $u < c$ behind the bore front. For the uniform bore case applying the bore relations with $h_i = 1$ for a supercritical bore gives:

$$h_B \left\{ \frac{1}{2} (1 + h_B) (2 + h_B) \right\}^{\frac{1}{2}} > (1 + h_B)^{\frac{3}{2}}, \quad (7.2.1)$$

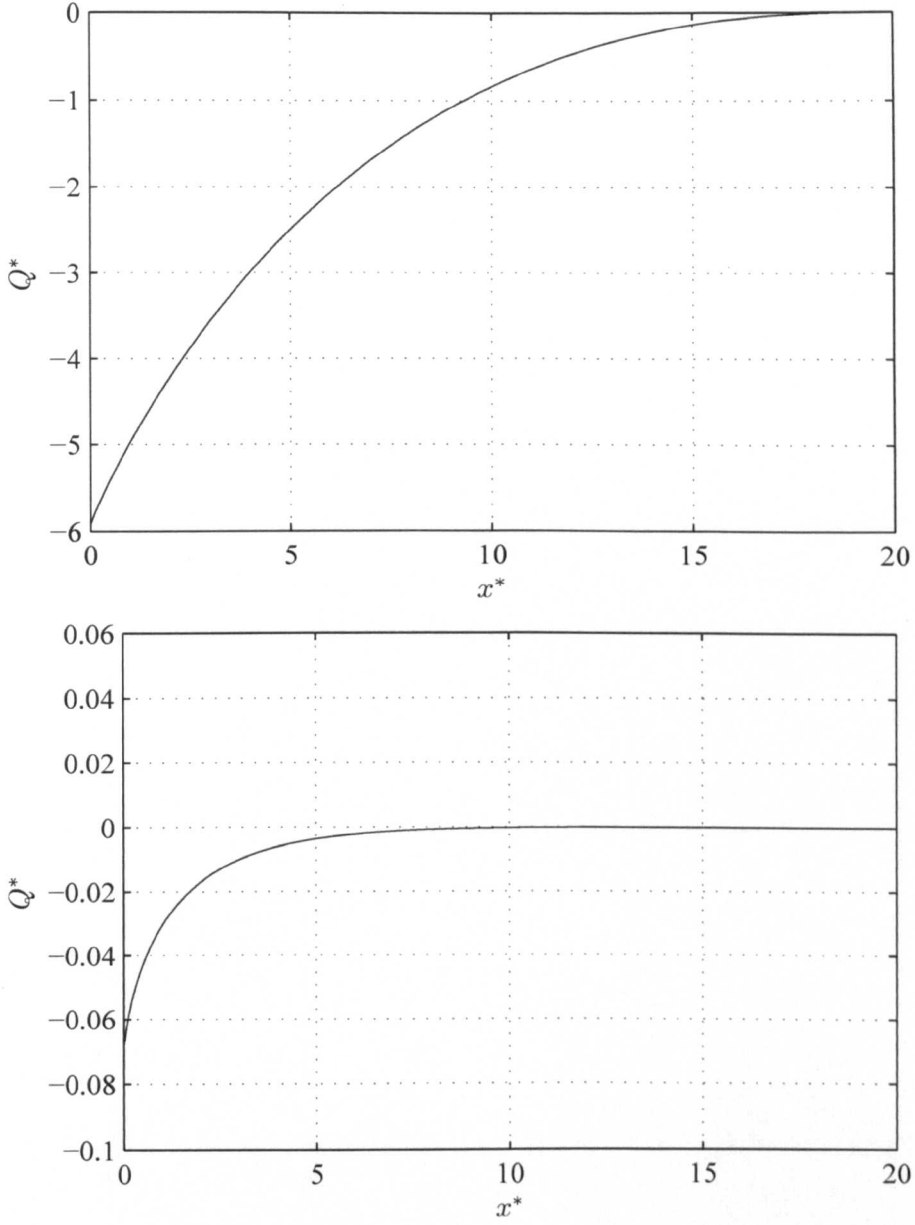


Figure 7.3: Top: Dimensionless net sediment flux (Q^*) after one SM63 swash cycle for uncoupled transport model using $Q^* = \int_{t_i(x^*)}^{t_d(x^*)} u^{*3} dt^*$. Bottom: dimensionless net sediment flux (Q^*) after one SM63 swash cycle for uncoupled transport model using $Q^* = \int_{t_i(x^*)}^{t_d(x^*)} u^{*3} h dt^*$.

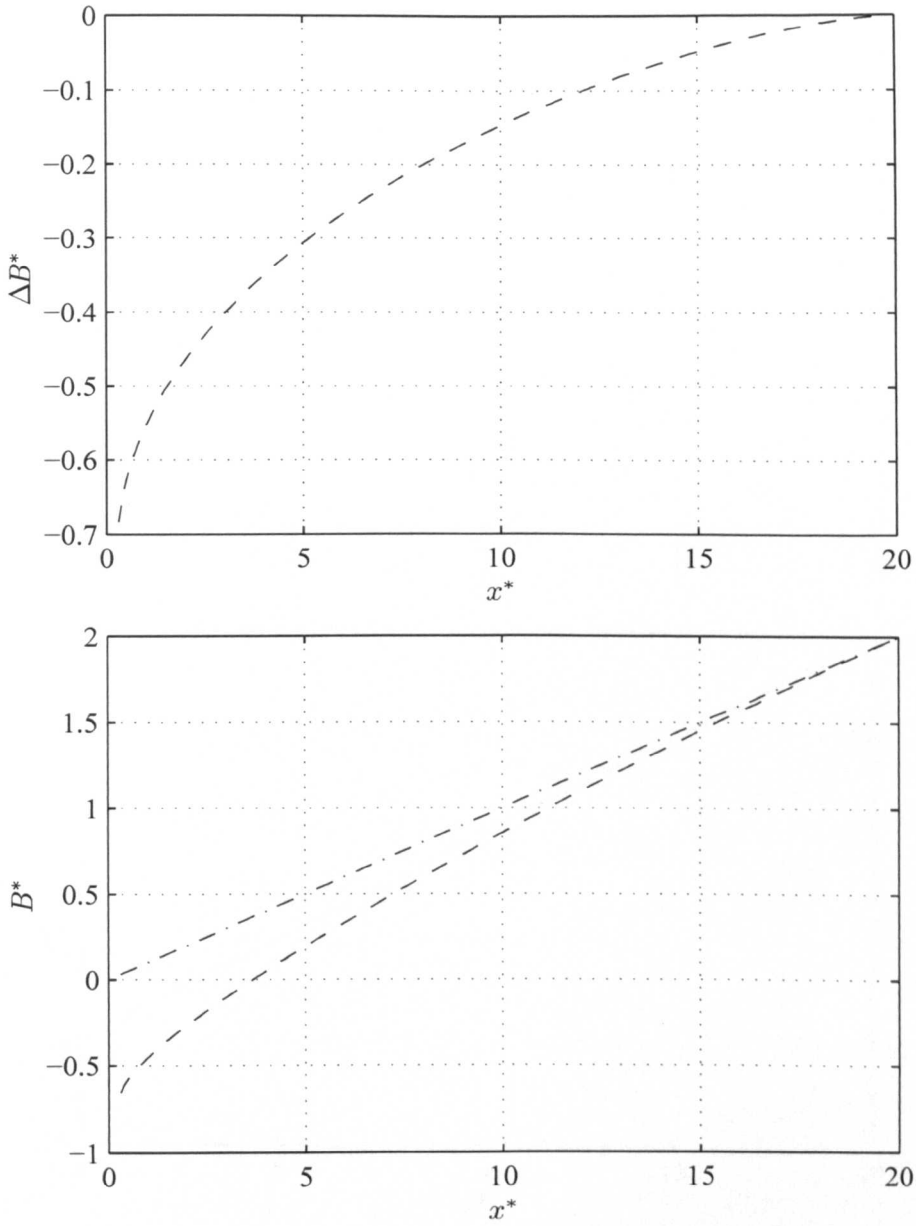


Figure 7.4: Top: Dimensionless change in bed level relative to the initially plane beach after one swash cycle with $q^* = u^{*3}$ using $\Delta B^* = -\sigma \frac{\partial Q^*}{\partial x^*}$ with $\sigma = 0.0654$. Bottom: Final beach profile for the same event. The initial (plane) beach profile is shown by a dot-dashed line.

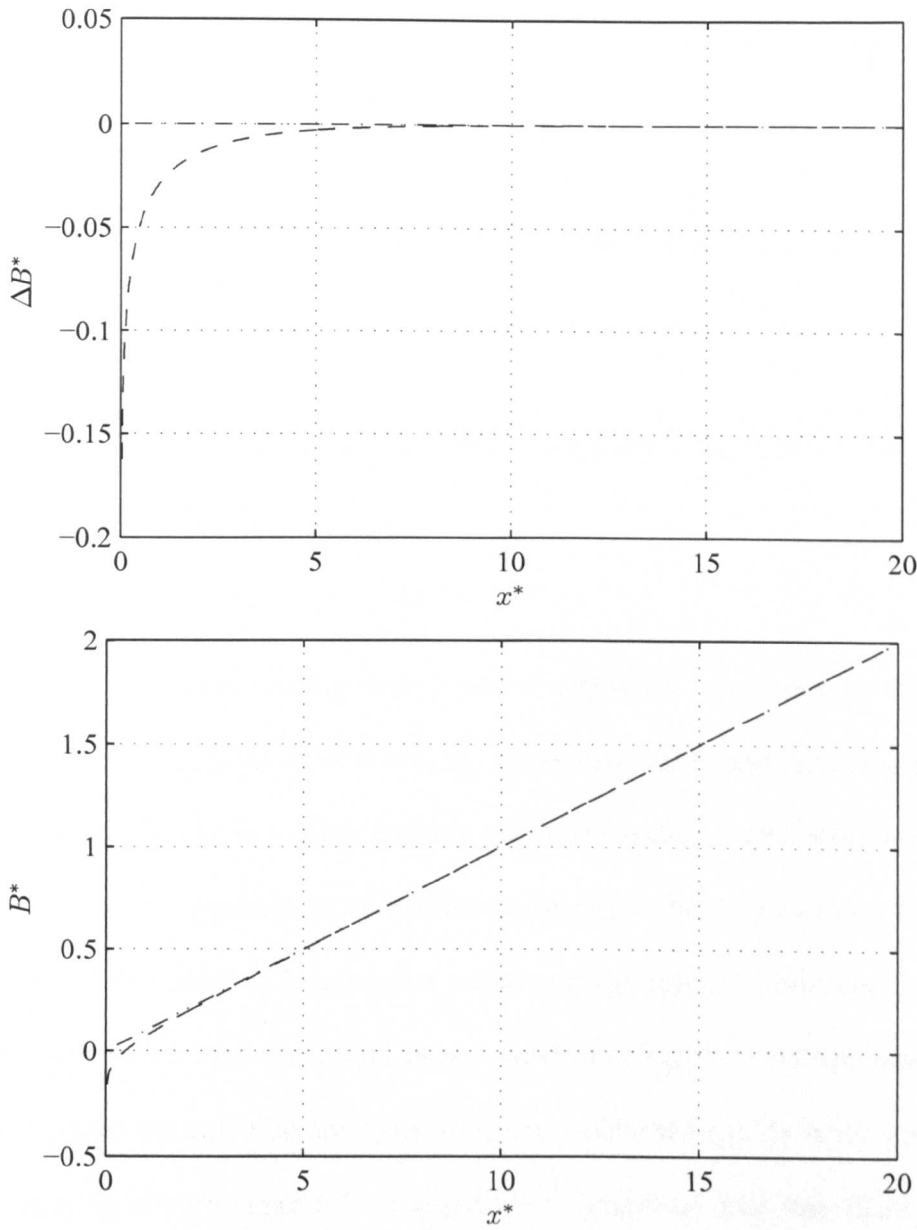


Figure 7.5: Top: Dimensionless change in bed level relative to the initially plane beach after one swash cycle with $q^* = u^{*3}h^*$ using $\Delta B^* = -\bar{\sigma} \frac{\partial Q^*}{\partial x^*}$ with $\bar{\sigma} = 0.15$. Bottom: Final beach profile for the same event. The initial (plane) beach profile is shown by a dot-dashed line.

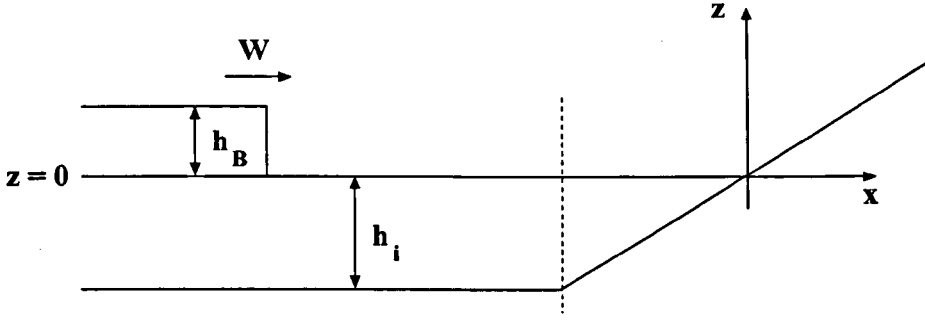


Figure 7.6: Notation and initial bathymetry for a uniform bore approaching a plane sloping beach.

up to the beach toe. Equation (7.2.1) is a cubic inequality in h_B that has only one real positive root (Hibberd, 1977):

$$h_B = 2.215. \quad (7.2.2)$$

Thus, a supercritical bore surfing over water of depth 1m must have $h_B > 2.215\text{m}$; all bores with $h_B \leq 2.215\text{m}$ are subcritical. Following HP79 and referring to Figure 7.6, a bore of amplitude $h_B = 0.6\text{m}$ moving into undisturbed water with $h_i = 1.0\text{m}$ is considered. This corresponds to an initial bore strength, defined as $(h_B + h_i)h_i^{-1}$, of 1.6. The toe of the beach is located at $x=-10\text{m}$ and the original shoreline position is at $x=0\text{m}$. For the test case illustrated here a mesh spacing of $\Delta x=0.01\text{m}$ was used as convergence tests indicate that any gain in accuracy obtained by any further reduction in mesh spacing is very small (cf. Appendix D). The time step was fixed at $\Delta t = \frac{1}{3}(gh_o)^{-\frac{1}{2}}\Delta x$. A problem associated with using a fixed time step is the possibility of exceeding the Courant number. Consequently, a check is made within the code that ensures the CFL condition is not violated.

7.2.1 Flow variables and instantaneous sediment fluxes

Figure 7.7 shows contours of non-dimensional water height and velocity in the physical plane for swash driven by a uniform bore. With the beach slope scaled out, the results are found to be in excellent qualitative agreement with those presented in HP79; a quantitative comparison is not possible as the HP79 data is no longer in existence (personal communication, S. Hibberd, 2006). Importantly, the shoreline trajectory is in excellent agreement with that shown in Figure 8 of HP79, confirming the robustness of the present algorithm. Contours of dimensionless instantaneous sediment fluxes with $q^* = u^{*3}$ and $q^* = u^{*3}h^*$ for this swash event are shown in Figure 7.8. While the discontinuity in $q^* = u^{*3}$ flux is relatively pronounced across the backwash bore, the discontinuity in the $q^* = u^{*3}h^*$ flux is much less severe. The primary differences between these instantaneous fluxes and those of SM63 swash are related to the time of flow reversal and the flow depth. The implications of these differences for beach face evolution are now examined.

7.2.2 Uncoupled beachface evolution for HP79 swash

Water motion for the swash event forced by a uniform bore on a fixed beach has been described in detail by HP79. Here the change in beach profile, as predicted using the uncoupled approach, is considered for this type of swash event. The primary hydrodynamical differences between HP79 and SM63 swash are that HP79 swash is deeper, leads to the formation of a backwash bore and involves the net influx of water thus establishing a new shoreline position. The influx of water and backwash bore have important implications for uncoupled beachface evolution. The deeper water at the seaward side of the backwash is relatively slow moving. The effect of this deeper wa-

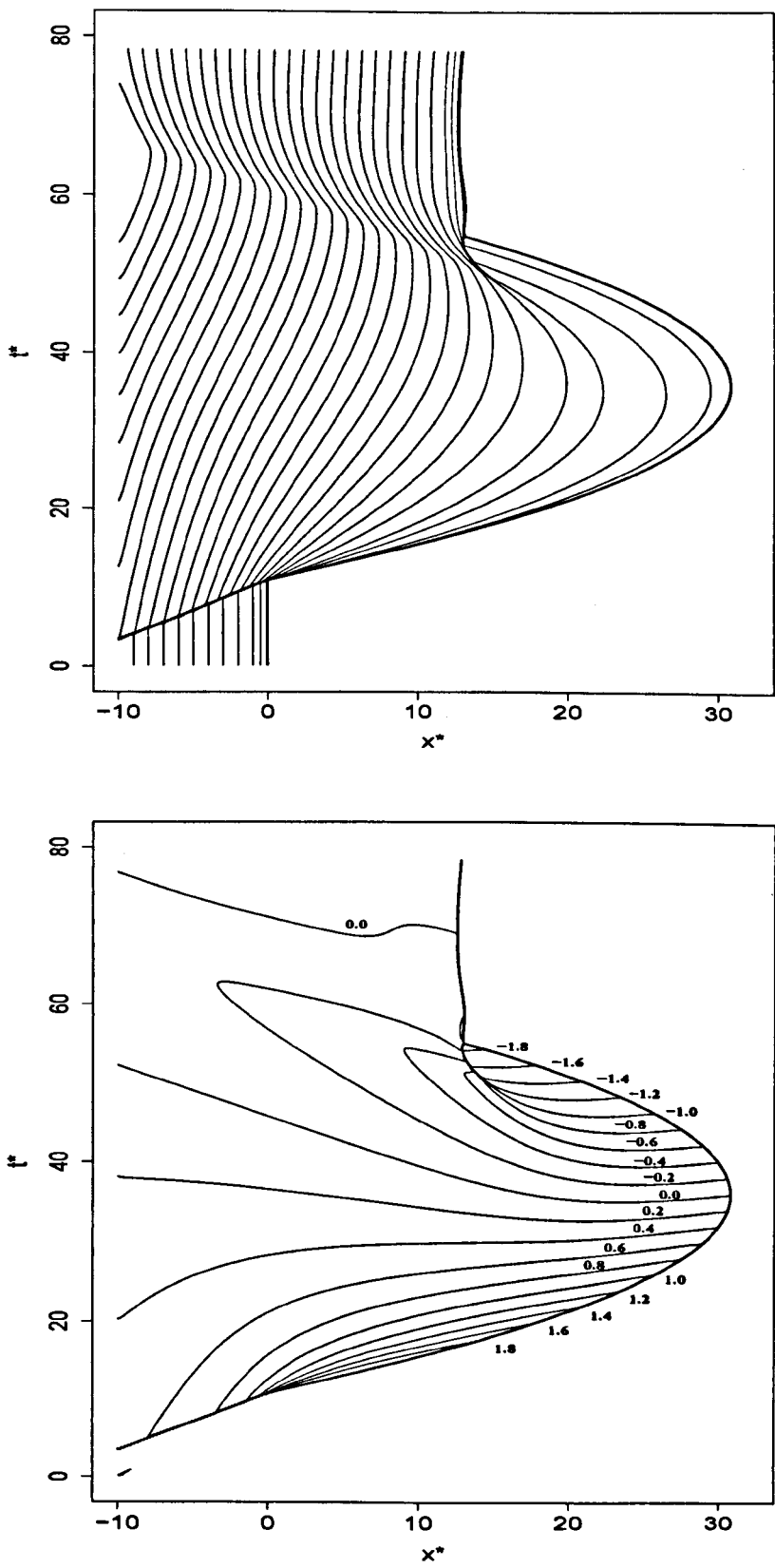


Figure 7.7: Top: contours of dimensionless water height $h^* = 0.1$ to 2.4 at intervals of 0.1 . Bottom: contours of dimensionless water velocity $u^* = -1.8$ to 1.8 .

ter is to retard the velocity of shallower water, further onshore, leading to the formation of a backwash bore. Thus, the backwash bore rapidly brings the shoreline motion to an effective standstill, it then collapses propagating energy offshore as a rarefaction wave, after which the body of water performs small oscillations on the beach eventually coming to rest. A new shoreline position, landward of the original shoreline, is established. The net influx of water onto the beach brings with it a net influx of sediment leading to a positive net sediment flux in the newly created subaqueous region between the original and new shoreline positions. This occurs for both sediment flux formulations. For sediment flux of the type $q = q(u)$, landwards of the new shoreline position the net sediment flux is everywhere negative, cf. Figure 7.10. This is in agreement with the findings for SM63 swash and occurs for the same reason; the larger values of sediment flux found in the run-up are more than offset by the amount of sediment transported in the longer duration backwash. However, seawards of the point of formation of the backwash bore the flow regime is very different. Here flow reversal occurs much later in the swash cycle than for the SM63 case. Moreover, when flow reversal does occur the negative velocities are relatively small and the water rapidly comes to rest. As a consequence of this there is a large velocity asymmetry between run-up and backwash in this region coupled with much deeper water than for SM63 swash. A comparison between the SM63 and HP79 instantaneous fluxes at fixed cross-shore locations equating to 30, 40, 60, and 80% of the run-up of each swash type is shown in Figure 7.9. The figure highlights the similarity of the fluxes for both swash types higher up the beach and the very different nature of the fluxes further seawards. This velocity skewness accounts for the positive net sediment flux in the newly created subaqueous region observed for both sediment flux formulations. As the change in bed level is effectively

given by:

$$\Delta B^* = -\frac{\partial Q^*}{\partial x^*}, \quad (7.2.3)$$

because σ and $\bar{\sigma} > 0$, it follows that wherever $\frac{\partial Q^*}{\partial x^*} < 0$ and $Q^* > 0$ a net deposition of sediment will occur. From Figure 7.10 the uncoupled model thus predicts net onshore transport for the entire newly created subaqueous region. As the new shoreline location is approached from the landward side the amount of offshore transport increases between the point of maximum run-up until just before the new shoreline at which point it begins to decrease. Note also that this model predicts a discontinuity in the final beach profile at the new shoreline position that connects the regions of net onshore and offshore transport. A similar "swash ridge" is also present in the final beach profile predicted by the fully coupled model with this sediment transport formula (see Chapter 8). For the $q = q(u, h)$ sediment flux Figure 7.11 illustrates that in the new subaqueous region the net flux is positive. Moreover, everywhere in this region $\frac{\partial Q^*}{\partial x^*} < 0$ and $Q^* > 0$ thus net accretion will again occur here. The close-up in Figure 7.11 shows that the net sediment flux landwards of the new shoreline is qualitatively similar to that governed by $q^* = u^{*3}$. The primary qualitative difference is that $\frac{\partial Q^*}{\partial x^*}$ remains < 0 slightly further up the beach than when $q^* = u^{*3}$. As for the SM63 swash, the magnitude of Q^* is greatly reduced in this region due to the shallow water depths found there. Importantly, no discontinuity is observable in the net sediment flux for this transport formulation.

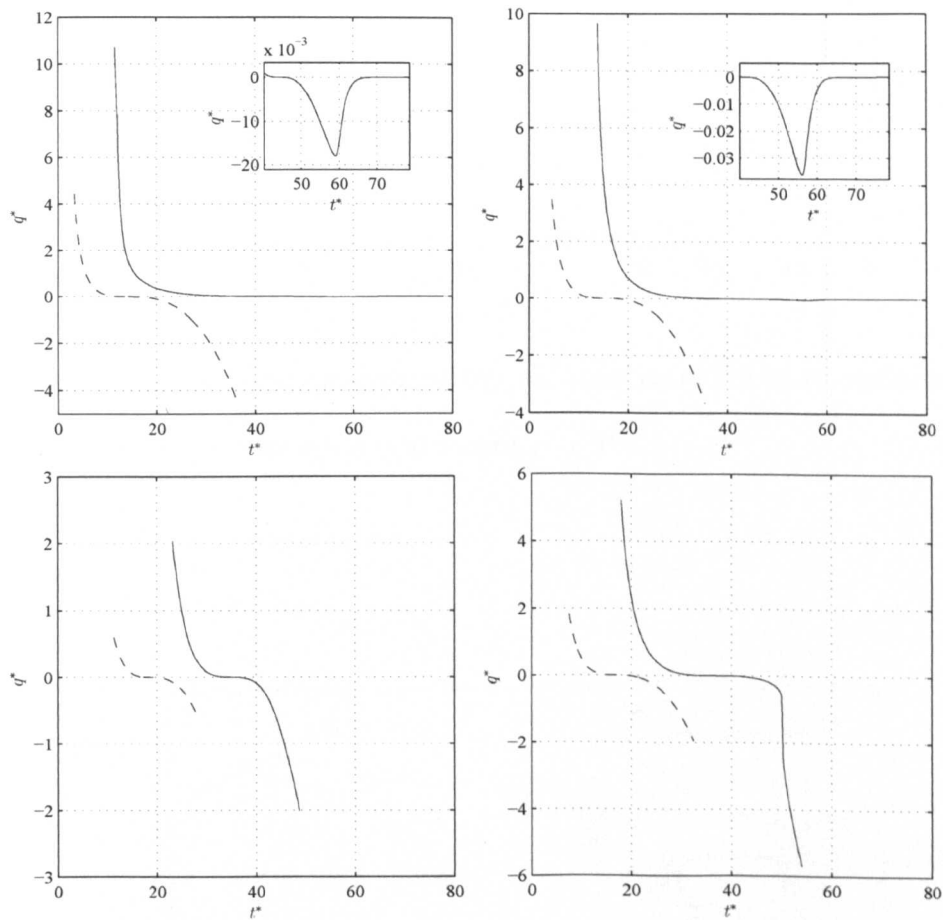


Figure 7.9: Dimensionless instantaneous sediment fluxes, $q^* = u^{*3}$, for SM63 (dashed line) and HP79 (solid line) swash at, clockwise from top, 30%, 40%, 60% and 80% of the respective maximum run-up distances.

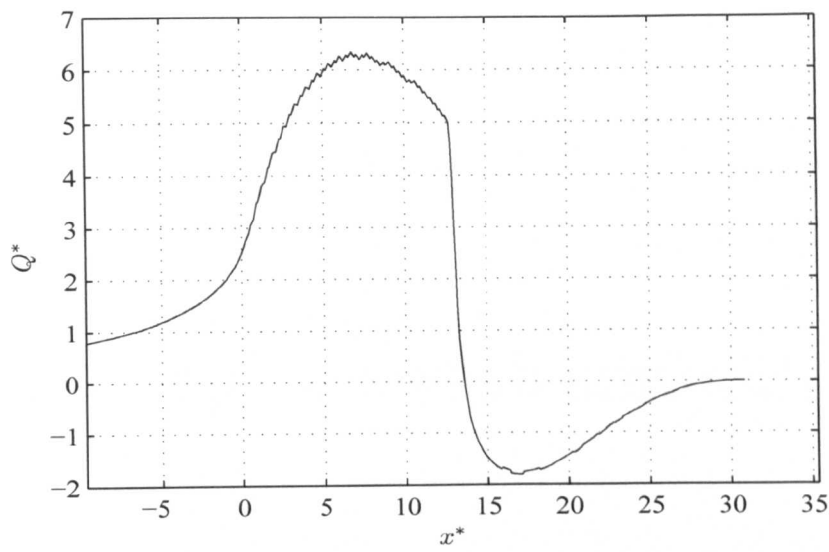


Figure 7.10: Dimensionless net sediment flux (Q^*) after one HP79 swash cycle for the uncoupled transport model using $q^* = u^{*3}$.

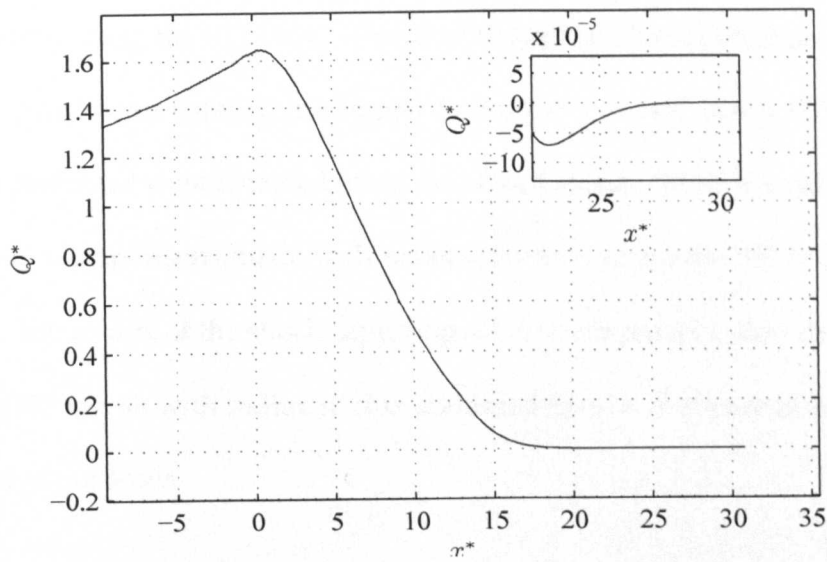


Figure 7.11: Dimensionless net sediment flux (Q^*) after one HP79 swash cycle for the uncoupled transport model using $q^* = u^{*3} h^*$.

Fully coupled swash simulations

In this chapter results for some representative swash simulations obtained using the fully coupled approach are presented. As the shallow water and Exner equations are solved simultaneously the evolution of the beach face has a direct and immediate impact on the hydrodynamics. Simulations of both SM63 and HP79 swash are run using the $q = Au^3$ sediment transport formula. For the $q = Au^3$ based SM63 simulations all data are obtained using the STI MOC scheme with explicit shock detection and fitting based on the procedures detailed in Chapter 5. For the $q = Au^3$ based HP79 simulations all data presented were obtained using the MacCormack-mLxF hybrid shock capturing scheme. Comparisons made with results obtained using the STI MOC scheme illustrate that the results of the shock capturing scheme are reliable. Results from simulations of HP79 swash with sediment flux governed by $q = \bar{A}u^3h$ are also presented for comparative purposes.

8.1 SM63 swash with $q = Au^3$

8.1.1 Model set-up

The initial bathymetry comprises a plane sloping beach whose slope $\tan\beta = 0.1$ (1:10). Using the hydrodynamical initial conditions (4.4.1) that, for a fixed bed, provide the SM63 flow field (see Peregrine and Williams (2001)) swash events are presented for three values of the bed evolution parameter σ . For all of the test cases illustrated here $h_o=1\text{m}$, and all calculations are run until the water has retreated back past the initial shoreline position set at $x=0$. The model uses a mesh spacing of $\Delta x=0.01\text{m}$ as convergence tests indicate that any gain in accuracy obtained by any further reduction in mesh spacing is very small indeed (cf. Appendix D); the time step is fixed at $\Delta t = \frac{1}{3}(gh_o)^{-\frac{1}{2}}\Delta x$. A problem associated with using a fixed time step is the possibility of exceeding the Courant number. Consequently, a check is made within the code that ensures the CFL condition is not violated.

8.1.2 Flow structure

Figures 8.1–8.3 show contours of h , u and B for a mobile beach for three distinct values of the bed evolution parameter σ . It is noted that the qualitative behaviour of all dependent variables is the same irrespective of the value assigned to σ . At the moment of dam/bore collapse there is an instantaneous acceleration of water and a sediment bore forms immediately at the shoreline. After this initial acceleration the flow is dominated by gravity and the consequent decrease in water velocity over time causes the sediment bore progressively to reduce in height as the swash climbs the beach. When flow at the tip finally reverses, although the sediment bore now vanishes to zero height

it leaves behind a berm formed over approximately the upper third of the beach.

Further back, within the main body of the flow, two gradient discontinuities form in all dependent variables at the instant of dam/bore collapse, these correspond to those marking the beginning and end of the constant state region for the mobile bed dam-break over an initially flat bed governed by (3.2.8), (3.2.18) and (3.3.5); see Chapter 6 for a detailed analysis of the flat bed problem. The first of these gradient discontinuities forms, and continues to move, seaward of the initial shoreline location and is therefore outside our domain of interest. The second gradient discontinuity forms landwards of the initial shoreline position and climbs the beach propagating along a characteristic until it, and the flow local to it, reverses. Once the flow has reversed a compression wave begins to build up on the downstream side of the gradient discontinuity and, as also occurs in analogous gas dynamical problems (Moretti and DiPiano, 1983), this very soon develops into a shock wave. The characteristic grid shown in Figure 8.5 illustrates this. It can be seen that the gradient discontinuity initially moves as a characteristic (the limit of a weak shock) and later grows into a fully developed shock. Here, the shock takes the form of a relatively slow-moving seaward facing bed step (i.e. it forms due to the coalescence of C_b characteristics). This moving bed step appears to be akin to the sediment bores found in steady alluvial flows (Needham and Hey, 1991). The water arriving from the landward side of the slowly retreating bed step meets it almost as though it were unmoving and, similar to flow over a fixed bed step, forms a hydraulic jump over it. The strength of the shock, defined as $B_H B_L^{-1}$, is relatively weak ($B_H B_L^{-1} < 1.1$ for $\sigma = 0.0654$); thus, the change in slope of the two hydrodynamic characteristics as they cross the shock path is barely noticeable in Figure 8.5.

If the wave structure is further examined using Figure 8.5 differences with the fixed bed structure immediately become apparent. The first difference relating to the fixed

bed case is that the wave speed of the incoming characteristics remains positive and these characteristics terminate at the shoreline; in fact, only the C_b characteristic slope changes sign. At the shoreline itself the governing equations do not degenerate from hyperbolic to parabolic as in the fixed bed case, i.e. three distinct eigenvalues remain. The analysis of §3.5 reveals that the tip follows the trajectory of a C_b characteristic.

8.1.3 Beachface evolution

Figure 8.6 shows the position of the shoreline in the physical plane for a mobile bed swash event with $\sigma = 0.0654$. The limiting effect of bed mobility on run-up is fairly severe with the maximum run-up of the coupled model only around 70% of the uncoupled solution for this σ value. For the entire range of σ values tested in this work, increasing σ leads to a decrease in the maximum run-up distance. A lower tip velocity at the point of bore collapse is ultimately responsible for this decrease in maximum run-up; however, the flow dynamics are also more complex than in the fixed bed case. Interestingly, over a mobile bed, maximum run-up is greater than that expected from the ballistics theory prediction based on the initial tip velocity; this is discussed further in §8.1.5.

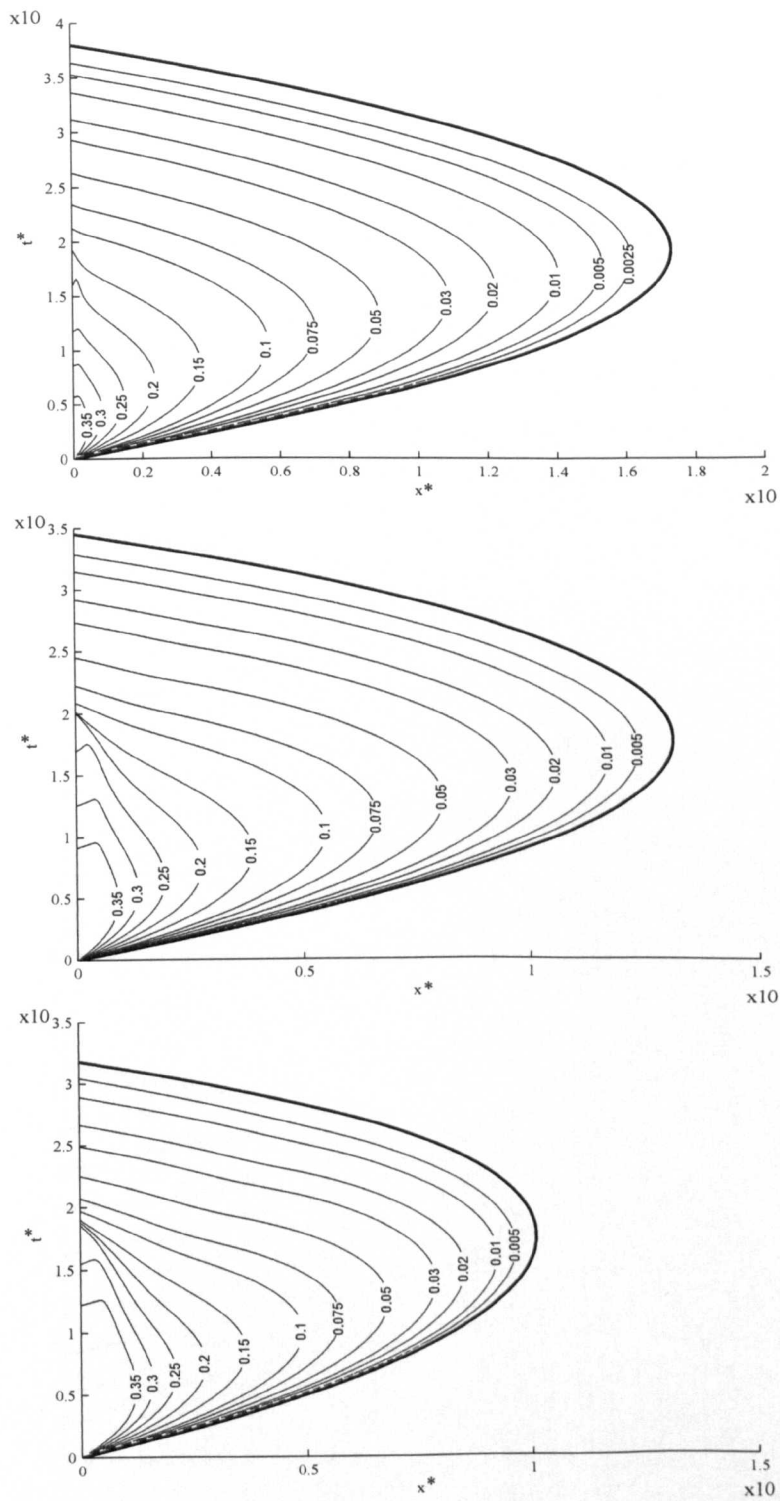


Figure 8.1: Space–time plot showing showing contours of dimensionless water depth (h^*) for SM63 type swash with $\sigma = 0.01$ top, $\sigma = 0.0654$ middle and $\sigma = 0.2$ bottom.

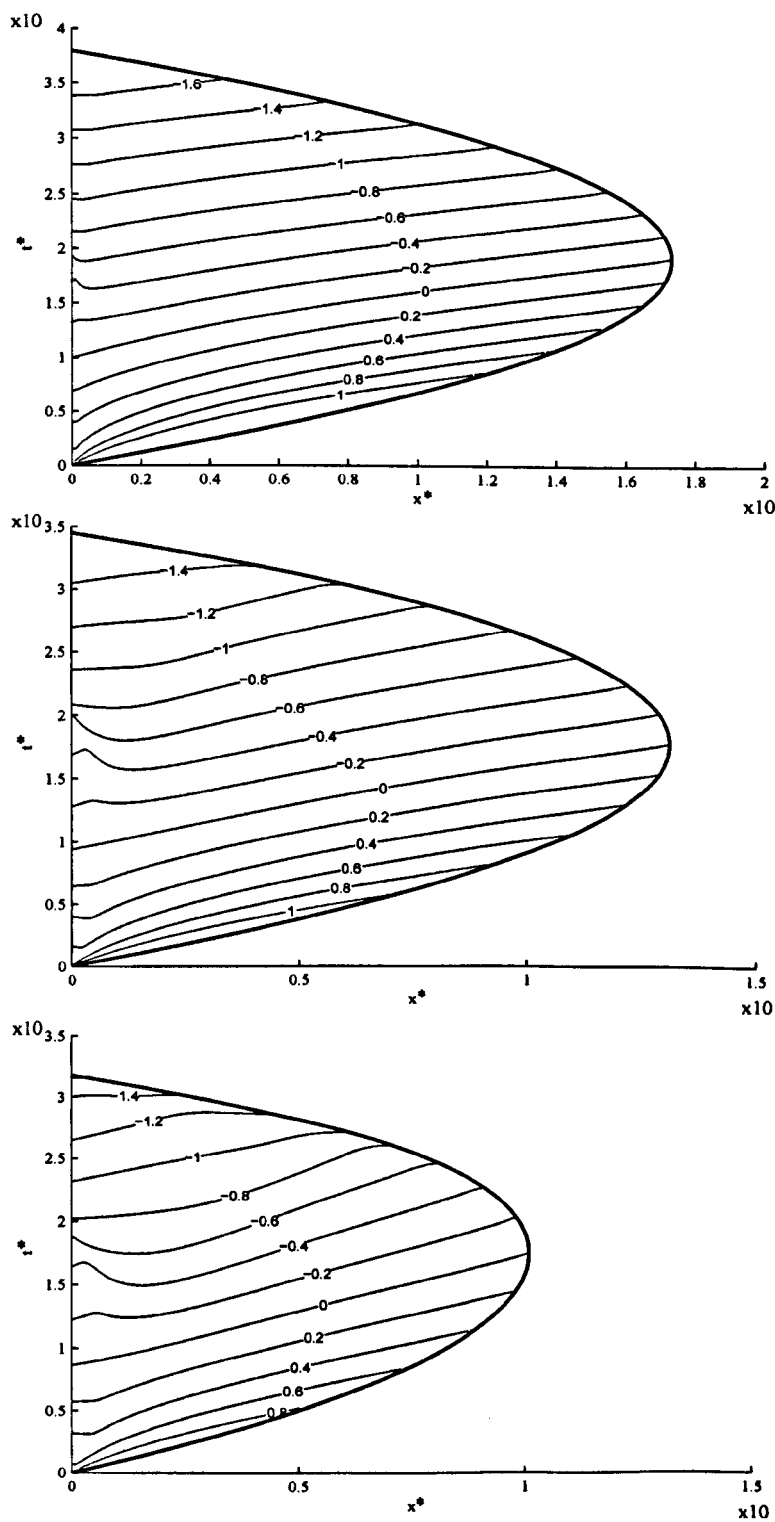


Figure 8.2: Space–time plot showing showing contours of dimensionless water velocity (u^*) for SM63 type swash with $\sigma = 0.01$ top, $\sigma = 0.0654$ middle and $\sigma = 0.2$ bottom.

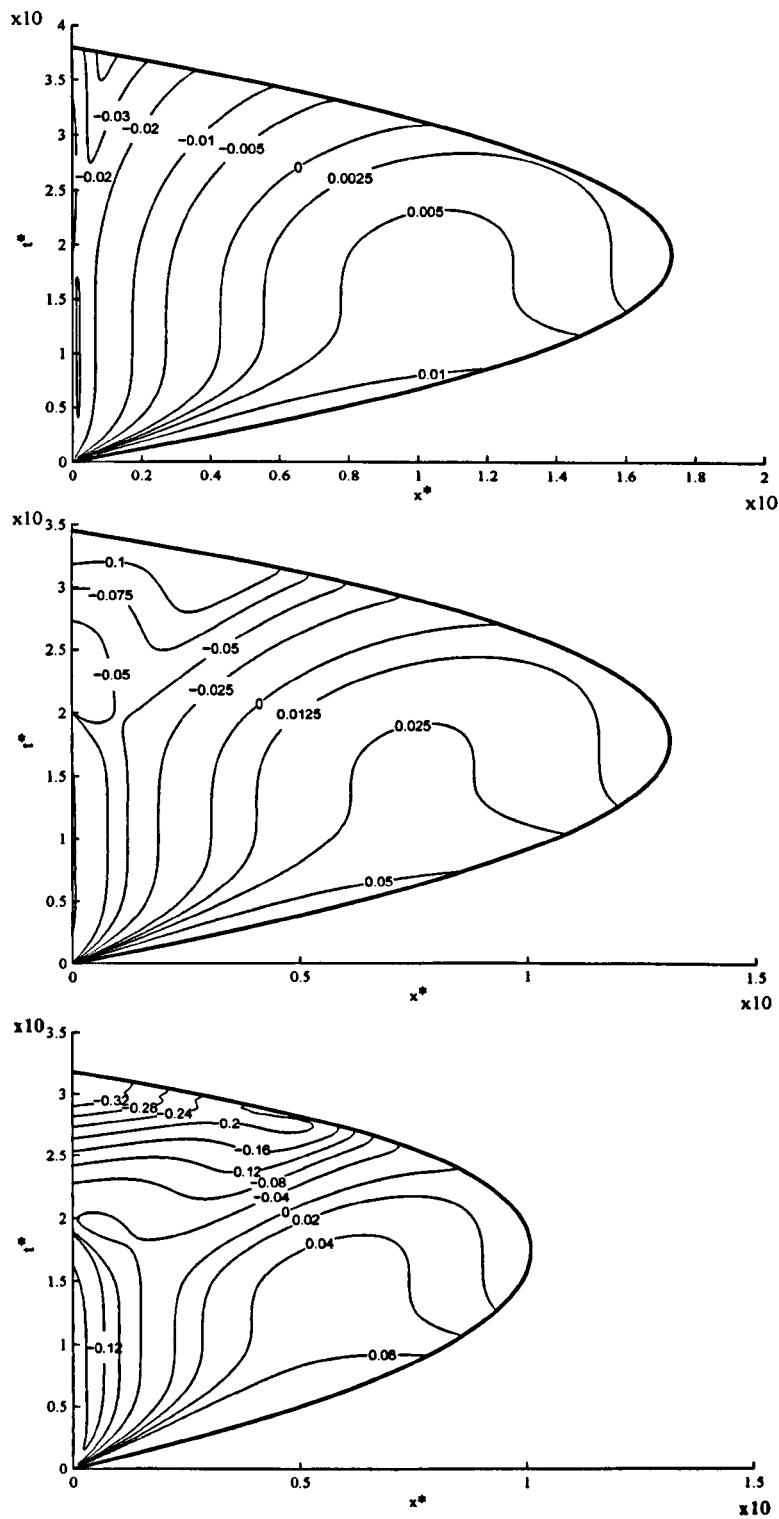


Figure 8.3: Space-time plot showing showing contours of dimensionless change in beach level (ΔB^*) for SM63 type swash with $\sigma = 0.01$ top, $\sigma = 0.0654$ middle and $\sigma = 0.2$ bottom.

The sediment bore at the tip is an extremely effective transporter of sediment as it causes a (progressively decreasing) jump in bed height at each cross-shore location it passes up until flow reversal at the tip. For the mobile beach case when flow reverses at the tip, initially it does not accelerate as quickly as it would on a fixed beach as the stoss side of the berm reduces the local beach gradient; note that it does not reverse the local gradient – a condition that would lead to a pool of water being left at the upper limit of the swash zone. Water in the backwash strips sediment from the beach as it retreats over the berm and although backwash velocities are high the mechanism of transport at the tip is not as efficient as the sediment bore associated with the run-up. Thus, a portion of the berm remains even when the water has drained back off it. Further seaward the trough created by the dam/bore collapse is extended and deepened as sediment is removed by the high velocity backwash.

8.1.4 Relationship between final beach profile and bed evolution parameter (σ)

Figure 8.7 illustrates the final beach profile for both coupled and uncoupled beach evolution for $\sigma = 0.01, 0.0654$ and 0.2 . Numerical experiments using the fully coupled model have shown that values of σ within the range $0.01 \leq \sigma \leq 0.2$ (see §6.3.3) all lead to net onshore transport. The final volume of onshore transport per unit width (Q^+) initially increases with increasing σ up to a limit value $\sigma = \sigma_{max}$. Interestingly, once σ_{max} is exceeded the net volume of sediment transported onshore begins to decrease.

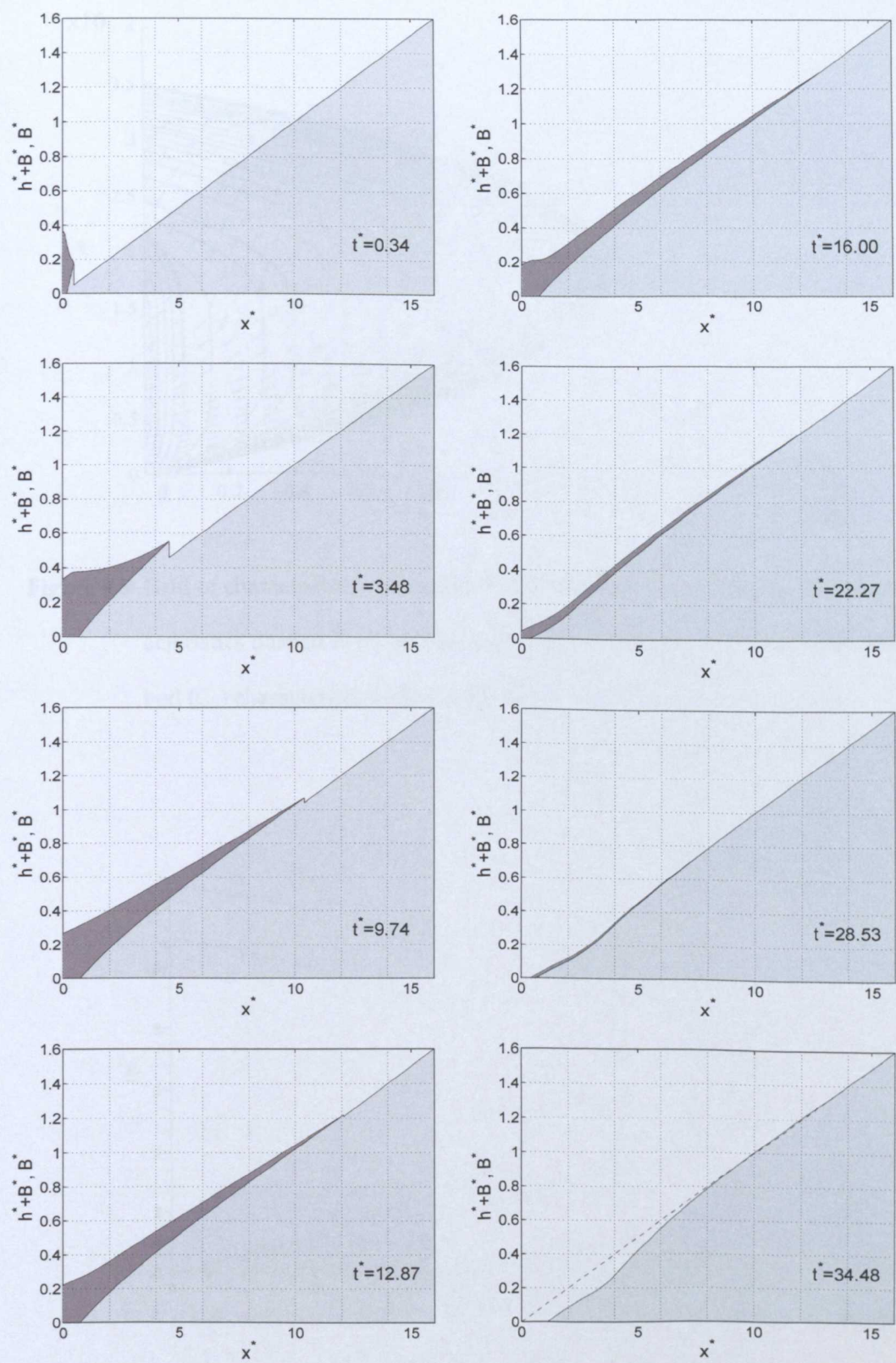


Figure 8.4: Sequence of run-up and backwash for SM63 initial conditions over a mobile beach where sediment flux is of the form $q = Au^3$ and $\sigma=0.0654$.

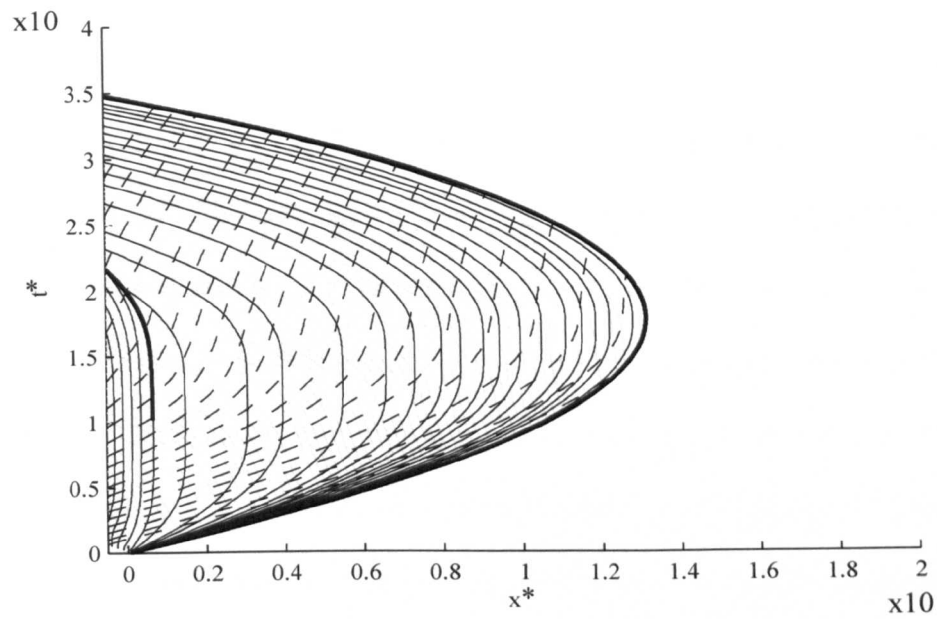


Figure 8.5: Grid of characteristics for mobile bed SM63 swash. Advancing (C^+) characteristics dashed lines, receding (C^-) characteristics grey solid lines and bed (C_b) characteristics black solid lines.

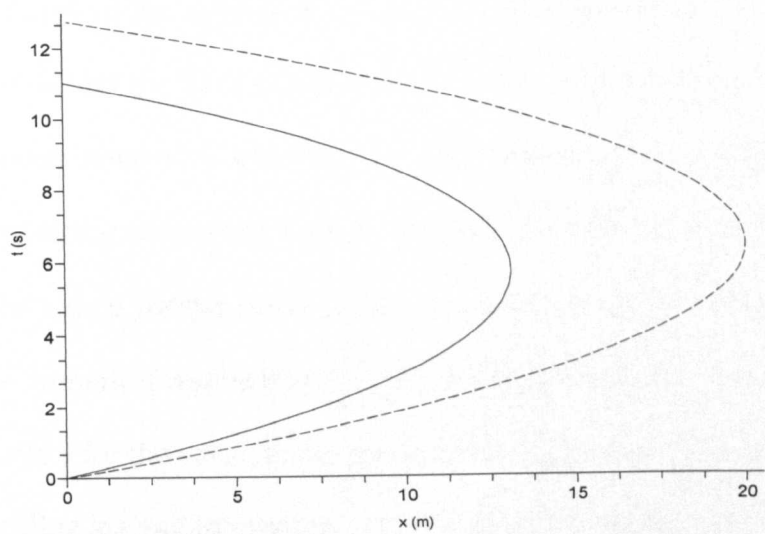


Figure 8.6: Comparison of the instantaneous shoreline position for SM63 swash on a fixed (dashed line) and mobile (solid line) beach.

The left hand panel of Figure 8.8 summarises the variation of Q^+ with σ obtained through numerical experiments. In the figure actual computed values are denoted by circles and the solid line represents values interpolated using a cubic spline procedure. From this figure σ_{max} appears to be around 0.045. Assuming a porosity of 0.4, the maximum onshore transport occurs for a sediment mobility value of $A \approx 0.003 \text{ s}^2\text{m}^{-2}$; this value for the sediment mobility parameter is consistent with those obtained from the Masselink et al. (2005) swash data for sand with a median grain size, D_{50} , in the range 0.27–0.29 mm, see §3.3.3. Interestingly, the right hand panel of Figure 8.8 shows that the amount of sediment mobilised at dam/bore collapse continues to increase with increasing σ within the range of σ values considered here. This implies that the initial tip velocity, which is directly linked to σ^1 , also plays an important rôle in determining the net amount of sediment transported onshore for a given swash event.

Within the range of σ values presented here the amount of sediment stripped off the beach seaward of the zero-crossing always increases with increasing σ . Final beach profiles and details of the regions of accretion are shown in Figure 8.9 for the typical value $\sigma = 0.0654$ and the limit values given in (6.3.20). It is worth pointing out that the use of a lower value of A , and thus σ , in the backwash, as suggested by a number of researchers (see for example Masselink and Li (2001); Masselink et al. (2005)), in the coupled model would further increase the net onshore transport. Thus, it would appear from the numerical results that feedback between hydro- and morphodynamics is enough to allow for the net onshore transport of sediment over a single swash event even when settling lag and infiltration are ignored. This is an important finding and is at odds with the uncoupled results of Pritchard and Hogg (2005) discussed in Chapter 7.

¹Initial tip velocity decreases with increasing σ , no quantitative analytical relationship has been found.

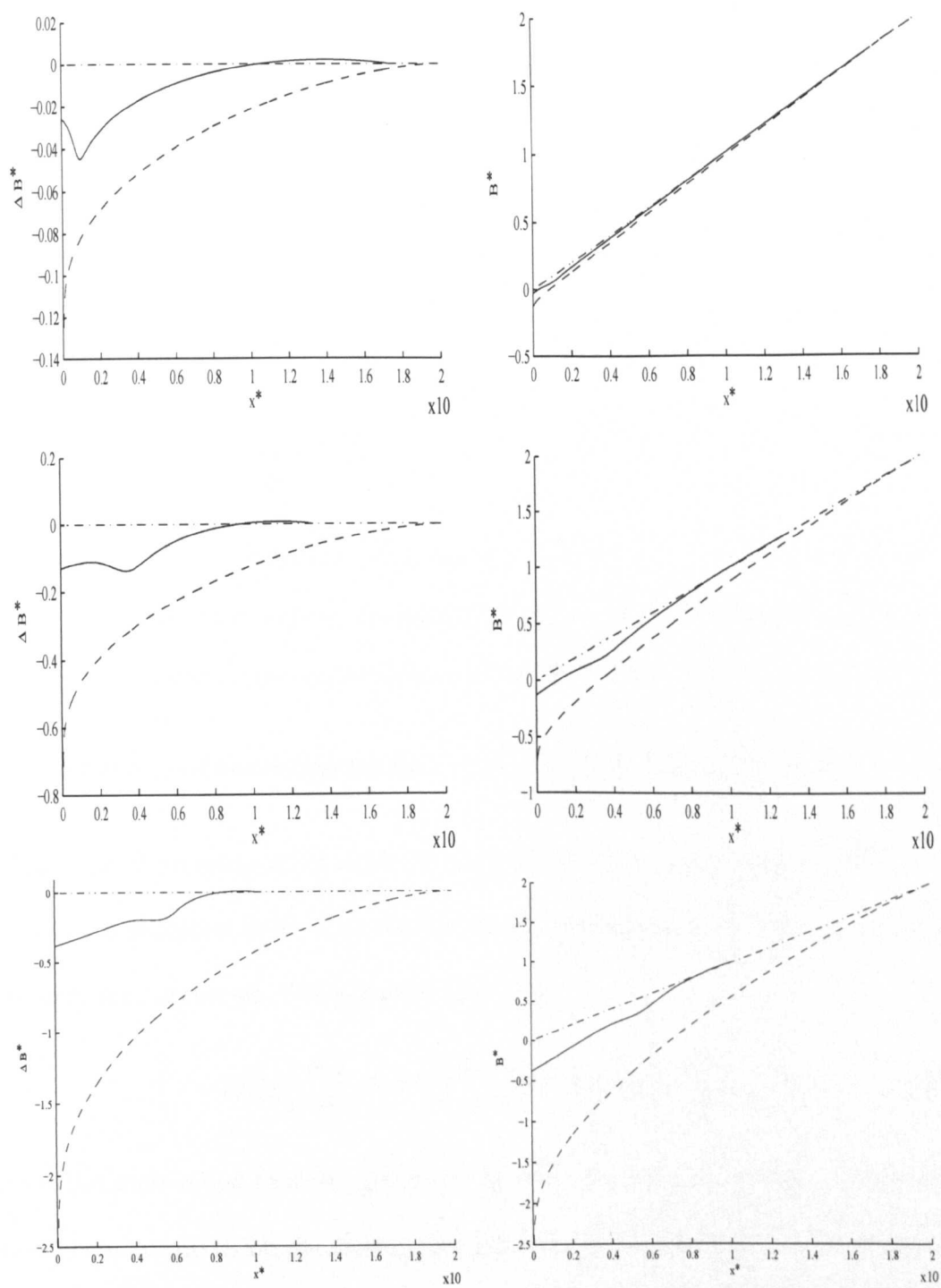


Figure 8.7: Left: change in bed level relative to the initially plane beach for uncoupled (dashed) and fully coupled (solid) transport models after one SM63 swash cycle. Right: final beach profile for uncoupled (dashed) and fully coupled (solid) transport models. Top: $\sigma = 0.01$, middle: $\sigma = 0.0654$, bottom: $\sigma = 0.2$. Dot-dashed lines show the initial bed profile.

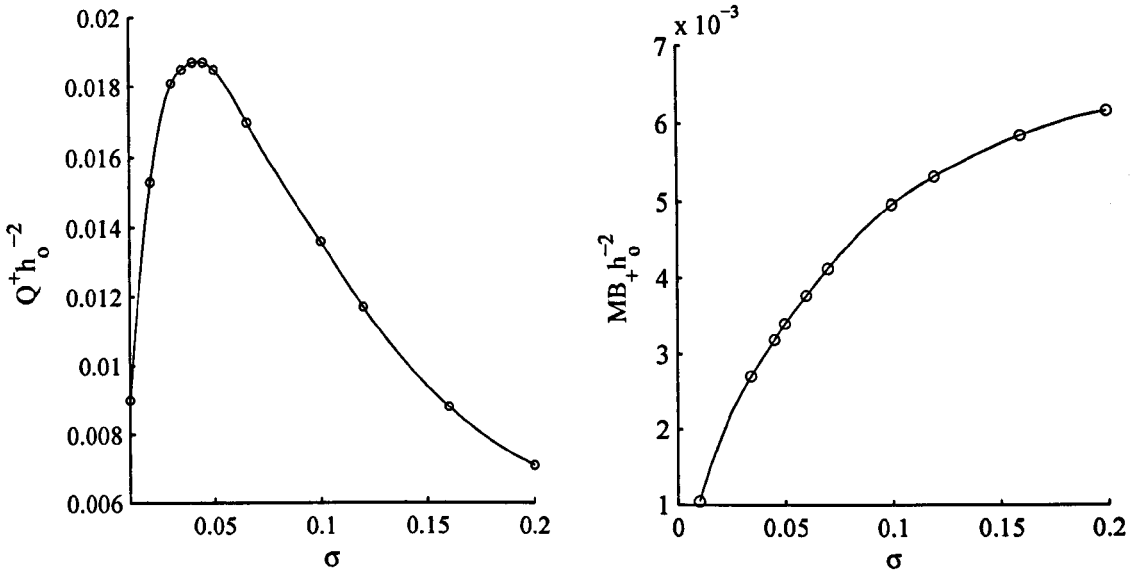


Figure 8.8: Left: variation of the (dimensionless) amount of net onshore transport with the bed evolution parameter σ . Right: variation of the (dimensionless) amount of sediment mobilised at t_I with the bed evolution parameter σ

8.1.5 Analysis of shoreline motion in the run-up when $q = Au^3$

In Appendix B an asymptotic equation is derived that enables analysis of the terms affecting the shoreline motion; as the derivation makes use of (5.3.38) the equation is valid only for the run-up. The equation (B.0.14) is:

$$\left(1 + 2A\zeta g\right) \frac{d^2 x_*}{dt^2} + 3A\zeta g \frac{\partial u}{\partial x} \frac{dx_*}{dt} + g\left(\tan \beta + \frac{\partial h}{\partial x}\right) = 0. \quad (8.1.1)$$

For the flat mobile bed case the quantities $\frac{\partial h}{\partial x}$ and $\frac{\partial u}{\partial x}$ can be accurately evaluated just behind the wave tip using the quasi-analytical solution derived in Chapter 6, although (B.0.14) does not, of course, hold in that case. Results for $\sigma=0.0654$ are shown in Figure 8.10 and reveal how both quantities change with time. Both $\frac{\partial h}{\partial x}$ and $\frac{\partial u}{\partial x}$, appear to asymptote to a small limiting value, possibly zero, as time increases, as would be expected for such a self-similar solution. Numerical experiments on a flat bed show that both the STI MOC and MacCormack solvers converge to the quasi-analytical solution

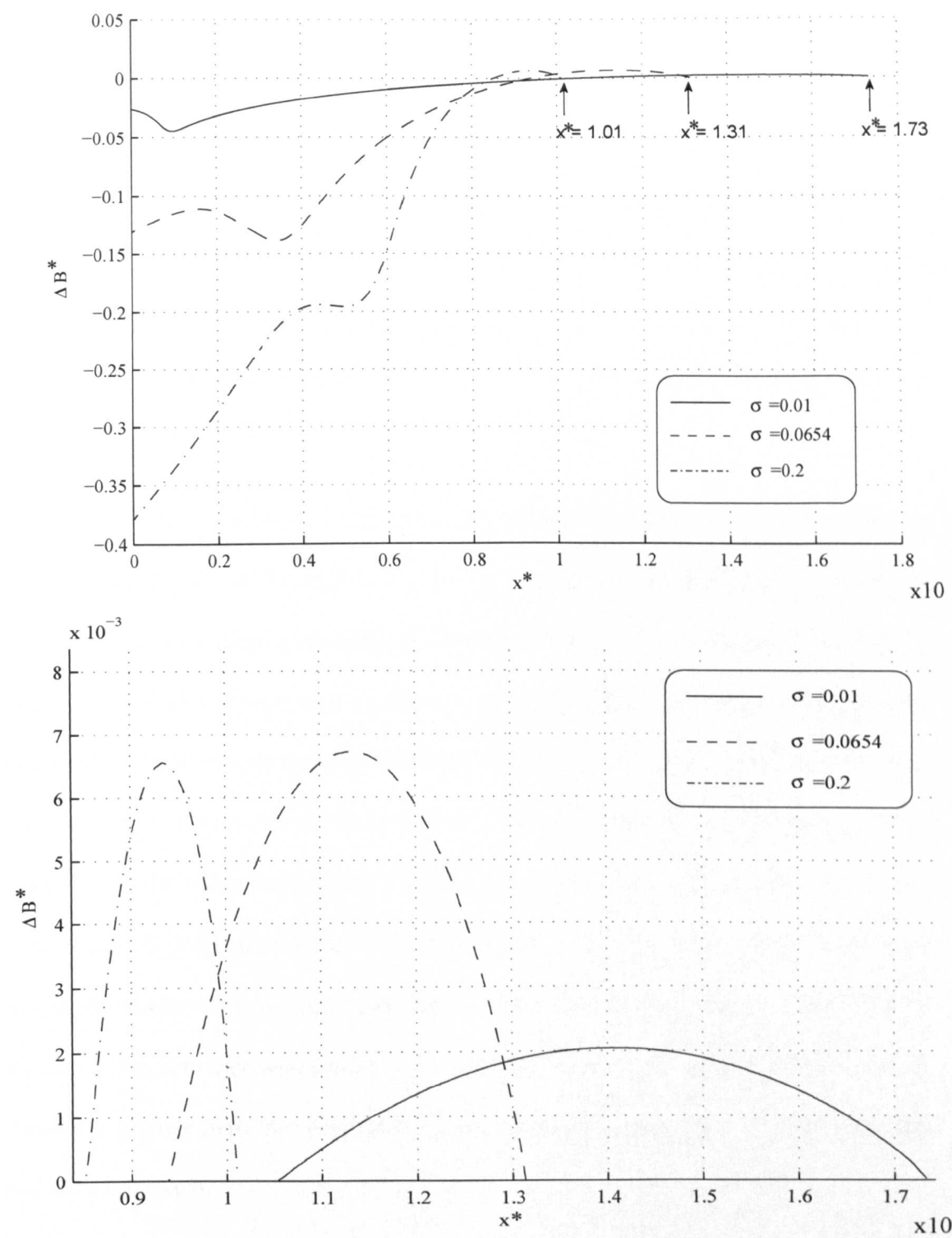


Figure 8.9: Top: Change in bed level relative to the initially plane beach for fully coupled transport model after one swash cycle for $\sigma = 0.01$, $\sigma = 0.0654$ and $\sigma = 0.2$. Bottom: close up of the regions of accretion for these swash events.

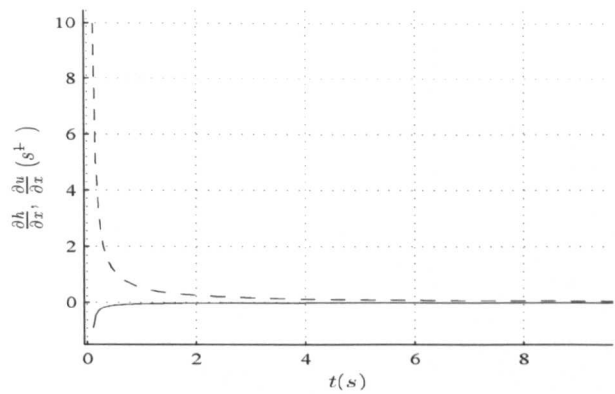


Figure 8.10: Variation of $\frac{\partial h}{\partial x}$ (solid line) and $\frac{\partial u}{\partial x}$ (dashed line) with t at the meshpoint immediately before the wave tip for the mobile bed dam-break when $\sigma = 0.0654$.

for $\frac{\partial h}{\partial x}$ and $\frac{\partial u}{\partial x}$ as Δx is decreased, providing a valuable check on the accuracy of these solvers. When the SM63 initial conditions are employed the behaviour of $\frac{\partial h}{\partial x}$ and $\frac{\partial u}{\partial x}$ in the run-up is qualitatively similar to the flat bed dam-break. Figure 8.11 shows the variation of $\frac{\partial h}{\partial x}$ and $\frac{\partial u}{\partial x}$ with time for the run-up of an SM63 swash event with $\sigma = 0.0654$ obtained using the second-order STI MOC scheme with $\Delta x = 0.01\text{m}$. No (quasi) analytical solution is available for comparison in this case. Both $\frac{\partial h}{\partial x}$ and $\frac{\partial u}{\partial x}$ tend to a small finite value; the magnitude of this value is at its minimum at the maximum run-up. The term $3A\zeta g \frac{\partial u}{\partial x} \frac{dx_*}{dt}$, which is always > 0 , and $\frac{\partial h}{\partial x}$, which is always < 0 , in (B.0.14) act to reduce and increase run-up respectively. Moreover, as the factor $(1 + 2A\zeta g)$ is always > 1 , it acts to increase run-up by decreasing the effect of gravity. Thus, the overall run-up is greater than that predicted for the same initial shoreline velocity using the ballistics approach.

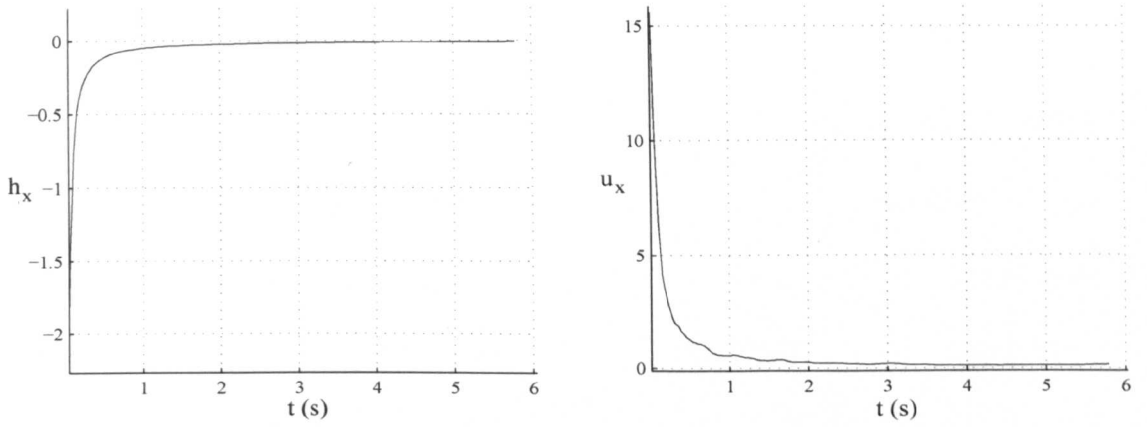


Figure 8.11: Variation of $\frac{\partial h}{\partial x}$ (left) and $\frac{\partial u}{\partial x}$ (right) with time at the meshpoint immediately before the shoreline during the run-up according to the Riemann wave solution with $\sigma = 0.0654$.

8.2 HP79 swash

8.2.1 Model set-up

The initial conditions for these simulations are identical to those described in §7.2 . However, rather than fixing the seaward boundary at $x=-10\text{m}$ like HP79, it is allowed to extend seaward far enough so that it is never reached by the simple wave issuing from the beach toe for the time interval considered. This is done to avoid the complexity of imposing a characteristics type boundary with a mobile bed; the procedure for a characteristics based transmissive boundary treatment for mobile bed flow is given in §4.3.1. As in HP79 the initial bed profile is a planar beach and for all the tests carried out here a beach slope ($\tan \beta$) of 0.1 (1:10) is used. Due to the mobility of the bed a new set of bore relations must be derived for the governing equations (3.2.8), (3.2.18) and (3.3.5), these are described in Chapter 5. As in §7.2 all of the test cases illustrated here use a mesh spacing of $\Delta x=0.01\text{m}$ and the time step is fixed at $\Delta t = \frac{1}{3}(gh_0)^{-\frac{1}{2}}\Delta x$. Again, a check is made within the code that ensures that the CFL condition is not violated.

8.2.2 Results for $q = Au^3$

Here comprehensive results are presented for representative values of the bed evolution parameter (σ). The contour plots of Figures 8.12 and 8.13, complemented by the snapshots given in Figures 8.14 and 8.15, illustrate that in both the run-up and backwash the behaviour of the hydrodynamical flow variables is in very close qualitative agreement to that found by HP79. The pattern of flow over time also appears to be the same as that for a fixed beach, i.e. bore collapse, run-up and formation of a backwash bore. However, if the wave structure is studied in depth using the characteristic grid, shown in the bottom panel of Figure 8.13, discrepancies with the fixed bed case are again apparent. In terms of the overall characteristic pattern results are similar to the SM63 mobile bed swash event up until formation of the backwash bore. The incoming uniform bore is similar to the fixed bed case in that it is a "hydrodynamical" bore formed by the coalescence of incoming hydrodynamic (C^+) type characteristics. The characteristics also indicate that, as is the case for the fixed bed (Ho and Meyer, 1962), when the bore climbing the mobile beach collapses at the initial shoreline position it "forgets" all of the boundary data that determined its development up until that point. Thus it is the information beyond the domain of dependence of the shoreline singularity that determines the flow structure within the main body of the swash lens. The primary difference compared with the fixed bed case lies in the properties of the backwash bore. As was noted in §8.1.3 the C^+ characteristic wave speeds always remain positive, so, unless the backwash bore were to move (at least initially) landwards it cannot form due to a coalescence of these characteristics, as it does for the fixed bed case. Instead, analysis of the characteristics shown in Figure 8.13 implies that the backwash bore in the mobile beach case is a relatively slow moving sediment bore,

or bed step, formed by the coalescence of C_b characteristics. Like the SM63 mobile bed swash event, the rapidly moving water meets the sediment bore almost as though it were stationary and forms a hydraulic jump over it. As in the HP79 solution the life of this backwash bore is cut short when the shoreline catches it up. Subsequent hydrodynamic motion is similar to that described in HP79 with the backwash bore collapsing and propagating energy seawards with a new shoreline position eventually being established close to this point of collapse. However, the sediment bore leaves behind a region of accretion comprising a bed profile that ramps up from the landward side terminating in a beach face discontinuity; thus, a wedge shaped form is left on the beach landwards of the final shoreline position, see the final panel of Figure 8.15.

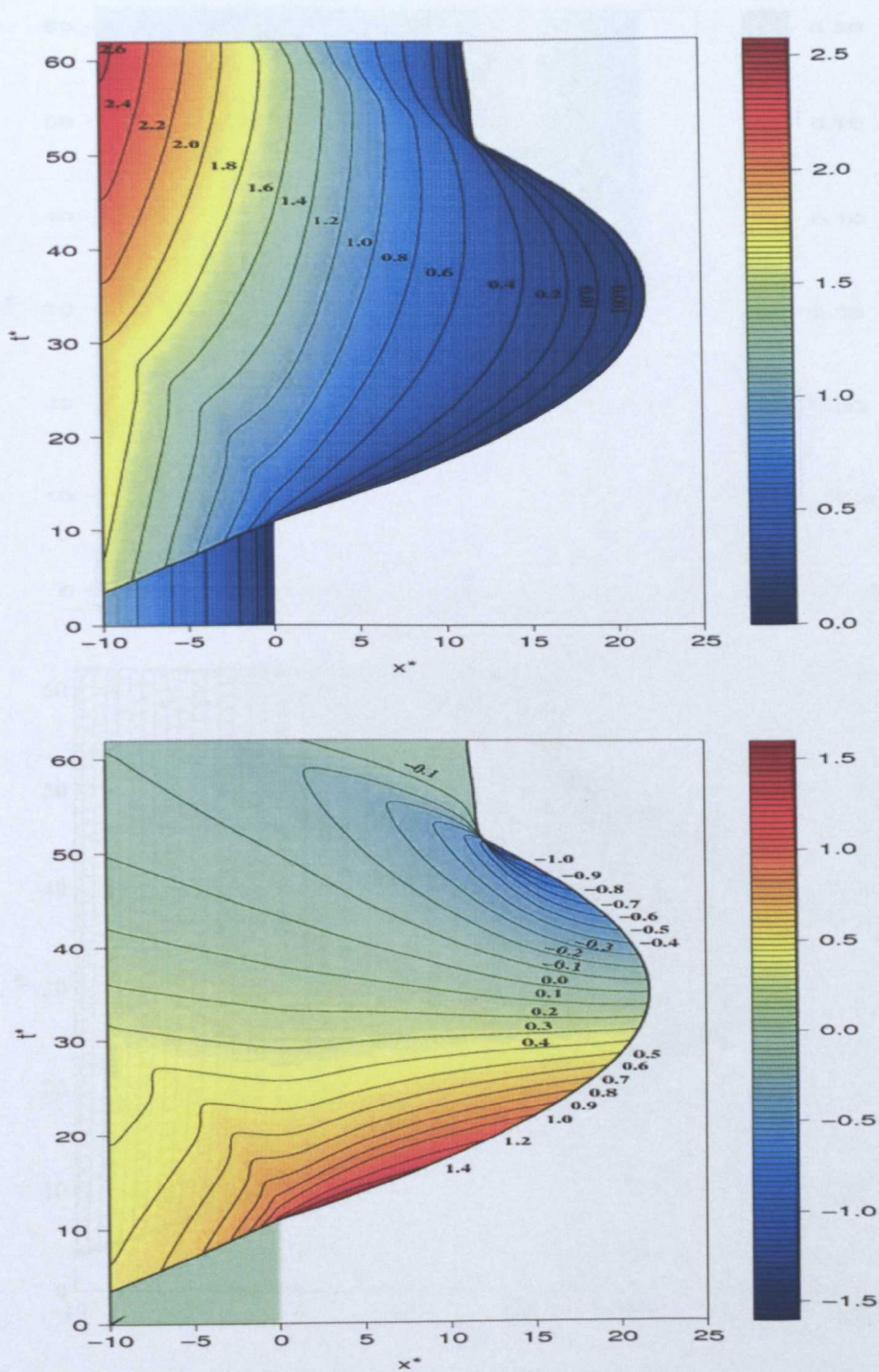


Figure 8.12: Space-time plot showing contours of (top) dimensionless water depth (h^*) and (bottom) dimensionless water velocity (u^*) for HP79 type swash with $q = Au^3$ ($\sigma = 0.0654$).

The region of net accretion is much more extensive than the SM63 case and covers the majority, though not all, of the beach landwards of the original shoreline position ($x > 0$). It is of interest to note that the gradient discontinuity that leads to a sediment bore for the mobile bed SM63 event does not do so in the corresponding uniform bore case as flow reversal on its downstream side occurs much later due to the extended duration of mass and momentum flux from the seaward side.

8.2.3 Results for $q = \bar{A}u^3h$

Here results are presented for the surf and run-up of the HP79 uniform bore over a mobile bed with the sediment flux determined using $q = \bar{A}u^3h$. It is important to stress that these results have not been subject to such rigorous cross-checking as those presented in §8.2.2. Although the characteristic decomposition for this sediment transport formulation is detailed in §3.4.2 the MOC solution has not been constructed. The results presented here are therefore obtained using a version of the MacCormack–mLxF shock capturing solver. Treatment of the shoreline boundary is the same as that detailed in §4.3.2, i.e. ΔB_* is set equal to zero at the wet–dry interface. This treatment is based on an assumption, but one that appears to be justified by the quasi-analytical dam-break solutions obtained in §6.0.4. The solver has been validated against the quasi-analytical solution detailed in §6.0.4; agreement between numerical and quasi-analytical results is found to be good.

Figures 8.16 – 8.17 again show that in the run-up and backwash the behaviour of the hydrodynamical flow variables is in very close qualitative agreement to that found by HP79. However, in contrast to the $q = Au^3$ case, net onshore transport of sediment occurs everywhere in the newly created sub-aqueous region of beach landward of the original shoreline location at $x^* = 0$. Interestingly, the model predicts a very small

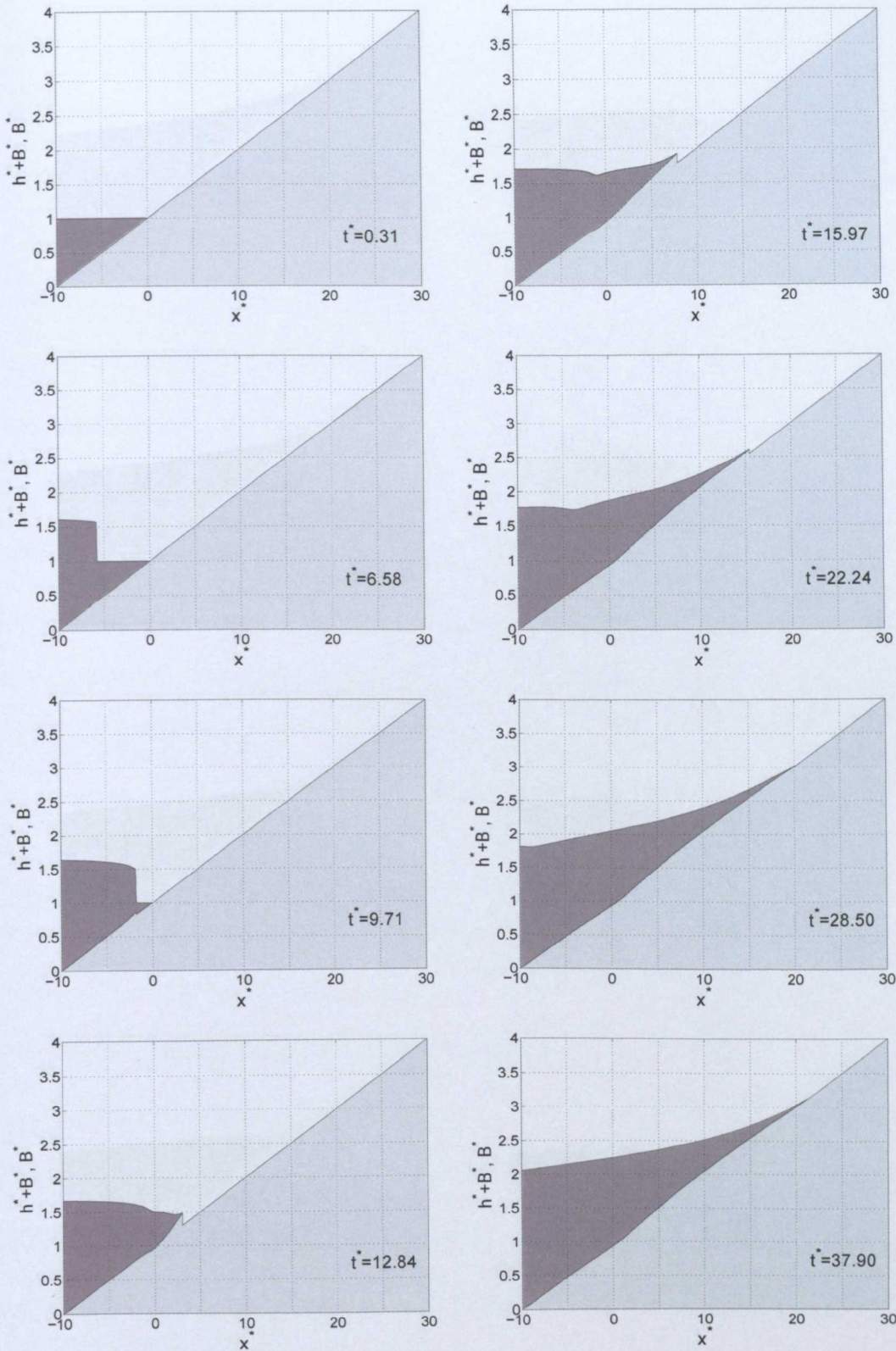


Figure 8.14: Run-up of the HP79 uniform bore over a mobile beach where sediment flux is of the form the $q = Au^3$ and $\sigma=0.004$

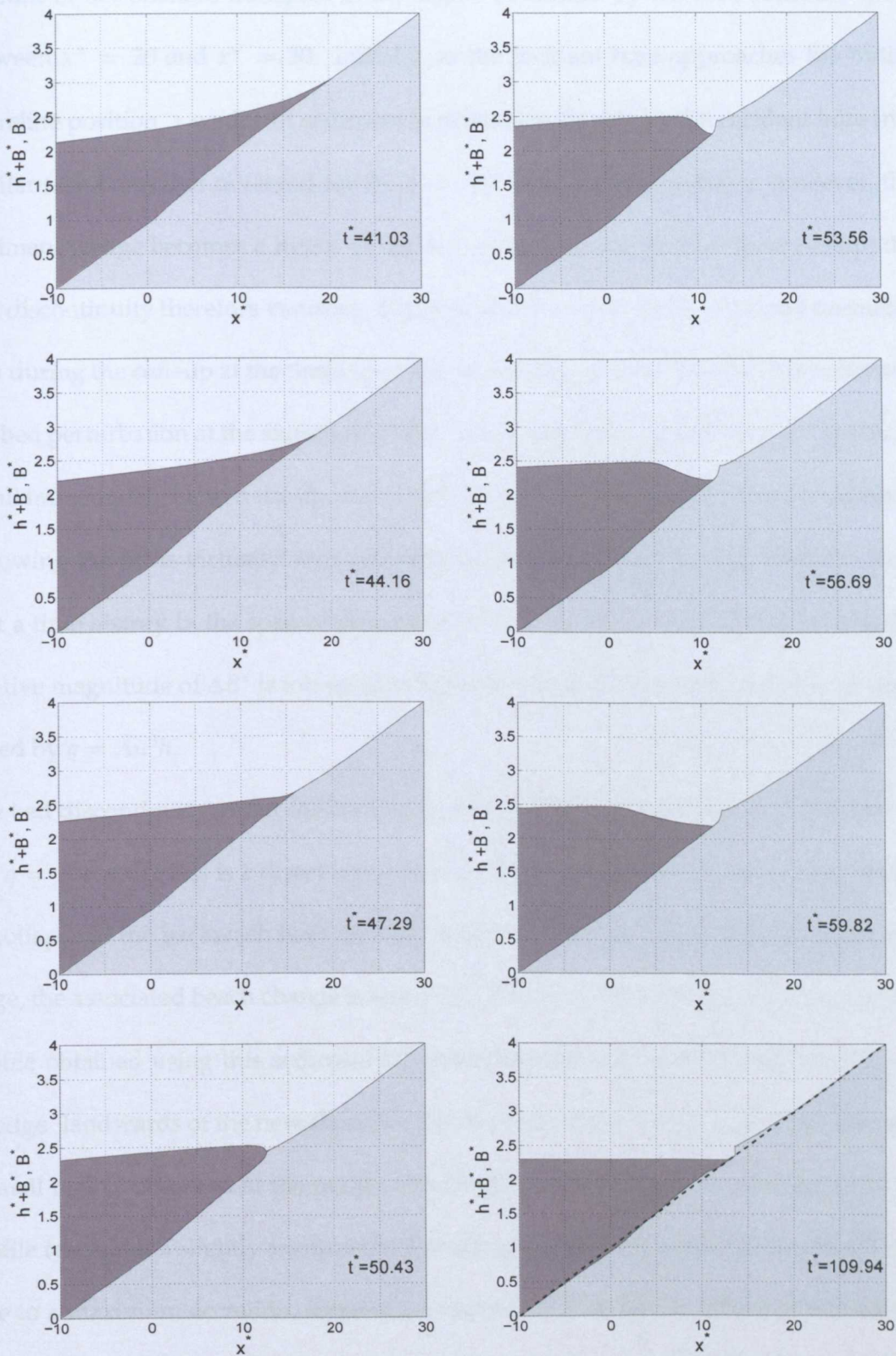


Figure 8.15: Backwash of the HP79 uniform bore over a mobile beach where sediment flux is of the form the $q = Au^3$ and $\sigma=0.004$

amount of net offshore transport in the region bracketed by the zero contours lying between $x^* = 20$ and $x^* = 30$. Initially, as the incident bore approaches the initial shoreline position, a wedge of sediment is driven landwards by the incident bore in a similar fashion to that observed for the $q = Au^3$ case. At bore collapse, however, the sediment wedge becomes a hump as the bed perturbation is zero at the wave tip; the bed discontinuity therefore vanishes. Figure 8.18 shows snapshots of the bed perturbation during the run-up at the times specified on the figure. Once the bore has collapsed the bed perturbation at the shoreline is zero and, initially, the perturbation is extremely small immediately behind the tip; the extent of the flow for which the bed perturbation following the tip is virtually zero increases as time progresses, cf. Figure 8.18. Note that a time history in the spirit of Figures (8.14) and (8.15) is not presented here as the relative magnitude of ΔB^* is too small to be seen clearly for sediment transport governed by $q = \bar{A}u^3h$.

The bed discontinuity under the backwash bore is not as pronounced as that found in the $q = Au^3$ case; this is a direct consequence of the fact that the values h at the point of collapse of the backwash bore are very small, so, although the discontinuity in u is large, the associated beach change is small as $q = q(u, h)$. Consequently, the final beach profile obtained using this sediment transport formula does not include the obvious "wedge" landwards of the new shoreline that is observed for the $q = Au^3$ case. Instead, a small nick is observed at the point of backwash bore collapse. The change in beach profile resembles a slightly asymmetrical hump gradually rising up from the landward side to a maximum accretion, somewhere around $x^* \approx 6$, before falling more rapidly down to zero seaward of the original shoreline position, cf. Figure 8.19. Importantly, with this sediment transport formulation, the effect of the swash event higher up the beach is far more limited than for the same event with a $q = Au^3$ sediment transport

formula. The beach seaward of the original shoreline is eroded everywhere offshore within the region shown. The same qualitative behaviour is observed for $\bar{\sigma}$ in the range $0.075 \leq \bar{\sigma} \leq 0.5$ and, Figure 8.18 shows snapshots of ΔB^* in the run-up as well as the final beach change for $\bar{\sigma} = 0.245$.

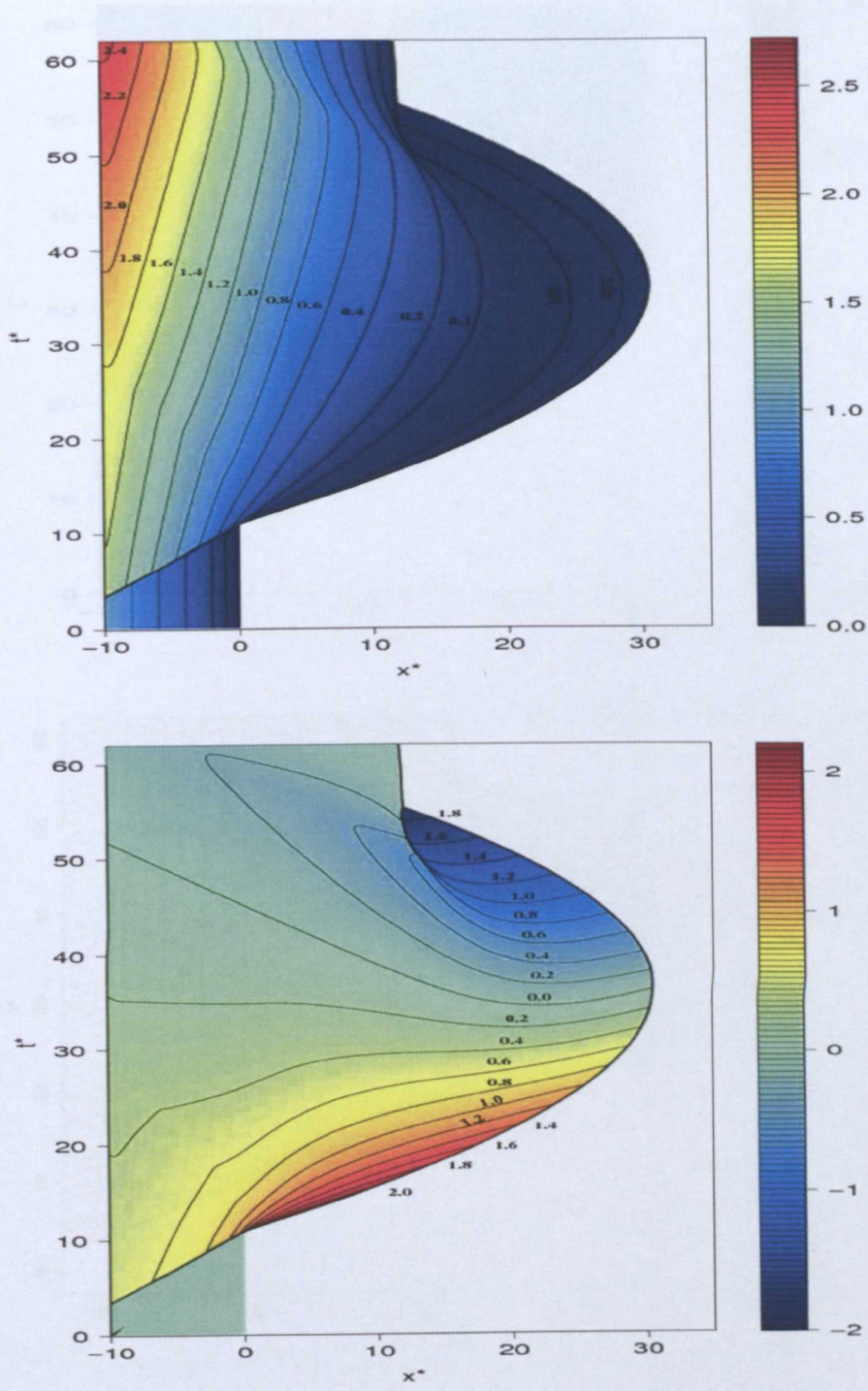


Figure 8.16: Space-time plot showing contours of (top) dimensionless water depth (h^*) and (bottom) dimensionless water velocity (u^*) for HP79 type swash with $q = \bar{A}u^3h$ ($\bar{\sigma} = 0.15$).

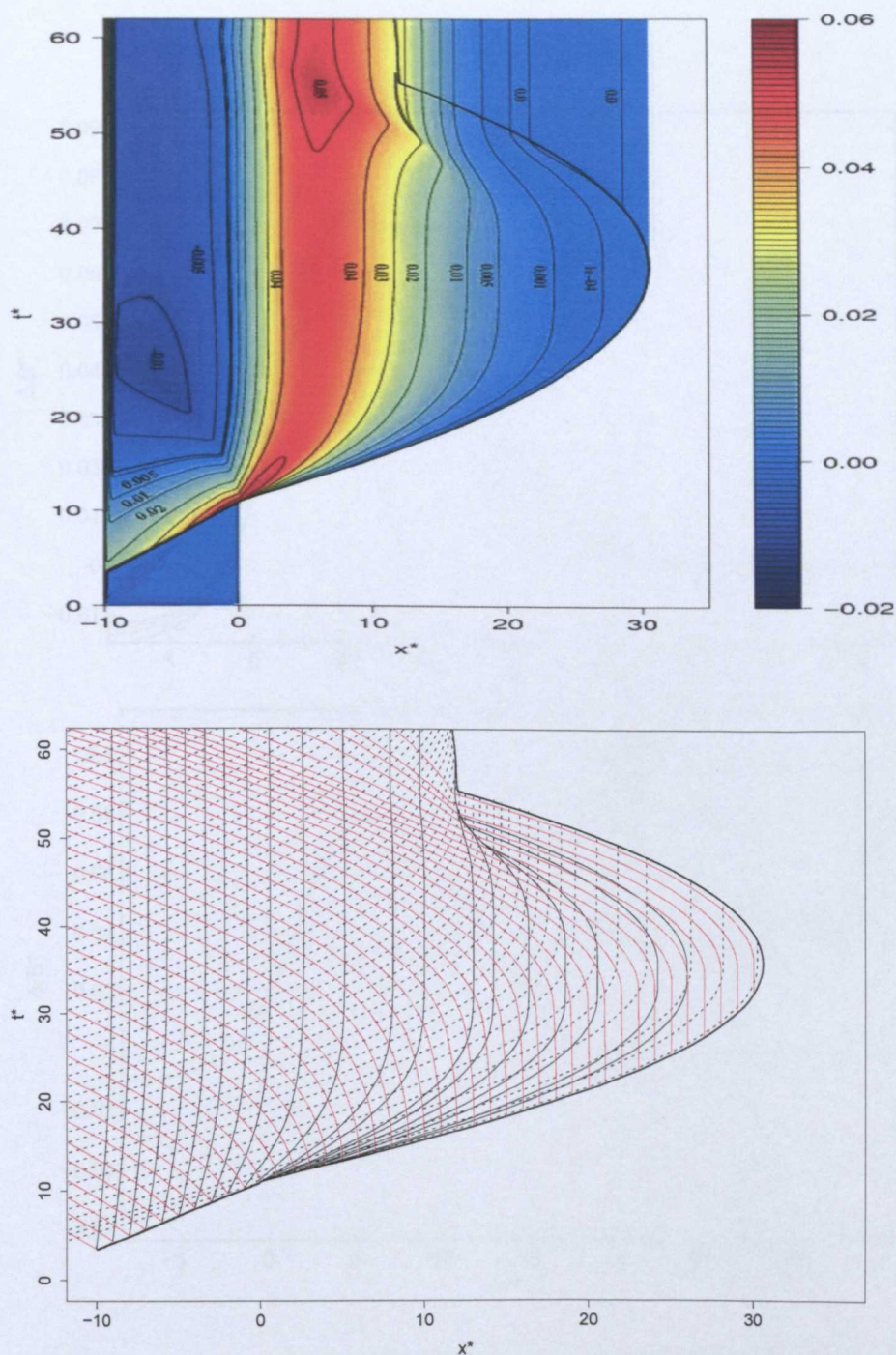


Figure 8.17: Space–time plot showing contours of (top) dimensionless change in beach height (ΔB^*) and (bottom) grid of characteristics for HP79 type swash with $q = \bar{A}u^3h$ ($\bar{\sigma} = 0.15$). Black dashed lines are C^+ characteristics, red solid lines C^- characteristics and black solid lines C_b characteristics.

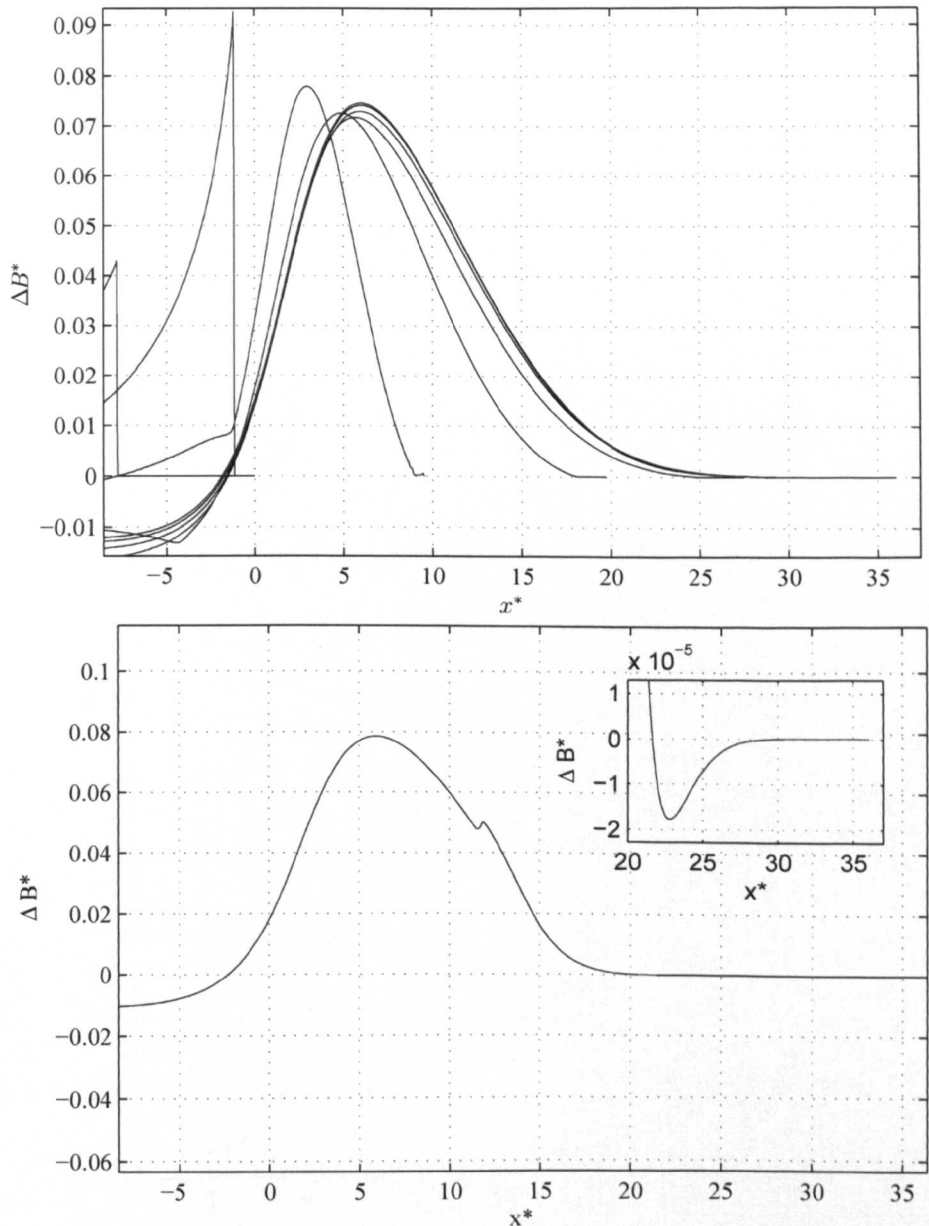


Figure 8.18: Top: Snapshots of ΔB^* in the run-up at $t^* = 5$ to 40 at intervals of 5 and bottom: Change in bed level relative to the initially plane beach for one HP79 swash cycle (inset close-up of erosion) with $q = \bar{A}u^3h$ ($\bar{\sigma} = 0.245$).

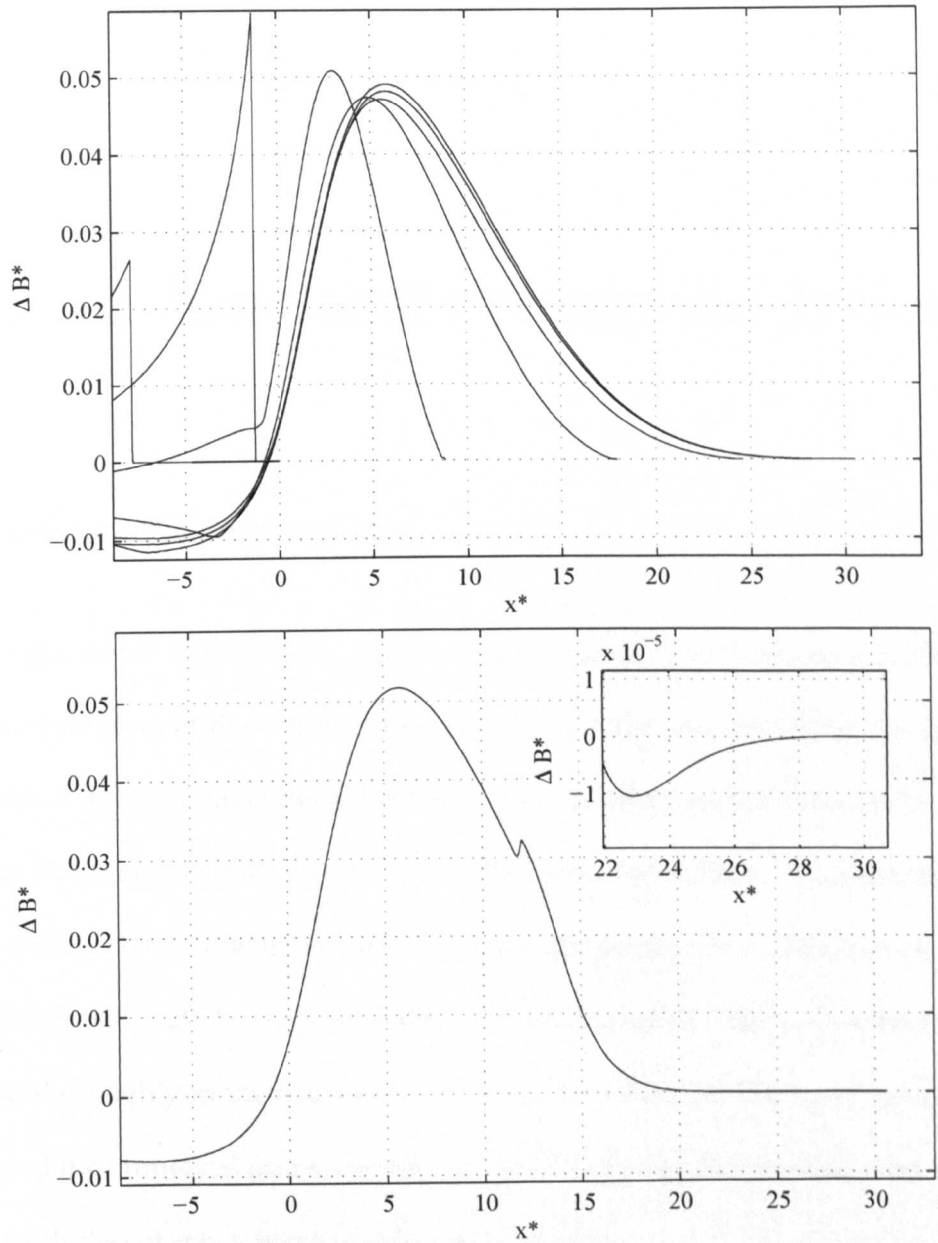


Figure 8.19: Top: Snapshots of ΔB^* in the run-up at $t^* = 5$ to 35 at intervals of 5 and bottom: Change in bed level relative to the initially plane beach for one HP79 swash cycle (inset close-up of erosion) with $q = \bar{A}u^3h$ ($\bar{\sigma} = 0.15$).

Conclusions and recommendations

9.1 Review and conclusions

The work presented in this thesis aims to improve understanding and modelling of beach face evolution in the swash zone forced by a single incident bore. In order to achieve this a fully coupled one-dimensional mathematical model based on the shallow water-Exner system with wet-dry capabilities has been utilised. A similar theoretical approach (in two-dimensions) was used in a swash context by Dodd et al. (2008) to successfully simulate beach cusp formation and evolution. Such a model was investigated thoroughly in the course of this work. In particular, the wave structure is detailed and the numerical problems associated with the wet-dry interface and formation and evolution of shock waves (bores) are addressed.

Two distinct numerical methods are presented to solve the shallow water-Exner equations in Chapter 4. One method is based on the highly accurate method of characteristics (MOC) in which the governing PDEs are decomposed into an equivalent system of ODEs. The characteristics based approach is useful as it gives a visual representation

of the flow structure that provides valuable physical insight into swash zone (morpho)dynamics. The specified time interval (STI) MOC scheme is very flexible and any order of accuracy in space is easily obtained by use of a polynomial of corresponding order for base point interpolations. Temporal accuracy above second-order is demanding on memory; however, second-order accuracy in both space and time is shown to be sufficient for swash simulations. The development of a STI MOC solver for rapid flow transients over a mobile bed is new. In fact, such a scheme dispels a popular belief that only multi-mode characteristics schemes¹ can accurately model rapid transients over a mobile bed when specified time intervals are used (Lai, 1991). A more conventional finite-difference approach using a MacCormack modified Lax Friedrichs self-adjusting hybrid scheme, that incorporates anti-diffusion filtering, is also presented. The work necessitated the development of a new algorithm to deal with the wet-dry (shoreline) boundary on a mobile bed. So that the algorithm would be of practical use it was made suitably generic enough to work with any conventional finite-difference or fixed grid MOC type solver. Variations of this algorithm for the $q = Au^3$ and $q = \bar{A}u^3h$ sediment transport formulations are detailed in §4.3.2. The algorithm is tested for a variety of different conditions and found to be both robust and reliable (Chapters 7 and 8).

When using a MOC approach it is necessary to treat bores explicitly whenever they occur using shock fitting procedures. In Chapter 5 suitable shock relations are derived and a new shock fitting algorithm suitable for flow over a mobile bed is developed based on those devised for gas dynamical problems by Moretti (1971). The shock fitting scheme is investigated and found to perform extremely well (Chapter 5). Explicit

¹Multimode schemes combine both spatial and temporal (reachback) interpolation at the base points of characteristics

shock fitting becomes prohibitively difficult when multiple shocks and shock–shock interactions occur in the flow. It is this reason that motivated the development of a more conventional shock capturing scheme in tandem with the shock fitting approach. A number of related shock capturing schemes are investigated in §5.1. Possible remedies for the problem of parasitic oscillations around discontinuities that include non–linear filtering and artificial dissipation are also investigated in §5.1. While direct non–linear filtering at each time step is suitable to render incident bores oscillation free, it is found that such a scheme is not capable of dealing with certain, high strength, backwash bores without blowing up. Primarily for stability reasons a hybrid scheme based on a weighted average of first and second–order solutions is found to be most suited to modelling swash flows. The smearing effect due to artificial dissipation around discontinuities is removed using a conservative anti–diffusion filter recently devised by Breuss and Welk (2006). Surprisingly good results are obtained using this filtered hybrid scheme. Numerical predictions are in excellent agreement with the analytical results for several challenging test problems even for relatively long run times. It should be relatively easy to extend the hybrid shock capturing scheme in order to model multiple swash events, however, this has yet to be attempted.

In Chapter 6 two new quasi–analytical solutions are developed for mobile bed dam–break flow. These quasi–analytical solutions are obtained using the Riemann wave approach pioneered for dam–break flow by Fraccarollo and Capart (2002). Such solutions provide detailed insight into the wave structure of morphodynamic dam–breaks from the perspective of two different sediment transport formulae. They also provide invaluable validation tools for morphodynamical solvers and are used to validate both the MOC and finite–difference schemes presented in Chapter 4 of this thesis. Qualita-

tive comparisons with the work of Fraccarollo and Capart (2002), Murray (2007) and Zech et al. (2008) indicate that for the relatively simple shallow water–Exner system the $q = Au^3$ sediment flux better represents the physical behaviour of mobile bed dam-breaks. Indeed, at the qualitative level, such a simple approximation performs surprisingly well capturing many of the important physical flow features such as the two rarefaction regions, roughly constant state region and sediment bore, or "debris snout", at the wave tip. The brief quantitative comparisons made with the experimental data given in Fraccarollo and Capart (2002) show that considerable additional analysis is required to improve the agreement between theory and reality.

Results of uncoupled beachface evolution obtained from analytical solutions developed in Chapter 7 illustrate that for SM63 swash net transport is everywhere offshore. This occurs for both sediment transport formulae and is to be expected following the work of Pritchard and Hogg (2005). However, for HP79 swash a net influx of water and sediment leads to a positive net sediment flux in the newly created subaqueous region between the original and new shoreline positions. In Chapter 8 results of fully coupled modelling are presented and some interesting observations are made. Importantly, when $q = Au^3$, the coupling of hydro- and morphodynamics leads to the net onshore transport of sediment on the beach for the entire range of bed evolution parameters tested. This finding suggests that the water sediment interaction could be primarily responsible for the net onshore transport of sediment observed on many natural beaches. For swash driven by the uniform bore described in Hibberd and Peregrine (1979) results are obtained for two different sediment transport formulae. The pattern of accretion is different for the $q = \bar{A}u^3h$ formulation; however, net onshore transport of sediment is also predicted for this sediment transport formulation.

9.2 Recommendations

Mathematical modelling of beach face evolution in the swash zone is still in its infancy. In particular, models in which the associated hydro- and morphodynamics are fully coupled are currently extremely rare. As such, there remains a great deal of work still to be done, meaning that swash zone sediment transport will remain an active research area for many years to come. A number of suggestions for future research, informed by the work undertaken in this thesis, are given below.

While a model based on the $q = Au^3$ sediment flux formulation was thoroughly investigated an in-depth investigation was not conducted for the $q = \bar{A}u^3h$ formulation. It is highly recommended that a method of characteristics based solver be developed for the $q = \bar{A}u^3h$ formulation. The development of such a solver would undoubtedly provide a great deal of insight into the associated dynamics. An investigation would allow for a more detailed comparison between the wave structure associated with the two sediment transport formulations.

The present model is rudimentary in that it does not account for infiltration, sediment storage, settling lag, advection of sediment from the surf zone or bed shear stress. It is recommended that infiltration be included in the model using Darcy's law following the work of Packwood (1983) and Dodd et al. (2008). There is also scope for the inclusion of exfiltration. The addition of a storage term to the shallow water-Exner equations is common place in work on alluvial flow (see for example Lai (1991)). Thus, the inclusion of such a term within the context of swash zone flows should present no major challenge. Similarly, the inclusion of settling lag and advection effects should

also be relatively straight forward with the former only requiring a modification to the sediment flux function. Modelling of bed shear stress in swash zone flow is, however, more complex. Ideally to achieve realistic results use should be made of boundary layer theory. A laminar boundary layer approach is known to be problematical in the backwash due to the boundary layer thickness exceeding the flow depth (Packwood, 1980). To date only a handful of numerical models based on the shallow water equations have successfully incorporated a boundary layer approach for bed shear stress in swash zone modelling (see e.g. Clarke et al. (2004)). While inclusion of all, or even just some, of these effects into a MOC based solver would doubtless prove extremely challenging, incorporation into the hybrid finite-difference scheme should be far more straightforward. It would be interesting to see how well the simple sediment transport model employed within this thesis compares with much more complex models that incorporate the effects listed above.

In this thesis hybrid solvers based on classical finite-difference schemes have proven to be more than capable of dealing with some of the most challenging flow regimes of the nearshore region. Classical difference schemes are extremely rapid, robust and straightforward to code without the need for lengthy decomposition of the governing equations. It would appear that classical finite-difference schemes have been given a new lease of life by the development of robust and efficient non-linear filters. In particular, filters that remove smearing due to artificial dissipation seem to be well suited for use in modelling swash flows. Such filters can be applied after thousands of time-steps without any apparent loss of accuracy. The results using hybrid schemes and filters obtained in Chapters 5, 7 and 8 are promising. In predicting the height and velocity of shocks they have even been shown to outperform the commonly used weighted aver-

age flux (WAF) schemes (§5.6). However, further work on the switch function is necessary to alleviate the excessive smearing of gradient discontinuities. Another interesting line of inquiry for swash modelling is the possible use of flux corrected transport (FCT) schemes first introduced by Boris (1971). The FCT scheme began as a semi-Lagrangian technique, however, FCT schemes are now fully Eulerian and employ two distinct calculation steps. In the first step, a high order difference scheme is used to obtain the solution at a new time, the scheme is stabilised through the explicit addition of artificial diffusion, this diffusion is then removed in an anti-diffusion step. FCT based algorithms have long been used in gas dynamics with a great deal of success (see for example Boris and Book (1973, 1976); Zalesak (1979); Boris et al. (1993)). Such schemes are comparable to the classical Lax Wendroff central difference schemes in continuous flow regions in terms of their accuracy, computational expense and ease of coding (Boris and Book, 1973). Moreover, they are known to model shocks extremely crisply and do not suffer from parasitic oscillations. Importantly, it should be possible to employ the tip algorithm developed in §4.3.2 in an FCT type solver thus making treatment of the shoreline relatively straightforward.

Finally, a comparison between data obtained from laboratory experiments, or the field, and the theoretical results obtained here is of course extremely important. A brief qualitative comparison with mobile bed dam-break experiments carried out in the flume at the University of Nottingham (Murray, 2007) reveals that the theory is able to capture most of the flows more salient features. In particular, photographs of bed and water surface profiles bear a striking resemblance to the profiles obtained in Chapter 6 when the $q = Au^3$ sediment flux formulation is used. Direct comparison of the Riemann wave solution to the shallow water-Exner system and the data provided by Fraccarollo

and Capart (2002) indicates that the theory needs to be extended to accurately predict the physical behaviour of rapid flows over mobile beds. In-depth quantitative analysis is thus deemed a fruitful avenue for further research.

Obtaining initial conditions for SM63 swash on a mobile beach

A.0.1 Discontinuous initial conditions

The discontinuity in all dependent variables at $t = 0$ prohibits the numerical solution from starting at this point when using the MOC STI solver, or the MacCormack–mLxF hybrid solver if a genuine wet–dry boundary treatment is to be employed. The MacCormack–mLxF hybrid solver can run directly from discontinuous initial conditions if the thin film approach is used downstream, see §4.3.2. If the thin film is on a slope, however, a special procedure must be employed to ensure that the film of water downstream of the shoreline does not begin to accelerate down the slope before the shoreline reaches it. When using genuine wet–dry boundary conditions for dam–break initial conditions it is a necessary requirement that the solution is started at a finite time t_I . To obtain initial conditions at t_I the flat bed Riemann wave solutions detailed in Chapter 6 are employed. Such an approach is typical when simulating purely hydrodynamical dam–break problems on sloping beds using MOC based solvers for which

the Ritter solution is used to provided initial values of h and u (Sakkas and Strelkoff, 1973). In this work the Riemann wave values of h , u and B obtained at t_I are employed directly as initial conditions for the main solver. The legitimacy of using initial values derived for flow over a horizontal bed for sloping bed problems does not appear to have been discussed in any of the previous literature. A scaling argument can be used to show that such an approach is in fact legitimate. Letting $B(x, t) = B_o(x) + b(x, t)$ and employing the following scaling:

$$x' = (Tg^{\frac{1}{2}}h_o^{\frac{1}{2}})^{-1}x, \quad (\text{A.0.1})$$

$$t' = T^{-1}t, \quad (\text{A.0.2})$$

$$h' = h_o^{-1}h, \quad (\text{A.0.3})$$

$$u' = g^{-\frac{1}{2}}h_o^{-\frac{1}{2}}u, \quad (\text{A.0.4})$$

$$b' = (\xi Ag h_o)^{-1}b, \quad (\text{A.0.5})$$

where T is a dimensional time parameter and daggers denote scaled variables. Putting these new scaled variables into the governing equations, with closure obtained using $q = Au^3$, gives:

$$\frac{\partial h'}{\partial t'} + u' \frac{\partial h'}{\partial x'} + h' \frac{\partial u'}{\partial x'} = 0, \quad (\text{A.0.6})$$

$$T^{-1}g^{\frac{1}{2}}h_o^{\frac{1}{2}} \left\{ \frac{\partial u'}{\partial t'} + u' \frac{\partial u'}{\partial x'} + \frac{\partial h'}{\partial x'} + g\xi A \frac{\partial b'}{\partial x'} \right\} + g \frac{\partial B_o}{\partial x} = 0 \quad (\text{A.0.7})$$

and:

$$T^{-1}\xi Ag h_o \left\{ \frac{\partial b'}{\partial t'} + 3(u')^2 \frac{\partial u'}{\partial x'} \right\} = 0. \quad (\text{A.0.8})$$

It therefore follows that in the limit as $T \rightarrow 0$ the $g \frac{\partial B_o}{\partial x}$ term in (A.0.7) becomes negligible and the equation system approaches that of a flat bed. This approach requires that u be characterised by a finite velocity and b by a finite perturbation; for the governing

equations used here both of these requirements are satisfied, cf. Chapter 6. The same argument can also be put forward for the fixed bed case.

A.0.2 Convergence

The validity of the above approach can also be checked numerically. As the time at which the initial solution is obtained, i.e. t_I , tends to zero values of the dependent variables h , u and B should converge to a limit. Figure A.1 shows the convergence of water height h as the value of t_I is reduced from an initial value of 1×10^{-1} s down to 5×10^{-3} s at a fixed location 0.4m up the beach. It is clear from the figure that the solution does indeed converge as $t_I \rightarrow 0$, further reduction of t_I leads to little discernable difference. Convergence was checked for a number of cross-shore locations and values of the bed evolution parameter (σ), the trend illustrated by the top panel of Figure A.1 was observed in all cases; similar results were obtained for the water velocity u and bed height B . The bottom panel of Figure A.1 illustrates convergence of the instantaneous shoreline position as t_I is decreased for a fixed Δx . Perhaps the most rigorous numerical test on the validity of this approach is to let $A \rightarrow 0$ and compare the resulting swash event with the SM63 analytical solution, this was done in §4.4 where excellent agreement was found.

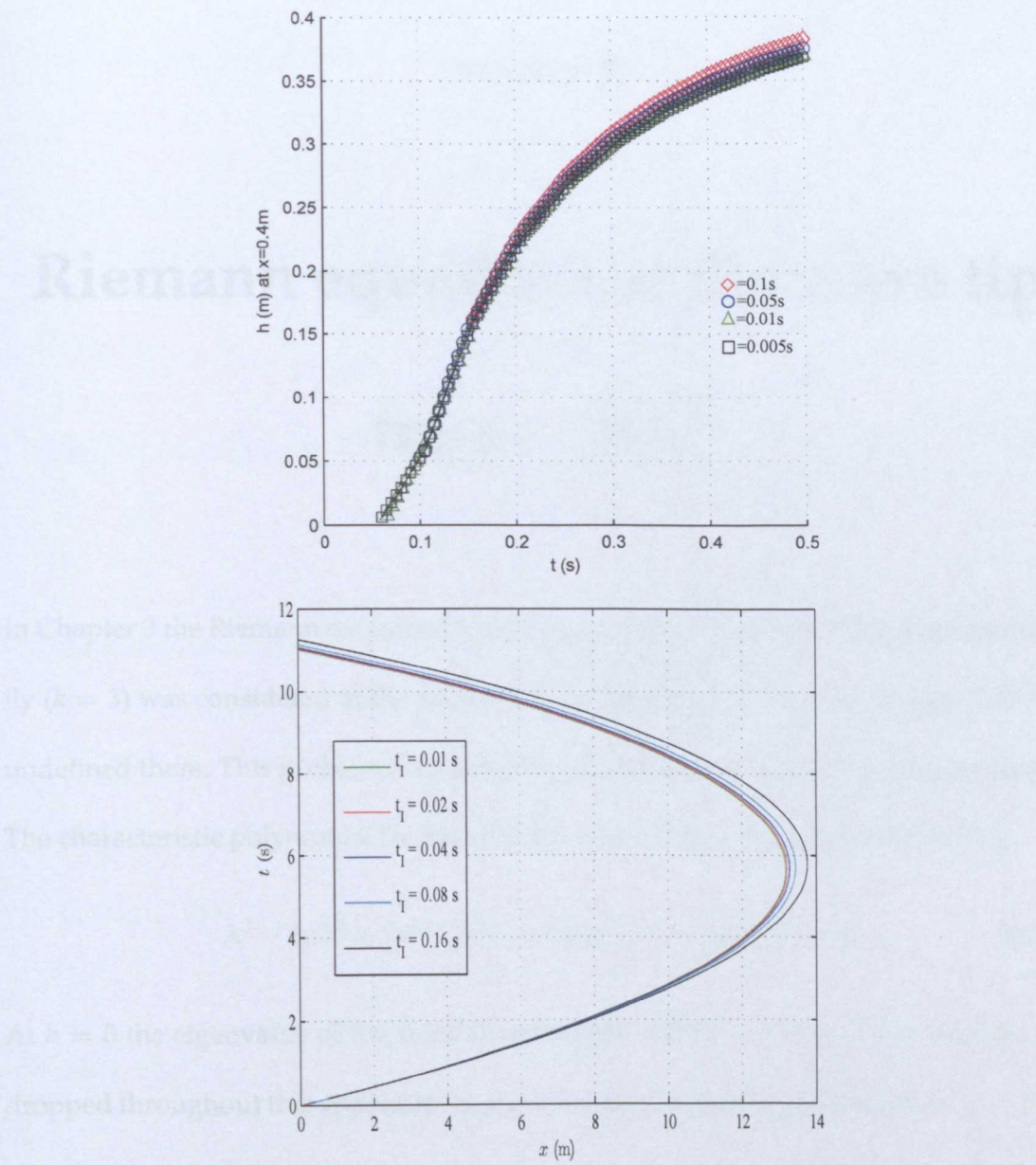


Figure A.1: Top: convergence of solution as $t_I \rightarrow 0$ for figure details refer to the accompanying text and bottom: convergence of the shoreline trajectory as $t_I \rightarrow 0$ with Δx fixed at 0.001m.

Riemann equations at the wave tip

for $q = Au^3$

In Chapter 3 the Riemann equation (3.4.23) associated with the third characteristic family ($k = 3$) was considered at the wave tip, i.e. where $h=0$. It was found that (3.4.23) is undefined there. This problem merits further investigation which is carried out here.

The characteristic polynomial for the shallow water–Exner system with $q=Au^3$ is:

$$\lambda^3 - 2u\lambda^2 + [u^2 - g(h + 3A\xi u^2)]\lambda + 3A\xi gu^3 = 0. \quad (\text{B.0.1})$$

At $h = 0$ the eigenvalue of the third characteristic family is $\lambda = u$. The subscript 3 is dropped throughout this appendix for convenience. Expanding λ in the limit $h \rightarrow 0$ as:

$$\lambda = \lambda_o + h\lambda_1 + h^2\lambda_2 + O(h^3). \quad (\text{B.0.2})$$

Then assuming that $O(h^2)$ terms are negligible and putting (B.0.2) into (B.0.1) gives:

$$\begin{aligned} &\lambda_o^3 + 3h\lambda_1\lambda_o^2 - 2u(\lambda_o^2 + 2h\lambda_1\lambda_o) \\ &+ (u^2 - gh - 3A\xi gu^2)\lambda_o + (u^2 - 3A\xi gu^2)h\lambda_1 + 3A\xi gu^3 + O(h^2) = 0. \end{aligned} \quad (\text{B.0.3})$$

Taking $\lambda_o = u$ it follows from (B.0.1) that:

$$\lambda_o^3 - 2u\lambda_o^2 + (u^2 - 3A\xi u^2)\lambda_o + 3A\xi gu^3 = 0. \quad (\text{B.0.4})$$

Therefore, at $O(h)$, (B.0.3) becomes:

$$\lambda_1(3A\xi gu^2) + gu = 0 \Rightarrow \lambda_1 = (-3A\xi u)^{-1}. \quad (\text{B.0.5})$$

From this analysis it follows that for the third eigenvalue at the wave tip:

$$\lim_{h \rightarrow 0} \lambda = u - (3A\xi u)^{-1}h + O(h^2)$$

. Next, considering the Riemann equation (3.4.23) for the third characteristic family:

$$\frac{du}{dt} + \frac{g}{(\lambda - u)} \frac{dh}{dt} + \frac{g}{\lambda} \frac{dB}{dt} = 0. \quad (\text{B.0.6})$$

Considering the second term on the LHS of (B.0.6) in the limit $h \rightarrow 0$ then:

$$\frac{g}{\lambda - u} \frac{dh}{dt} = -3A\xi guh^{-1} \frac{dh}{dt}. \quad (\text{B.0.7})$$

Employing the material derivative and recalling that $\lambda \approx u - (3A\xi u)^{-1}h$ close to the tip it follows that:

$$\frac{dh}{dt} \approx \frac{\partial h}{\partial t} + (u - (3A\xi u)^{-1}h) \frac{\partial h}{\partial x}. \quad (\text{B.0.8})$$

From (3.2.7):

$$\frac{\partial h}{\partial t} + u \frac{\partial h}{\partial x} = -h \frac{\partial u}{\partial x}, \quad (\text{B.0.9})$$

combining (B.0.8) and (B.0.9) and simplifying, then in the limit $h \rightarrow 0$:

$$\frac{g}{\lambda - u} \frac{dh}{dt} \approx 3A\xi gu \frac{\partial u}{\partial x} + g \frac{\partial h}{\partial x}. \quad (\text{B.0.10})$$

If x_* is the shoreline position then (B.0.10) can be re-written as:

$$\frac{g}{\lambda - u} \frac{dh}{dt} \approx 3A\xi g \frac{dx_*}{dt} \frac{\partial u}{\partial x} + g \frac{\partial h}{\partial x}. \quad (\text{B.0.11})$$

Next, considering the third term on the LHS of (B.0.6). In the limit $h \rightarrow 0$ it is possible to use the shock relation associated with the Exner equation (see §5.3.3) and write B as:

$$B = A\zeta \left(\frac{dx_*}{dt} \right)^2 + x_* \tan \beta, \quad (\text{B.0.12})$$

where the second term on the RHS represents the undisturbed bed height of an initially planar beach. Thus:

$$\frac{dB}{dt} = 2A\zeta \left(\frac{dx_*}{dt} \right) \frac{d^2x_*}{dt^2} + \tan \beta \frac{dx_*}{dt}. \quad (\text{B.0.13})$$

Combining (B.0.6), (B.0.11) and (B.0.13) and simplifying gives the equation:

$$\left(1 + 2A\zeta g \right) \frac{d^2x_*}{dt^2} + 3A\zeta g \frac{\partial u}{\partial x} \frac{dx_*}{dt} + g \left(\tan \beta + \frac{\partial h}{\partial x} \right) = 0, \quad (\text{B.0.14})$$

which is valid as the tip is approached, i.e. in the limit $h \rightarrow 0$.

APPENDIX C

Rankine Hugoniot conditions for the shallow water system

Consider a discontinuity in water height h and water velocity u , where $h(x, t)$ and $u(x, t)$, at the point $x = \zeta(t)$ between the two points in space $x = x_1(t)$ and $x = x_2(t)$ so that $x_1(t) < \zeta(t) < x_2(t)$. Rather than splitting the region of integration, as was done in §5.1, here a Galilean coordinate system is employed. This is done in order to facilitate the proof that a characteristic represents the limit of a weak shock. This coordinate system is set so that it moves parallel to the bottom with the velocity of the discontinuity W (where $W = \frac{d\zeta}{dt}$). This yields the two velocities relative to the discontinuity v_{x_1} and v_{x_2} where:

$$v_{x_1} = u_{x_1} - W \quad (\text{C.0.1})$$

and:

$$v_{x_2} = u_{x_2} - W. \quad (\text{C.0.2})$$

Here u_{x_1} and u_{x_2} are the absolute velocities of the water either side of the discontinuity relative to a stationary coordinate system. Applying the law of conservation of mass or

continuity to the system:

$$\frac{d}{dt} \int_{x_1(t)}^{x_2(t)} \rho h \, dx = 0. \quad (\text{C.0.3})$$

Application of Leibnitz's theorem for the differentiation of an integral gives:

$$\int_{x_1(t)}^{x_2(t)} \rho \frac{\partial h}{\partial t} \, dx + \rho h|_{x_2} \frac{dx_2}{dt} - \rho h|_{x_1} \frac{dx_1}{dt} = 0. \quad (\text{C.0.4})$$

If we let the spatial extent of the shock become very small then $x_1 \rightarrow x_2$ hence:

$$\int_{x_1(t)}^{x_2(t)} \rho \frac{\partial h}{\partial t} \, dx \rightarrow 0. \quad (\text{C.0.5})$$

Recalling that:

$$\frac{dx_1}{dt} = v_{x_1}, \quad \frac{dx_2}{dt} = v_{x_2} \quad (\text{C.0.6})$$

and rearranging we are left with:

$$v_{x_1} h_{x_1} = v_{x_2} h_{x_2}. \quad (\text{C.0.7})$$

(C.0.3) states that the rate of change of mass within the region x_1 to x_2 is zero. That is, the mass of water in the column between x_1 and x_2 remains constant. (C.0.7) states that the mass flux is constant, and identical on both sides of the discontinuity ($x = \zeta(t)$).

Next, consideration of momentum gives:

$$\frac{d}{dt} \int_{x_1(t)}^{x_2(t)} \rho h v \, dx = \int_0^{h_{x_1}} p_{x_1} \, dz - \int_0^{h_{x_2}} p_{x_2} \, dz. \quad (\text{C.0.8})$$

If we assume hydrostatic pressure (i.e. $p = \rho gh$) this reduces to:

$$\frac{d}{dt} \int_{x_1(t)}^{x_2(t)} \rho h v \, dx = \frac{1}{2} \rho g h_{x_2}^2 - \frac{1}{2} \rho g h_{x_1}^2. \quad (\text{C.0.9})$$

Applying Leibnitz's theorem for the differentiation of an integral to the LHS of (C.0.9) gives:

$$\frac{d}{dt} \int_{x_1(t)}^{x_2(t)} \rho h v \, dx = \int_{x_1(t)}^{x_2(t)} \rho \frac{\partial(hv)}{\partial t} \, dx + \rho(hv)|_{x_2} \frac{dx_2}{dt} - \rho(hv)|_{x_1} \frac{dx_1}{dt}. \quad (\text{C.0.10})$$

This simplifies to:

$$\int_{x_1(t)}^{x_2(t)} \rho \frac{\partial(hv)}{\partial t} dx + \rho v_{x_2}^2 h_{x_2} - \rho v_{x_1}^2 h_{x_1}, \quad (\text{C.0.11})$$

but the spatial extent of the shock is very small and $x_1 \rightarrow x_2$ so:

$$\int_{x_1(t)}^{x_2(t)} \rho \frac{\partial(hv)}{\partial t} dx \rightarrow 0 \quad (\text{C.0.12})$$

and the LHS of (C.0.9) becomes:

$$\rho v_{x_2}^2 h_{x_2} - \rho v_{x_1}^2 h_{x_1}. \quad (\text{C.0.13})$$

Substituting this back into (C.0.9) and re-arranging yields:

$$\frac{1}{2} g h_{x_1}^2 + v_{x_1}^2 h_{x_1} = \frac{1}{2} g h_{x_2}^2 + v_{x_2}^2 h_{x_2}. \quad (\text{C.0.14})$$

Here it is worth mentioning the point made by Stoker (1948) that water particles cannot gain energy on crossing a shock front. Therefore, water particles will always move from a region of lower total depth into a region of higher total depth¹. This allows us to define the front, or low, side of a bore as that side from which water particles depart. The back, or high, side is the side at which water particles arrive. From (C.0.7) it follows that:

$$v_{x_2}^2 = \frac{v_{x_1}^2 h_{x_1}^2}{h_{x_2}^2}. \quad (\text{C.0.15})$$

Substituting this relation into (C.0.14) then:

$$\frac{1}{2} g h_{x_1}^2 + v_{x_1}^2 h_{x_1} = \frac{1}{2} g h_{x_2}^2 + \frac{v_{x_1}^2 h_{x_1}^2}{h_{x_2}}. \quad (\text{C.0.16})$$

Hence, re-arranging and simplifying leads to the following relation (still in a moving coordinate system):

$$v_{x_1} = \left(\frac{g h_{x_2} (h_{x_1} + h_{x_2})}{2 h_{x_1}} \right)^{\frac{1}{2}}. \quad (\text{C.0.17})$$

¹Stoker credits this discovery to Rayleigh (1914)

In the same fashion it can be shown that:

$$v_{x_2} = \left(\frac{gh_{x_1}(h_{x_1} + h_{x_2})}{2h_{x_2}} \right)^{\frac{1}{2}}. \quad (\text{C.0.18})$$

These relations lead to some interesting conclusions. Firstly, as the height of the discontinuity tends to zero, i.e. as $h_{x_2} \rightarrow h_{x_1}$, it follows that:

$$v_{x_1} \rightarrow (gh)^{\frac{1}{2}} \text{ and } v_{x_2} \rightarrow (gh)^{\frac{1}{2}}. \quad (\text{C.0.19})$$

That is v_{x_1} and v_{x_2} tend to the characteristic celerities as the discontinuity becomes vanishingly small². Thus, a characteristic is the limit of a weak shock; a fact that is often alluded to in the literature but seldom explained. Secondly, from (C.0.17) and the fact that $h_{x_2} < h_{x_1}$, then $v_{x_1} < (gh_{x_1})^{\frac{1}{2}}$. As v_{x_1} represents the velocity of the bore relative to the velocity u_{x_1} of the water particles behind it, then the wave celerity in the water behind the bore is greater than the relative bore velocity. This means that disturbances originating behind the bore will eventually catch up the bore and therefore modify it: see Stoker (1948), Freeman and LeMéhauté (1964), or Amein (1964)).

Derivation of bore velocity

Putting (C.0.2) into (C.0.18) and multiplying out gives a quadratic in W :

$$W^2 - 2u_{x_2}W + u_{x_1}^2 - gh_{x_1} \left(\frac{h_{x_1} + h_{x_2}}{2h_{x_2}} \right) = 0. \quad (\text{C.0.20})$$

This yields the roots:

$$W = u_{x_2} \pm (gh_{x_1})^{\frac{1}{2}} \left(\frac{h_{x_1} + h_{x_2}}{2h_{x_2}} \right)^{\frac{1}{2}}. \quad (\text{C.0.21})$$

By definition $W > |u_{x_2}|$ so it follows that:

²This result was first pointed out by Abbott (1966)

$$W = u_{x_2} + (gh_{x_1})^{\frac{1}{2}} \left(\frac{h_{x_1} + h_{x_2}}{2h_{x_2}} \right)^{\frac{1}{2}}. \quad (\text{C.0.22})$$

Similarly, putting (C.0.1) into (C.0.17) gives:

$$W = u_{x_1} + (gh_{x_2})^{\frac{1}{2}} \left(\frac{h_{x_1} + h_{x_2}}{2h_{x_1}} \right)^{\frac{1}{2}}. \quad (\text{C.0.23})$$

Validation of numerical schemes

In this appendix results for various validation tests are presented for the numerical schemes described in Chapters 4 and 5. The first two figures were constructed using the second-order accurate GC MOC scheme developed in §4.1.2 for flow on a fixed bed. Note that for all of the results presented the relative error between numerical and analytical results is $< 0.4\%$. Figure D.1 illustrates the ability of the scheme to reproduce the SM63 analytical height and velocity fields visually perfectly for both the run-up and backwash. Figure D.2 shows a swash event due varying the incoming Riemann invariant linearly on the seaward boundary characteristic $R^+ = 2c_o + 1.5B_x g t_{SB}$ (see §4.1.2). Variables in the figure have been non-dimensionalised according to the scaling employed by Peregrine and Williams (2001) which also scales out the beach slope. The entire run-up and backwash up until the point of backwash bore collapse is shown. There is no analytical data to verify the solution against but it is clear from the figure that the backwash bore is resolved extremely crisply with no oscillations present in the solution. The figure also illustrates how well the GC MOC scheme implicitly handles the wet-dry (shoreline) boundary.

Figures D.4 and D.5 compare results of the first and second order accurate mobile

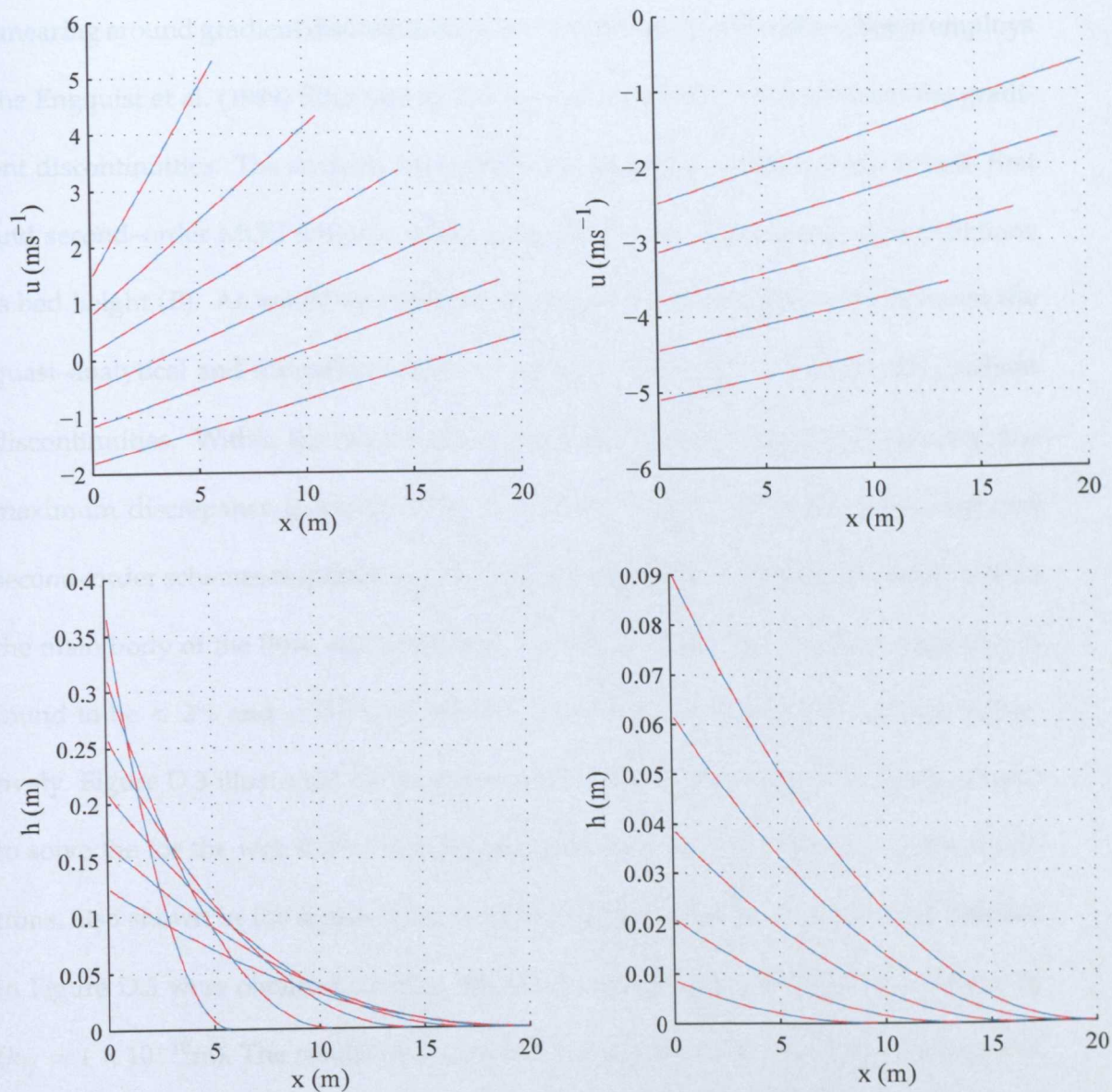


Figure D.1: Snapshots of water velocity (top) and depth (bottom) at 1s intervals computed using second-order GC MOC scheme (red dashed) and SM63 analytical solution (cyan solid) for run-up (left) and backwash (right).

bed STI MOC solvers with the quasi-analytical solution developed in Chapter 6 for the wet-dry mobile bed dam-break. Results for both the first and second-order schemes are clearly very good although the first-order scheme does exhibit a rather pronounced smearing around gradient discontinuities. Note that the second-order scheme employs the Engquist et al. (1989) filter (see §5.1.4) to reduce parasitic oscillations at the gradient discontinuities. The variable that suffers the maximum relative error in both first and second-order MOC schemes when compared to the quasi-analytical predictions is bed height (B). As would be expected the region where disagreement between the quasi-analytical and numerical solutions is most pronounced is around the gradient discontinuities. Within the main body of the flow, and at the bed discontinuity, the maximum discrepancy is found to be $< 3.5\%$ and $< 0.75\%$ for the first-order and second-order schemes respectively. For the other dependent variables (h and u) within the main body of the flow, and at the bed discontinuity, the maximum discrepancy is found to be $< 2\%$ and $< 0.5\%$ for the first-order and second-order schemes respectively. Figure D.3 illustrates the results when the MacCormack-mLxF scheme is used to solve the for the wet-dry mobile bed dam-break with discontinuous initial conditions, also shown in the figure is the quasi-analytical solution. The results presented in Figure D.3 were obtained using a "thin film" treatment for the shoreline boundary ($h_{tf} = 1 \times 10^{-10}\text{m}$). The results provide a valuable check on the wave structure as well as illustrating certain limitations of the "thin film" technique. It is clear from the velocity plot that the MacCormack-mLxF scheme underestimates the tip velocity at smaller times and that this estimation gets better as time goes on. Also evident in the figure are some under- and overshoots at gradient discontinuities. Not so clear from the figure is the small discontinuity in water depth observed at the wave tip; this bore is a consequence of approximating a genuine wet-dry problem with a wet-wet one. Importantly,

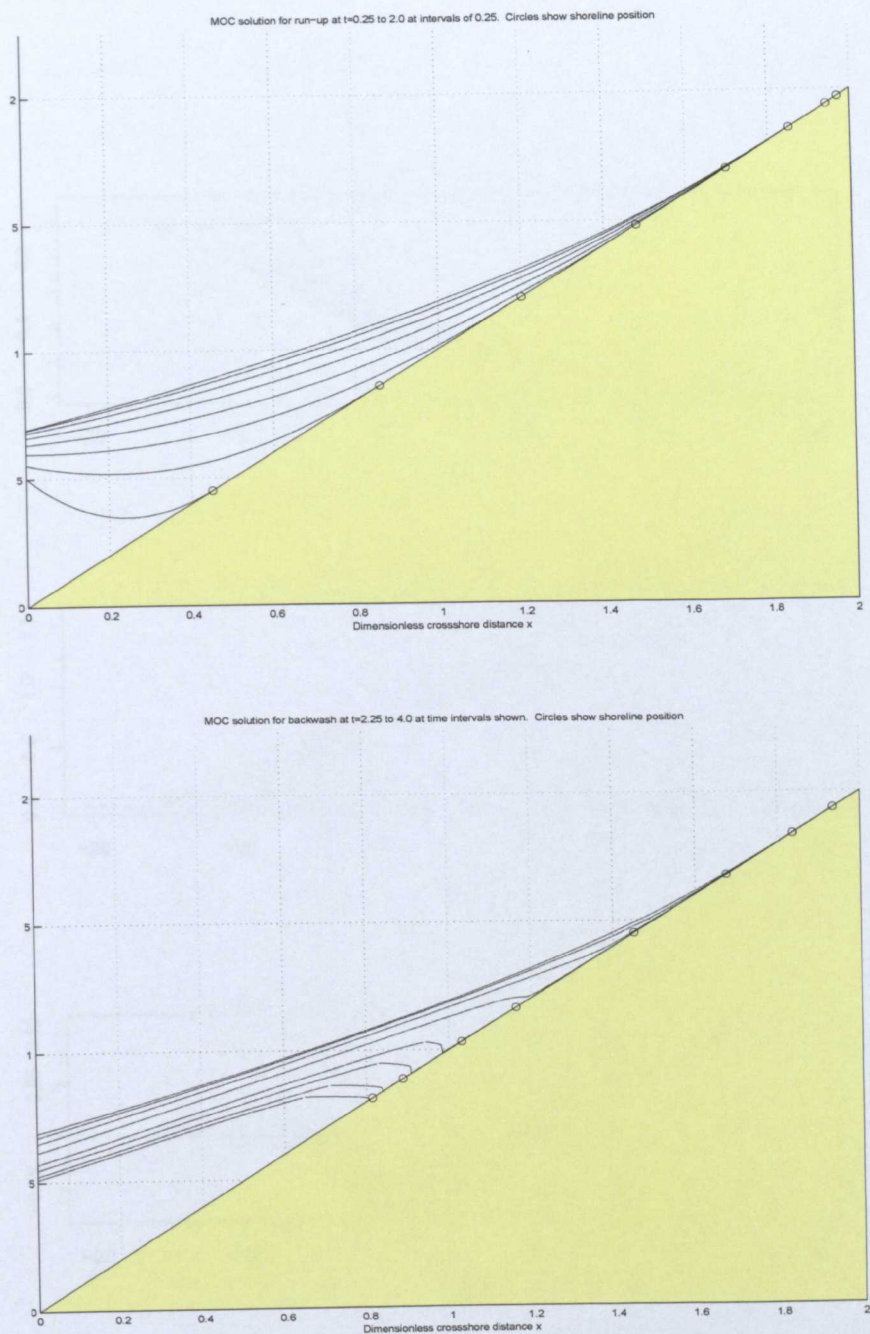


Figure D.2: Non-dimensional water surface elevation for a single swash event showing run-up (top) and backwash (bottom) computed using second-order GC MOC scheme. The backwash bore was detected and fitted using the techniques detailed in §§5.4.2 and 5.4.4. Circles indicate the shoreline position.

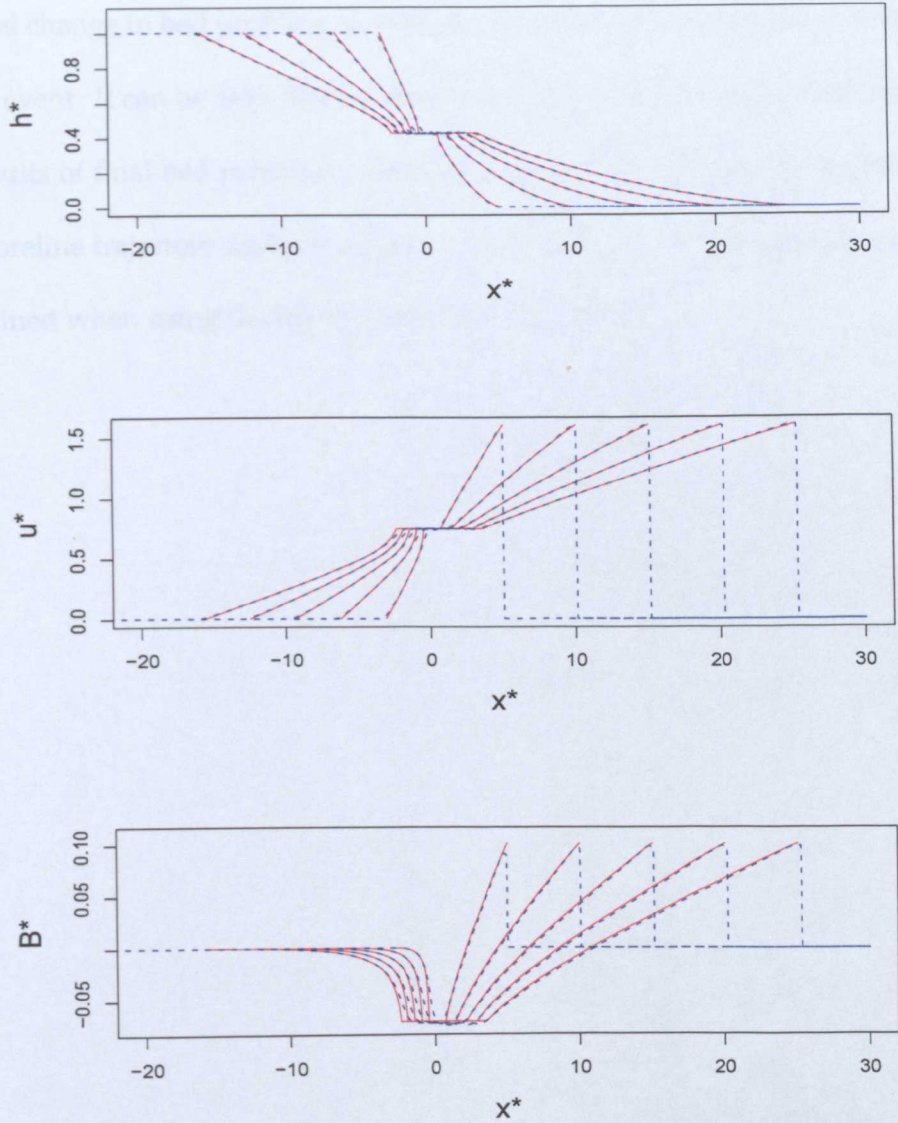


Figure D.3: Snapshots of the wet-dry mobile bed dam-break problem with $q = Au^3$ solved using the MacCormack-mLxF scheme (blue dashed lines) compared with the quasi-analytical solution (red solid lines). Here $\Delta x = 0.01\text{m}$.

the wave structure is in excellent agreement with that predicted in Chapter 6. Finally, as no analytical solution is available for mobile bed SM63 type swash events, in Figure D.6 a check for convergence is shown for the STI MOC solver. The check is made for the final change in bed profile and instantaneous shoreline position for an entire SM63 swash event. It can be seen that for mesh spacings of 0.01m and 0.005m agreement in the results of final bed profile are visually perfect. It is also clear from the figure that the shoreline trajectory also converges as Δx is reduced. A similar level of agreement is obtained when using the MacCormack-mLxF solver.

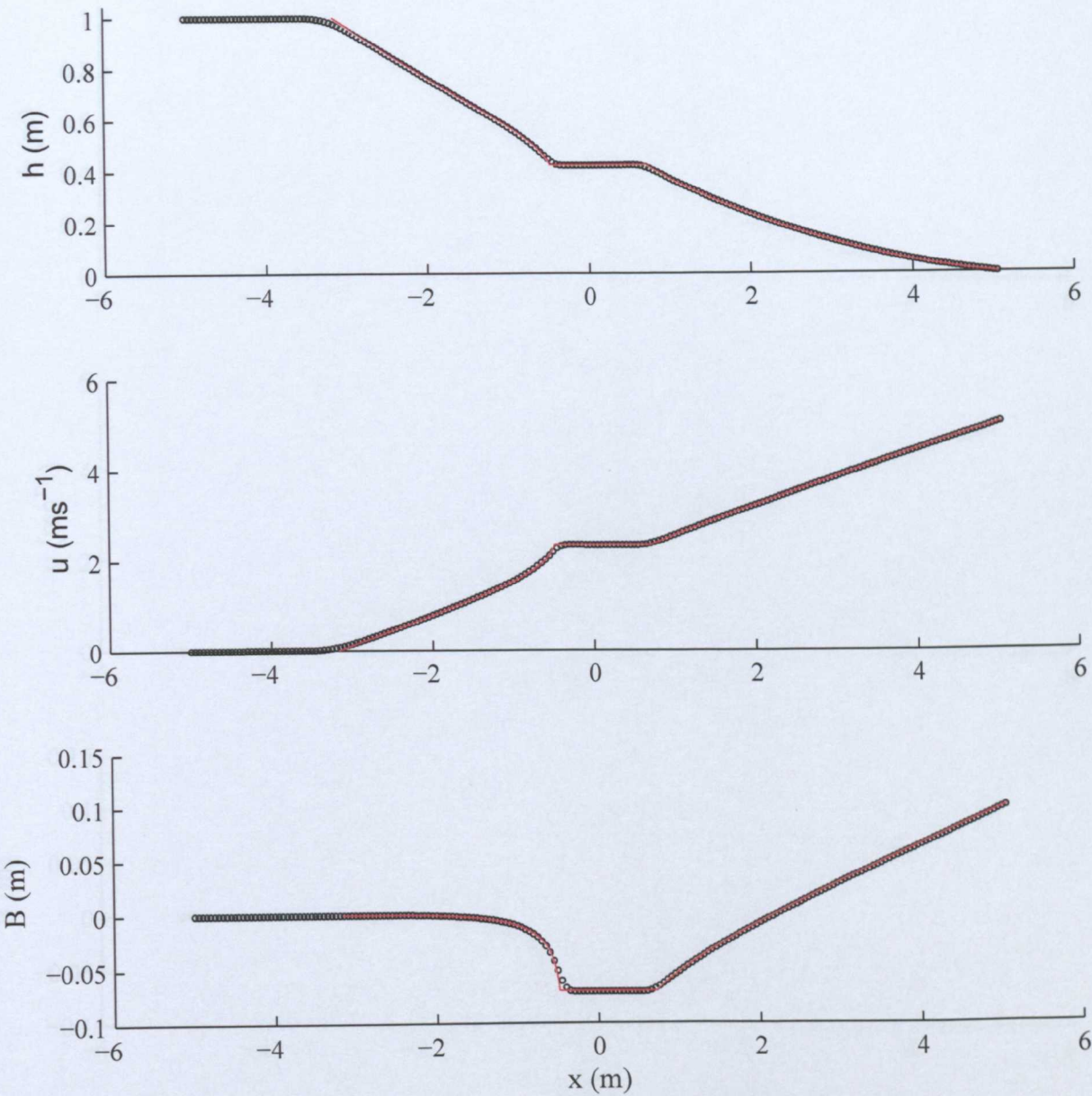


Figure D.4: Snapshots of all dependent variables at $t=1\text{s}$ for mobile bed dam-break with $\sigma=0.03924$. First-order STI MOC results with $\Delta x=0.01\text{m}$ plotted every 5 data points (circles) and quasi-analytical solution (lines).

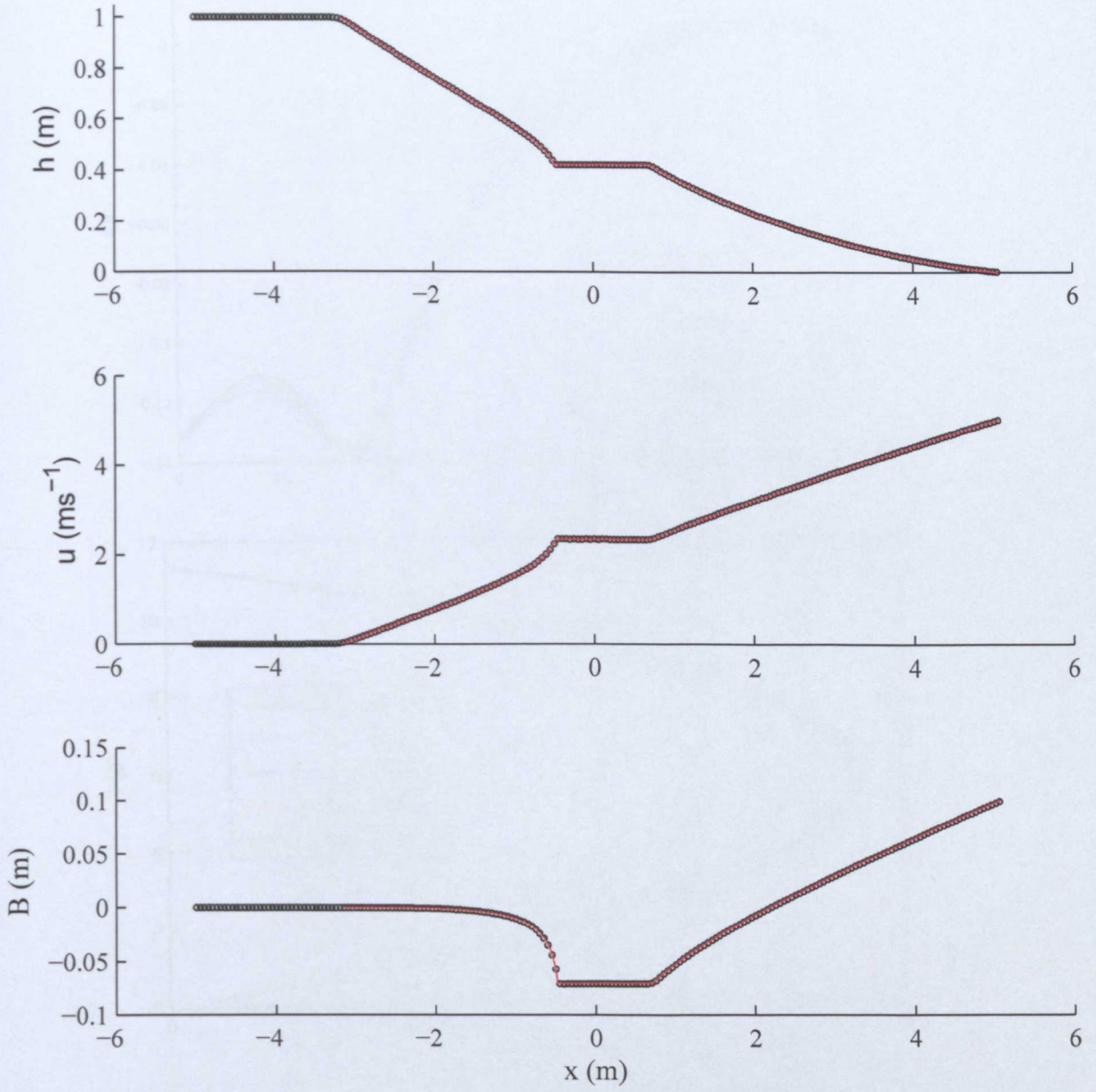


Figure D.5: Snapshots of all dependent variables at $t=1\text{s}$ for mobile bed dam-break with $\sigma=0.03924$. Second-order STI MOC results with $\Delta x=0.01\text{m}$ plotted every 5 data points (circles) and quasi-analytical solution (lines).

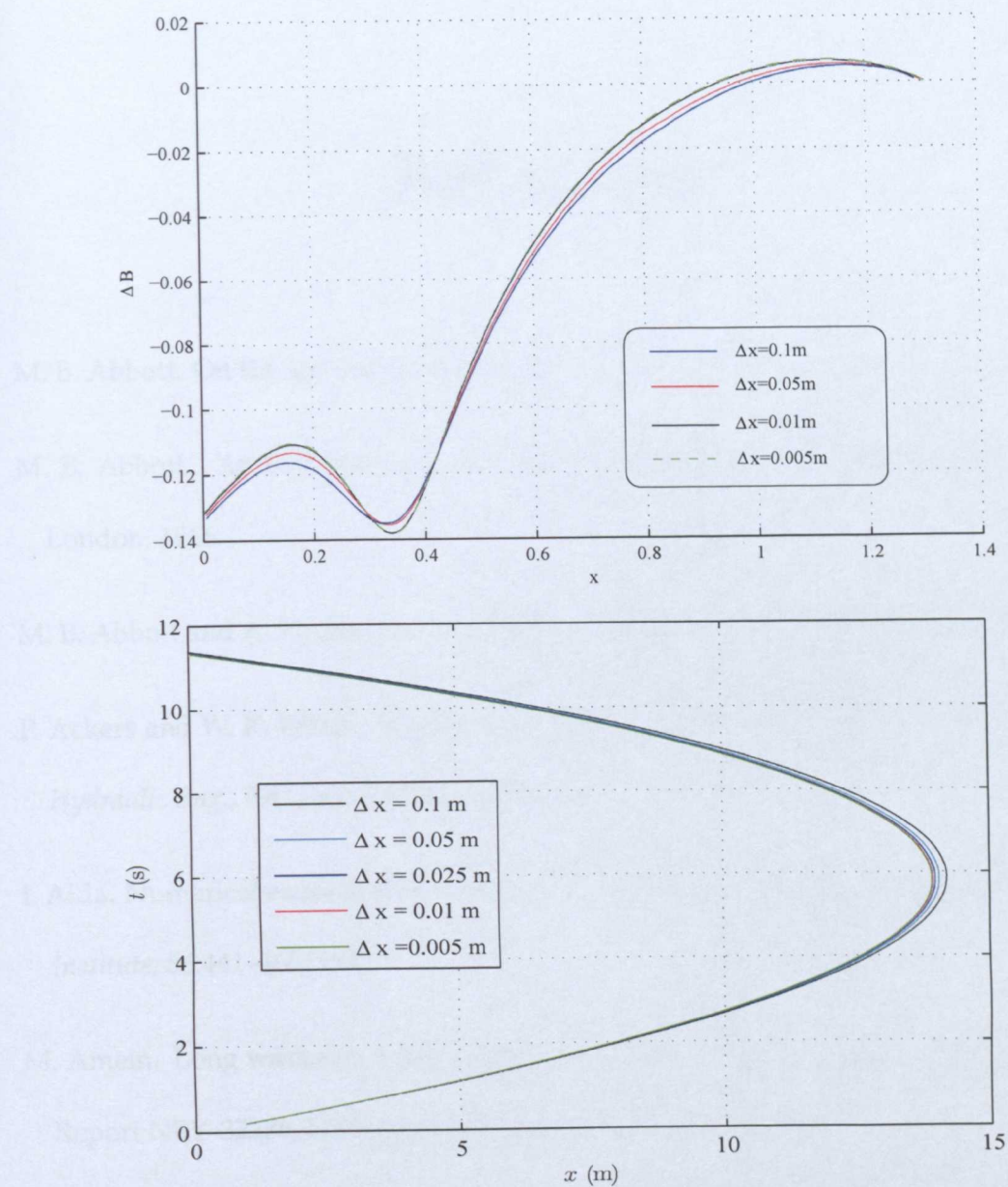


Figure D.6: Testing convergence of the STI MOC scheme as Δx is meshed down using (top) final bed level change (ΔB) as an indicator and (bottom) using the instantaneous shoreline position ($x_*[\text{m}]$) as an indicator ($\sigma=0.0654$ and t_I is fixed at 0.2s).

References

- M. B. Abbott. On the spreading of one fluid over another. *La Houille Blanche*, 5, 1961.
- M. B. Abbott. *An Introduction to the method of characteristics*. Thames and Hudson, London, 1966.
- M. B. Abbott and A. W. Minns. *Computational Hydraulics*. Pitman, New York, 1979.
- P. Ackers and W. R. White. Sediment transport – new approach and anaysis. *ASCE J. Hydraulic Eng.*, 99(11):2041–2060, 1973.
- I. Aida. Numerical experiments for inundation of tsunami. *Bulletin Earthquake Research Institute*, 56:441–460, 1977.
- M. Amein. Long waves on a sloping beach and wave forces on a pier deck. Technical Report NBY-32236, US Navy Civil Engineering Lab., 1964.
- C. Ancey and M. Rentschler. An exact solution for ideal dam-break floods on steep slopes. *AGU J. Wat. Res. Research*, 44, 2008.
- M. Antuono, M. Brocchini, and G. Grosso. Integral properties of the swash zone and averaging. part 3. shoreline boundary conditions: the longshore flow. *J. Fluid Mech.*, 573:399–415, 2007.

- R. A. Bagnold. *The physics of sediment transport by wind and water*, chapter An Approach to the Sediment Transport Problem From General Physics, pages 231–291. ASCE, New York, 1966.
- J. W. Barker and G. B. Whitham. The similarity solution for a bore on a beach. *Comm. Pure Appl. Math.*, 33:447–460, 1980.
- J. Boris. *Proceedings of the seminar course on computing as a language of physics*, chapter 1. A fluid transport algorithm that works, pages 2–20. ICTP, Trieste, Italy, 1971.
- J. P. Boris and D. L. Book. Flux-corrected transport 1: Shasta, a fluid transport algorithm that works. *J. Comp. Physics*, 11:38–69, 1973.
- J. P. Boris and D. L. Book. Solution of the continuity equation by the method of flux-corrected transport. *Methods in Computational Physics*, 16:85–129, 1976.
- J. P. Boris, A. M. Landsberg, E. S. Oran, and J. H. Gardner. Lcpfct – flux corrected transport algorithm for solving generalised continuity equations. Technical Report NRL/MR/6410-93-7192, US Naval Research Laboratory, 1993.
- M. Breuss. An analysis of the influence of data extrema on some first and second order central approximations of hyperbolic conservation laws. *Mathematical Modelling and Numerical Analysis*, 39:965–993, 2005.
- M. Breuss. Conservative shock filtering of numerical solutions of the 1-d euler equations. Technical Report Preprint No. 178, Fachrichtung Mathematic Universität des Saarlandes, 2006.
- M. Breuss and M. Welk. A conservative shock filter model for the numerical approximation of conservation laws. *Applied Mathematics Letters*, 19:954–959, 2006.

REFERENCES

- R. Briganti and N. Dodd. Shoreline motion in non-linear shallow water coastal models. *Coastal Eng. To appear*, 2008.
- M. Brocchini and T. Baldock. Recent advances in modelling swash zone dynamics: The influence of surf swash interaction on nearshore hydro- and morphodynamics. *Reviews of Geophysics*, 46, 2008.
- M. Brocchini, R. Bernetti, A. Mancinelli, and G. Albertini. An efficient solver for nearshore flows based on the waf method. *Coastal Eng.*, 43:105–129, 2001.
- T. Butt and P. Russell. Hydrodynamics and cross shore sediment transport in the swash zone of natural beaches: a review. *J. Cont. Shelf Res.*, 16:255–268, 2000.
- T. Butt, P. Russell, J. Puleo, J. Miles, and G. Masselink. The influence of bore turbulence on sediment transport in the swash and inner surf zones. *J. Cont. Shelf Res.*, 24:757–771, 2004.
- Z. Cao, G. Pender, S. Wallis, and P. Carling. Computational dam-break hydraulics over erodible sediment bed. *ASCE J. Hydraulic Eng.*, 130:689–703, 2004.
- H. Capart and D. L. Young. Formation of a jump by the dam-break wave over a granular bed. *J. Fluid Mech.*, 372:165–187, 1998.
- G. F. Carrier and H. P. Greenspan. Water waves of finite amplitude on a sloping beach. *J. Fluid Mech.*, 4:97–109, 1958.
- H. Chanson. Applications of the saint-venant equations and method of characteristics to the dam break wave problem. *Report No. CH55/05*, 2005.
- Y. Chen and D. B. Simons. An experimental study of hydraulic and geomorphic change

REFERENCES

- in an alluvial channel induced by the failure of a dam. *AGU J. Wat. Res. Research*, 15: 1183–1188, 1979.
- A. J. Chorin and J. E. Marsden. *A mathematical introduction to fluid mechanics*. Springer Verlag, New York, 1993.
- S. Clarke, N. Dodd, and J. Damgaard. Modeling flow in and above a porous beach. *J. Waterway, Port, Coastal and Ocean Eng.*, 130:223–233, 2004.
- R. Courant and K. O. Friedrichs. *Supersonic flow and shock waves*. New York, reprint edition, 1976.
- J. A. Cunge. Calcul de propagation des ondes de rupture de barrage. calculation of dam-break waves. *La Houille Blanche*, 96:25–33, 1970.
- J. A. Cunge, F. M. Holly, and A. Verwey. *Practical aspects of computational river hydraulics*. Pitman Advanced Publishing Program, Boston, 1980.
- D. Dicker. *Flow through porous media*, chapter Transient free surface flow in porous media, pages 293–330. Academic, New York, 1969.
- M. DiGiacinto and M. Valorani. Shock detection and discontinuity tracking for unsteady flows. *Computers and Fluids*, 17:61–84, 1989.
- N. Dodd, A. Stoker, D. Calvete, and A. Sriariyawat. On the evolution of beach cusps. *J. Fluid Mech.*, 597:145–169, 2008.
- T. Dracos. Die berechnung instationärer abflüsse in offenen gerinnen beliebiger geometrie (*The calculation of non-constant flow in open channels of any geometry*). *Schweizerische Bauzeitung (Swiss Construction)*, 19:1–8, 1970.

REFERENCES

- R. F. Dressler. Hydraulic resistance effects upon the dam-break functions. *Journal of Research National Bureau of Standards*, 49:217–225, 1952.
- P. Dronkers. *Tidal Computations in rivers and coastal waters*. North Holland Publishing Co., Amsterdam, 1964.
- B. Engquist, P. Lötstedt, and B. Sjögreen. Nonlinear filters for efficient shock computation. *Mathematics of Computation*, 52:509–537, 1989.
- L. Erikson, M. Larson, and H. Hanson. Prediction of swash motion and run-up including the effects of swash interaction. *Coastal Eng.*, 52:285–302, 2004.
- J. Faure and N. Nahas. étude numerique et expérimentale d'intumescences à forte courbure du front. a numerical and experimental study of steep fronted surge waves. *La Houille Blanche*, 16:576–586, 1961.
- R. M. L. Ferreira and J. G. A. B. Leal. 1d mathematical modelling of the instantaneous dam-break flood wave over mobile bed: application of tvd and flux-splitting schmes. Technical report, Departamento de engenharia civil instituto superior técnico, Lisboa, 2003.
- L. Fraccarollo and H. Capart. Riemann wave descriptions of erosional dam-break flow. *J. Fluid Mech.*, 461:183–228, 2002.
- J. Fredsøe and R. Deigaard. *Mechanics of coastal sediment transport*. World Scientific Publishing, Singapore, 1994.
- J. Fredsøe and R. Deigaard. *Mechanics of coastal sediment transport*. World Scientific Publishing, New Jersey, 1992.

- J. C. Freeman and B. LeMéhauté. Wave breakers on a beach and surges on a dry bed. *ASCE J. Hydraulic Eng.*, 90:187–216, 1964.
- C. J. Galvin. Breaker type classification on three laboratory beaches. *J. Geophysical Res.*, 73:3651–3659, 1968.
- C. J. Galvin. Waves on beaches and resulting sediment transport. chapter Wave breaking in shallow water, pages 413–456. Academic Press, London, 1972.
- A. J. Grass. Sediment transport by waves and currents. Technical Report FL29, London Centre for Marine Technology, University College London, 1981.
- P. A. Guard and T. Baldock. The influence of seaward boundary conditions on swash zone hydrodynamics. *Coastal Eng.*, 54:321–331, 2007.
- G. Guderly. Starke kugelige und zylindrische verdichtungsstöße in der nähe des kugelmittelpunktes bzw. der zylinderachse (*Strong spherical and cylindrical impacts near the centre of a sphere*). *Luftfahrtforschung (Aviation Technology)*, 19:302–311, 1942.
- B. Gustafsson, H. O. Kreiss, and J. Oliger. *Time dependent problems and difference methods*. Pure and Applied Mathematics. Wiley Interscience, New York, 1992.
- F. H. Harlow and A. A. Amsden. A simplified mac technique for incompressible fluid flow calculations. *J. Comput. Physics*, 6:322–325, 1970.
- A. Harten. From artifical viscosity to eno schemes. Technical Report CAM 89–24, UCLA Department of Mathematics, 1989.
- A. Harten and G. Zwas. Self-adjusting hybrid schemes for shock computations. *J. Comput. Physics*, 9:568–583, 1972.

REFERENCES

- F. M. Henderson. *Open Channel Flow*. Macmillan Series in Civil Engineering, New York, 1966.
- S. Hibberd. *Surf and Run-Up*. PhD thesis, School of Mathematics, University of Bristol, UK, 1977.
- S. Hibberd and D. H. Peregrine. Surf and run-up on a beach : a uniform bore. *J. Fluid Mech.*, 95:323–345, 1979.
- C. Hirsch. *Numerical computation of internal and external flows: Volume 2*. John Wiley and sons, New York, 1988.
- D. V. Ho and R. E. Meyer. Climb of a bore on a beach part 1: Uniform beach slope. *J. Fluid Mech.*, 14:305–318, 1962.
- A. Hogg. Lock-release gravity currents and dam-break flows. *J. Fluid Mech.*, 569:61–87, 2006.
- H. Holden and N. H. Risebro. *Front tracking for hyperbolic conservation laws*. Springer, New York, 2002.
- D. P. Horn and T. Mason. Swash zone sediment transport modes. *J. Mar. Geology*, 120: 309–325, 1994.
- D. D. Houghton and A. Kasahara. Non-linear shallow fluid flow over an isolated ridge. *Comm. Pure Appl. Math.*, 21:1–23, 1968.
- H. C. Hsu and P. C. Chu. Study of river bed variation by the method of characteristics. *Scientia Sinica (Hyd. Eng.)*, 11:1674–1690, 1965.
- T. J. Hsu and B. Raubenheimer. A numerical and field study on inner-surf and swash sediment transport. *J. Cont. Shelf Res.*, 26:589–598, 2006.

REFERENCES

- M. Hubbard and P. Garcia-Navarro. Flux difference splitting and the balancing of source terms and flux gradients. *J. Comp. Physics*, 165:89–125, 2000.
- J. Hudson and P. K. Sweby. Formulations for numerically approximating hyperbolic systems governing sediment transport. *Journal of Scientific Computing*, 19(8):225–252, 2003.
- B. Hunt. Asymptotic solution for dam-break problems. *ASCE J. Hyd. Division*, 108: 115–126, 1982.
- B. Hunt. Perturbation solution for dam-break floods. *J. Hydraulic Eng.*, 110:1058–1071, 1984.
- A. Jeffrey. *Quasilinear Hyperbolic Systems and Waves*. Pitman, London, 1976.
- J. T. Jenkins and E. Askari. Boundary conditions for rapid granular flows. *J. Fluid Mech.*, 223:497–508, 1991.
- R. S. Johnson. *A modern introduction to the mathematical theory of water waves*. Cambridge University Press, Cambridge, 1997.
- T. V. Karambas and C. Koutitas. Surf and swash zone morphological evolution induced by non-linear waves. *ASCE J. Waterways, Ports, Coastal and Ocean Eng.*, 128:102–113, 2002.
- H. B. Keller, D. A. Levine, and G. B. Whitham. Motion of a bore over a sloping beach. *J. Fluid Mech.*, 7:302–316, 1960.
- D. M. Kelly and N. Dodd. Floating grid characteristics method for unsteady flow over a mobile bed. *Comp. and Fluids To appear*, 2008.

REFERENCES

- N. Kobayashi, A. K. Otta, and I. Roy. Wave reflection and run-up on rough slopes. *ASCE J. Waterways Ports and Coastal Eng.*, 113:282–298, 1987.
- N. Kobayashi, G. S. DeSilva, and K. D. Watson. Wave transformation and swash oscillations on gentle and steep slopes. *J. Geophysical Res.*, 94:951–966, 1989.
- C. Lai. *Advances in Hydrosience (Vol.14)*, chapter Numerical modelling of unsteady open channel flow, pages 95–121. Academic Press, London, 1986.
- C. Lai. Modelling alluvial-channel flow by multimode characteristic method. *ASCE J. Engineering Mech.*, 117:32–53, 1991.
- V. M. L'atkher and S. Y. Shkol'nikov. *Tsunami research in the open ocean*, chapter Calculation of the tsunami run-up. NAUKA, Moscow, 1978.
- P. Lax. Weak solutions of nonlinear hyperbolic equations and their numerical computation. *Comm. Pure and Applied Mathematics*, 7:159–193, 1954.
- P. Lax and B. Wendroff. Systems of conservation laws. *Comm. Pure and Applied Mathematics*, 13:217–237, 1960.
- B. LeMéhauté. On non-saturated breakers and the wave run-up. In *Proceedings of Eighth Conference on Coastal Engineering Mexico*, pages 77–92. Council on Wave Research, 1963.
- A. Lerat and R. Peyret. Noncentred schemes and shock propagation. *Computers and Fluids*, 2:35–52, 1974.
- R. J. LeVeque. *Finite volume methods for hyperbolic problems*. Cambridge University Press, Cambridge, 2002.

- R. J. LeVeque. *Numerical methods for conservation laws*. Lectures in mathematics. Birkhäuser Verlag, Basel, 2nd edition, 1992.
- Y. Li and F. Raichlen. Non-breaking and breaking solitary wave run-up. *J. Fluid Mech.*, 456:295–318, 2002.
- M. Lister. Mathematical methods for digital computers. chapter 4. The numerical solution of hyperbolic differential equations by the method of characteristics, pages 165–179. John Wiley & Sons, New York, 1960.
- M. Lister and L. Roberts. On the numerical solution of spherical waves of finite amplitudes. Technical Report MIT-Proj DIC6915, Massachusetts Institute of Technology, 1956.
- R. W. MacCormack. The effect of viscosity on hypervelocity impact cratering. Technical Report Paper 69–354, AIAA, 1969.
- C. L. Mader. Numerical simulation of tsunamis. *J. Phys. Oceanography*, 4:74–82, 1974.
- G. Masselink and M. G. Hughes. Field investigation of sediment transport in the swash zone. *Cont. Shelf Res.*, 18:1179–1199, 1998.
- G. Masselink and L. Li. The role of swash infiltration in determining the beachface gradient: a numerical study. *J. Mar. Geology*, 176:139–156, 2001.
- G. Masselink and J. A. Puleo. Swash-zone morphodynamics. *Cont. Shelf Res.*, 26:661–680, 2006.
- G. Masselink, D. Evans, M. G. Hughes, and P. Russell. Suspended sediment transport in the swash of a dissipative beach. *J. Mar. Geology*, 216:169–189, 2005.
- N. Matsunaga and H. Honji. The backwash vortex. *J. Fluid Mech.*, 99:813–815, 1980.

- C. C. Mei. *The Applied Dynamics of Ocean Surface Waves (Advanced Series on Ocean Engineering-Volume1)*. World Scientific Publishing, 1989.
- R. L. Miller. Experimental run-up of undular and fully developed bores. *J. Geophys. Res.*, 73:4497–4510, 1968.
- A. Mohammadian, D. Y. Le Roux, and M. Tajrishi. A conservative extension of the method of characteristics for 1-d shallow flows. *Applied Mathematical Modelling*, 31: 332–348, 2007.
- G. Moretti. A critical analysis of numerical techniques: the piston-driven inviscid flow. Technical Report Pibal 69–25, Polytechnic inst. of Brooklyn dept. of aerospace engineering and applied mechanics, 1969.
- G. Moretti. Complicated one-dimensional flows. Technical Report Pibal 71–25, Polytechnic inst. of Brooklyn dept. of aerospace engineering and applied mechanics, 1971.
- G. Moretti. Experiments in multi-dimensional floating shock-fitting. Technical Report Pibal 73–18, Polytechnic inst. of Brooklyn dept. of aerospace engineering and applied mechanics, 1973.
- G. Moretti. Thirty-six years of shock fitting. *Computers and Fluids*, 31:719–723, 2002.
- G. Moretti. Computation of flows with shocks. *Ann. Rev. Fluid Mech.*, 19:313–337, 1987.
- G. Moretti and T. DiPiano. An improved lambda-scheme for one-dimensional flows. Technical Report NASA contractor report 3712, NASA Langley Research Centre, 1983.
- E. M. Murman. Analysis of embedded shock waves calculated by relaxation methods. *AIAA Journal*, 12:626–633, 1974.

REFERENCES

- J. Murray. Experimental investigation of mobile bed dam-break events. Master's thesis, School of Civil Engineering, University of Nottingham, UK, 2007.
- D. J. Needham and R. D. Hey. On nonlinear simple waves in alluvial river flows: a theory for sediment bores. *Philosophical Transactions of the Royal Society London*, 334A: 25–53, 1991.
- P. D. Osborne and G. A. Rooker. Sand re-suspension events in a high energy infragravity swash-zone. *J. Coastal Res.*, 15:74–86, 1999.
- A. R. Packwood. *Surf and Run-Up On Beaches*. PhD thesis, School of Mathematics, University of Bristol, UK, 1980.
- A. R. Packwood. The influence of beach porosity on wave uprush and backwash. *Coastal Eng.*, 7:29–40, 1983.
- R. B. Payne. A numerical method for a converging cylindrical shock. *J. Fluid Mech.*, 2: 185–200, 1957.
- D. H. Peregrine. *Waves on beaches and resulting sediment transport*, chapter 3. Equations for water waves and the approximation behind them, pages 95–121. Academic Press, London, 1972.
- D. H. Peregrine and S. M. Williams. Swash overtopping a truncated beach. *J. Fluid Mech.*, 440:391–399, 2001.
- M. Petti and S. Longo. Turbulence experiments in the swash zone. *Coastal Eng.*, 43: 1–24, 2001.
- W. H. Press, S. A. Teukolsky, W. T. Vetterling, and B. P. Flannery. *Numerical Recipes: The Art of Scientific Computing*. Cambridge University Press, 3rd edition, 2007.

REFERENCES

- D. Pritchard and A. Hogg. On the transport of suspended sediment by a swash event on a plane beach. *Coastal Eng.*, 52:1–23, 2005.
- D. Pritchard, P. A. Guard, and T. E. Baldock. An analytical model for bore-driven run-up. *J. Fluid Mech.*, 610:183–193, 2008.
- J. A. Puleo, T. Butt, and N. G. Plant. Instantaneous energetics sediment transport model calibration. *Coastal Eng.*, 52:647–653, 2005.
- R. Rajar. Mathematical simulation of dam-break flow. *ASCE J. Hydraulic Eng.*, 104:1011–1026, 1978.
- Lord Rayleigh. On the theory of long waves and bores. *Proc. Royal Soc.*, 90A, 1914.
- R. Ré. étude du lacher instantané d’une retenue d’eau dans un canal par la méthode graphique. a study by the graphical method of the instantaneous release of a reserve of water into a channel. *La Houille Blanche*, 1, 1946.
- A. Ritter. Die fortpflanzung der wasserwellen. *Vereine Deutcher Ingenieure Zetswchrift*, 36:947–954, 1892.
- P. L. Roe. Approximate riemann solvers, parameter vectors and difference schemes. *J. Comp. Physics*, 43:357–372, 1981.
- S. C. Ryrie. Longshore motion generated on beaches by obliquely incident bores. *J. Fluid Mech.*, 129:193–212, 1983.
- J. G. Sakkas. *Analysis of surge propagation in a dry channel*. PhD thesis, School of Civil Engineering, University of California (Davis), USA, 1972.
- J. G. Sakkas and T. Strelkoff. Dam-break flood in a prismatic dry channel. *ASCE J. Hydraulic Eng.*, 99:2195–2216, 1973.

- C. Savary. *Transcritical transient flow over mobile beds boundary conditions treatment in a two layer shallow-water model*. PhD thesis, Faculty of applied sciences, Université catholique de Louvain, Belgium, 2007.
- M. C. Shen and R. E. Meyer. Climb of a bore on a beach part 3: Run-up. *J. Fluid Mech.*, 16:113–125, 1963.
- J. Sieben. *Modelling of hydraulics and morphology in mountain rivers*. PhD thesis, School of Civil Engineering, Delft University of Technology, Netherlands, 1997.
- J. Sieben. A theoretical analysis of discontinuous flow with a mobile bed. *J. Hydraulic Res.*, 37(2):199–212, 1999.
- A. Sielecki and M. G. Wurtele. The numerical integration of the nonlinear shallow water equations with sloping boundaries. *J. Comp. Physics*, 6:219–236, 1970.
- R. Soulsby. *Dynamics of Marine Sands*. Thomas Telford Ltd, 1997.
- M. R. Spiegel and J. Liu. *Mathematical handbook of formulas and tables*. McGraw-Hill, New York, 1999.
- L. Q. Spielvogel. Single wave run-up on beaches. *J. Fluid Mech.*, 74:685–694, 1976.
- J. J. Stoker. The formation of breakers and bores. *Comm. Pure Appl. Math.*, 1:1–87, 1948.
- C. E. Synolakis. *The run-up of long waves*. PhD thesis, School of Mathematics, California Institute of Technology, USA, 1986.
- E. Tadmor. Numerical viscosity and the entropy condition for conservative difference schemes. *Mathematics of Computation*, 43:369–381, 1984.
- T. Takahashi. *Debris Flow*. IAHR Monograph, 1991.

- H. Takeda. Numerical simulation of run-up by variable transformation. *J. Ocean. Soc. Jap.*, 40:271–278, 1984.
- V. V. Titov and C. E. Synolakis. Modelling of breaking and nonbreaking long wave evolution and run-up using vtcs-2. *ASCE J. Waterway Ports and Coastal and Ocean Eng.*, 121:308–316, 1995.
- E. Toro. *Shock-capturing methods for free-surface shallow flows*. Wiley, New York, 2001.
- E. F. Toro. *Riemann solvers and numerical methods for fluid dynamics : a practical introduction*. Springer Verlag, 2nd edition, 1999.
- S. Vincent, J. P. Caltagirone, and P. Bonneton. Numerical modelling of bore propagation and run-up on sloping beaches using a macormack tvd scheme. *J. Hydraulic Res.*, 39: 41–49, 2001.
- J. von Neumann and R. D. Richtmyer. A method for the numerical calculation of hydrodynamic shocks. *J. Applied Physics*, 21:232–237, 1950.
- G. Watson, D. H. Peregrine, and E. F. Toro. Numerical solution of the shallow-water equations on a beach using the weighted average flux method. *Computational Fluid Dynamics*, 1:495–501, 1992.
- G. B. Whitham. The effects of hydraulic resistance on the dam-break problem. *Proc. Royal Soc.*, 227A:399– 407, 1955.
- G. B. Whitham. On the propagation of shock waves through regions of non-uniform area or flow. *J. Fluid Mech.*, 4:337–360, 1958.
- G. B. Whitham. *Linear and Nonlinear Waves*. Wiley Interscience monographs. John Wiley and Sons, New York, 1st edition, 1974.

REFERENCES

- C. M. Wu. *Unsteady flow in open channel with movable bed*. International symposium on river mechanics, Bangkok, 1973.
- S. T. Zalesak. Fully multi-dimensional flux-corrected transport algorithms for fluids. *J. Comp. Physics*, 31:335–362, 1979.
- Y. Zech, S-F. Soares, B. Spinewine, and N. Le Grelle. Dam-break induced sediment movement: experimental approaches and numerical modelling. *J. Hydraulic Res.*, 46: 176–190, 2008.
- C. Zoppou and S. Roberts. Explicit schemes for dam-break simulations. *ASCE J. Hydraulic Eng.*, 129:11–34, 2003.